Fermilab FERMILAB-THESIS-1995-01

Omega Meson Production at High Transverse Momentum by Negative 515 GeV/c Pions Incident on Beryllium and Copper Targets

by

Lucyna de Barbaro

Submitted in Partial Fulfillment
of the
Requirements for the Degree

DOCTOR OF PHILOSOPHY

Supervised by: Professor Paul Slattery

Department of Physics and Astronomy
The College
Arts and Sciences

University of Rochester
Rochester, New York

1995

Curriculum Vitae

The author was born in Cracow, Poland on February 11, 1961. She attended Jagellonian University in Cracow from 1979 to 1985, and graduated with a Master of Science degree in 1985. She came to the University of Rochester in the fall of 1987 and began graduate studies in Physics. She has been involved in research projects related to Fermilab experiment E706 throughout her studies. She pursued her research under the direction of Professors Paul Slattery and Fred Lobkowicz and received a Master of Arts degree in 1989.

Acknowledgments

I would like to express my gratitude to Professor Paul Slattery for his attention and continued support throughout my graduate study and research work at E706. While at Fermilab, I also received guidance from professors Tom Ferbel, Fred Lobkowicz, Carl Bromberg and Phil Guttierez, for which I am thankful. I had a chance to interact with and learn from generations of researchers, postdoctoral fellows, graduate students and supporting personnel involved in this experiment including George Alverson, Lenny Apanasevich, John Bacigalupi, Win Baker, Giuseppe Ballocchi, Richard Benson, David Brown, Michael Begel, Steve Blusk, Paoti Chang, Brajesh Choudhary, Woohyun Chung, Bill DeSoi, Bud Dickerson, Wieslaw Dlugosz, Jim Dunlea, Sajan Easo, Gene Engels, George Fanourakis, Jan Ftacnik, David Garelick, George Ginther, Mike Glaubman, Casey Hartman, Joey Huston, Carol Johnstone, Vijay Kapoor, Bud Koecher, Ioanis Kourbanis, John Kuehler, Armando Lanaro, Chris Lirakis, Pat Lukens, Paul Madsen, Sudhindra Mani, John Mansour, Andre Maul, Robert Miller, Ai Nguyen, Ben Oh, George Osborne, Ed Pothier, Eric Prebys, Rob Roser, Dan Ruggiero, Paul Shepard, Mr. Shi, R. Shivpuri, Alex Sinanidis, Dane Skow, Lee Sorrell, David Striley, Roger Tokarek, Bill Toothacker, Jim Tweed, Nikos Varelas, Dhammika Weerasundara, Jim Whitmore, Takahiro Yasuda, Carlos Yosef, Marek Zielinski and Vishnu Zutshi. I am impressed with their skills, their work style and their commitment to make this experiment a success. Thank you all, my colleagues and collaborators!

George Ginther was instrumental in introducing me to and guiding me through the complexity of this high energy experiment, including the analysis work described in this document. I join the multitude of students grateful to George for his attention and dedication.

I graciously acknowledge the welcoming spirit which I encountered upon my arrival and while studying in this country. I was among the beneficiaries of the federally funded medical program when my daughter Izabella was delivered at the Stanford Hospital in California in 1986. I can only wish that the generosity extended to us will continue to be provided to other needy persons, and that the social programs grow, rather than be cancelled.

There are only a few places in the world where scientific research is done on a scale and with the expenditure of resources similar to that of Fermilab. I am grateful for having had the chance to participate in the work done at this laboratory. I am also personally greatly enchanted with the natural environment preserved and developed on the grounds of Fermilab. It is a wonderous fact that the cutting-edge technology and instrumentation of high energy physics coexists here with populations of over 200 species of birds and amongst the tall grasses of restored prairie!

Omega Meson Production at High Transverse Momentum
by Negative 515 GeV/c Pions Incident on
Beryllium and Copper Targets

by

Lucyna de Barbaro

The inclusive cross section for $\omega(783)$ meson production by 515 GeV/c π^- beam incident on Be and Cu targets has been measured as a function of transverse momentum (p_T). The data were collected during the 1990 run of experiment E706 at Fermilab. The E706 trigger selected events containing high p_T electromagnetic showers detected in a finely segmented lead liquid argon calorimeter. The ω mesons were reconstructed in the neutral decay mode $\omega \rightarrow \pi^0\gamma$. Results are reported averaged over the center of mass rapidity interval -0.5 $< y <$ 0.75, and in the transverse momentum range from 3.5 to 8 GeV/c. The ω to π^0 production ratio was measured and used to obtain the ratio of vector to pseudoscalar mesons directly produced in the fragmentation process. Measurements are compared with HERWIG 5.7 Monte Carlo results, and with data from other experiments. The nuclear dependence of ω meson production is also discussed.

Chapter 1 Introduction

This thesis describes a study of the inclusive production of high transverse momentum omega mesons in $\pi^- + Be \rightarrow \omega + X$ interactions at 515 GeV/c. The data analyzed here were collected by experiment E706 at Fermi National Accelerator Laboratory during the 1990 fixed target run. The experiment was designed to perform precise measurements of high transverse momentum phenomena in hadron-nucleus and hadron-proton interactions.

1.1 Historic Overview

Like many other elementary particles, the omega meson has only been known to physicists for a few decades. The development of the quantum theories of electromagnetic, weak, and strong interactions and the accumulation of experimental data pertinent to testing these theories are also relatively recent endeavors. The history of the discovery of the omega meson has been tightly interwoven with the advances made in the field of high energy particle physics. The first suggestion of the existence of the ω was purely theoretical. It came from Yoichiro Nambu[1] at the Rochester Conference on High Energy Nuclear Physics in 1957. Nambu called for the existence of a heavy neutral meson with zero isotopic spin and $J^P = 1^-$ in an attempt to explain the electromagnetic form factors (or charge distributions) of the proton and neutron measured in Stanford electron scattering experiments. He called the proposed particle a π^0 prime and attributed to it a role similar to the π^0 in mediating the nuclear interactions. In 1960, Sakurai[2] suggested that strong interactions should arise from a gauge principle, that is, the full Lagrangian of the theory should be determined from the requirement of symmetry under the chosen group of transformations. Eventually Sakurai's model and the choice of the $SU(2)_{flavor} \times U(1)_Y$ symmetry group did not

survive as a gauge theory of strong interactions, but it did predict the existence of the ρ and the, at that time still undiscovered, ω meson. It was only a year later, in 1961, that the experimentalists B. Maglic, L. Alvarez, A. Rosenfeld and M. Stevenson[3] reported the discovery of the ω particle and determined its isotopic spin and angular momentum. The group assumed $m_\omega > 3m_\pi$ and searched for the decay $\omega \to \pi^+\pi^-\pi^0$ in 2.29 GeV antiproton on hydrogen collisions $\bar{p}+p \to \pi^+\pi^-\omega$. About 83 ± 16 ωs were observed in 800 $\bar{p} + p \to 2\pi^+2\pi^-\pi^0$ reactions.

In 1964, M. Gell-Mann[4] and G. Zweig[5] introduced the concept of quarks, spin 1/2 fractionally charged particles, now recognized as the building blocks of all nuclear matter. Using the quark concept, the observed regularities and patterns among the known meson and baryon resonances, related to isospin and angular momentum of the particles, could be understood. The omega meson, an isospin singlet, for example, is represented by a combination of up and down quarks with spins aligned ($\uparrow$) in the following fashion:

$$|\omega >= \sqrt{\frac{1}{6}} \sum_{a=R,G,B} (\bar{u}_a u_a + \bar{d}_a d_a)(\uparrow\uparrow)$$

where the sum extends over all color states: R("red"),G("green"), B("blue") and u_a, d_a and $\bar{u}_a$, $\bar{d}_a$ denote up and down quarks of color a, and their respective antiparticles[1].

The color quantum number was postulated to explain quark confinement, that is, the fact that only colorless objects like mesons ($q_a\bar{q}_a$) and baryons ($q_R q_G q_B$) could be observed but not the quarks themselves. Color provided a means for the

[1] This representation assumes "ideal" mixing between a member of the vector meson octet ω_8 and a unitary singlet ω_1, such that the physical particles ω and ϕ, which are superpositions of ω_8 and ω_1, contain only either $\bar{u}_a u_a$ and $\bar{d}_a d_a$ or $\bar{s}_a s_a$ combination.

construction of a totally antisymmetric wave function for baryons like Δ^{++}, built of 3 spin up u_a quarks. Such a state could not otherwise have satisfied the Pauli exclusion principle for fermions. The success and predictive power of the quark model was greatly expanded after the discovery of proton substructure in Deep Inelastic electron Scattering experiments (DIS) performed at the Stanford Linear Accelerator Center[6]. Further experiments showed that the proton momentum was not only carried by quarks but also by spin 1 particles called gluons. The experimental scene soon saw further confirmations of the quark and gluon model – e.g., the discovery of charm and beauty quarks and a host of new charm and beauty resonances. Several confirmations of the existence of the color quantum number – e.g., the measurement of the cross section ratio for $e^+e^- \to hadrons$ relative to $e^+e^- \to \mu^+\mu^-$ production, were also found[7].

All these observations as well as new theoretical advances of that decade, including the formulation of the Glashow - Weinberg - Salam model[8] of electromagnetic and weak interactions, paved the way for the development of Quantum Chromodynamics (QCD), the theory of strong interactions. Current quantum field theories rely on a simple symmetry principle. In these theories, the interactions between particles and fields emerge in the theory from the requirement that the Lagrangian be invariant under local gauge transformations. Since the observed hadrons are colorless, or unchanged under rotations in color space, a $SU(3)_{color}$ group was taken to generate the gauge transformation for QCD. A set of 8 independent bi-color fields, corresponding to the generators of the transformation, became identified as the gluons, which are the mediators of the strong force. The gluons possess color and interact with each other, which directly stems from the non-Abelian properties of $SU(3)_{color}$ (commutation relations of the group dictate the existence of such an interaction).

The non-Abelian character of the group of gauge transformations is also responsible for a property of the theory called asymptotic freedom. The effective coupling constant, or strength of the interaction, α_S, decreases to zero as the characteristic energy Q^2 of the process goes to infinity. Asymptotically, this implies that at very large energy transfers between the colliding (hadronic) particles, the constituents of the these particles act as free, point-like, hard objects. At the other extreme however, with increasing separation between partons[2], the strength of the interaction increases. This increase is responsible for quark confinement.

The property of asymptotic freedom provides a means by which the cross sections for some interactions between partons can be calculated. The cross sections are expanded as a perturbative series in powers of α_S, and only lower order terms are retained. The kinematic regime where α_S is small, and perturbative QCD is applicable, is characterized by large Q^2 transfer and is experimentally manifested by large angle, high transverse momentum scattering.

Figure 1.1 pictorially represents a model of an interaction between two hadrons in a high energy-transfer collision. To obtain the cross section for the production of an observable hadron C in the inclusive reaction $A+B \to C+X$, we convolute the cross section for the elementary process between partons within these particles, $a+b \to c+d$, with the gluon and quark contents of initial hadrons and with the probability of obtaining the final state hadron C from parton c described by a fragmentation function $D_{C/c}$[9].

$$E_C \frac{d\sigma}{d^3p_C}(A+B \to C+X) = \sum_{abcd} \int dx_a dx_b dz_c G_{a/A}(x_a, Q^2) G_{b/B}(x_b, Q^2)$$
$$\times D_{C/c}(z_c, Q^2) \frac{\hat{s}}{z_c^2 \pi} \frac{d\sigma}{d\hat{t}}(a+b \to c+d) \delta(\hat{s}+\hat{t}+\hat{u})$$

[2] Partons are either quarks (q) or gluons (g).

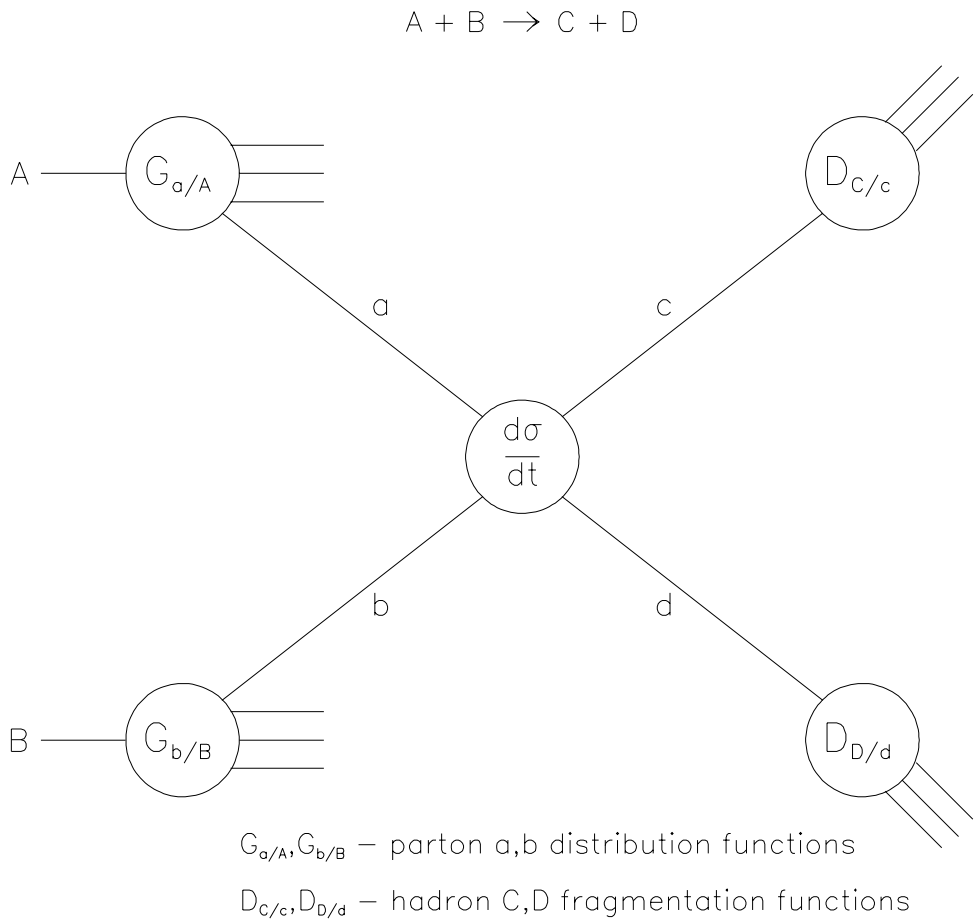

Figure 1.1 Pictorial representation of a high p_T hadronic interaction.

In this equation, the sum is over the constituent partons a and b of the original hadrons A and B, and over all possible products c and d which could result from the interaction; x_i are fractions of momentum of hadron I which are carried by parton i; $G_{i/I}$ are the probability distributions of parton i within hadron I having momentum fraction x_i. The variables $\hat{s}, \hat{t}$, and $\hat{u}$ are the Mandelstam variables for the constituent scattering. They are given by:

$$\hat{s} = (p_a + p_b)^2$$

$$\hat{t} = (p_a - p_c)^2$$

$$\hat{u} = (p_a - p_d)^2$$

where p_i are the four vector momentum of partons i. The parton distribution functions $G_{i/I}$ and the fragmentation functions $D_{I/i}$ have to be derived from the experimental data. The description of the hadronization process, which is how the outgoing quarks or gluons transform into observable hadrons, can not be carried out within the framework of perturbative QCD due to the large value of α_S at the small values of Q^2 characteristic of hadronization. However, in the regime of high energy transfer between colliding particles, the predictions of perturbative QCD are testable. Also, measurements of the cross section provide tests of currently available parametrizations for $G_{i/I}$ and $D_{I/i}$, and data that can be used to improve these parametrizations.

1.2 Physics Goals of E706

1.2.1 Direct Photon and Neutral Meson Production

The E706 experiment was designed to study direct photon production at high transverse momentum. Direct photons are photons emerging from the constituent scattering vertex $a + b \rightarrow c + d$, as the outgoing parton c or d, as opposed to photons from the electromagnetic decay of particles. Two types of interactions, quark - antiquark annihilation ($\bar{q} + q \rightarrow g + \gamma$) and Compton scattering ($q + g \rightarrow q + \gamma$) contribute to direct photon production in the first order (LO) of the perturbative expansion of QCD. To this order, the cross section for direct photons is proportional to $\alpha\alpha_S$, with α being the coupling constant of electromagnetism, compared to α_S^2 in the case of hadronic production. For this reason, and due to the larger number of Feynman diagrams contributing to the cross section for hadronic processes, direct photons are produced at about $1/1000^{th}$ of the rate of jets. However, unlike hadrons, the emerging direct photons carry all of the parton's momentum and therefore compete well with hadroproduction at higher p_T.

In addition, the measurement of a photon's momentum does not involve ambiguities inherent in reconstruction of jets. Also, the theoretical prediction for the direct photon cross section is free from a complicated description of hadronization, rendering direct photon a "clean" probe of QCD partonic interactions.

Leading logarithm and next-to-leading logarithm (NLO) calculations for the cross section for direct photon production are currently available. NLO diagrams with direct photons include Compton and annihilation diagrams in which a gluon is perturbatively emitted from a quark line or is split into a

$\bar{q}q$ pair. In addition, many LO diagrams with two $\sqrt{\alpha_S}$ vertices and with a bremsstrahlung photon emitted from either an incoming or outgoing quark line, contribute to direct photon production. One also includes in the calculation contribution from diagrams in which photons originate from a non-perturbative (soft bremsstrahlung) fragmentation of a final state parton. Since the parton-to-photon fragmentation function is unknown experimentally, this introduces some uncertainty in the theoretical prediction. Theoretical uncertainty arises also from the dependence of the calculation on the choice of (unphysical) scales, such as the renormalization and factorization scale, and from a presence of non-perturbative effects such as the intrinsic k_T of the incoming partons. Despite both theoretical and experimental uncertainties, the measured data, combined with the predictions of the theory, can be used to extract information on the parton distribution and fragmentation functions. In proton–nucleon collisions, where the Compton scattering diagram dominates, the data can be used to constrain the gluon distribution of the nucleon[3], whereas in π^-–nucleon collisions, where the annihilation diagram is more important, the data can be used to study gluon fragmentation[10].

[3] Direct photon data are used in conjunction with Deep Inelastic Scattering and Drell-Yan data to measure the gluon structure function. A precise determination of quark densities in DIS constrains the gluon distribution due to the momentum sum rule. Measurements of scaling violations of structure function of the proton, F_2^p in DIS, or evolution of the sea-quark distributions measured in Drell-Yan processes, give access (in NLO) to the gluon distribution through evolution equations. In addition, a direct study of the gluon structure function has recently been performed at HERA[11] by measuring (2+1) jet events from boson-gluon fusion in DIS. Nevertheless, a direct measurement of the gluon structure function at moderate Feynman x_F values (from 0.2 to 0.6 in fixed target experiments and from 0.01 to 0.36 in collider experiments) can only be achieved at this time by utilizing direct photons.

Fermilab Experiment E706 collected a variety of data to achieve these goals. During the 1988, 1990 and 1991 Fixed Target runs the experiment accumulated large samples of events generated with π^-, π^+ and proton beams at 500, 515 and 800 GeV/c. An overview of the E706 data sample is presented in Table 1.1.

The measurement of direct photon production is challenging experimentally. Not only are direct photons produced at a much lower rate than quarks and gluons in primary interactions, but they also consequently suffer from a large background of photons arising from neutral mesons decay. The Meson West spectrometer was designed to study direct photons. Fine segmentation of electromagnetic calorimeter allowed for the reconstruction of partially overlapping photons from high p_T π^0s. The calorimeter was split into front and back sections to help eliminate any hadronic contribution to the background. The tracking system was used to identify showers caused by incident charged particles and to reconstruct the vertex of the event. The experiment detected high p_T π^0s, ηs and ωs that contribute to the direct photon background. These neutral mesons productions are measured in E706 [12][13][14] [15][16] (and this thesis). These results are important in their own right, not just as a measurement of the background to direct photons. The data span a large range of transverse momentum in the central rapidity region and allow for the highest statistics, highest p_T measurements of neutral meson cross sections in their energy range to date.

Run	Interaction	Beam Momentum GeV/c	Number of Events	Sensitivity (events/pb)
	π^- Be			0.5
			2×10^6	
	π^- Cu			0.1
1988		500		
	(p,π^+)Be			0.75
			3×10^6	
	(p,π^+)Cu			0.1
	π^-Be			8.6
1990		515	30×10^6	
	π^-Cu			1.4
	pBe			7.3
	pCu	800	23×10^6	1.8
	pH			1.5
	(p,π^+)Be			6.4
1991	(p,π^+)Cu	515	14×10^6	1.6
	(p,π^+)H			1.3
	π^-Be			1.4
	π^-Cu	515	4×10^6	0.3
	π^-H			0.3

Table 1.1 Summary of E706 data sets.

1.2.2 Nuclear Dependence

Nuclear target effects of the cross sections for particle production can be parametrized as $\sigma = \sigma_0 A^\alpha$, where A is the atomic mass of the target material and σ_0 and α are parameters. At low p_T, inelastic cross sections are found to be proportional to $A^{\frac{2}{3}}$, which corresponds to the area shadowed by a nucleus of radius proportional to $A^{\frac{1}{3}}$. For higher energy-transfer interactions, the bombarding particles penetrate deeper into the nucleus and interact with nucleon constituents, quarks and gluons. The high p_T cross section should therefore become proportional to A. In the seventies, experiments on the production of charged hadrons at high p_T revealed that the cross sections increased more rapidly than A with the increasing nuclear size[17][18]. Any deviation of the production rates from $\sigma = \sigma_0 A^1$ is an indication of the effect of nuclear matter on the particle production process. The rise of the parameter α above 1 may be attributed to either possible rescattering of outgoing partons in the nuclear medium or to secondary scattering of the incident partons.

In E706, beryllium and copper targets were utilized to provide data for nuclear dependence measurements. During the 1991 fixed target run, the set of targets also included a hydrogen target. The nuclear dependence of direct photon production (which has not been measured previously) can be compared with that for the neutral mesons. The direct photons emerging from the collisions differ from mesons in that they are unlikely to undergo rescattering as they leave the nucleus. Therefore our measurements can provide new insights into the effect of nuclear matter on particle production.

1.3 Measurement of Omega Meson Production

Since its discovery, the ω meson has been observed and studied in a multitude of experiments. In recent years, there have been several measurements reported on vector meson production at high energies. The interest in studying vector mesons, such as the ρ, ω, $K^\star$ and ϕ, stems from the fact that these mesons contribute through their decay products to a large fraction of the final state particles observed in high p_T collisions. These measurements provide data which guide the development and parameter tuning of the Monte Carlo simulations of hadronic interactions used in high energy physics. By studying these resonances, one may also gain better insight into the underlying interaction dynamics since the vector mesons are more directly related to the partonic interactions than are the π^+, π^-, π^0, K^+, K^-, K^0, $\bar{K}^0$ mesons which often emerge from the interaction as products of the decay of more massive particles.

A wealth of information on particle production and quark fragmentation properties comes from e^+e^- experiments – e.g., from the TASSO[19] and JADE[20] collaborations, or the SLAC HRS[21] experiment. Recent e^+e^- studies at higher energies resulted in measurements of inclusive distributions of pseudoscalar, vector, and tensor mesons in hadronic Z^o decays[22][23][24][25]. There was no data on ω production reported from these experiments.

Among experiments that studied the hadronic production of vector mesons are the CERN SPS experiments: NA22 and NA27. The ω meson differential cross sections were measured versus x_F and p_T. Experiment NA27 (LEBC - EHS Collaboration) utilized a hydrogen target and π^- and proton beams at 360 and 400 GeV/c[26][27]. The NA22 experiment measured the inclusive production of vector mesons in π^+ and K^+ p interactions at 250 GeV/c[28][29]. NA22 and NA27 were designed to cover a forward rapidity range (from 0 to 4), and their

p_T coverage does not exceed 2.0 GeV/c. These measurements of ω production were performed in a very different kinematic region than E706, where the ω signal is reconstructed with p_T from 3.5 to 8 GeV/c in the central rapidity range from -0.5 to 0.75.

Among the studies of interest conducted in several experiments is the measurement of V/P, that is the ratio of directly produced vector mesons (1^-) to directly produced pseudoscalars (0^-), obtained separately for non-strange, strange, and charm mesons. To measure this ratio, the experiments subtract out the contributions from any vector or pseudoscalar mesons that were themselves products of the decay of other resonances. Alternatively, if the necessary measurements of higher mass resonances are not available, the experiments use fragmentation models to separate mesons produced directly in the fragmentation process from the total meson production rates. The V/P ratio is generally observed to be on the order of 1, which is in disagreement with the naive spin-statistics expectation of 3/1. Such discrepancy results in an increased interest in the V/P measurement and interpretation.

A possible explanation of a suppression of vector mesons production compared to the pseudoscalar mesons was formulated in a semi-classical approach, where the formation of the bound $q\bar{q}$ states was treated as a tunneling phenomenon. The spin - spin interactions between recombining quarks in this model result in additional potential energy and change the tunneling probability in favor of the pseudoscalar mesons[30].

In E706, a comparison of the total number of (vector) omega mesons produced relative to pseudoscalar π^0 production is obtained versus transverse momentum. We can compare this result with the prediction of the HERWIG[31] Monte Carlo, and then derive from the Monte Carlo a correction factor for the indirect

contribution to ω/π^0 from higher mass resonance decays. In HERWIG, the production rates for various particles are based on a phase-space ansatz. The available phase-space times spin factors determine the relative probability of occupying of the possible channels[4]. The ω/π^0 ratio will also be compared with the prediction of PYTHIA[32] Monte Carlo, in which the modeling of hadron fragmentation is based upon and tuned to e^+e^- data. The E706 result on ω/π^0 will be discussed in relation to currently available measurements of V/P ratio.

Two FNAL experiments [33][34] utilizing Be target and 200 GeV/c proton beams reported measurements of the ω/π^0 production ratio, as did a CERN ISR experiment [35] (pp at $\sqrt{s} = 62$ GeV). The p_T coverage of these experiments is relatively high with $p_T > 2.2$ GeV/c for the FNAL experiments and $3.0 < p_T < 7.0$ GeV/c at 90° in the center of mass for the ISR measurement. The E706 measurement will be compared with these results.

[4] It is characteristic of this Monte Carlo program that the number of free parameters (which would be adjusted to match the data) is at a minimum and only describe the splitting of large parton clusters into smaller ones. When the clusters decay to hadrons, the choice of particle species, and their momenta are completely determined by the cluster mass spectrum, phase-space, and spin.

Chapter 2 The Experimental Apparatus

The E706 spectrometer was located in the Meson West (MWEST) area of the Fermi National Accelerator Laboratory. The assembly of this complicated set of detectors and supporting structures began in 1983 and lasted until 1987, when the first period of data taking occurred. Numerous changes and improvements to the apparatus continued through 1988-1990 and 1990-1991, in the periods prior to the 1990 and 1991 fixed target runs. The layout of the various detectors as well as of experiment E672 is presented in Figure 2.1. Experiment E672 shared the same equipment and ran simultaneously with E706, but used an independent high-mass dimuon trigger. Detailed descriptions of the design considerations and of the construction of Meson West detectors can be found in the theses of students involved in the construction phase of experiment E706[36][37][38][39] [40][41][42][43] [44][45][46][47][48][49] [50][51][52]. The experimental apparatus is also described in E706 publications[12][13][14].

2.1 Beam Line and the Target Region

The beam delivered to Meson West during 1990 run was a negative secondary beam of primarily π^- particles with an average momentum of 515 GeV/c. The secondary beam was produced by bombarding a beryllium primary (production) target by 800 GeV/c protons extracted from the Tevatron. The beam intensity on the primary target was 2-5 $\times 10^{12}$ protons per spill. Beam was extracted during 23 seconds spills and the accelerator cycle time was about one minute. Secondary particles of selected momentum and polarity were transported via quadrupole and dipole magnets to the MWEST experimental area. One of the elements of the beam line was a Cerenkov detector which allowed for identification of

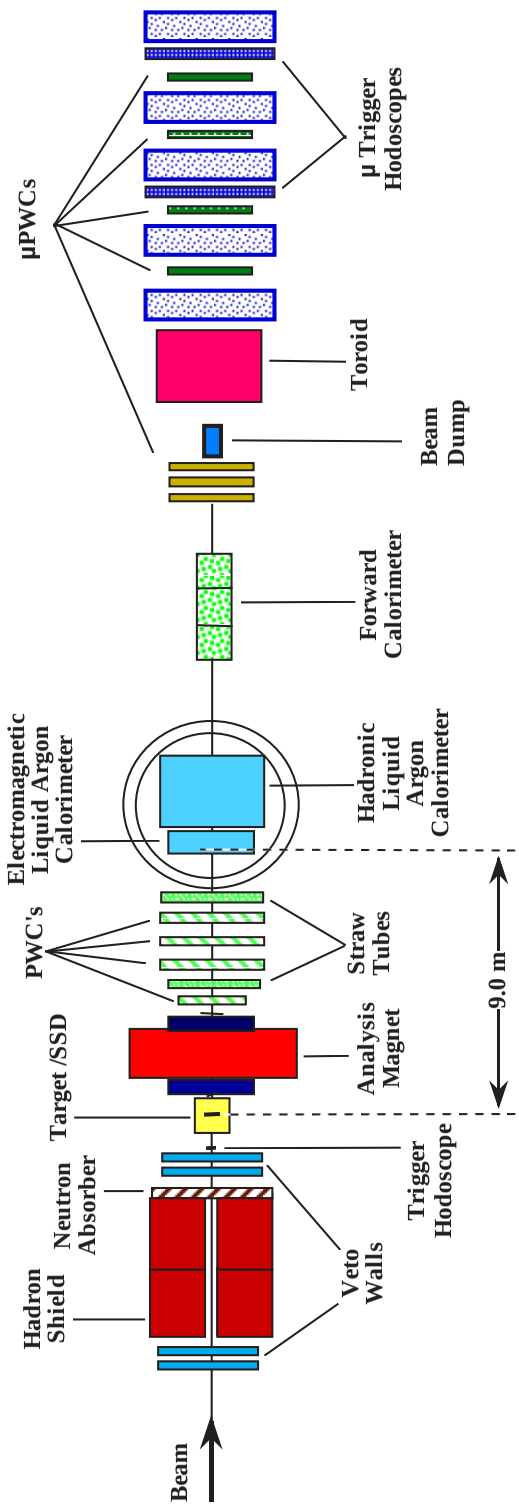

Figure 2.1 Schematic layout of MWEST detectors.

particle species (the beam contained a small fraction of K^- (2.9%) and antiprotons (0.25%) in addition to the π^- particles[53]).

During high intensity running the experiment received 1-2 $\times 10^8$ secondary beam particles per spill. The accelerator maintained a 19.1 nanoseconds separation between adjacent bunches (RF buckets) of beam particles. In order to define a presence of a beam particle in a beam bucket a set of scintillator counters referred to as the Beam Hodoscope and Hole Counter were used. The Beam Hodoscope, placed in the beam, had 3 planes each consisting of 12 small scintillator paddles which covered the area of 2×2 cm^2. The Hole Counter, used in the veto mode, was a scintillator plane with a 1 cm hole in the center. The interaction of the beam particle in the target was detected through a set of Interaction Counters positioned just before and just behind the analysis magnet. The Hodoscope, Beam Hole and Interaction Counter information was used in the formation of the trigger and was also recorded with each accepted event.

The experiment utilized copper and beryllium for target materials to allow for a study of nuclear dependence of the production of direct photons and mesons. For any beam particle there was a 0.8% chance to interact in Cu and 8.4% chance to interact in Be. Thin targets were employed to minimize photon conversion probability as well as secondary interactions.

2.2 The Tracking System

The charged particles produced in the interaction were detected and measured in the tracking system, consisting of

- Silicon Strip Detectors (SSD)
- Dipole Analysing Magnet
- Proportional Wire Chambers (PWC) and Drift Tube Chambers (STRAWs)

The SSDs measured the tracks in the immediate vicinity of the target. The set contained 5 pairs of X and Y view planes. The first pair of planes was of 25 micron pitch in the central region and 50 micron pitch on the outside, and the remaining planes were 50 micron pitch. The resulting angular resolution on the tracks was about 0.1 mrad. In addition to vertex SSD there were 3 pairs of beam SSD located upstream of the target. Total number of instrumented SSD channels was 8918.

A Dipole Magnet, of the length of 2 m, produced a fairly uniform magnetic field in the Y direction. The particles passing through the magnet aperture experienced a "momentum kick" of about 445 MeV/c in the X direction. By measuring the difference in the angle to the Z axis, before the magnet (in SSDs) and after the magnet (in PWC and STRAWs) a charged particle's momentum could be determined.

A set of Proportional Wire Chambers, located downstream of the magnet allowed for a spacial measurement of the line of flight of a charged particle. Four sets of planes, spaced by about 80 cm, consisted of X, Y, U (plane rotated by 37°) and V (plane rotated by -53°) chambers. The anode tungsten wires had a 2.5 mm spacing. The resolution was improved when additional chambers – Straw Drift Tubes – were added to the tracking system. Each STRAW chamber consisted of 4 X view and 4 Y view planes of aluminized mylar tubes. The measurement of the drift time of ionized electrons allowed for a precise hit position determination ($\approx$ 200-300 microns).

2.3 Liquid Argon Calorimeter

The Liquid Argon Calorimeter (LAC) consisted of two separate and structurally different detectors – the electromagnetic calorimeter (EMLAC) and the hadron calorimeter (HALAC). Both devices were immersed in liquid argon used as an active material which was ionized due to the passage of high energy particles. Both detectors measured the energy of incident particles by sampling – that is only a fraction of the energy of a particle was collected and used in the measurement while most of it was absorbed in either lead (EMLAC) or stainless steel (HALAC) absorber plates.

2.3.1 EMLAC

The structure of the EMLAC is presented in Figure 2.2. There were 4 quadrants each formed of a set of 66 vertically oriented "cells". One cell was an anode board, argon gap, and lead absorber board, serving as cathode. High voltage was applied to the lead sheets and the collected ionization charge summed in the Z direction. The first 22 cells of about 10 radiation lengths (called the Front Section) were added up and read out separately from the remaining 44 cells (the Back Section). A varying pattern of channels was etched in a copper cladding on each side of the anode boards. Radially oriented strips characterized Φ boards while circular strips spanning 45° in azimuth formed R boards. The 5.5 mm wide radial strips totaled 256 in the front and 238 strips in the back sections of each of 2 octants into which the quadrant was electrically subdivided. There were 48 inner strips on the Φ boards and 96 outer strips in each quadrant. This fine segmentation was crucial for achieving one of the goals of the experiment: separation of two photons from the high energy π^0 decay that might otherwise be reconstructed as one shower mimicking a single photon. The achieved position resolution of the EMLAC was about 0.5 mm.

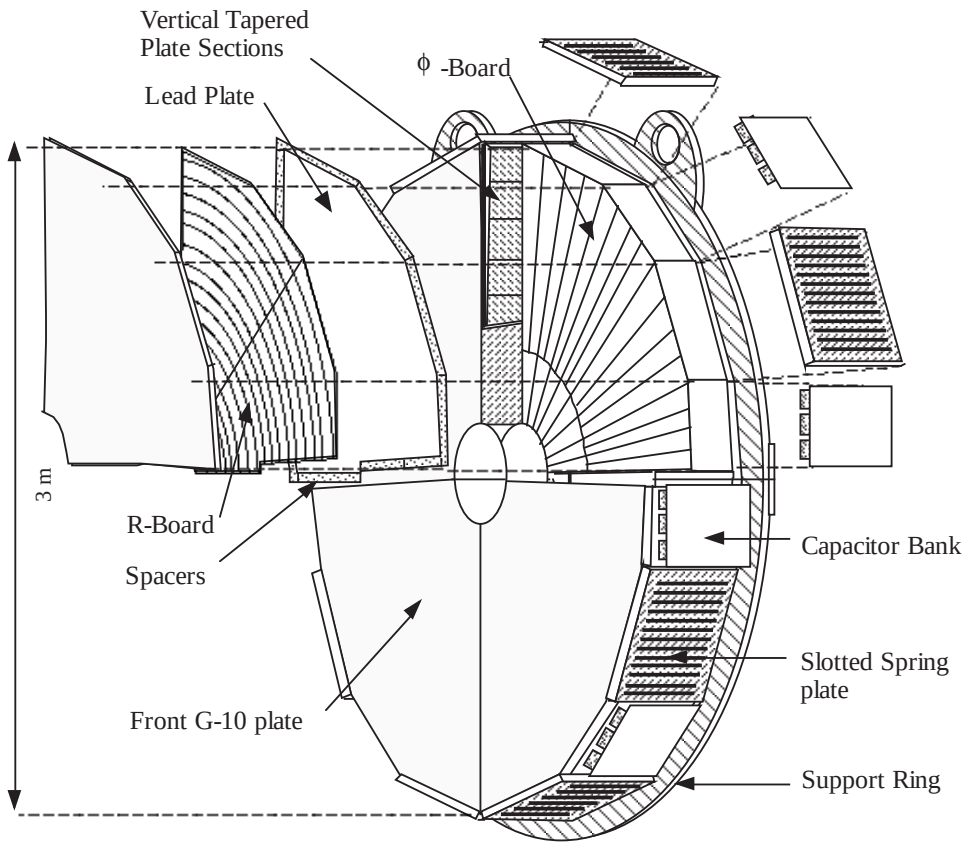

Figure 2.2 Detailed view of the electromagnetic calorimeter.

2.3.2 The Gantry and Cryogenic Support System

The body of the Liquid Argon Calorimeter was suspended from a gantry – a large movable support structure, shown in Figure 2.3. Since the liquid argon needed to be thermally isolated and maintained at about 88 K, the gantry also supported the cryogenic system needed to maintain this temperature. Coils for liquid nitrogen were installed inside the cryostat that contained the EMLAC and HALAC. The boiling temperature of the nitrogen and the speed of thermal exchange with liquid /gaseous argon could be adjusted by modifying the gaseous nitrogen venting rate. The complicated system of cryogenic pipes and safety devices connecting the LAC dewar with the nitrogen and argon storage tanks outdoors as well as with control and monitoring panels in the counting house of MWEST were all designed to be movable along with the gantry for calibration or relocation of the detectors.

In addition to the cryostat, the gantry also supported the Faraday Room – an electrically isolated and metal-shielded room that contained the calorimeter readout electronics. Low impedance cables carried the charge from the detector strips to feedthrough boxes located in the Faraday Room. The signals were then integrated in time, amplified and read utilizing Fermilab RABBIT crates and electronics to perform these functions. The electrical signals sent to and from the Faraday Room passed through optical couplers or pulse transformers. The power delivered to the Faraday Room was also isolated through transformers – to minimize the electronic noise on the LAC electronics.

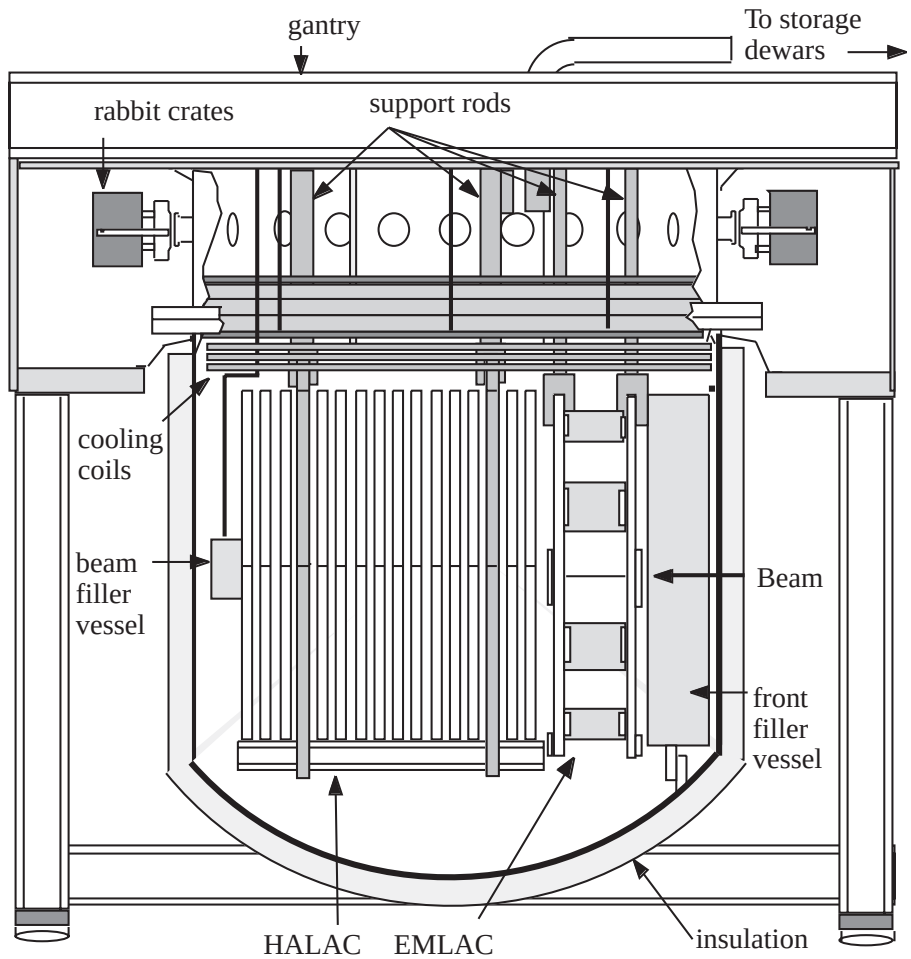

Figure 2.3 The gantry and cryostat of the LAC.

2.3.3 HALAC

The hadronic calorimeter was designed to measure the energy and position of strongly interacting neutral and charged particles. The HALAC was 8 interaction lengths in order to longitudinally contain the hadronic energy. A triangular pad geometry was selected for readout with pad sizes increasing from 10 cm on the upstream edge of HALAC to 14 cm on the downstream edge. The pads were arranged in the tower structures in the z direction. Typically 93% of hadron's energy was contained within a 6-pad hexagon. There were 2368 readout channels.

2.4 Forward Calorimeter

The purpose of the Forward Calorimeter was to measure energy in the forward region of rapidity and to provide information about beam jets not detected by the tracking system or the LAC. It consisted of 3 modules build of 33 layers of steel and scintillator. The light signals from the scintillator were wave-shifted, photomultiplied and summed over layers. The light was proportional to the total energy deposited in the detector.

Chapter 3 Data Acquisition and Trigger Systems

3.1 Overview of the Data Acquisition System

The data acquisition (DA) system in E706 was developed from both standard Fermilab elements of hardware and software and using E706-designed custom built devices. A block diagram of the DA system employed by the experiment is presented in Figure 3.1. The overall control of the DA operation occurred on the Host μ-VAX computer via the Fermilab Vaxonline[54] program. Vaxonline had several subprograms to perform different tasks. Run Control allowed for the control of the data taking process and beginning and ending runs. Three PDP-11 microcomputers and a Fastbus system were responsible for reading out data from various detectors. Then the program Event Builder received the data read-out from these independent sources and concatenated them into one event. The program Output wrote the data to 8 mm magnetic tapes. Several Consumer Programs allowed for on-line monitoring and displaying of a fraction of the collected events. The Fastbus system was divided into two subsystems: one read out the STRAWs using LeCroy 1879 TDC modules, the second consisted of the E706/Fermilab designed Intelligent Control and Buffer Modules (ICBM) that were interfaced with the RABBIT system (see below) and readout the LAC.

3.2 LAC DA System

3.2.1 RABBIT System

The name RABBIT stands for Redundant Analog Bus Based Information Transfer - a system developed by the Fermilab Particle Instrumentation Group. In E706 the RABBIT system was utilized to read the information from the electromagnetic (EMLAC) and hadronic (HALAC) calorimeters. As the name

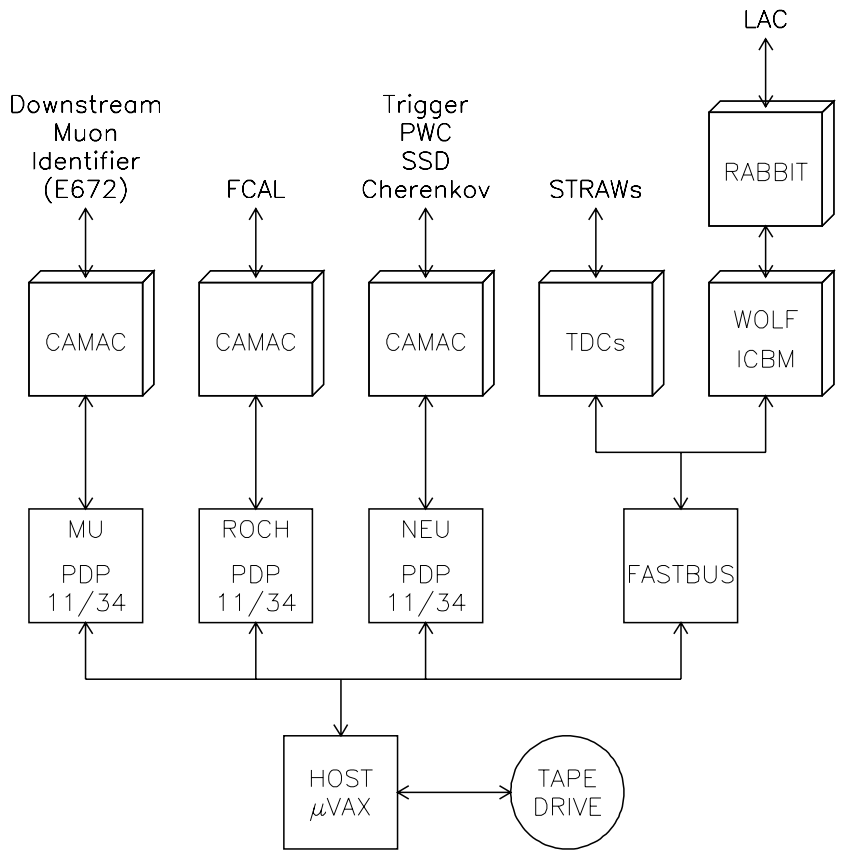

Figure 3.1 Schematic diagram of the E706 DA system.

suggests, the system has two redundant buses over which analog and digital signals were passed. Each bus had a controller, called the EWE and was terminated in a BAT module. The components of our RABBIT system are illustrated in Figure 3.2 and will be briefly described below.

LACAMP

The RABBIT crate provided power and hosted up to 20 LACAMP electronic boards directly connected to EMLAC and HALAC channels. Each LACAMP had 16 channels. The functions of the LACAMP were manifold. It contained the integrating amplifiers for the incoming signals, provided fast output of that signal for trigger consideration, and latched the integrated analog signal in the Sample and Hold circuitry prior to either digitization/readout or clearing of the event. A schematic diagram of the LACAMP board is presented in Figure 3.3. In addition to the above functions the LACAMP held the TVC time to voltage converter circuitry which provided the timing information about the arrival of the signals in the detector.

BAT

The Before and After Timer board (BAT) provided timing signals to the RABBIT crate. It was connected with the trigger system and received and broadcast EVENT and RESET signals. The EVENT signal, signifying the satisfaction of the trigger requirement invoked the BEFORE and AFTER timing strobes which allowed the measurement of the size of the integrated signal pulse. The BAT contained also the digital to analog converters which were used to set voltage levels throughout the crate, a function that was necessary for the calibration purposes.

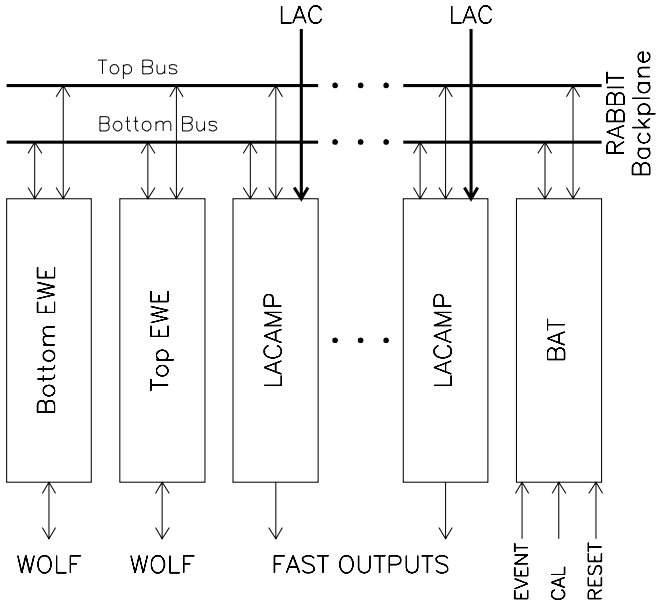

Figure 3.2 Modules of the RABBIT crate.

EWE

The RABBIT crate controller (EWE) was capable of addressing any of the slots and channels of the crate and either write to or read from them. EWEs contained analog to digital converters (ADCs). The ADC digitized the signals from the Sample and Hold circuitry for the LACAMP channel that the EWE was addressing at a given time. Since there was only one ADC per EWE in the crate the LACAMP channels needed to be read out sequentially, each channel requiring about 17 μsec for digitization. In order to speed up the reading process, two EWE controllers per RABBIT crate, each using a separate bus, were employed simultaneously.

3.2.2 Fastbus System

The Fastbus crate assigned to the readout of the LAC contained 17 ICBM modules. The ICBM was a programmable module that used a Motorola DSP56001 Digital Signal Processor. Each was equipped with 192k memory locations partially used by the software instructions, but mostly for the storage of the readout values of ADC counts as returned to the ICBM from EWEs. There were 14 ICBMs which orchestrated the communication with EWEs (situated in a total of 28 RABBIT crates) in the Faraday Room. Upon receiving a start scan signal, the ICBMs sent commands to EWEs to perform the readout of the detector channels and stored the received data. When the task was completed a global DONE signal was asserted. The data transfer to the large memory modules (LeCroy 1892 modules) could then begin and the BUSY signal from the LAC Fastbus to the trigger system could be lifted – allowing the next event to be taken. An average readout time for the LAC was about 8 milliseconds. It took much longer to transfer the data through the memory modules to the Vax and to write them to tapes. During the 23 seconds of the spill the events were buffered in memory in order to make

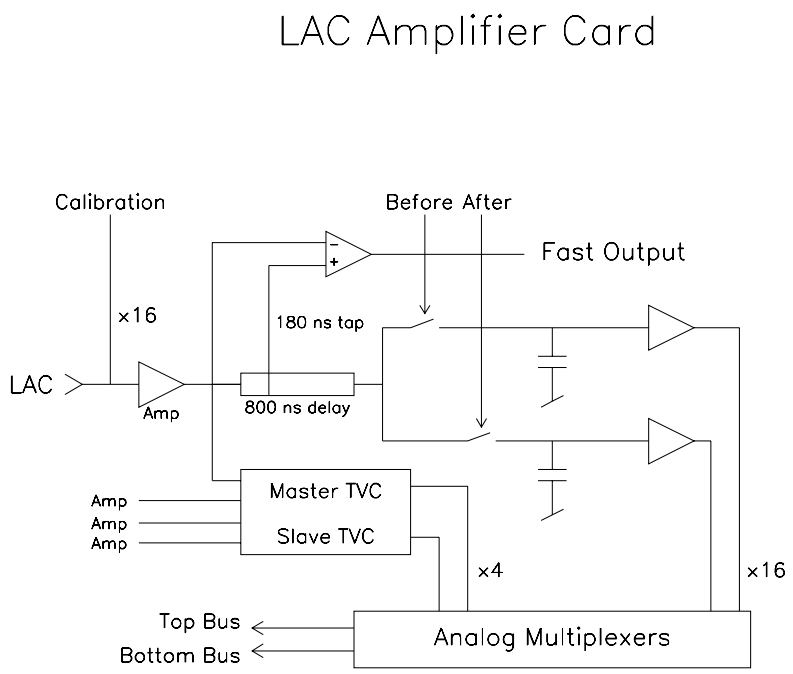

Figure 3.3 Partial schematic of LACAMP board. The electronic elements presented here were reproduced either 16 times (LACAMP channel) or 4 times (TVC system) on the LACAMP board.

maximum use of the incoming beam. The transfer of the data and writing to tape continued through the full 58 seconds of the accelerator cycle.

In between spills, the ICBMs kept communicating with the Faraday Room and performed several tasks aimed at continuous monitoring of the hardware and transfer lines. The tasks varied from one between spill to another and could be one of the following:

- path check – check of the 250 foot cable lines connecting the counting house, where the Fastbus system was located, with the Faraday Room
- pedestal readout and comparison with previous readings
- amplifier gain readout and comparison
- BAT voltage levels and RABBIT power supply readout
- PROM check – inventory of RABBIT cards

About every 8 hours, the ICBMs performed a cold start, that is a readout of various quantities associated with LACAMP channels, including pedestals and gains. This data was then permanently stored in a data base of run constants. A given run constants set was usually used for the several runs taken between the cold starts. However, if a hardware change needed to be made in the Faraday Room, or anywhere along the DA system path, a new cold start was initiated. Many changes of equipment occurred throughout the 1990 run. Some of them were replacements of failing module, but many were attempts to decide which element of the readout path was causing the system to malfunction. We learned that the system could fail in unpredictable ways. The list of these could begin with not always reliable power supplies to the RABBIT crates, loose or misplaced cables, intermittently failing cable connections, bent pins of the RABBIT backplane which connected LACAMPs to the transfer buses, dropped bits in the digital transfer,

corrupted program memories on ICBMs, etc.,etc.. It is therefore a matter of pride that E706 managed to collect so much beautiful data!

3.2.3 Amplifier Gain Measurement

Among the tasks performed during a cold start was the amplifier gain measurement. Each electronically readout channel of the LAC was characterized by a gain, or a scale factor, by which the energy deposited in the channel was modified due to the channel specific capacitance as well as through the amplification and readout process. To remove the dependence of the measured energy on the electronic characteristics, the gains of the LACAMP channels were measured. Calibration circuitry, including a charge injection capacitor, located on each LACAMP provided means by which this task was performed. An adjustable charge was injected into the detector channel and the calibration timing sequence of EVENT, BEFORE and AFTER signals was initiated to allow for the measurement of the channel response. Eight measurements at 6 different pulse height settings provided the data that were fitted with a straight line to extract the slope, or gain, of the channel. The uncertainties returned by the fitting program were very small for the majority of channels but could reach about 3% for a channel characterized by non-linearity or unstable response. LACAMPs with such channels were flagged and replaced with other boards to the extent to which spare boards were available.

The gain measurement was somewhat dependent on the hardware with which the measurement was performed. For example, the differences between the charge capacitors residing on LACAMPs influenced the values obtained for the gain factors. To compensate for the differences between charge injection capacitors, LACAMP boards were measured in an external system and the injection capacitance value related to a common reference. That provided an

injection capacitance correction distribution which had a width of about 0.8%. The BAT module responsible for the control of the calibration pulse height (through a voltage level setting) could also introduce dependence of the measured gain values on the specific hardware. That was verified by exchange of BAT modules between sets of RABBIT crates and comparison of the average gain values measured in these crates before and after the exchange. The typical variation was about 1%. To remove the dependence of the gain measurement on the BAT module, the voltage levels corresponding to a given voltage setting were measured for each BAT (in an external system) and the gains were corrected by that value. The EWE board, which contained the ADC circuitry, also introduced a dependence of the gain on a particular hardware board used. This dependence was however left intact since it was also present in the real data measured with that EWE - the dependence for which the gain correction was intended to compensate.

The gain distributions for a typical cold start, after all applied corrections, are presented in Figure 3.4 and Figure 3.5 for Front and Back Sections of the LAC. The channels of similar capacitance are grouped together in so called inner Φ, outer Φ, left R, right R groups, which are Φ and R strips with either inner or outer, left or right location within a quadrant. One may notice a lower mean value of the gain for Φ channels as well as channels in the Back Section, which were characterized by larger capacitance. The time stability of the gain values was also studied and the gains were found to be stable to within 0.2%. That allowed us to use the gain values obtained in earlier (or later) cold starts for runs for which the cold start data was not taken or was for some reason corrupted.

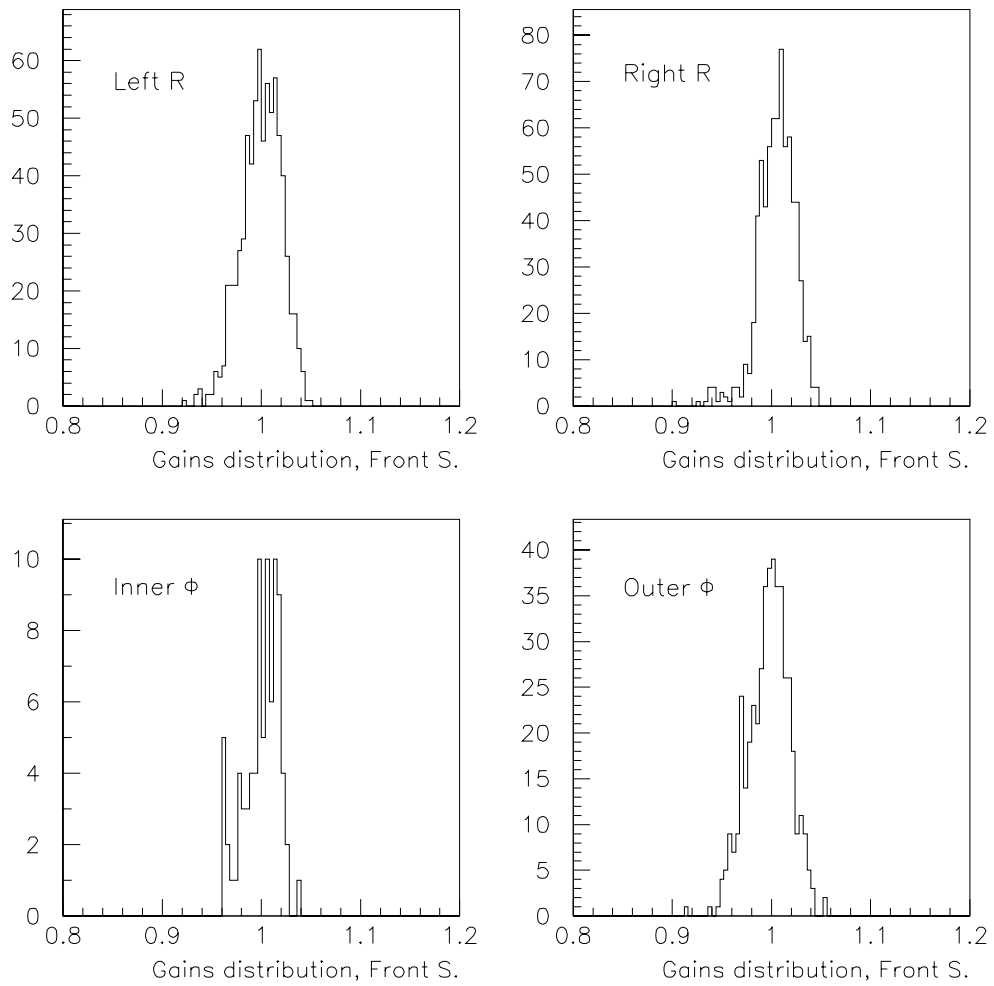

Figure 3.4 Amplifier gains distribution for a typical cold start, divided into left R, right R, inner Φ, outer Φ groups for the Front Section of the LAC.

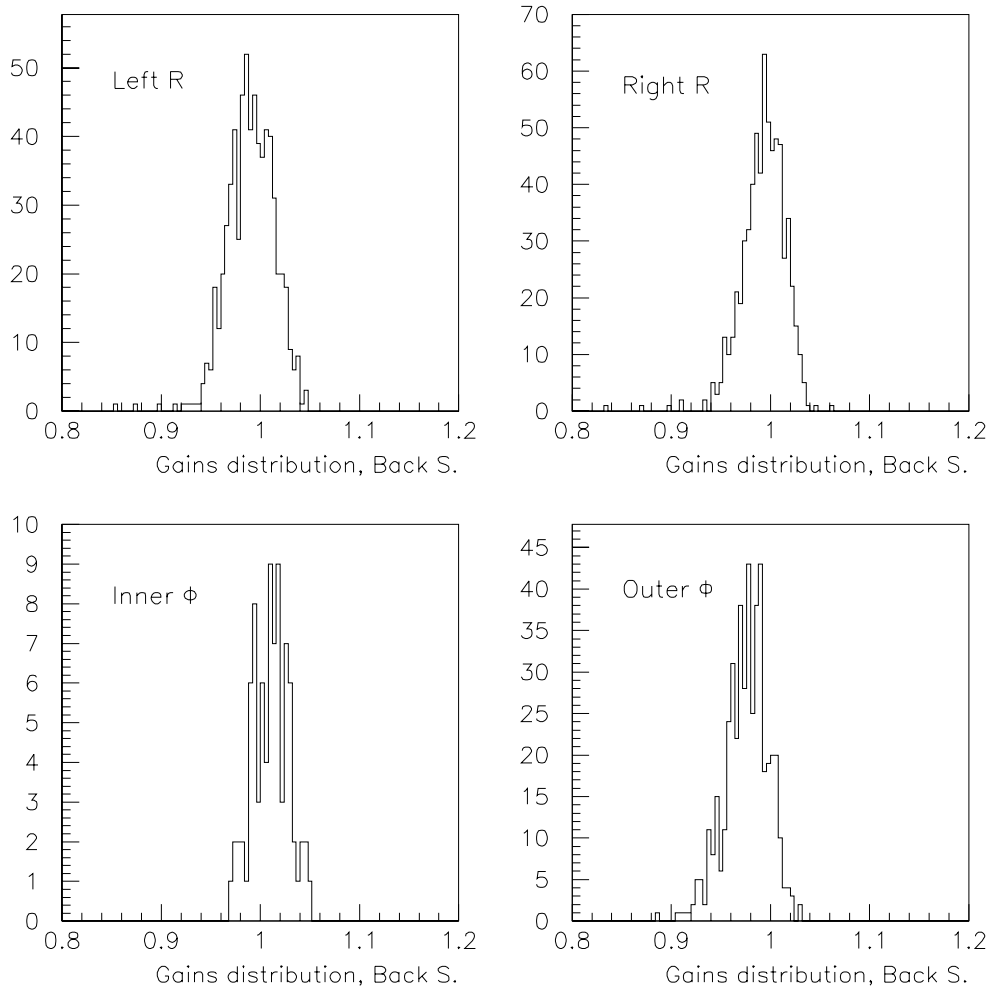

Figure 3.5 Amplifier gains distribution divided into left R, right R, inner Φ, outer Φ groups for Back Section of the LAC.

3.3 E706 Trigger

The high p_T events are produced rarely due to the exponentially falling nature of the p_T spectrum of particle production. In order to study the direct photons and neutral mesons in high p_T regimes, the experiment needed to select events characterized by electromagnetic showers with high transverse momentum, that is, events containing either direct photons or photons from the decay of π^0s, ηs, ωs etc. The E706 trigger system was responsible for the event selection. Out of the 10^7 interaction in the target in a single spill only a small fraction (on the order of 500) were written out to tapes to be analyzed. The elements of the selection process – that is beam and interaction definition, pretrigger and then trigger formation will be described below. A much more throughout discussion can be found in [55].

3.3.1 Beam and Interaction Definition

For the normalization of the cross section, it is important to count the number of beam particles that are capable of producing an interaction of interest. An incident beam particle (BEAM) was defined as a coincidence of signals from at least 2 of the 3 Beam Hodoscope planes. To reject events with multiple beam particles in a RF bucket, the signal BEAM1 also required that no more than one of the hodoscope planes detected 2 or more hit clusters. In addition to the hodoscope signals, the absence of a signal from the beam hole counter (BH) was required.

Interaction gate (INT) was set when BEAM was detected and at least 2 of the 4 interaction counters had signals. To minimize confusion in the detectors due to interaction in close time proximity (and to provide timing protection for the pretrigger level logic units), we required that there be at least 3 RF buckets

without INT before and after any interaction that was considered by the trigger system. This is referred to as the CLEAN requirement.

Interactions of the beam particles which occurred during the time of event readout or trigger formation were not capable of triggering. Therefore in the formation of the definition of triggerable beam/interaction we included the computer ready (CMPRDY) signal as well. The final live interaction (LIVE_INT1) definition was

$$\text{LIVE_INT1} = \text{INT} \otimes \text{BEAM1} \otimes \overline{\text{BH}} \otimes \text{CMPRDY} \otimes \text{CLEAN}$$

With each LIVE_INT1 signal, the trigger system started on a task of determining if the event was to be read out or abandoned. Details of trigger formation are discussed below. At the end of each spill, the scalers that counted various beam related signals were written out. We calculated live triggerable beam (N_{LTB}) based upon these scalers. N_{LTB} enters the cross section formula as a measure of a total number of incident beam particles arriving while the experiment was ready to accept a trigger.

$$N_{LTB} = N_{BEAM1 \otimes \overline{BH}} \times Live_Fraction$$

$Live_Fraction$ is a fraction of time when computers, pre-trigger and trigger systems were "live", or ready to accept events combined with a fraction of time the CLEAN condition was satisfied among all interactions. The trigger live fraction included veto wall requirements and other trigger related vetoes. These vetoes rendered the N_{LTB} octant dependent, and therefore the data from each octant were normalized in the cross section measurement independently.

3.3.2 RABBIT PT System

The measurement of the transverse energy deposited in the LAC for the purpose of trigger consideration occurred in the PT system. The p_T summing modules, hosted in RABBIT PT crates, received the fast output lines from the LACAMPs. Only the R-strips of the LAC were utilized in the trigger formation. The radial geometry of the detector strips allowed for a simple method of p_T measurement. The energy from the strips was attenuated according to $\frac{R}{Z_{LAC}}$, where R is the distance of the strip from the z-axis and Z_{LAC} the distance between the target and the detector. Transverse energies in consecutive 8 channels were then added together and formed the so called sums-of-8 values, as represented in Figure 3.6. There were 32 sums-of-8 per octant that were made available for the further trigger formation. The RABBIT PT system provided also a protection against an image charge effect. Due to the capacitive coupling of all of detector channels a large (negative) charge deposition in a region of the LAC caused small signals of positive sign on the remaining channels. Diodes were used to prevent the positive sign signals from interfering with the true signal in the trigger system.

3.3.3 Pretrigger Formation

The pretrigger was formed to reject the bulk of the low p_T interactions occurring in the target. Its formation was less specialized than that of higher-level triggers and therefore allowed for a faster decision regarding the event. With each LIVE_INT1 signal, the sums of transverse energies from inner or outer regions of the LAC were tested against the pretrigger threshold. In addition no signal from veto walls quadrant that shadowed the tested octant was permitted and the octant's signals were protected against early p_Ts. The early p_T system was included in the pretrigger definition to prevent the experiment from triggering on pile-up signals in the LAC. The pile-up of the charge deposition in the LAC,

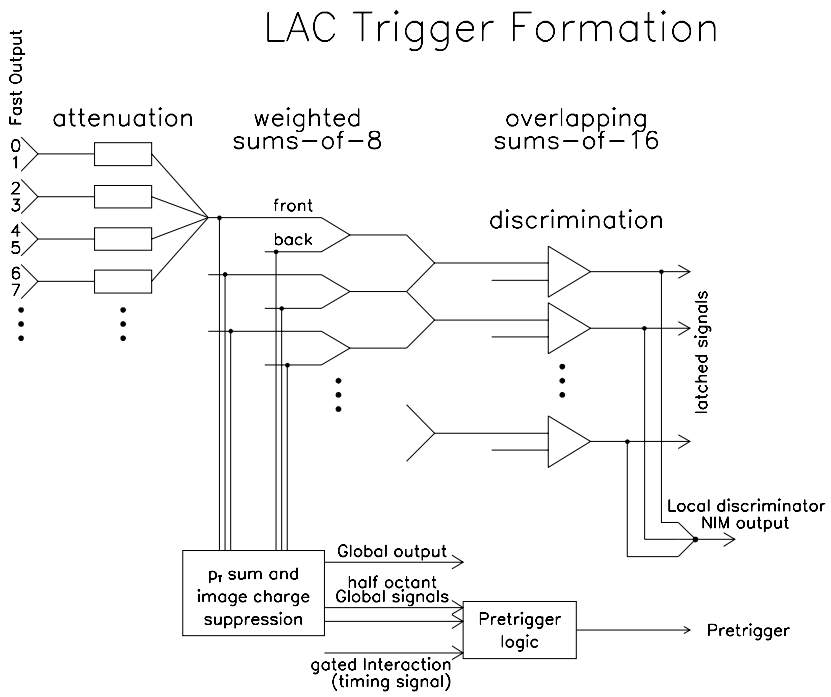

Figure 3.6 Trigger signal formation in the RABBIT PT system

created by earlier signals in the same octant which did not decay fully by the time the next event occured was likely in the high-intensity running environment and could boost the effective trigger p_T significantly. The early p_T protection consisted of a measurement of global transverse momentum of untriggered events that occurred earlier in time and using that information as a veto to the pretrigger, in case when the significant signal was observed. The pretrigger threshold values were about 1.7 GeV/c and 0.8 GeV/c. The two values were used for either high or low threshold triggers respectively.

3.3.4 Trigger Level

There were several types of specialized high and low threshold triggers used by the experiment. Their design was aimed at covering the largest possible p_T spectrum of interest and at providing some overlaps between different triggers to allow for a measurement of trigger efficiencies. Prescaling was used for triggers of lower thresholds to allow high triggers to receive a larger share of the events. Some triggers, like Single Local Low and Single Local High required that the electromagnetic transverse energy be localized within 16 consecutive R strips (2 sums-of-8 groups) of an octant. The local triggers were aimed at direct photon and π^0 detection. The global triggers – e.g., 1/2 Global Low or Global High – measured total p_T deposited in the inner 128 strips or in the outer strips of an octant. These triggers could be more sensitive to higher mass states such as ηs and ωs. The two-gamma trigger was a two arm trigger defined by the logical AND of the Local Low signal from one octant and Local Low signal from any other of the 3 octants on the opposite side of the LAC. Its physics aims were double direct photon and high mass π^0 pair production.

Table 3.1 lists all the trigger types and their approximate characteristics as implemented during the 1990 data run. Trigger threshold were being adjusted

during the course of the run as the intensity of the beam delivered to MWEST increased. The trigger settings presented there correspond to the last period of 1990 running, except for the last column of Table 3.1, where the 75% turn-on point is listed for the different triggers averaged over the course of 1990 run. The 75% point indicates at what p_T value the trigger turns on 75% of the time.

Trigger	**Trigger Fraction(%)**	**Prescale Factor**	**75% Point GeV/c**
Single Local High	40	1	3.8
Single Local Low	18	40	3.2
Local Global High	35	1	4.2
Local Global Low	20	40	3.0
Two Gamma	20	1	
Local 1/2 Global High	35	1	
Interaction	3	15^5	none
Beam	2	15^6	none
Prescaled Pretrigger	7	2925	1.7
Di-Muon (E672)	20	1	1

Table 3.1 E706 trigger characteristics

Chapter 4 Event Reconstruction

The software reconstruction programs used by the E706 collaboration were developed by several generations of physicists and students involved in the experiment. The programs have been modified and re-tuned as the group's understanding of the collected data evolved and as increasingly refined measurements and studies were made. The raw data, written out on-line to 8 mm magnetic tapes, consisted of channel pulse-height information from all detectors, discriminator status, status and timing of various counters, etc. To proceed with the physics analysis, we must transform this data into a physical description of the events: particle 4-momenta, charges, and general event characteristics. The process that led from raw data to the Data Summary Tapes (DSTs), where the results of the reconstruction of the events were written out, was definitely not simple, and the final results were not uniquely/absolutely determined. To the contrary – we could only approximately describe the physical processes registered in the detectors. The sections that follow give an overview of the reconstruction procedures.

4.1 Charged Particle Reconstruction

The process of reconstruction of charged particles involved the following:

- PWC track reconstruction
- STRAW track reconstruction
- SSD view tracking
- linking of SSD and PWC/STRAW track segments through the magnet region
- primary and secondary vertex finding
- momentum determination

Tracks could not be reconstructed properly if the positions and angles in space of each of the tracking chambers as well as STRAW tubes locations were not known precisely. These measurements, called alignment constants, were run-dependent, and were determined from the data itself through an iterative and involved process. The details of this work can be found in [56][57][58][59]. Raw data were transformed into hit positions using the alignment constants. To reconstruct track from hit positions, both SSD and PWC tracking used view-based track algorithms. Hits in two seed planes gave the starting trajectories for possible tracks and other planes were searched for hits consistent with these trajectories. View tracks from X,Y and U,V views were then correlated in the case of PWC track reconstruction and the final trajectory was refitted. PWC tracks with 16,15,14 or 13 hits were allowed at this stage. Tracks that shared many hits with other tracks in the event were rejected. The hits belonging to reconstructed tracks were then eliminated and the process of track finding repeated to allow the reconstruction of tracks which might have missed some of the chambers.

The resolution of the tracking system has was improved with the installation of STRAW tubes prior to the 1990 run. STRAW chambers provide increased spatial resolution because they not only registered the hits on the wires but also the time it took the ionized electrons to travel from the place of passage of the high energy particle to the wires. With the proper calibration of the drift time to distance for a given chamber voltage and threshold setting, one could accurately measure the hit position. When STRAW hits associated with PWC tracks were identified, the PWC and STRAW hits (up to 32 hits) were refitted and physical track parameters updated.

The linking process attempted to connect the SSD X and Y view tracks with the PWC/STRAW track at the other side of the analysis magnet. While passing

through the magnet, charged particles experienced a momentum kick in the X direction but the Y view trajectories were, to a good approximation, unperturbed. Therefore the linking code matched the SSD tracks to PWC/STRAW tracks based upon the Y slopes of upstream and downstream segments of the tracks as well as the separation of the projected trajectories at the center of the magnet (ΔY). In X view, only the separation of projected trajectories in the X plane, ΔX, was used. Small corrections due to fringe field and geometrical effects were applied to ΔX, ΔY, and ΔY slope prior to matching[60]. Track combinations for which the ΔX, ΔY, and ΔY slope, weighted with the corresponding resolutions, were within the linking window criteria were linked together. The linking windows criteria were momentum dependent. The larger the estimated momentum of the track the closer the two track segments projections were required to be at the center of the magnet to satisfy the linking requirements. Track matching was not unique. A given downstream track could have up to 5 SSD view tracks associated with it and one of these was judged to be the best link. Tracks for which links were not found within the linking windows were assumed to have come from the vertex for the purpose of calculating their momentum.

SSD track reconstruction relied on the linking information to reduce the number of accidental SSD tracks. This approach was effective due to the fact that the PWC tracks required a higher coincidence level and were fully determined in space, and thus were less likely to be fake tracks than the SSD track which could only be reconstructed from at most 5 hits in X and Y view planes[1]. Linked SSD tracks were given preference in the vertex finding algorithm. To identify the vertex location in the X and Y views, the χ^2 of the impact parameters of all tracks to the fitted vertex position was minimized. Information on the vertex Z position determined in one view was then used to refit the Z position of the vertex

[1] There was no U, V information upstream of the magnet.

in the perpendicular view. The vertex Z resolution averaged around 400 microns. If there were more than one vertices found in an event the most upstream vertex was used as the primary vertex[59].

After the vertex finding, the SSD best links corresponding to PWC/STRAW tracks were reevaluated using their impact parameter to the vertex as an additional selection criteria. The charged particle's energy, momentum, and charge were evaluated using its downstream and upstream track segment parameters. Additional details regarding E706 track reconstruction can be found in several theses of students involved in this project[57][58][59][61].

4.1.1 Momentum Scale

The magnetic field of the dipole analysing magnet and hence the size of the momentum impulse experienced by charged particles passing through it depends on the current setting. We needed to determine the value of the momentum impulse in order to calibrate the momentum scale. The decays of two particles $K_S^0 \rightarrow \pi^+\pi^-$ and $J/\psi \rightarrow \mu^+\mu^-$ were used for this calibration. K_S^0s were identified by searching for events with a secondary vertex and plotting the invariant mass of the oppositely charged tracks. J/ψs were reconstructed from the E672 dimuon triggers using the muon chambers and then were linked to match the PWC/STRAW track segments at the center of the toroid magnet. The momentum of muons reaching the E672 muon detectors were generally much larger (above 40 GeV/c) than the average values of momenta of the more copiously produced K_S^0s from the jet fragmentation. Hence we had a good check on the momentum scale averaged over all values of momentum reconstructed by the system. A single adjustment to the magnetic field strength was used to simultaneously set both particle masses to their Particle Data Group values within one standard deviation in the uncertainty on the mass measurement.

The momentum scale was also tested for stability in time. Changes in the magnet current or misplacements of the tracking chambers could influence the momentum scale. There were no significant deviations found in the measured K_S^0 and J/ψ masses from their nominal values throughout the span of the 1990 run.

Figure 4.1 shows the fitted mass distributions for $\pi^+\pi^-$ and $\mu^+\mu^-$ pairs. The $\pi^+\pi^-$ pairs have $\pi^+\pi^-$ vertices reconstructed either in the target region or within the coverage of the SSD system and represent a K_S^0 sample based upon about 1 million DST events. About 10 000 events with high mass dimuons were preselected by the E672 collaboration from a sample of 5 million events and the resulting J/ψ mass peak is shown in Figure 4.1(b). The J/ψ mass is fitted with a sum of two gaussian distributions with a common mean to allow for a visible change (widening) in the mass resolution for some events. There were two classes of $\mu^+\mu^-$ tracks with poorer resolution: muons with very large momentum and tracks with missing or only partially reconstructed STRAW segments. The widths of the two gaussians are 51 ± 5 MeV and 148 ± 11 MeV.

4.2 Electromagnetic Shower Reconstruction

4.2.1 Raw Data Preparation

As in the case of charged particle reconstruction, the information from the calorimeter channels was pre-processed before the actual photon finding algorithm was called. The preliminary steps included pulse height to energy conversion, subtraction of the channel pedestals, and rescaling of the energy by gain factors. The channel pedestals were subtracted from the raw pulse-height counts. Final pedestal corrections were determined from the data via the observed energy values per channel in regions of the LAC where no photons were detected (accumulated over many events). We have also observed that large groups of

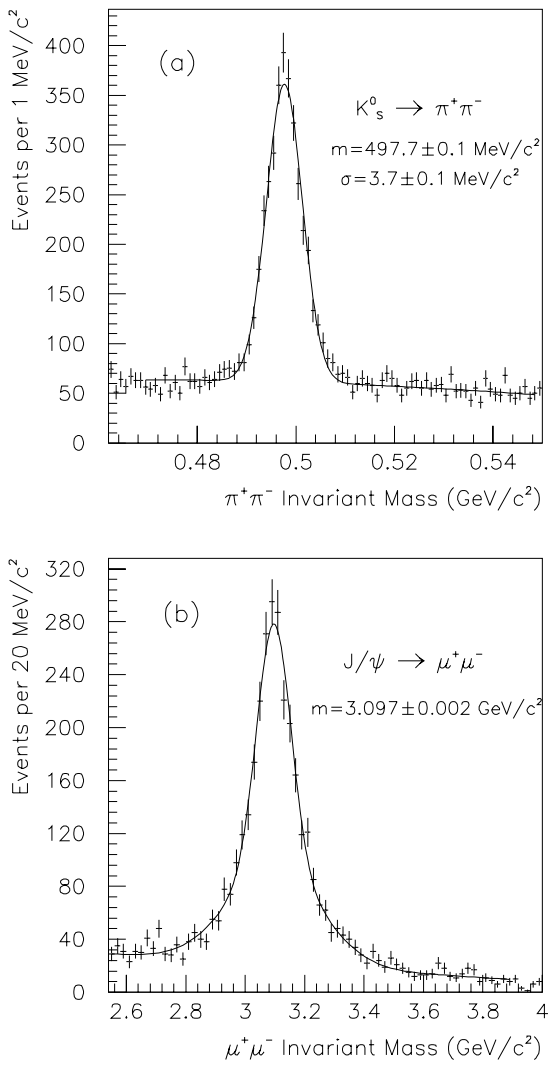

Figure 4.1 K^0_S and J/ψ signals used in the tracking system momentum calibration, after the momentum scale adjustment.

channels occasionally shifted up or down in a correlated manner – resulting in a distortion of the measured energy values. To account for this effect, which may be related to the image charge issue mentioned in the Trigger Section, linear fits to the pedestal base line across R or Φ values were performed and the channel energies were adjusted accordingly[62]. The few dead channels in the detector were filled with the energy values interpolated from the neighboring strips on an event-by-event basis. Front section and back section energies were added together prior to the particle search.

4.2.2 Shower Finding Algorithm

The pattern recognition algorithm first searched through the R and Φ views for clusters of channels with energies above the minimum threshold of 80 MeV. If at least 3 consecutive strips (2 in outer Φ region of the detector) contained energy above threshold, a group was found. Significant peaks and valleys within each group were identified. The approximate positions of the peaks and the approximate energies associated with those peaks were then determined. If the group contained only one peak, but was of large energy (greater than 25 GeV), a search for shoulders was initiated. Two showers, even if separated in space, could coalesce in one of the views, possibly producing an asymmetric shower with a shoulder on one side. Information about the presence of such a shoulder would later be valuable in the correlation routines that attempted pairing of showers found in R and those found in Φ views.

Monte Carlo simulation of the calorimeter and of physics processes occurring throughout the shower development provided simulated single-photon detector responses used in the shower shape determination. Fitting of a functional form to the Monte Carlo showers was done separately for the front and back sections, since the showers were distinctly wider in the back compared to the front. When

we fitted the shower shape to the data, however, the sum of the front and back strip energies was fitted to a combination of front and back shower shapes. This approach was chosen to minimize the sensitivity to the strip energy fluctuations. The parametrization of the shower shape function was done versus radial distance from the center of the shower[16].

The fitting of shower shape functions to the peaks found in R and Φ views allowed for a more precise energy and position determination. In the case of overlapping showers the fitting split the energies of the showers and minimized the overall χ^2. The shower energy was then corrected with the tail correction – an estimated fraction of the shower energy deposited outside of the valleys surrounding the peak. Showers close to the boundary of the LAC were also corrected for the fraction of the energy deposited outside the sensitive volume of the LAC.

4.2.3 View Photon Correlations

The precise determination of showers energies detected in each view (E_R and E_Φ) was very important to the success of the correlation routines. R and Φ view showers within a quadrant were matched to each other based on matching their energies. In addition, the longitudinal shower development in each view (measured by a fraction E_{Front}/E_{Total}, where E_{Front} is the energy deposited in the front section and E_{Total} is the total energy of a shower) was used to aid the correlation process. The correlation algorithm also used the segmentation of the quadrant into octants and into inner and outer Φ regions in matching pairs. Sometimes a correlation of a type 1:1 (one shower from each view) to match the view showers into photons was not sufficient. That would occur when all matches of showers with small E_R and E_Φ energy differences were found, but a large amount of energy in the octant still remained uncorrelated. In such a case 1:2 (one R view shower to

two Φ showers), 2:1, 1:3 types or even more complicated schemes of correlations were attempted. The final photon energies were a sum of the fit energies of R and Φ gammas. A more detailed description of the photon reconstruction and correlation algorithms can be found in [63].

4.2.4 Energy Scale

The precise calibration of the energy scale of the calorimeter is very crucial for any high p_T experiment: an uncertainty of 0.5% in the energy scale results in a 6% systematic uncertainty in a differential cross-section measurement as a function of p_T due to the rapid fall of the cross section with p_T.

While the gain of the electronic channels was found to be very stable over time, the observed reconstructed π^0 mass showed a significant increase with the run number, or the time of recording of the events. This effect is illustrated in Figure 4.2, where the uncorrected mean π^0 mass is plotted versus time. The 1991 Fixed Target run data are also included in this plot. This behavior was found to correlate with the cumulative exposure of the LAC detector to the interacting beam particles. Although difficult to explain theoretically, the effect was empirically parametrized and the energy scale adjusted accordingly.

After the time dependence of the energy was removed, an extensive and systematic study of the remaining effects pertinent to energy scale was performed. The study used π^0s, ηs and $\gamma \to e^+e^-$ conversion electrons[15]. The reconstructed π^0 and η masses measured separately in each of the LAC octants were found to deviate from the standard values by a few percent. Octant-dependent scale factors were used to correct the photon energy by setting the reconstructed meson masses at their nominal values.

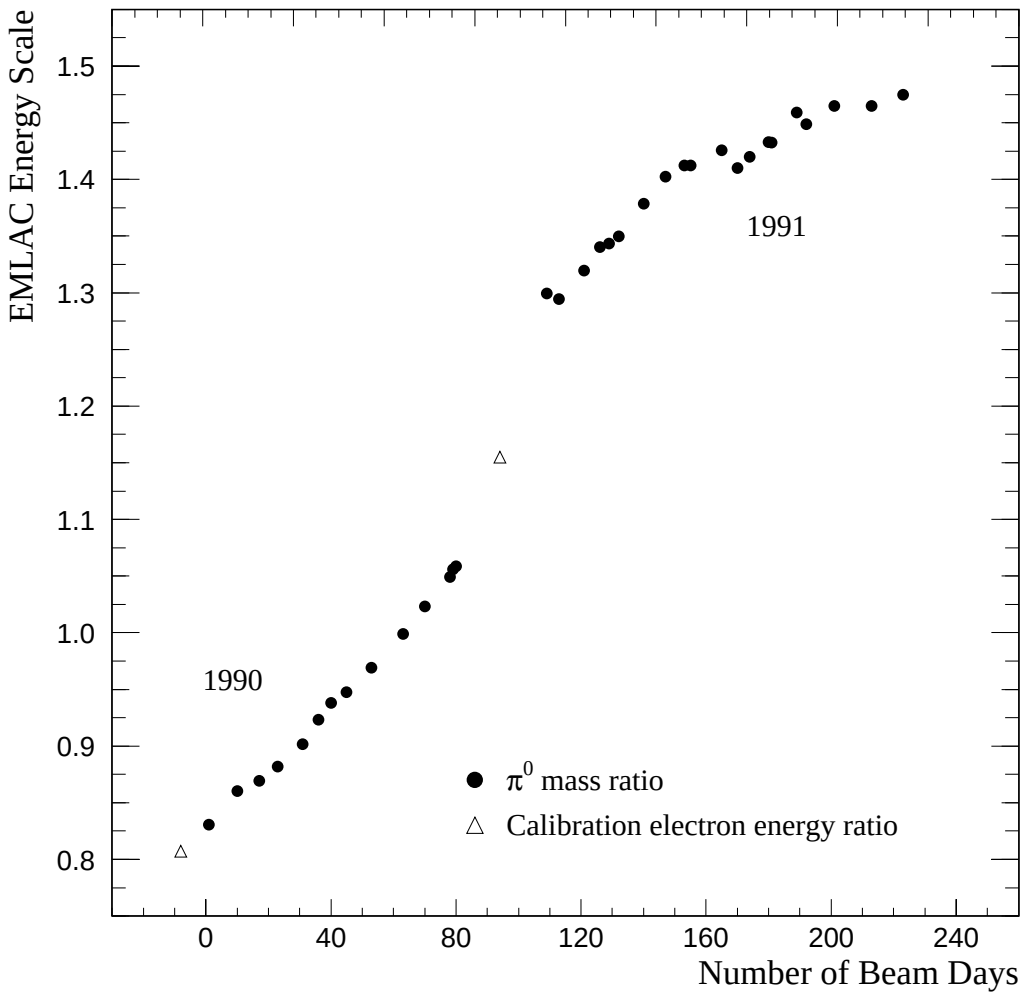

Figure 4.2 Time dependence of the reconstructed π^0 mass normalized to the Particle Data Group value.

Each of the photons or electrons passed through several layers of material before reaching the active region of the calorimeter. The mean energy lost, E_{loss}, modeled in the Monte Carlo, was added to the reconstructed energy to account for this effect. The E_{loss} varied from 0.5 GeV to 2 GeV for photons and to 3 GeV for electrons, depending on their energy.

A selected set of π^0s and ηs were studied for the dependence of the reconstructed mass on the position of the particles in the detector. Attention was given to the fact that for a given p_T cut, the energy distribution of photons would change with radius, with the large energy particles being concentrated in the inner parts of the LAC while the lower energy photons dominated the outer regions. The difficulty in reconstructing two overlapping showers from high energy π^0 could affect the π^0 mass of the photons in the inner region. Hence a set of low p_T (p_T >2 GeV) π^0s from a low threshold trigger, as well as a sample of ηs whose photons are widely separated, were used to determine the radially dependent correction. The radial dependence of the reconstructed π^0 mass prior to this correction and normalized to the nominal value is presented in Figure 4.3. A similar radial dependence of the reconstructed mass is displayed for the ηs. The parametrized form of E versus r dependence, obtained for each octant separately, was used to correct for that dependence in the energy of the photons.

Electron showers, identified by the presence of a reconstructed charged track pointing at the shower, were additionally corrected for the observed E/P dependence on energy. The electron momentum P measured in the tracking system was larger than the corresponding energy E measured in the calorimeter at low energies, as shown in Figure 4.4, where both data and Monte Carlo results are plotted. The effect is understood as due to the use of a parametrized photon shower shape in the reconstruction of electron showers.

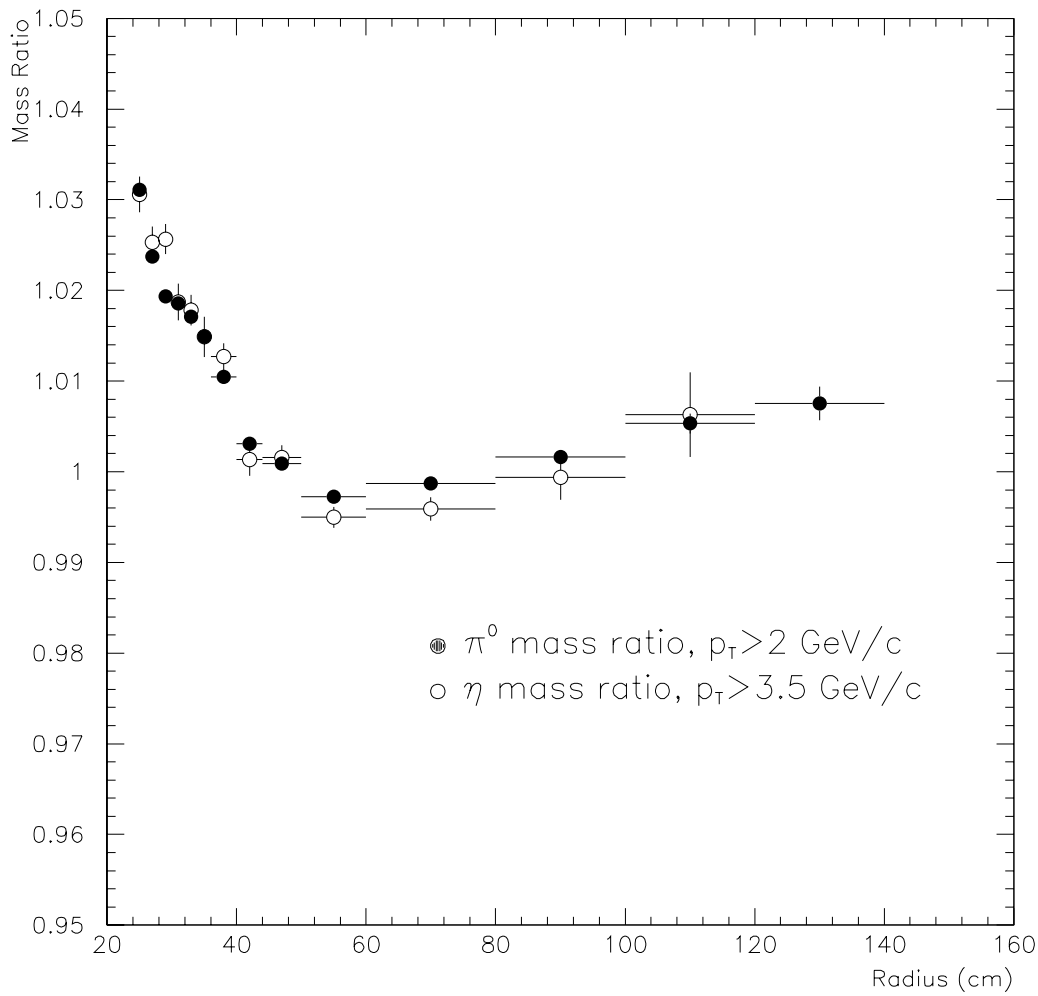

Figure 4.3 Radial dependence of the reconstructed π^0 (solid points) and η (open points) masses relative to the PDG values.

Figure 4.5 shows the dependence of the π^0 and η masses on octant number, particle p_T and the radial position in the detector, after all the above mentioned corrections were applied. The resulting energy scale has been extensively tested using independent sets of data, including the high p_T sample[15][64]. The uncertainty in the energy scale was found to be within 0.5%.

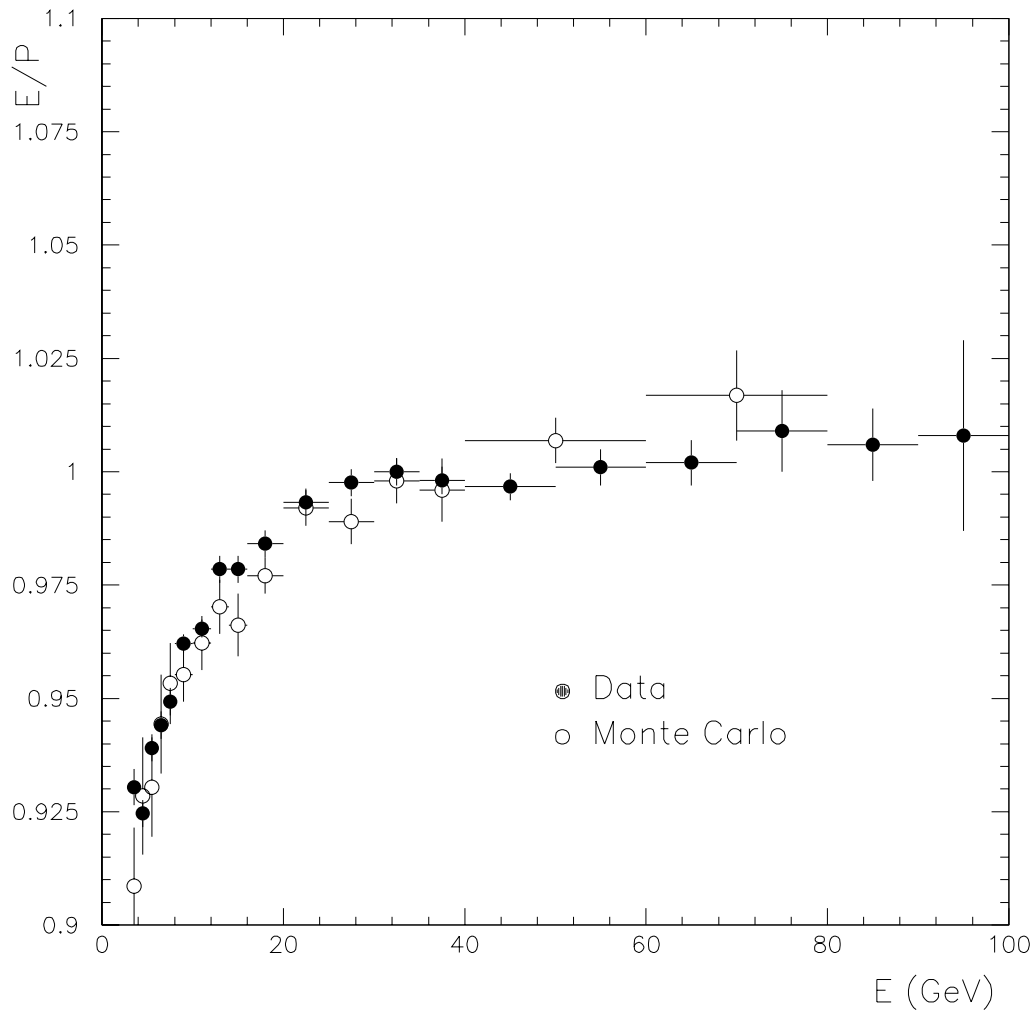

Figure 4.4 E/P ratio for $\gamma \to e^+e^-$ electrons as a function of electron energy for data (black points) and Monte Carlo (open cirles).

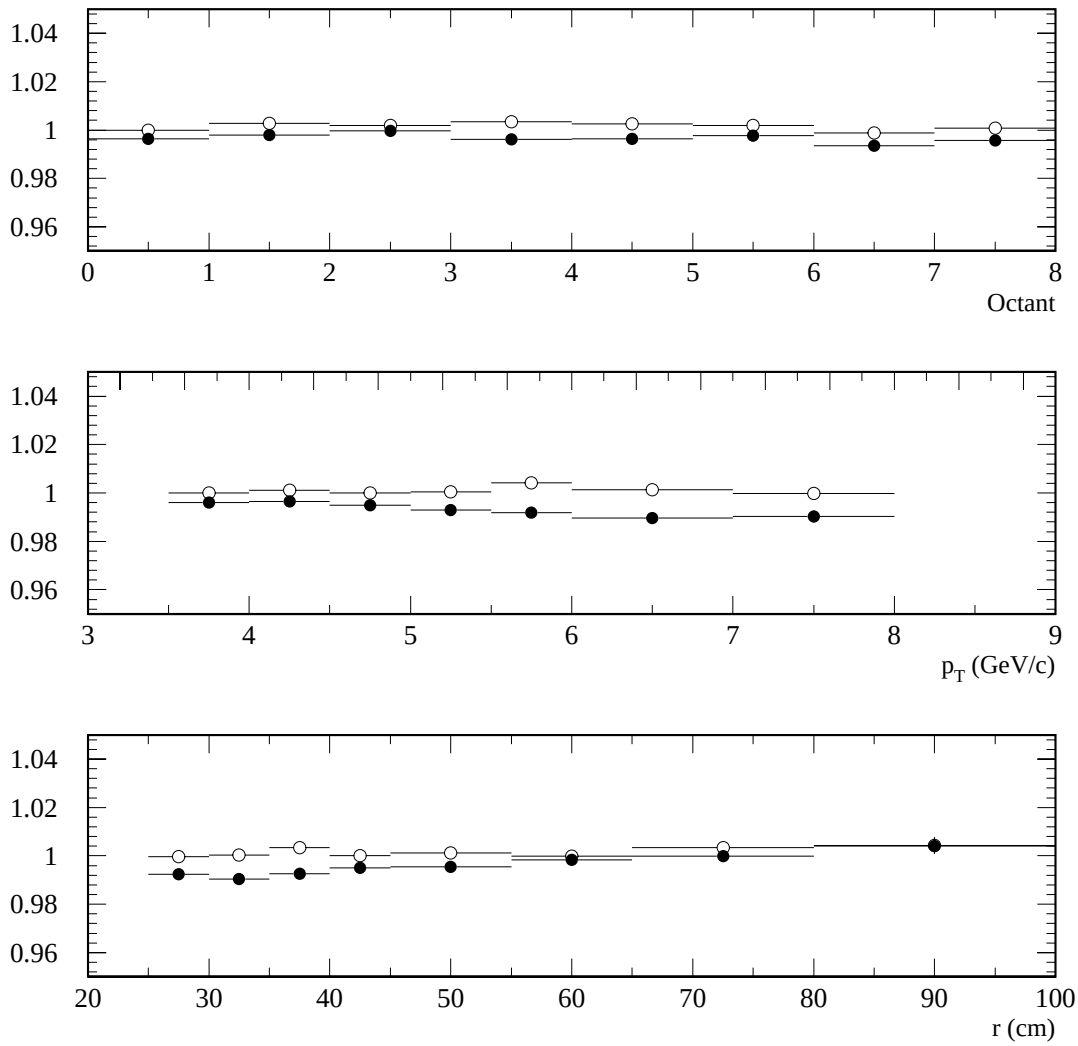

Figure 4.5 The π^0 (solid points) and η (open points) masses as a function of the octant number, p_T and radial position of the particle. Masses are normalized to the PDG values.

Chapter 5 Search for the Omega Meson

5.1 Data Selection

The data analyzed in this thesis were collected during the Fermilab fixed target run that spanned the period between February and August of 1990. A total of 30 million triggers generated by 515 GeV/c π^- beam incident on Cu and Be targets were recorded. Table 5.1 shows how the data are divided into sets of constant trigger thresholds and relative stability of the detector performance as well as the corresponding numbers of processed events written onto Data Summary Tapes (DSTs).

Trigger Set	**Run Number Range**	**Number of Events Processed onto DSTs**
1	9181 - 9434	5,904,400
2	8989 - 9180	4,051,100
3	8629 - 8988	5,839,100
4	8240 - 8628	3,931,700
5	8055 - 8239	2,864,500
6	7594 - 8054	4,966,500
Total		27,557,300

Table 5.1 1990 Data Subdivided into Trigger Sets

The search for events containing ω mesons was facilitated by a further compression of the overall data sample. A secondary DST stream of selected events that could potentially have a high p_T ω decaying to a π^0 and a γ

were retained while the remaining events were dropped. The selection criteria, discussed in more detail below, can be summarized as follows:

- Only showers reconstructed within the LAC fiducial boundaries were considered
- Showers with $E_{front}/E_{total} < 0.2$ were rejected
- Showers associated with charged tracks were rejected
- A triggering LAC octant must have had at least 3 photon showers satisfying the previous criteria and the p_T of at least one combination of 3 such photons must have been > 3.0 GeV/c

A fiducial region of the LAC, which is smaller than the instrumented region, was defined in order to reject showers hitting the edges of the detector, gaps between quadrants or octant boundaries, etc. Figure 5.1(a) shows the Y vs X position of photons after the fiducial cut was implemented. The E_{front}/E_{total} requirement discriminated against hadrons and muons which were less likely to interact in the front section of the LAC. E_{front} is the energy deposited in the front section of the LAC, while E_{total} is the total energy of the shower reconstructed in the electromagnetic calorimeter. Figure 5.1(b) presents the E_{front}/E_{total} distribution for all neutral and charged particles hitting LAC. If the projection of a reconstructed track to the front face of the LAC was within 1 cm of a shower, the shower was assumed to be due to that charged track. The E_{front}/E_{total} distribution for showers associated with charged tracks exhibits two maxima, in the vicinity of 0 and 1. The maximum near 1 is attributed to electrons, many of which we can clearly identify by the invariant mass of a e^+e^- pair. The maximum near 0 is characteristic of hadrons or muons. The charged track cut removed the majority of electrons and some remaining charged hadrons which survived the

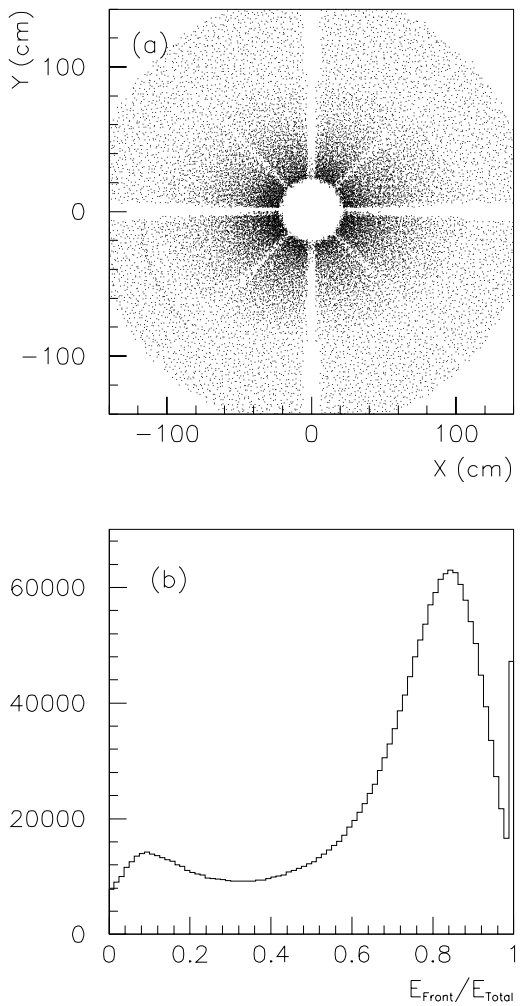

Figure 5.1 (a) Positions of photons at the front face of the LAC after the fiducial volume cut was implemented. (b) E_{front}/E_{total} ratio for reconstructed LAC showers. Photon candidates with E_{front}/E_{total} below 0.2 are rejected.

E_{front}/E_{total} cut. Requiring that all 3 photon candidates for ω be in the same octant facilitated calculation of the trigger corrections.

The above pre-selection criteria reduced the amount of DST data by a factor of 5 and allowed the storage of selected data on about 20 8 mm magnetic tapes. Further data analysis cuts instituted on pre-selected data, pertinent to the measurement of the omega signal, are described in the sections below. Some other analysis cuts (including the vertex cut, muon rejection cuts and trigger cuts) that have been adapted for most of the E706 analysis will be discussed in later chapters. The trigger types selected for this analysis were the Single Local High (SLH) and Local Global High (LGH) triggers[1].

5.2 Definition of the π^0 Signal

All pre-selected ω candidate events satisfying the SLH trigger were first searched for a π^0 signal. Any two photons in the triggering octant satisfying the photon criteria defined above were considered as a π^0 candidate. Photon momenta were calculated from their corrected energy and position at the LAC assuming that the photons originated from the reconstructed interaction vertex. The 4-vector momenta of the two photons were added to form a $\gamma\gamma$ momentum 4-vector with components denoted by E, p_x, p_y, p_z. The invariant mass ($m_{\gamma\gamma}$) of the $\gamma\gamma$ system was calculated according to the formula

$$m_{\gamma\gamma}^2 = (E - p_z)(E + p_z) - p_x^2 - p_y^2$$

A $\gamma\gamma$ combination was considered a π^0 if the invariant mass $m_{\gamma\gamma}$ was within the range $0.11-0.165$ GeV$/c^2$. Figure 5.2 presents the $\gamma\gamma$ invariant mass distributions.

[1] All trigger types available in E706 data were searched for evidence of an ω signal. The only other data set besides the SLH and LGH sets that displayed any significant signal was the Local Global Low trigger set. However, the ω signal was statistically very limited in that set, and it was not included in this analysis.

The four different plots correspond to four energy asymmetry A_{π^0} intervals, where A_{π^0} is defined as

$$A_{\pi^0} = \frac{|E_1 - E_2|}{(E_1 + E_2)}$$

and E_1 and E_2 are the energies of the two photons. Among all $\gamma\gamma$ pairs only those which formed a three photon combination with $p_T > 4.0$ GeV/c when combined with another photon from the same octant contributed to these plots. An additional requirement on the relative energy asymmetry of the $\pi^0\gamma$ pairs, (called the $cos\theta^*$ cut, and described in the next section), has been imposed on $\gamma\gamma$ pairs entering the figures. These two cuts allow us to view the π^0 signal and its background exactly as it is used to form $\pi^0\gamma$ combinations.

The π^0 signal to background ratio is very poor in the highest asymmetry region $A_{\pi^0} > 0.75$. This is due to the presence of many low energy photons in the event; π^0s from that asymmetry bin will not be used in the evaluation of the ω signal.

5.3 $Cos\theta^\star$ Cut

5.3.1 Motivation

Angle $\theta^\star$ is formed between the π^0 direction of motion in the $\pi^0\gamma$ rest frame and the direction of motion of the $\pi^0\gamma$ system in the LAB frame, as illustrated in Figure 5.3. The π^0, defined in the previous section, is paired with the remaining photons from the triggering octant to form a potential ω. The π^0 4-vector is then boosted to the rest frame of the $\pi^0\gamma$ object and the $cos\theta^\star$ distribution is formed. The ω is a 1^- vector meson and thus the orientation of the back-to-back π^0 and γ momentum vectors in space is not random but carries information about the ω spin. Nevertheless, only an overall polarization of ω particles could produce

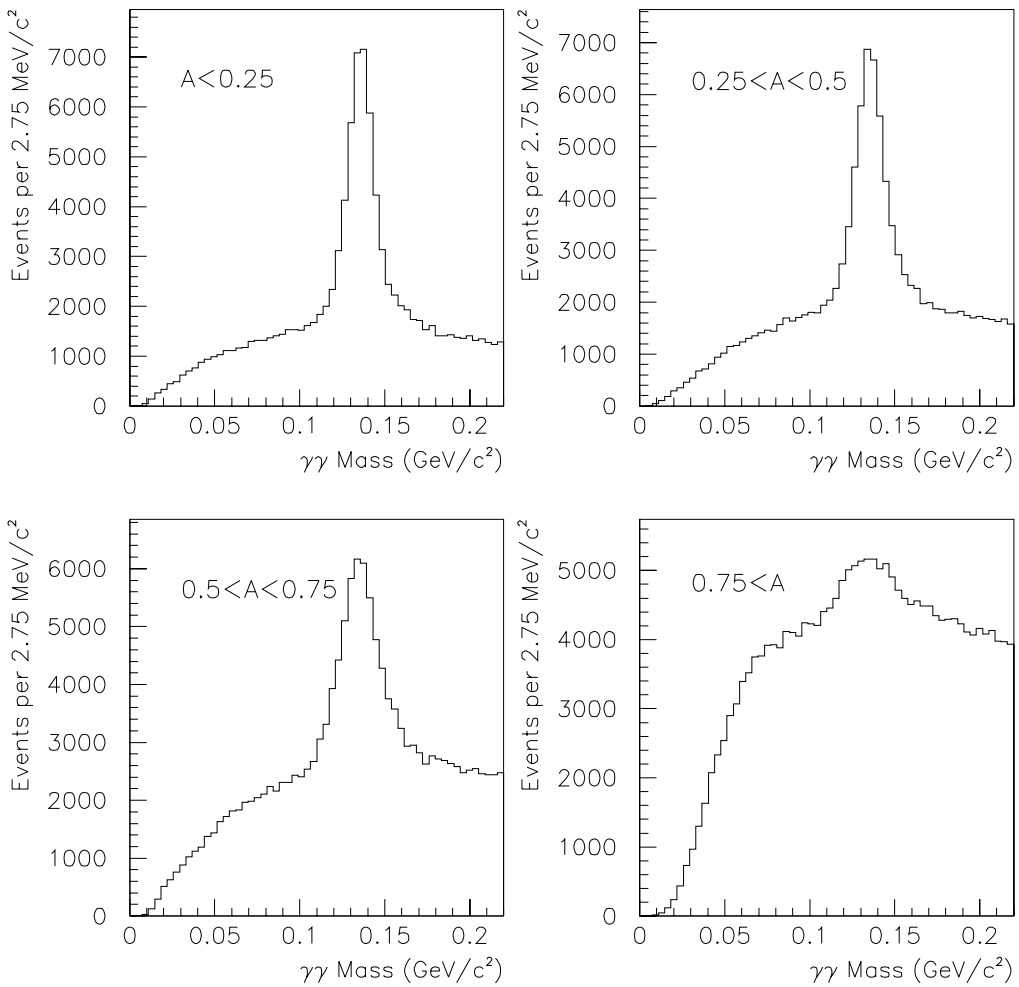

Figure 5.2 Two photon invariant mass distributions in the π^0 region for $\gamma\gamma$ pairs that could form an object of $p_T > 4.0$ GeV/c when combined with other photons in the event. The four plots correspond to four different π^0 photon energy asymmetry regions. The $cos\theta^\star$ cut on $\pi^0\gamma$ pairs was applied.

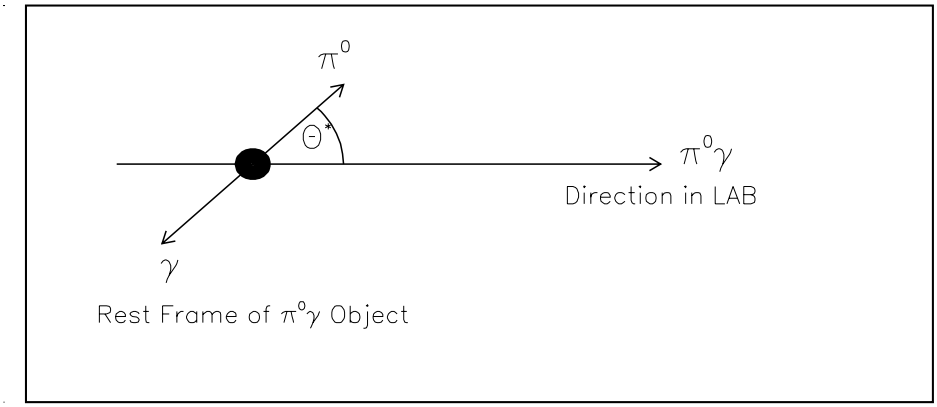

Figure 5.3 Illustration of the definition of $\theta^\star$.

a non-uniform distribution of the π^0 (or γ) direction with respect to ω's line of flight. Since we have no reason to expect such a polarization, it is assumed, for the purpose of this analysis, that the ωs are produced unpolarized, with spins oriented randomly in space, and that therefore the resulting $cos\theta^\star$ distribution of decaying ωs is flat.

The $cos\theta^\star$ distribution for the reconstructed $\pi^0\gamma$ pairs is presented in Figure 5.4. Overlaid is a Monte Carlo simulation of these events, weighted by the probability that the events satisfied the SLH trigger. Most of the MC events are high p_T π^0 events entering the $\pi^0\gamma$ spectrum combined with accidental photons in the octant. From the identification of the particles in the Monte Carlo, and also from kinematic considerations, we deduce that the majority of the $\pi^0\gamma$ combinations contributing to these distributions could not be coming from a physical, bound $\pi^0\gamma$ state because their energies are too often asymmetric. $Cos\theta^\star$ is related to the $\pi^0\gamma$ energy asymmetry (A_ω) by the following formula:

$$A_\omega = \beta cos\theta^\star \times (1 - \frac{m^2_{\gamma\gamma}}{m^2_{\pi^0\gamma}})$$

with β denoting the velocity of the the $\pi^0\gamma$, $\vec{\beta} = \vec{p}/E$, $m_{\gamma\gamma}$ and $m_{\pi^0\gamma}$ the invariant masses of the 2 or 3 photon combinations. For high energy showers $\beta \approx 1$ and $cos\theta^\star$ is almost identical with A_ω. The shape of the $cos\theta^\star$ distribution in Figure 5.4 suggests that a kinematic cut around $|cos\theta^\star| < 0.6$ could remove a large fraction of the background combinations and thus potentially improve the signal to background ratio for ωs. The impact of this cut can be seen by comparing Figure 5.5 and Figure 5.6, where the first invariant mass distribution shows all $\pi^0\gamma$ combinations while the second requires $|cos\theta^\star| < 0.6$. An indication of the ω particle presence can be observed in the first of these distributions, but after the $cos\theta^\star$ cut the ω signal becomes unmistakable. Only π^0s with asymmetry $A_{\pi^0} < 0.75$ contribute to these plots.

5.4 Structure in the Background

The plot of the $\pi^0\gamma$ mass spectrum for π^0s with energy asymmetry $A_{\pi^0} > 0.75$, shown in Figure 5.7, reveals several peaks. The insert in the plot emphasizes the ω mass region. An enhancement in the $\pi^0\gamma$ distribution near the mass of 0.8 GeV/c^2 can be interpreted as a presence of a small ω signal. The larger peaks, at about 0.25 GeV/c^2 and at 0.58 GeV/c^2, have a more complicated origin. There are no known particles in these mass regions that could decay to $\pi^0\gamma$. The puzzle was resolved when the two photon mass distribution was formed for these events using the larger energy photon from the π^0 candidate and the single photon. The resulting $\gamma\gamma$ mass distribution is presented in Figure 5.8. The π^0 and η particles are now easily recognizable with their masses centered around 0.135 GeV/c^2 and 0.55 GeV/c^2. We can therefore identify the peaks in Figure 5.7 as reflections of π^0

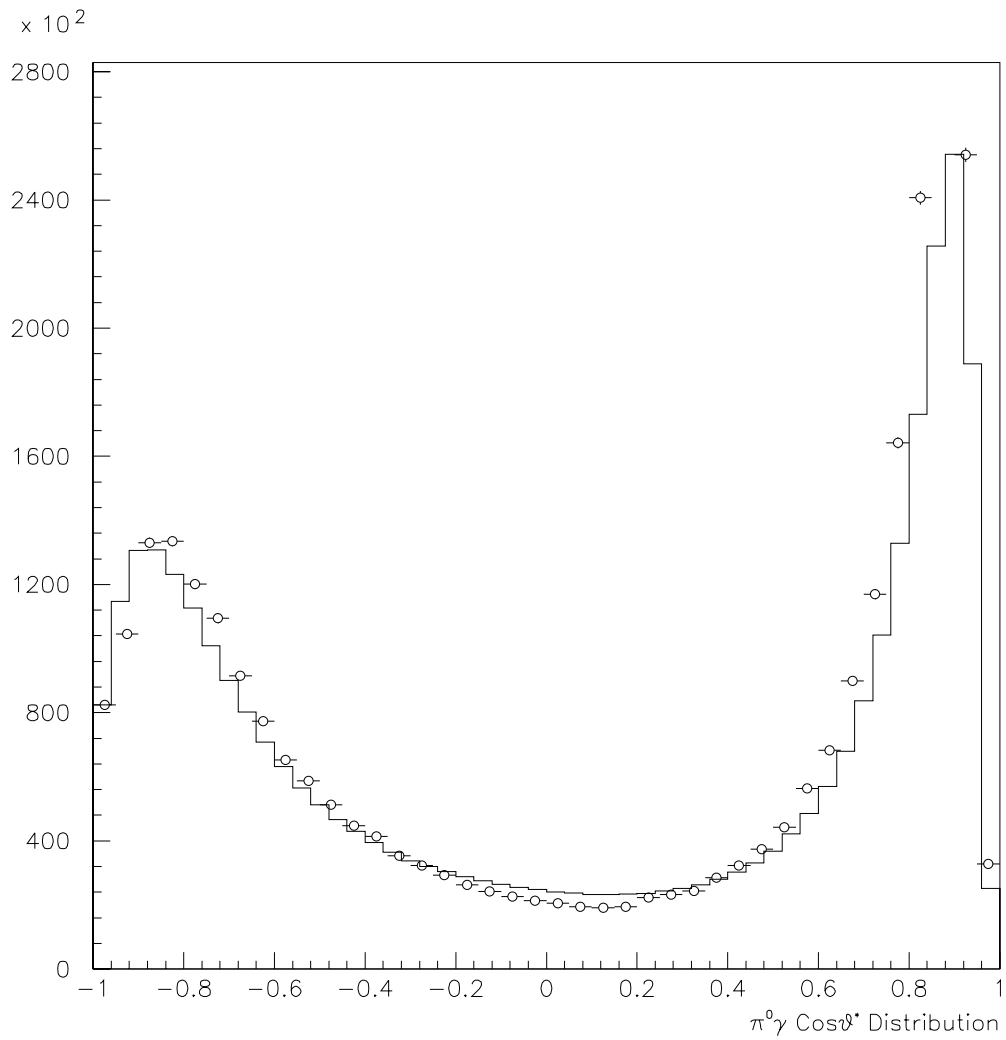

Figure 5.4 The $cos\theta^{\star}$ distribution for the π^0 γ pairs from the triggering octant for the data events (histogram) and Monte Carlo (points). Events were selected via SLH trigger and the distribution is shown for $\pi^0\gamma$ combinations with invariant mass between 0.6 and 0.96 GeV/c^2.

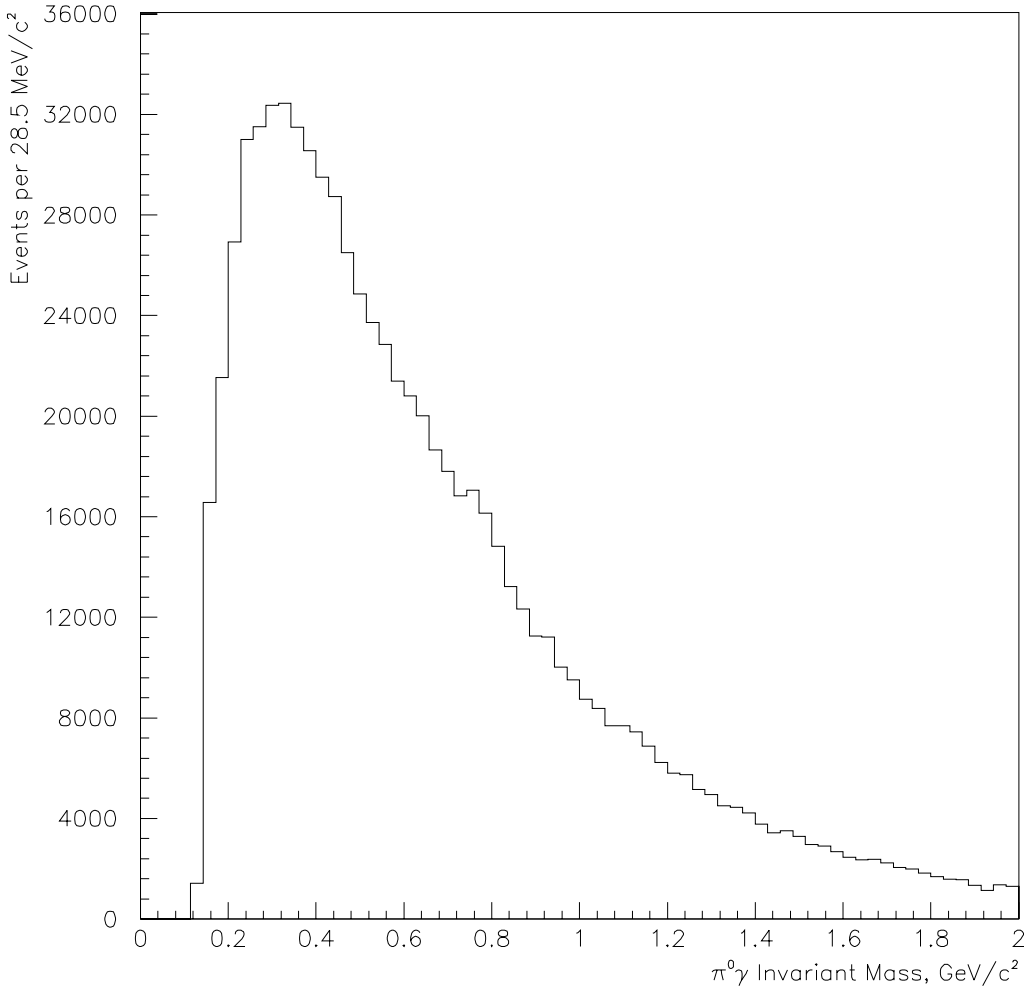

Figure 5.5 The $\pi^0\gamma$ mass distribution for all combinations of photons found in the triggering octant for which $4.0 < p_T < 10$ GeV/c and for π^0 energy asymmetry $A_{\pi^0} < 0.75$. Events were selected by the SLH trigger.

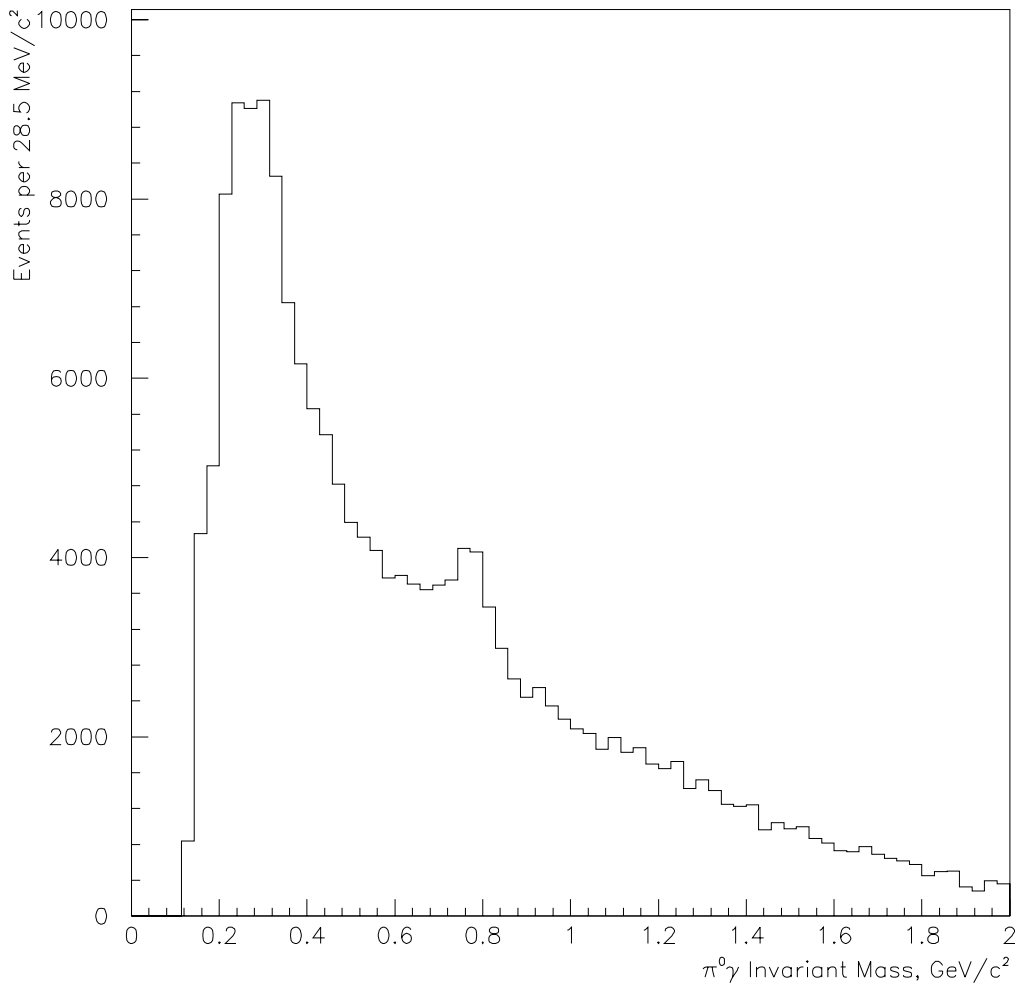

Figure 5.6 The $\pi^0\gamma$ mass distribution for all combinations of photons found in the triggering octant with π^0 energy asymmetry $A_{\pi^0} < 0.75$ after the $|cos\theta^\star| < 0.6$ cut. The p_T of $\pi^0\gamma$ is in the range $4.0 < p_T < 10$ GeV/c and the events were selected by the SLH trigger.

and η particles in the $\pi^0\gamma$ spectrum [2]. These structures arise because a true π^0 or η photon, paired with an accidental photon in the event passes the π^0 candidate definition and then, when combined with the remaining true photon of the π^0 or η, contributes to the enhancement in the $\pi^0\gamma$ spectrum.

5.5 π^0 Sideband Subtraction

The study of the $\pi^0\gamma$ mass spectrum for high π^0 asymmetry revealed evidence for structures in the background due to reflections. We were able to identify a significant structure in the vicinity of the ω mass as coming from $\gamma\eta$ combinations. Although the η reflection is not obviously present in the $\pi^0\gamma$ mass spectrum for candidate π^0 asymmetries less than 0.75 (see Figure 5.6), a study of Monte Carlo events was undertaken to determine if the eta interferes with the omega signal measurement in that asymmetry range. A Monte Carlo simulation of events which each contained a high p_T eta (called the η MC) was available. This sample was originally generated to determine the eta meson reconstruction efficiency. The η MC event sample was processed in the same fashion as the data and a search for $\pi^0\gamma$ was performed. It should be noted that due to the method of generation of the η MC events the presence of a true high p_T omega was very unlikely in this sample. The resulting $\pi^0\gamma$ invariant mass spectra in two π^0 asymmetry bins $A_{\pi^0} > 0.75$ (solid line) and $A_{\pi^0} < 0.75$ (dashed line) are presented in Figure 5.9. A peak in the vicinity of the omega mass range can be observed in both distributions. The dashed line histogram in Figure 5.9 exhibits a much lower and broader peak than the solid line histogram. It is harder to find a photon in a high p_T eta event

[2] The term "reflection" is most often used in the literature to describe a structure in a mass spectrum arising from misassignment of particle identities as for example in $K^{0\star} \rightarrow K^+ \pi^-$ case, were the K^+ and π^- identities are interchanged. However, it is also used in the sense described in this thesis, – e.g., in [65].

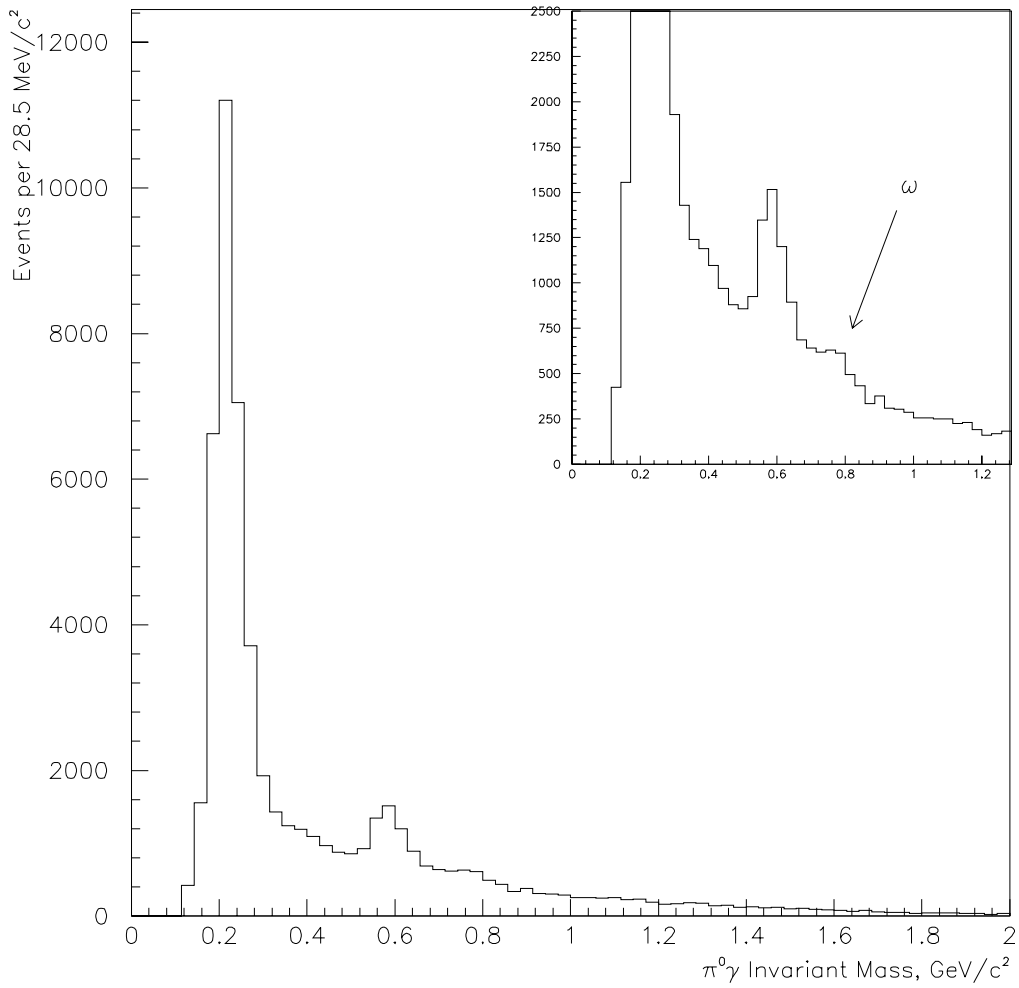

Figure 5.7 The π^0 γ mass distribution for photons passing $|cos\theta^\star| < 0.6$ when π^0 energy asymmetry $A_{\pi^0} > 0.75$ and the p_T of the 3 photons is in the range 4.0 to 10 GeV/c.

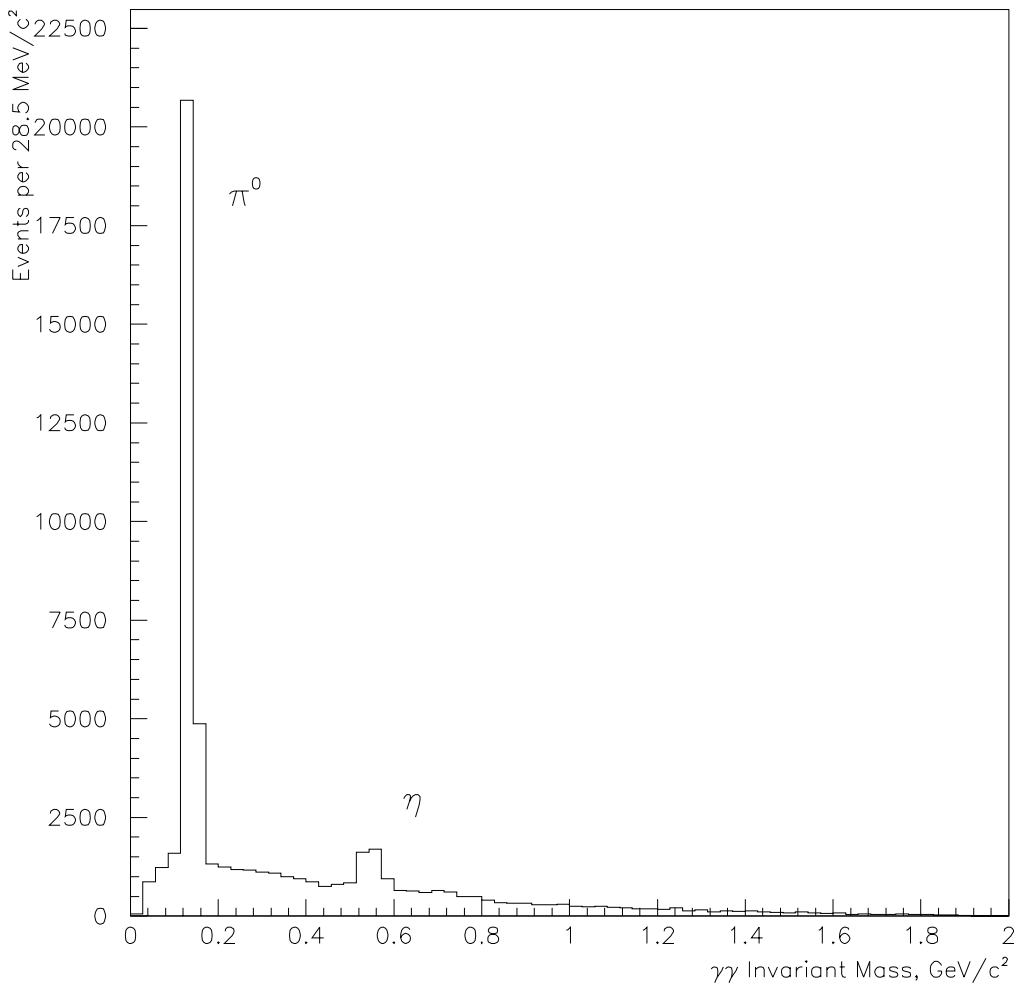

Figure 5.8 The $\gamma\gamma$ mass distribution of the larger energy photon of the π^0 candidate and the third photon originally used to make $\pi^0\gamma$. The candidate π^0 energy asymmetry A_{π^0} was > 0.75. The π^0 and η peaks are clearly visible indicating that a substantial fraction of the high asymmetry candidate π^0s are accidental combinations of a photon from another source with a photon from a π^0 (or η).

that can accidentally combine with a high energy photon from an η to form a candidate π^0 with low asymmetry than high asymmetry. The broadness of the $\gamma\eta$ peak depends on the amount of energy the γ contributes to the $\gamma\eta$ pair and also their separation. The larger the energy of the γ, the smaller is the resemblance of the resultant $\gamma\eta$ pair to the η mass.

Figure 5.9 shows that the η reflection contributes to the $\pi^0\gamma$ mass spectrum even when the candidate π^0 asymmetry is less than 0.75. This is the kinematic sample in which we intend to measure the omega signal, and the presence of the η reflection is undesirable. To remove it, a method of π^0 sideband subtraction was considered. It is the background under the true π^0 that contributes to the $\gamma\eta$ bump, and hence there will likely be no difference between taking a $\gamma\gamma$ from the mass range of 0.11-0.165 GeV/c^2 or, for example, from the π^0 sidebands 0.07-0.1 and 0.18-0.21 GeV/c^2. This hypothesis was tested using the eta Monte Carlo. A three photon mass spectrum was formed using the π^0 sideband entries (π^0_{sb}) combined with any other photon in the octant, and then subtracted from the original $\pi^0\gamma$ mass spectrum. The η reflection disappeared almost entirely as shown by the dotted histogram in Figure 5.9. Hence the π^0 sideband subtraction technique provided a method of suppressing the background structures around the omega mass range. This method was applied to $\pi^0\gamma$ mass spectrum prior to fitting the background and counting the ω signal. In this method we have assumed that the background inside the signal region in the $\pi^0\gamma$ distribution could be approximated by a linear interpolation between background regions on either side of the signal. The validity of this assumption will be tested by studying the sensitivity of the number of measured omegas to the definition of the sideband region.

The combined width of the π^0 sideband regions, defined above, is larger than the width of the π^0 mass range (0.11-0.165 GeV/c^2) to account for the observed

curvature of the $\gamma\gamma$ background. A more precise determination of the amount of background under the π^0 peak was performed. A second order polynomial (P2) and a gaussian shape were fitted to the $\gamma\gamma$ distributions in each of the p_T bins selected for the omega measurement. The P2 functions were then used as the background representations in the π^0 mass range and the numbers of combinations under the P2 ($N_{\pi^0 mr}$) were determined. The numbers of $\gamma\gamma$ combinations in π^0 sideband region ($N_{\pi^0 sb}$) were obtained by simple counting. The ratios of $N_{\pi^0 mr}$ to $N_{\pi^0 sb}$ gave scale factors by which the $\pi^0_{sb}\gamma$ invariant mass histograms were multiplied prior to π^0 sideband subtraction. The scale factors were approximately 1.1 but varied between 0.8-1.2 in the low statistics region at high p_T. The $\pi^0\gamma$ sideband subtracted histogram (denoted below as $\pi^0\gamma_{sbs}$) in each p_T bin was obtained by:

$$\pi^0\gamma_{sbs} = \pi^0\gamma - \pi^0_{sb}\gamma \times \frac{N_{\pi^0 mr}}{N_{\pi^0 sb}}$$

5.6 Definition of the ω Signal

Once the existence of the ω signal was established in the E706 data sample, methods of extracting the number of ωs above background were investigated. The difficulty in obtaining this number rested mainly in the lack of a precise knowledge of the behavior of the background in the vicinity of the ω peak even after the π^0 sideband subtraction. The study of the signal and background behavior was done in several p_T bins of widths of 0.33, 0.5 or 1 GeV/c, covering the range between 3.5 to 8 GeV/c – the full range where the signal was visible. The background shape changed substantially with p_T, so that the functions describing the background in low p_T bins could be very different from the functional form used for high p_T bins. We could not obtain any guidance from Monte Carlo sample due to the lack of agreement between the shapes of the $\pi^0\gamma$ mass distributions in MC sample and

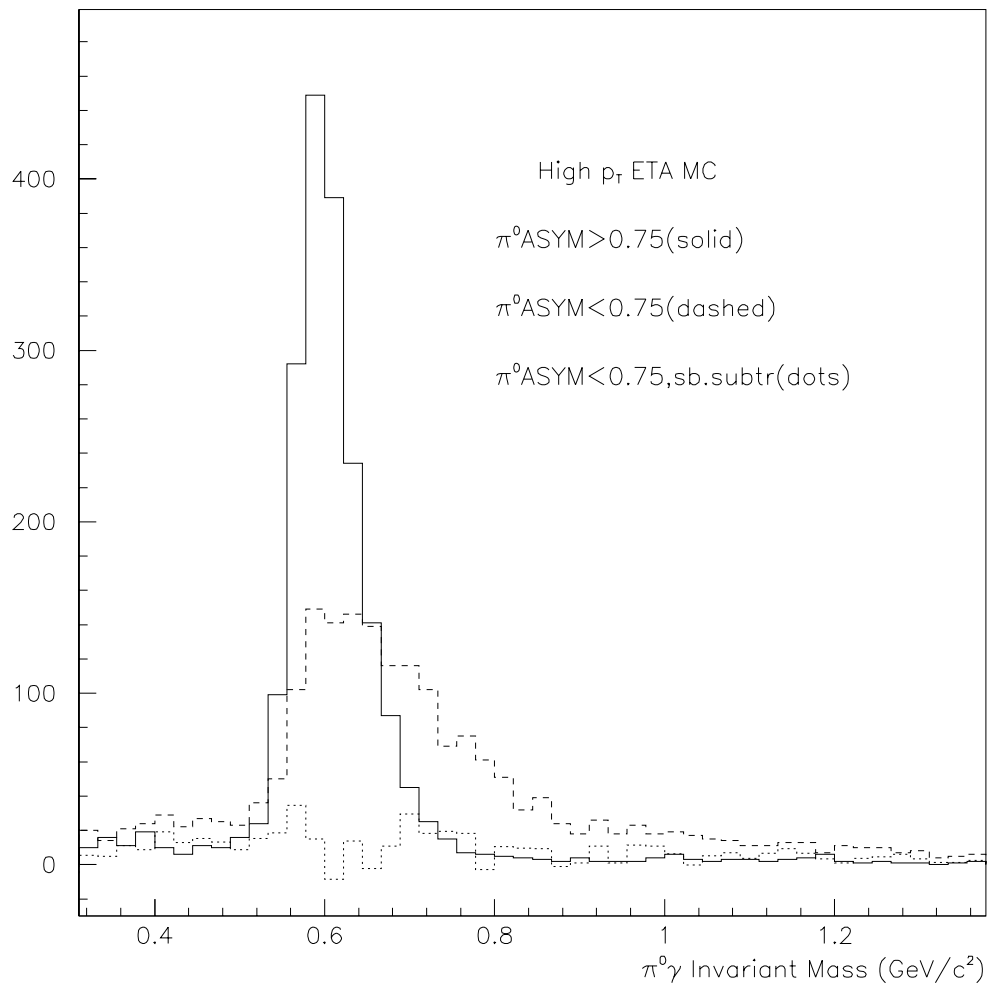

Figure 5.9 Monte Carlo events with high p_T ηs reconstructed in the $\pi^0\gamma$ mode, for π^0 energy asymmetry $A_{\pi^0} < 0.75$ (dashed line) and $A_{\pi^0} > 0.75$ (solid line). Dotted line shows the mass spectrum after the π^0 sideband subtraction. P_T of the combinations ranged from 4 to 10 GeV/c.

the data, as will be described in the chapter on the Monte Carlo (and Figure 6.6). The extraction of the signal is described in the Analysis chapter, after a discussion of the corrections.

High p_T π^0s and ηs are reconstructed in the LAC detector with widths of about 7 and 20 MeV/c^2, respectively [16], and it is clear that detector resolution effects in the ω mass range will dominate over the natural width of the resonance (which is 8.5 MeV/c^2). Thus the mass peak is expected to have a gaussian shape rather than be described by a Breit-Wigner formula used for resonance states. The ω signal region is defined as a three sigma interval around a fitted mean mass. For the width of the gaussian (sigma) we take an average width from fits measured at different p_Ts (38 MeV).

Chapter 6 Monte Carlo

Monte Carlo simulation of the response of the E706 apparatus to hard scattering processes and particle production is important to our cross section measurements. The Monte Carlo is used to account for the unavoidable biases introduced into event selection during data taking. It permits measurement of losses due to the geometrical acceptance of the detectors and provides a means of evaluating the reconstruction efficiency for a given process. By simulating high energy π^- collisions with proton and neutron targets we can investigate the generated events, including those not found in the actual data sample. The closer the Monte Carlo describes the scattering processes and simulates the detectors, the more accurately we can determine the fraction of undetected particles and apply this information to the cross section measurements.

The Monte Carlo used by the E706 collaboration consisted of three major elements: an event generator (HERWIG), a detector simulation package (GEANT), and an additional E706-specific software package called the Preprocessor. GEANT[66], a software program developed at CERN, simulates the passage of elementary particles through matter. Essential physics processes that occur in the development of electromagnetic showers are incorporated. GEANT provides a data base of standard geometrical shapes and material properties that were used to model the E706 detectors. The input to the GEANT program was provided by the HERWIG[31] particle generator. Event generators used in high energy physics experiments utilize current knowledge of parton-parton interactions, fragmentation functions, and various particle production and decay rates in modeling the physical processes occurring in collisions. E706 evaluated both PYTHIA[32] and HERWIG as possible event generators. HERWIG was selected for our purposes because it provided a closer match of event characteristics between Monte Carlo

(MC) and data. From events generated by HERWIG in simulating hard-scattering processes, those events which contained a π^0 or γ with p_T in excess of a specified generation threshold (e.g., 3.0 GeV/c) were selected and allowed to progress through various E706 detectors. This selection scheme was later expanded to allow for selection of events based on the transverse electromagnetic energy after the particles reached the LAC, to closer simulate the actual data selection process.

Detector inefficiencies, dead channels, electronic noise, and resolution smearing were all added via the Preprocessor program. MC events were then reconstructed just as real data and stored in the form of DSTs. During the reconstruction stage, trigger sums-of-8 were formed for each 8 consecutive r-strips of the LAC detector, and the response of the trigger logic for SLH/LGH triggers was simulated. The effect of the time-dependence of the energy scale of the LAC (as discussed in Energy Scale section of chapter 4) and various other smaller scale effects were also modeled.

6.1 Comparison of Data with Monte Carlo

In this section several distributions are presented to illustrate how well the simulated events agreed with the data. Figure 6.1 shows the total number of photons and the number of photons in the triggering octant for events in which a high p_T π^0 was reconstructed, both for the MC and for the data. For this and the remaining comparison plots, the Monte Carlo events were weighted with the simulated SLH trigger probability and data events were selected via the SLH triggers. On average, the MC events have more photons than observed in the data. However, the multiplicities of neutral particles agree well in the triggering octant. The energy and energy asymmetry distribution for photons from the π^0 mass region are compared in Figure 6.2. The agreement between MC (open circles) and the data (histogram) is good. The excess of $\gamma\gamma$ combinations in the

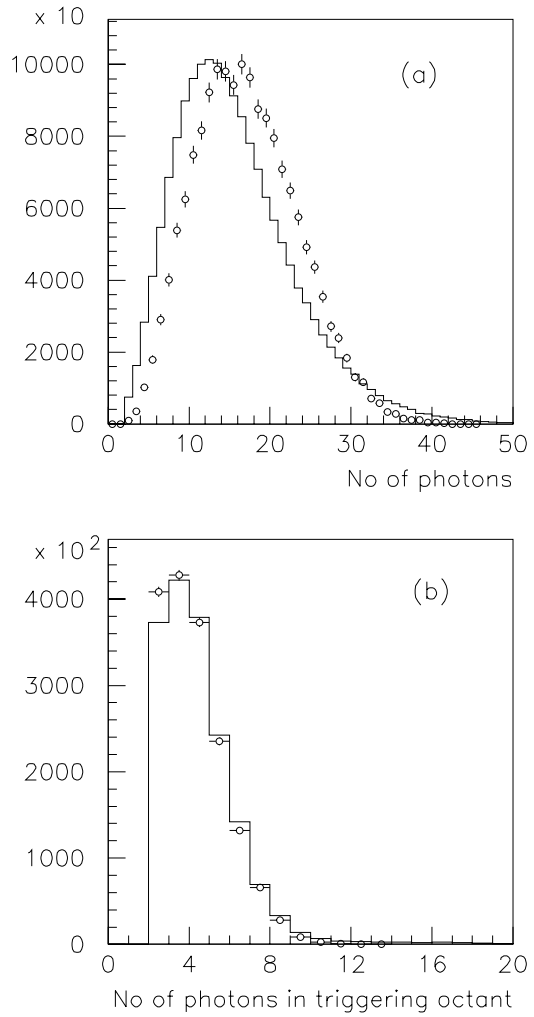

Figure 6.1 (a) Multiplicity of photons in events with reconstructed π^0s of $p_T >$ 3.5 GeV/c for SLH triggers in data (histogram) and for MC events (open circles). (b) Number of photons in the triggering octant of these events. MC distributions were scaled to match the data histograms near the maximum of the distributions.

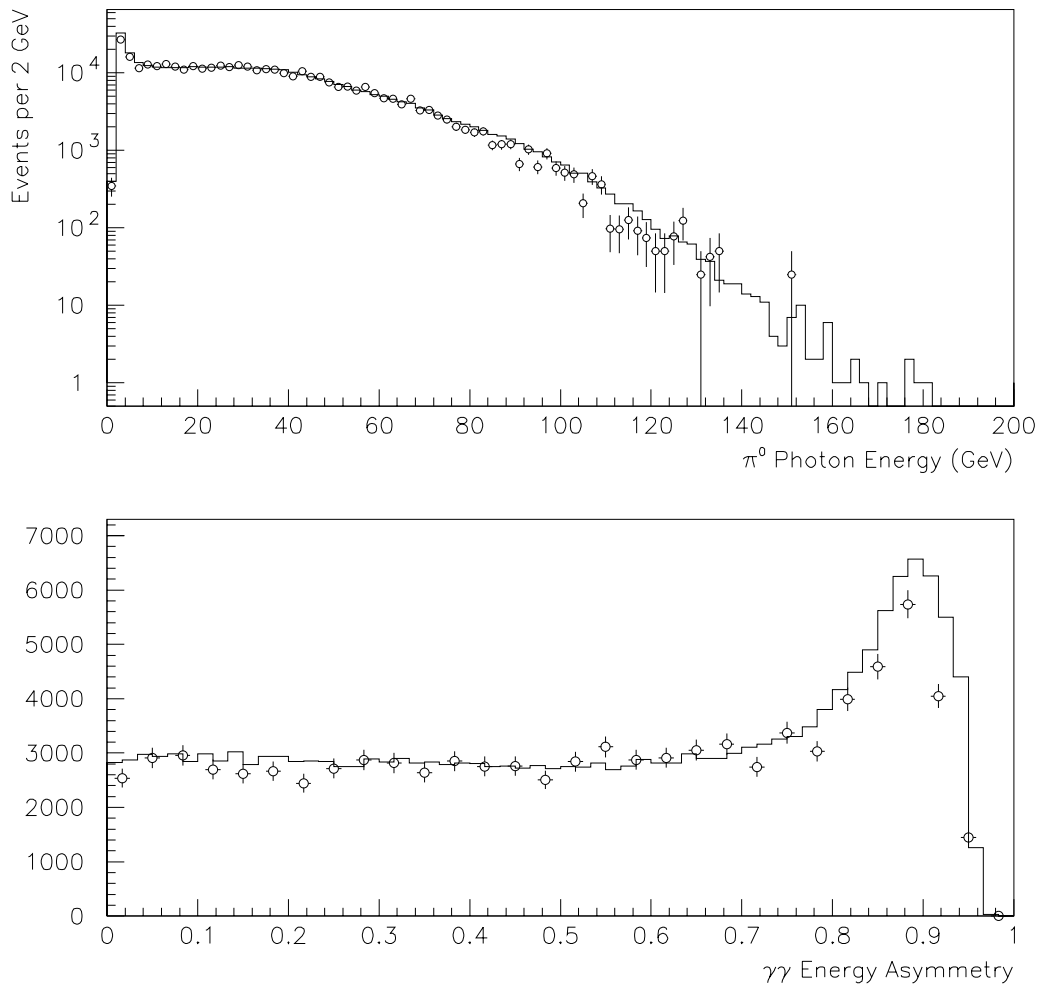

Figure 6.2 Energy distribution for photons with $0.11 < m_{\gamma\gamma} < 0.165$ GeV/c^2 (a) and their energy asymmetry A_{π^0} (b), for data (histogram) and Monte Carlo (open circles) events. Data events were selected via the SLH triggers, and MC events were weighted with SLH trigger probability. The MC distributions were scaled to the data.

large energy asymmetry region relative to the flat distribution expected for π^0 pairs is characteristic of the soft photon background. Figure 6.2(b) indicates that this background is somewhat larger in the data than in MC events.

To study $\pi^0\gamma$ distributions, MC events with 3 or more photons in an octant were chosen. The same selection criteria were used for the Monte Carlo events and the data (as discussed in the Data Selection section of the previous chapter). In the sample selected, two and three photon mass distributions were evaluated and compared to the data. The plots of high p_T $\gamma\gamma$ pairs in the π^0 mass region are shown in Figure 6.3. Only those $\gamma\gamma$ pairs which formed three photon combinations with p_T from 3.5 to 5.0 GeV/c (Figure 6.3(a)) or from 5.0 to 10 GeV/c (Figure 6.3(b)) when combined with a photon from the same octant contributed to these plots. We observe again that the data events are characterized by a larger background compared to Monte Carlo.

The two photon mass spectra plotted in several transverse momentum bins were fitted with Gaussian distributions for the π^0 signal and second order polynomials to describe the background for both the MC and data distributions. Figure 6.4 presents the mean values of the reconstructed π^0 masses and the widths. The MC and data energy scales agree quite well. The level of agreement between the widths of the mass distributions indicates proper modeling of the detector resolution.

The rapidity distributions of $\pi^0\gamma$ combinations in the omega mass range are compared in Figure 6.5, for events selected by the SLH as well as the LGH trigger. The agreement between the data (solid histogram) and the Monte Carlo (open points) improves with increasing p_T of the $\pi^0\gamma$, as can be seen in Figure 6.5, where distributions for two different p_T intervals are presented. The dotted histograms shown in these plots are rapidity distributions obtained with "dedicated" omega Monte Carlo events (described below).

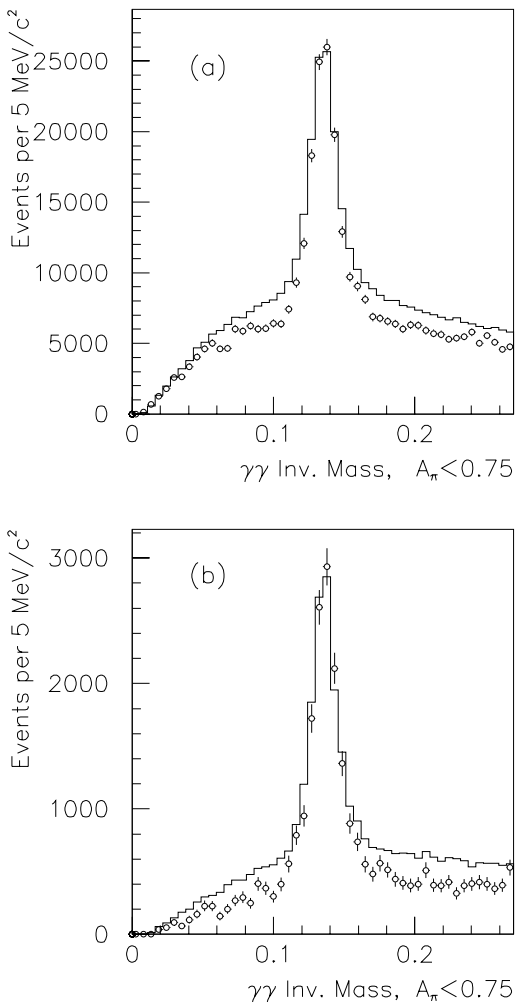

Figure 6.3 Comparison of invariant mass distributions for $\gamma\gamma$ pairs between the data(histogram) and E706 Monte Carlo (open points). Events were preselected for omega analysis. The p_T of $\pi^0\gamma$ combinations was from 3.5 to 5 GeV/c (a) or from 5 to 10 GeV/c (b). The distributions were normalized at their peaks.

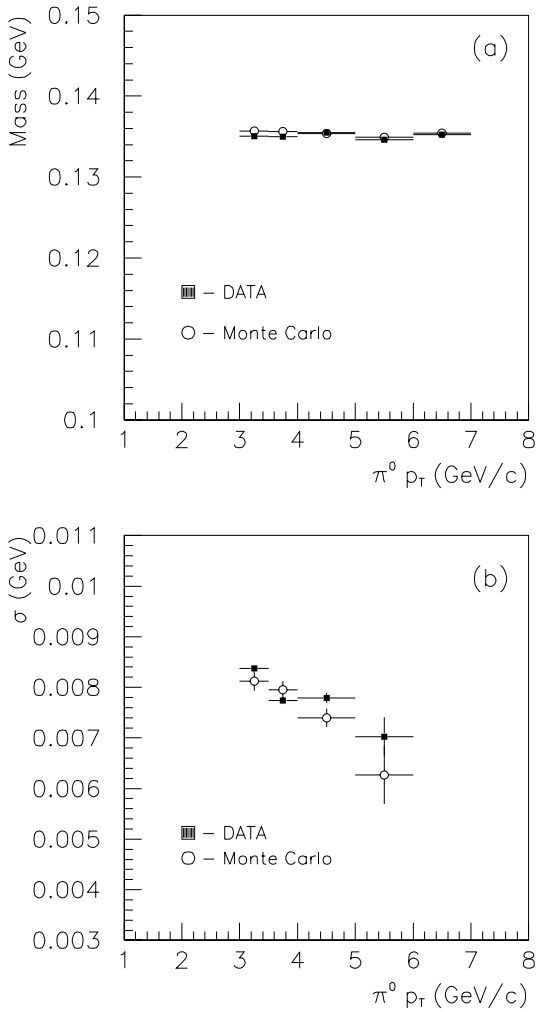

Figure 6.4 The mean π^0 mass versus π^0 p_T in the data (square) and the Monte Carlo (open circle) for π^0s with asymmetry $A_{\pi^0} < 0.75$; (b) is the comparison of the widths of the π^0 peak versus the p_T of the π^0.

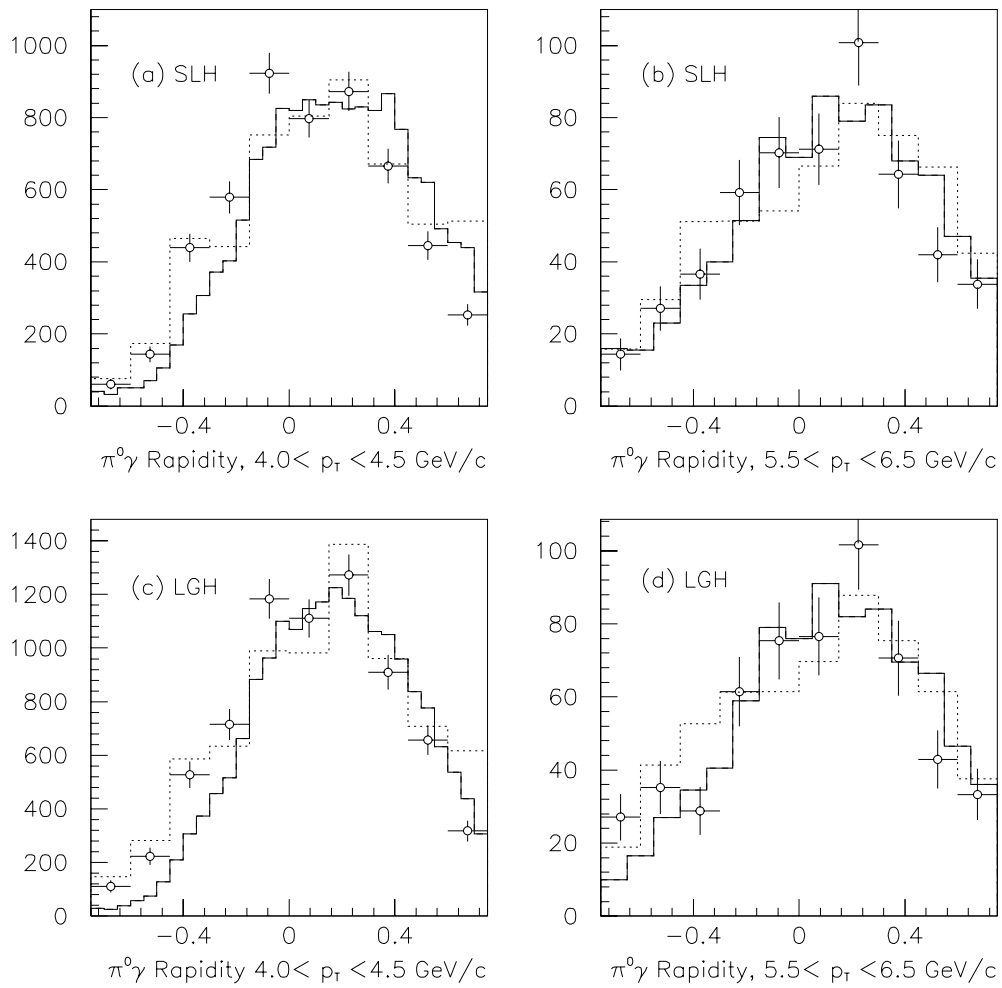

Figure 6.5 Comparison of $\pi^0\gamma$ rapidity distribution between data (histogram) and E706 Monte Carlo (open circles), for $\pi^0\gamma$ combinations from the omega mass range. Dotted histograms were obtained with the dedicated omega Monte Carlo. The MC distributions are scaled to the data in an arbitrary manner.

In the next step, the $\pi^0\gamma$ mass distribution was formed for the MC events and compared to the data, as presented in Figure 6.6, for two different ranges of $\pi^0\gamma$ transverse momentum. The general shape of the distributions are similar. However, in the mass range between 0.5-0.9 GeV/c^2 the Monte Carlo exhibits an excess of events relative to the data (the two distributions were normalized in the high mass region). It was established that the excess was unrelated to omega meson production, but was the result of $\pi^0\pi^0$ correlations present in the MC when two high p_T π^0s came from the same fragmentation cluster. This was established through the study of the fragmentation history (provided by the HERWIG generator) of the particles contributing to the 0.5-0.9 GeV/c^2 mass range. When mass combinations were formed from a π^0 and one photon from another π^0 in the same cluster, they contributed to the excess in the 0.5-0.9 GeV/c^2 mass range. This type of correlation is not expected to be present in the true physical processes, and it is not present in events generated with the PYTHIA generator. Because of this effect, one could not measure the reconstruction efficiency for omega mesons with the standard E706 Monte Carlo. Consequently, a relatively small number of "dedicated" ω events were produced as follows: QCD $2 \rightarrow 2$ hard parton scattering events were generated in HERWIG until an $\omega(783)$ meson of p_T in excess of the pre-set generation threshold was found among the hadrons into which the quarks and gluons fragmented. These events were subsequently propagated through the E706 detectors using the GEANT package. Omega branching ratios were altered to allow only the $\omega \rightarrow \pi^0\gamma$ decay. Table 6.1 details the numbers of events containing high p_T omegas that were generated at various p_T thresholds in this MC pass.

Generation Threshold(GeV/c)	**Number of Events**
2.5	4,900
3.0	73,000
3.5	55,000
4.0	9,700
4.5	7,000
5.5	5,000
6.5	3,000
Total	157,600

Table 6.1 Number of MC ω events generated in various p_T bins.

The problematic $\pi^0\pi^0$ correlations were less likely to affect the selected omega events in this sample, since it was improbable that a high p_T $\pi^0\pi^0$ pair would accompany ω photons in the same hemisphere of the detector. The $\pi^0\pi^0$ pairs could occur in the recoil (or opposite hemisphere) jet, but these were not allowed to contribute to the background because of same octant requirement. Since it was argued in an earlier part of this section that the general characteristics of events produced by HERWIG matched the data quite well, the dedicated ω events produced by HERWIG are expected to have the event structure, p_T spectrum, and other relevant quantities (in the omega hemisphere) characteristic of the data. We thus can learn about the spectrometer's response to omega mesons by studying the dedicated ω MC sample, while cautiously treating the problem of now very different background characteristics between the data and the simulated events.

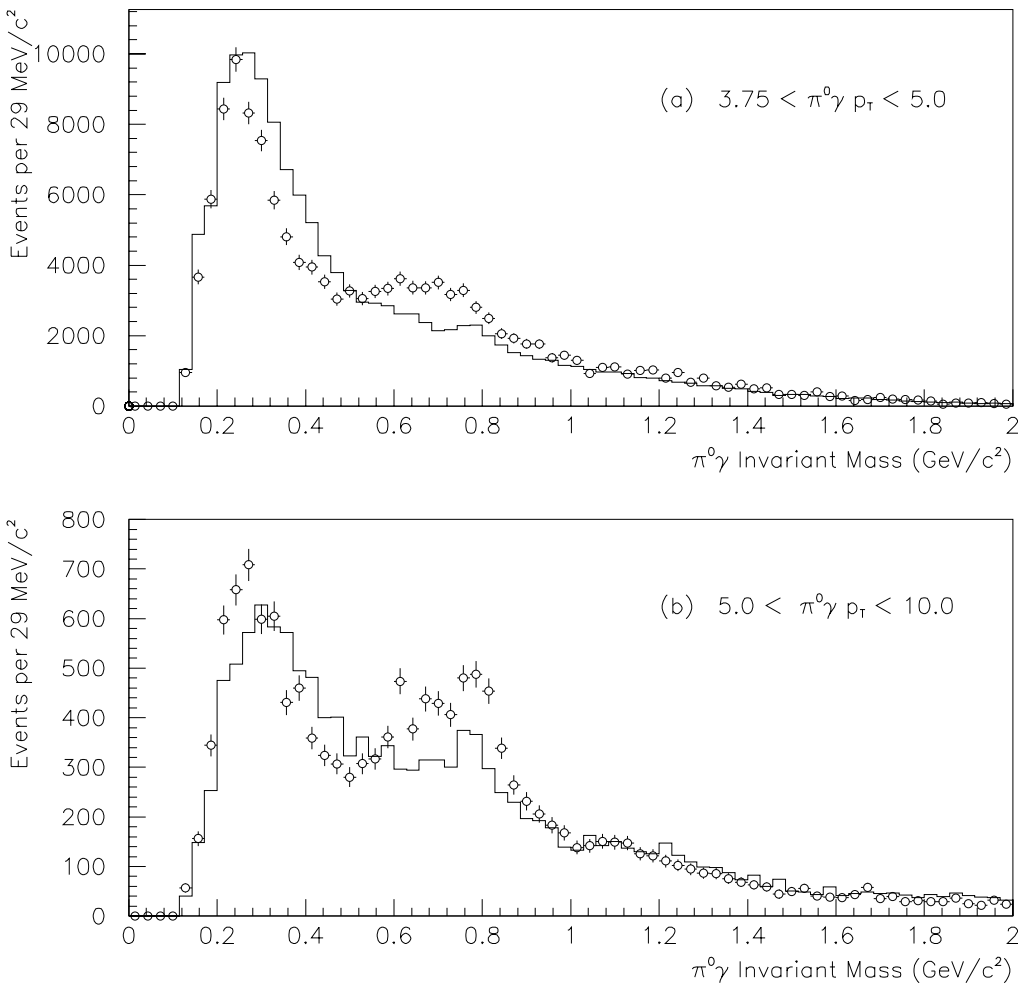

Figure 6.6 Comparison of $\pi^0\gamma$ invariant mass distributions between data (histogram) and E706 Monte Carlo (open circles). Monte Carlo points were scaled to match the data histogram in the high mass region; $A_{\pi^0} < 0.75$

6.2 Geometrical Acceptance

The omega meson $\omega(783)$ is a relatively heavy particle, and in its decay to $\pi^0\gamma$ the opening angle between the products of the decay is not small. The spatial separation of the π^0 photons and the γ at the front of the LAC is on average 27 cm with a tail to 90 cm. It is therefore very likely that not all 3 photons of the ω hit the same octant or even quadrant of the LAC. In order to determine the losses of produced ωs attributable to the geometrical acceptance of the E706 detector and its segmentation into triggering octants, the dedicated ω Monte Carlo events were studied. We do find that only about 65% of the omega mesons produced in a central rapidity range have all 3 photons within the fiducial region of the LAC. This is illustrated in Figure 6.7 (a). Figure 6.7 (b) shows the percentage of omegas accepted when all 3 photons were required to deposit their energy within the same octant [1]. The effect of the "same octant" requirement is presented versus rapidity (Y) of the ω in Figure 6.8 (a). This function varies slowly with Y except for the fall-off in the most forward region. To avoid this region the condition $-0.75 < Y < 0.75$ was imposed upon the ω rapidity. This restriction was later modified to $-0.5 < Y < 0.75$ to remove an interval in Y without proper trigger corrections[2].

In this analysis we average over the rapidity range and give results versus p_T only due to statistical limitations in the number of omega events in the data. It

[1] The requirement that 3 photons of the ω fall into the same octant was imposed to reduce uncertainties in the corrections for trigger effects. All triggers were octant-based.

[2] The π^0 cross section, measured in the SLH triggered sample exhibits a substantial fall-off at π^0 p_T below 4.2 GeV/c in backward rapidities when compared to the cross section measured in the sample that satisfied the Single Local Low (SLL) trigger. Unfortunately, the ω signal could not be found in the small SLL sample.

is possible that in the process of averaging over the rapidity a systematic shift is introduced into the cross section measurement. This effect would stem from differences between the MC and the data ω rapidity distributions (compare $\pi^0\gamma$ distributions in Y in Figure 6.5); see also the discussion of the systematic errors in section 9.2.

We establish that the geometrical acceptance does not have a dependence on the z-position of the generated vertex in the target. Figure 6.8 (b) shows the percentage of geometrically accepted ωs versus the position of the vertex of the event and the distribution is found to be independent of that position. Both the geometrical acceptance correction and the reconstruction efficiency correction are averaged over the location of the vertex in the target.

6.3 Trigger Acceptance for ω

There is a class of ω events that will not satisfy the SLH trigger even for ωs with relatively high transverse momentum (such as 5 or 6 GeV/c). The splitting of the ω's energy between 3 photons and their wide spread over the octant could prevent the local trigger requirements from being satisfied. To account for the omegas not triggered upon, we relied on the Monte Carlo simulation of the trigger. The distribution presented in Figure 6.9 was produced with the dedicated ω MC. The percentage of ω events satisfying the SLH trigger is plotted versus p_T. The π^0 and γ of the ω were required to fall into the fiducial volume of the same octant and to pass $cos\theta^\star$ and π^0 asymmetry cuts. From the plot, we can estimate the magnitude of the loss of omega events encountered during the data taking phase. For example, only about 8% of omegas with p_T between 3 and 4 GeV/c passed the SLH trigger requirements.

The large losses result in large correction factors that are determined from the MC. In order to verify that the trigger effects are modeled accurately in the Monte

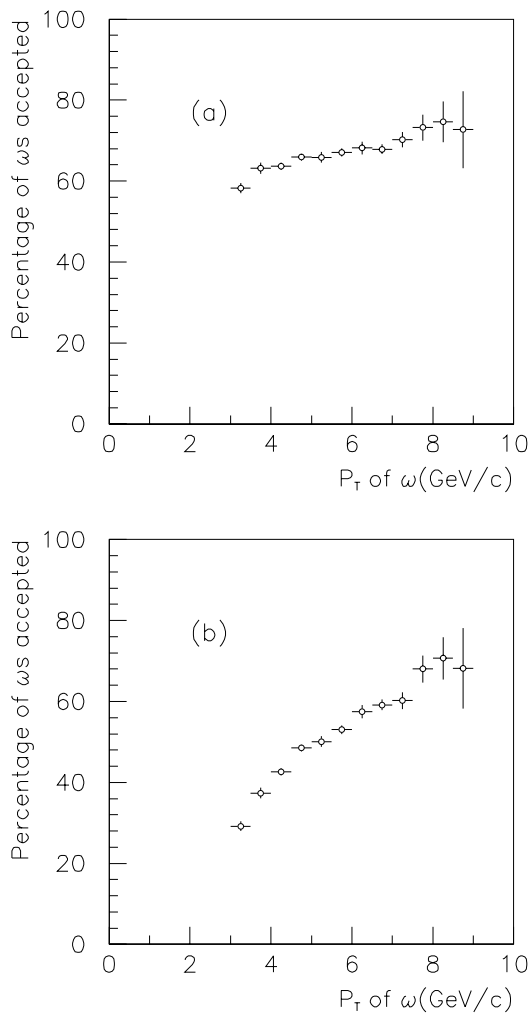

Figure 6.7 (a) Effect of the fiducial region requirement on the 3 photons of the $\omega \rightarrow \pi^0\gamma$ versus ω p_T. (b) All 3 photons of the ω are required to fall into the fiducial region of the same octant. Only particles passing $|cos\theta^\star| < 0.6$ and $-0.75 < Y < 0.75$ cut are considered.

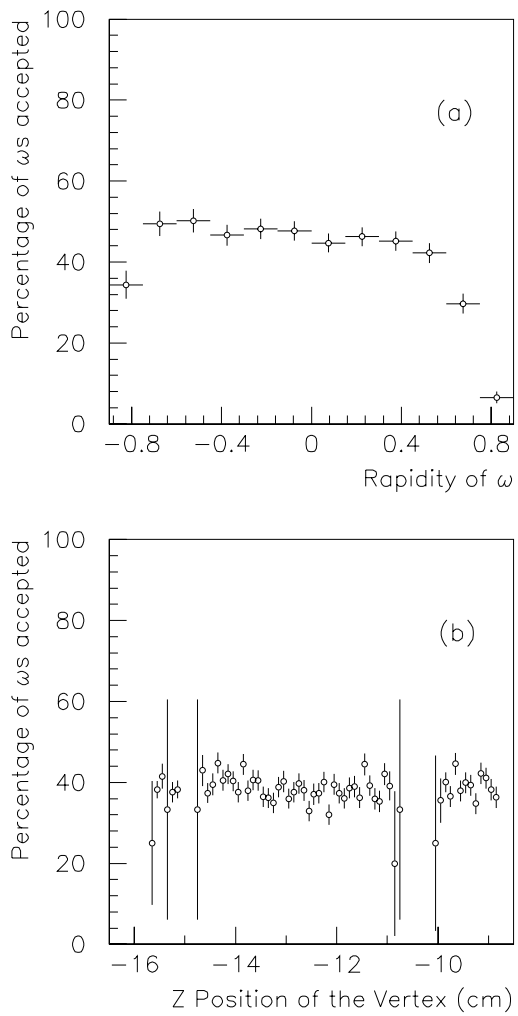

Figure 6.8 (a) Geometrical acceptance for $\omega \rightarrow \pi^0\gamma$ plotted as a function of rapidity Y; $|cos\theta^\star| < 0.6$ is required. Transverse momentum is between 4 and 5 GeV/c. (b) Percentage of ωs accepted within fiducial region of one octant versus the z-position of the event vertex. The points with large error bars correspond to the edges of the target where only a few events are reconstructed.

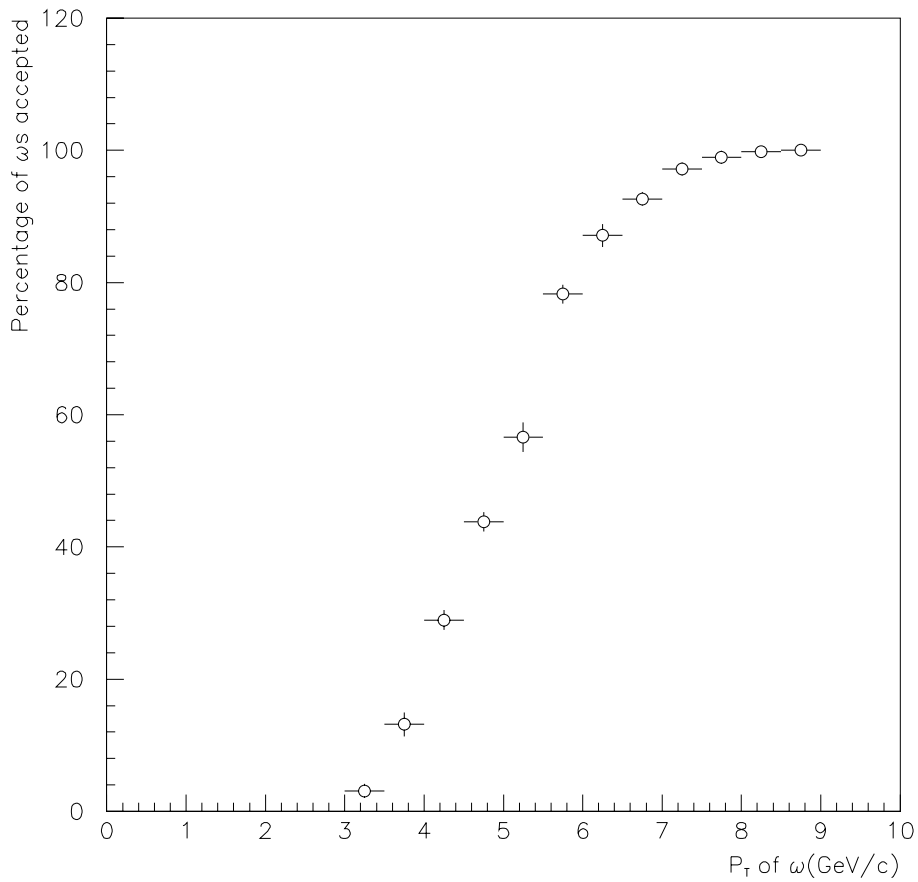

Figure 6.9 Simulation of the trigger acceptance for $\omega \rightarrow \pi^0\gamma$ events versus p_T. Even at 6 to 7 GeV/c p_T, well above the SLH trigger turn-on for a single local group, the acceptance is not 100 % due to the spread of ω's energy over several triggering units.

Carlo program (and that the correction factors are reliable) a comparison of trigger probabilities in MC and data was performed. For this comparison, we turned to the standard MC sample rather than the dedicated omega events. This choice was motivated by two factors: (1) Trigger characteristics in the data for events from the omega mass range are dominated by the behavior of the background $\pi^0\gamma$ combinations rather than the true ωs; (2) Triggering probability is higher for background $\pi^0\gamma$ events than for ω events, because the background is usually more asymmetric in energy at a given p_T. Thus in order to compare to the data sample (mostly background) we need to consider the standard MC events (also mostly background). Figure 6.10 presents the trigger probability distribution obtained for octants containing a π^0 and a γ with mass in the ω signal region and with $\pi^0\gamma$ $p_T > 3.5$ GeV/c. The distribution for data events (histogram) is compared with the trigger probabilities for the standard Monte Carlo events (solid points). There is a large excess of Monte Carlo events over the data in the region of low triggering probability. No trigger requirement was imposed on this MC (solid points). The open circles in the same plot are Monte Carlo events weighted with the probability of satisfying the SLH trigger. This distribution agrees well with the data. We therefore conclude that when the trigger is simulated in the MC and events are weighted by the probability of satisfying that trigger, the resulting distributions properly represent the trigger mechanisms in the data.

6.4 Trigger Probability and the $Cos\theta^\star$ Cut.

The interdependence between the likelihood of satisfying the trigger and the shape of the $cos\theta^\star$ distribution has been investigated. The distribution in $cos\theta^\star$ for the $\omega \to \pi^0\gamma$ is flat in the Monte Carlo, and we assume it is also flat in the data for the produced ωs. However, the trigger preferentially selects ω events with a high

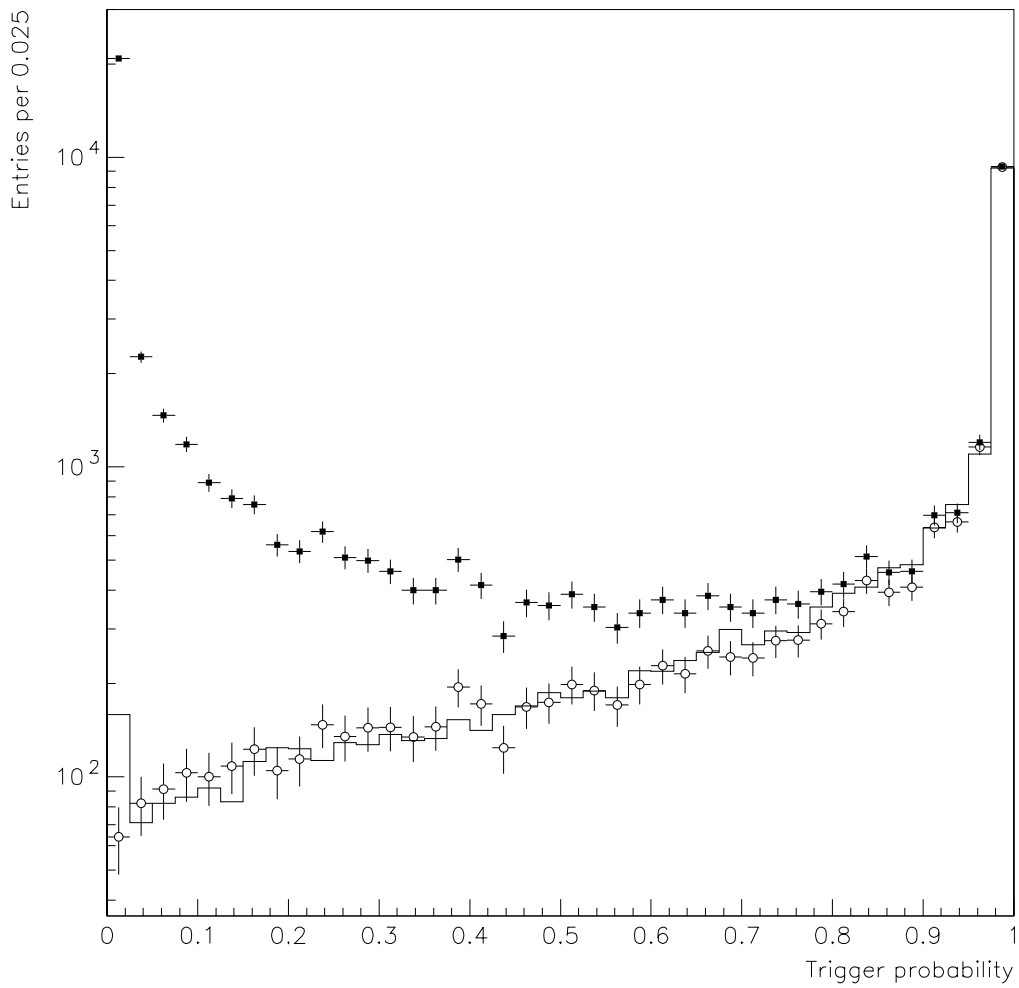

Figure 6.10 Probability to fire the SLH trigger for $\pi^0\gamma$ combinations from the ω mass region, with $p_T > 3.5$ GeV/c, for both data (histogram) and MC (points). The squares are for all reconstructed MC $\pi^0\gamma$s, the open circles are the same MC events weighted with the simulated SLH trigger.

energy asymmetry [3]. This can be seen in 3 plots on the left side of Figure 6.11. The percentage of ω events satisfying the SLH trigger among all events geometrically accepted in one octant is plotted versus the ω energy asymmetry, for 3 different ranges of ω p_T. The most asymmetric decays of $\omega \rightarrow \pi^0\gamma$ have the largest trigger acceptance. However, these regions in asymmetry are removed by the $|cos\theta^\star| < 0.6$ cut. This result does not have as bad a consequence as it might seem. The plots on the right side of Figure 6.11 represent the combined trigger and geometrical acceptance for ω (measured now relative to all generated ωs) versus ω's energy asymmetry. The increased trigger acceptance at large absolute values of ω asymmetry competes with the much reduced geometrical acceptance in this kinematic region, and the overall result turns out to be relatively flat. We can therefore conclude that the $cos\theta^\star$ cut does not adversely affect the numbers of observed omega mesons.

6.5 Reconstruction Efficiency

The reconstruction efficiency measures how likely it is to reconstruct a $\pi^0\gamma$ from an ω when all 3 photon showers are within the fiducial region of one octant and none of the 3 photons convert into a e^+e^- pair. For the event to be considered as reconstructed, the probability for the photon configuration in the octant to satisfy the trigger must be greater than 10%. To measure the reconstruction efficiency, the ω Monte Carlo events were passed through the program used to reconstruct the data. Only those events which contained ωs with p_T at least 0.5 GeV/c greater than the generation threshold for each MC sample contributed to the reconstruction efficiency evaluation. This condition was invoked to avoid unphysical behavior near the sharp p_T threshold introduced by the MC event

[3] $cos\theta^\star$ and energy asymmetry of the ω are very closely related, as shown in section 5.3.1., and are used interchangeably here.

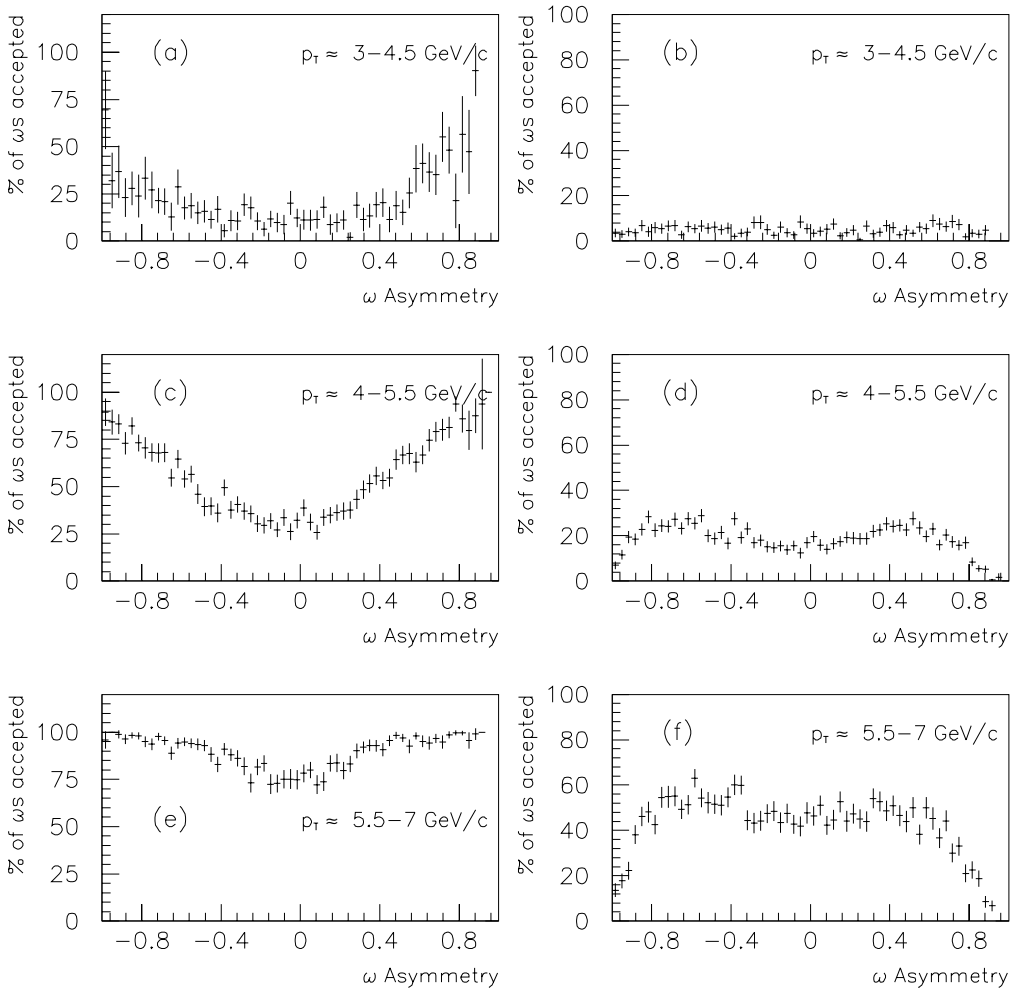

Figure 6.11 (a),(c),(e) Trigger acceptance for $\omega \to \pi^0\gamma$ plotted as a function of ω's energy asymmetry, for 3 different ranges of p_T, relative to all geometrically accepted ω particles in this decay mode. (b),(d),(f) Trigger acceptance now calculated relative to all generated ωs, in the same p_T ranges. The fall-off of the geometrical acceptance towards -1 and 1 in the ω asymmetry evens out the overall (trigger and geometrical) acceptance.

selection process. All mass combinations satisfying our definition of the ω were counted, in p_T bins, and related to the total number of generated, unconverted, geometrically accepted ωs in a given p_T bin. The same mass interval (0.63-0.93 GeV/c^2) was used in the Monte Carlo and the data as the omega signal region. Background under the omega peak in the MC was subtracted using the sideband subtraction method[4]. The requirement that the triggering probability be greater than 0.1 was applied to the data as well as the MC and set a limit on the value of the trigger correction with which the data events were to be weighted. In this way, the trigger correction can be used to weight events with triggering probability between 0.1 and 1.0, while the remaining events are accounted for on average through the reconstruction efficiency correction.

The reconstruction efficiency takes into account many pertinent reconstruction issues. Omegas can be lost if the shower due to a photon is misreconstructed – e.g., as a result of miscorrelation of the r- and ϕ-view gammas yielding an incorrect location for the photon. There are several reconstruction cuts that each photon has to pass before it is used to form mass combinations and the reconstruction efficiency accounts for the losses of true photons from the omega due to these effects as well. As an example, the cut that rejects all photon candidates which have a charged track associated with them will from time to time remove a true omega photon that happened to land in the vicinity of a charged particle in the event. Another example, the sampling fluctuation in the energy measurement in the calorimeter will occasionally yield $E_{front}/E_{total} < 0.2$ for a photon, which would cause us to reject this photon and thus lose the ω. The $|cos\theta^{\star}| < 0.6$ and

[4] Sidebands were defined as mass intervals on each side of the ω peak, and with the combined size corresponding to the signal mass range. The $\pi^0\gamma$ combinations from the sidebands were subtracted off from the combinations in the signal region.

$A_{\pi^0} < 0.75$ cuts cause a large loss in the number of omegas and will be corrected for through the reconstruction efficiency.

It should be noted that an increase of the reconstructed signal relative to the generated numbers of ω particles is also possible. There are two main effects that contribute to that — the smearing of reconstructed p_T relative to true p_T and combinatorial multiplication. The effect of spilling of entries from highly populated low p_T bins to the higher p_T bins occurs due to the steeply falling character of the differential cross section in p_T and the smearing of the reconstructed value for the p_T (caused by the detector energy resolution). In the evaluation of the reconstruction efficiency, the reconstructed value of the p_T of the $\pi^0\gamma$ combination is used to determine the number of reconstructed ωs while the generated value of the p_T is used to determine the generated numbers. This, together with a very good agreement between the generated ω p_T spectrum and the measured spectrum (as will be illustrated in a later chapter), and adequate modeling of the detector resolution in the Monte Carlo, is expected to reproduce and account for the smearing observed in the data.

The combinatorial multiplication comes into play because photons from the ω are used by the algorithm to make all possible mass combinations with other photons in the octant. Figure 6.12(a) illustrates this effect by showing an overlay of the mass spectrum reconstructed through the algorithm and the mass spectrum formed of unique combinations of true omega photons. The latter was determined from the match between the generated MC tracks and the showers found in the detector. The two mass spectra are clearly not identical. The fractional difference between the reconstructed and true signal is about 20% at low p_T and becomes less significant above p_T of 5 GeV/c. Two effects were found to contribute to this difference. One was the recombination of true photons from omega meson

among themselves. Another source was related to combinations of 2 photons from an omega with some other soft photon in the event. The count of what we call an omega signal depends therefore on the characteristics of the remainder of the event and is not exactly the count of true omegas, both in the data and in Monte Carlo. The π^0 sideband subtraction method that is used in the MC and in the data removes some of these background combinations and reduces the sensitivity of the result to how well the overall event, and especially the soft photons, are modeled in MC.

Figure 6.13 shows the reconstruction efficiency combined with geometrical acceptance versus the p_T of the ω for SLH and LGH triggers. The dependence on transverse momentum is mostly introduced by the requirement on the minimum triggering probability. A hyperbolic tangent function of p_T is fitted to the points. The value of the fit at the center of the p_T intervals was inverted and used as a combined geometrical acceptance and reconstruction efficiency correction. The uncertainty in the correction was determined by measuring the width of the residuals between the Monte Carlo points and the fits to the efficiencies. Using this technique the uncertainties were estimated to be 7.0%. The first p_T bin in the SLH sample was assigned an error of 15% due to the statistical limitation on accepted events in that region. Possible inaccuracy in the event simulation, and in the simulation of the trigger (the trigger introduces the largest loss of ω particles), is expected to contribute an additional systematic error. In this chapter, we demonstrated that the trigger modeling in the MC was adequate. However, most of the ω particles with $3.5 < p_T < 8$ GeV/c produced in the MC were found to have very low triggering probability, and we were forced to accept trigger probability results down to very low values. Even small uncertainties can result in large changes in trigger probability in regions of steeply falling trigger turn-ons. Therefore the trigger turn-on issue and several other issues related to

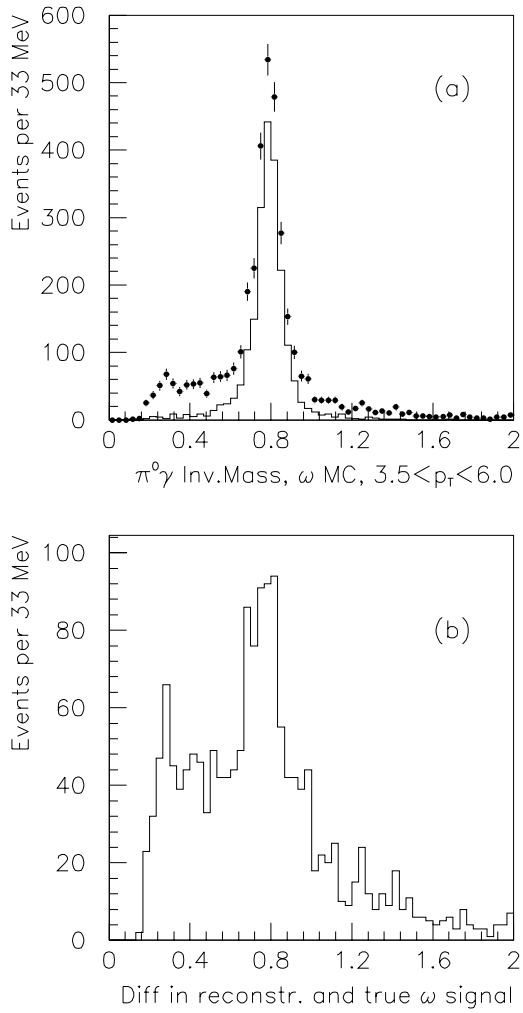

Figure 6.12 $\pi^0\gamma$ invariant mass reconstructed in ω MC (solid points) compared to the true ω mass spectrum (one entry per one generated omega) as determined from the generated information (histogram); P_T of ω is from 3.5 to 6.0 GeV/c. Fig.(b) shows the difference between the two spectra.

the uncertainty of the results will be further discussed in the chapter on systematic uncertainties.

Figure 6.14 presents the combined reconstruction efficiency and geometrical acceptance versus ω p_T for a selected sample of Monte Carlo events. If any of the three photons fell into "rapidity holes", the ωs were rejected from both generated and reconstructed samples. These rapidity holes will be defined and discussed in the Analysis chapter. The reconstruction efficiencies with the cut on rapidity holes are presented here for completeness.

To summarize, to the extent to which we can assure an adequate match of the topology and kinematic characteristics between Monte Carlo events and the data, various complications of the reconstruction process are accounted for through the reconstruction efficiency.

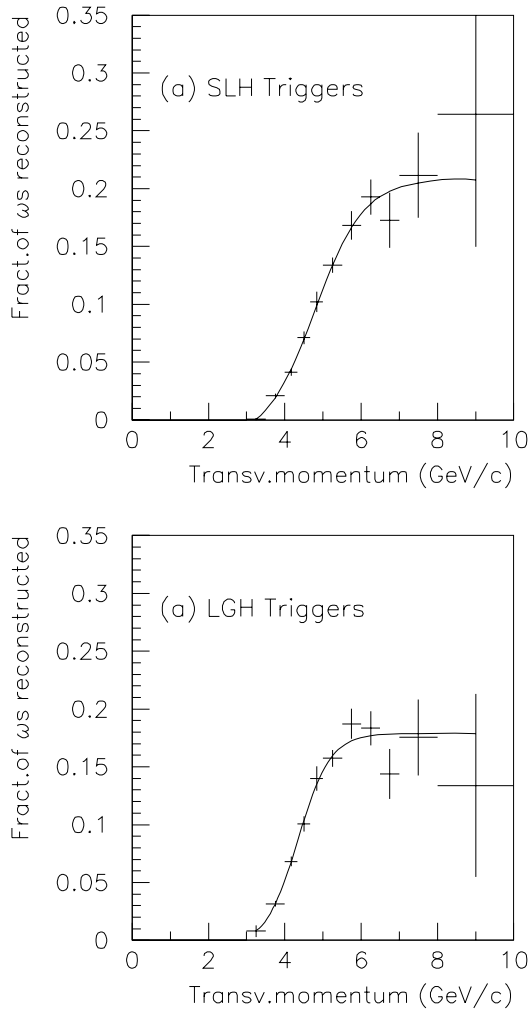

Figure 6.13 Reconstruction efficiency, as defined in the text, combined with geometrical acceptance for the $\omega \to \pi^0\gamma$ versus ω's p_T for SLH (a) and LGH (b) triggers.

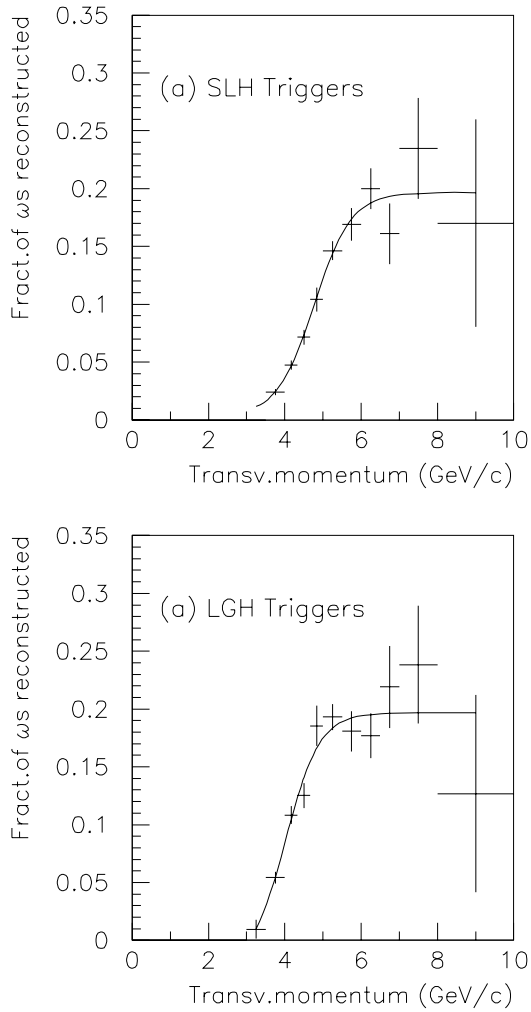

Figure 6.14 Reconstruction efficiency combined with geometrical acceptance for the $\omega \to \pi^0\gamma$ versus ω's p_T for SLH (a) and LGH (b) triggers. Only the Monte Carlo ωs which decay to photons not falling into any of rapidity holes were used in this measurement.

Chapter 7 Analysis

This chapter describes many of the analysis cuts and corrections necessary to evaluate the omega production cross section. Among others, muon rejection techniques, vertex fiducial cuts and trigger corrections including trigger rapidity hole corrections are discussed. Reconstruction efficiency and geometrical acceptance, which contribute the largest correction factor that need to be applied to the data, have already been described and illustrated in the Monte Carlo chapter. It should be noted here that several of the analysis cuts (e.g. $|cos\theta^{\star}| < 0.6$, π^0 energy asymmetry cut, etc.) are accounted for through the reconstruction efficiency correction. Event weights to correct for losses of photons converting to e^+e^- pairs, and for loss of beam particles absorbed in the target material, complete the list of corrections necessary for the cross section measurement. A sizable part of this chapter is devoted to counting omegas reconstructed in selected p_T intervals, as well as to a discussion of the fitting procedures and the calculation of related uncertainties.

7.1 Muon Rejection

The secondary meson beam of 515 GeV/c π^- used by E706 was generated by bombarding a beryllium target by 800 GeV/c protons, and selecting and transporting of the negative particles produced in the appropriate momentum range down the secondary beam line. This process had as a byproduct copious numbers of muons produced either at the primary beam dump or as a result of in-flight decays of secondary beam particles. Some of these muons traveled along the beam direction and reached the E706 apparatus at r-distances from the LAC center at which energy depositions were likely to mimic high transverse

energy photons. When the muons interacted in the LAC in coincidence with low-p_T reactions in the spectrometer target, they contaminated the high p_T photon sample. Therefore muon identification and rejection techniques were developed in E706.

Firstly, muon spoilers, magnets that deflected muons away from the spectrometer, were placed in the beam line. Secondly, three large acceptance veto walls were situated upstream of the Meson West spectrometer and used for an on-line veto. Any event containing a "high p_T" shower in the LAC quadrant coinciding in time (within $\pm$75ns) with the signal from the two downstream veto walls logically AND-ed with the same quadrant hit from the upstream wall was rejected. Further utilization of veto wall information was performed off-line, when the veto walls were searched for a coincidence of hits in a wider window ($\pm$110ns) around the time of interaction.

The LAC was designed to provide a measurement of the incident directions of particles generating showers. The focused design of the r-strip towers provided discrimination between showers from the target direction and showers from particles nearly parallel to the beam. Directionality, defined below, is a variable that utilizes this feature:

$$Directionality = R_{fr} - (Z_{fr}^{LAC}/Z_{back}^{LAC}) \times R_{back}$$

R_{fr} is the reconstructed radial position of the shower in the front section of the LAC and R_{back} is the radial position of the shower in the back section. Z_{fr}^{LAC} and Z_{back}^{LAC} are the distances from the target to the front and back sections of the LAC. For objects from the target, $R_{fr}/Z_{fr}^{LAC} \approx R_{back}/Z_{back}^{LAC}$, and therefore directionality should be approximately equal to zero, whereas for muons directionality is positive, as illustrated in Figure 7.1. A radially dependent

cut on directionality ($Dircut$), for photons with $p_T > 3.0$ GeV/c, given by $Dircut = 0.0048 * R$ for $R > 40$ cm and $Dircut = 0.2$ for $R < 40$ cm eliminated additional muons from the high p_T data sample.

Lastly, the concept of the momentum balance in the true high p_T event was used to distinguish them from halo muon-triggered events, in which the total momentum tends to be highly imbalanced. The variable $BAPT$, the ratio of the sum of the transverse momenta of the charged and neutral particles in the 120 degree cone opposite the trigger particle to the trigger particle p_T was calculated and a cut of $BAPT < 0.3$ was used to reject muons.

Further details regarding muon rejection cuts and an illustration of their effectiveness in eliminating muon-induced showers from the data can be found in [15], where the π^0 cross section measurement is described. Muon rejection was less important to the ω analysis. The presence of at least 3 photons in the triggering octant as well as the demand of a relative energy symmetry ($cos\theta^\star$ cut), already reduce the number of purely muonic events in the sample. The effect of the muon cuts on the two photon distribution, in the highest p_T bin in which the omegas are reconstructed (7 to 8 GeV/c), is presented in Figure 7.2; there is a clear reduction of the background under the π^0 peak (although the effect is much less dramatic than in the case of π^0 analysis).

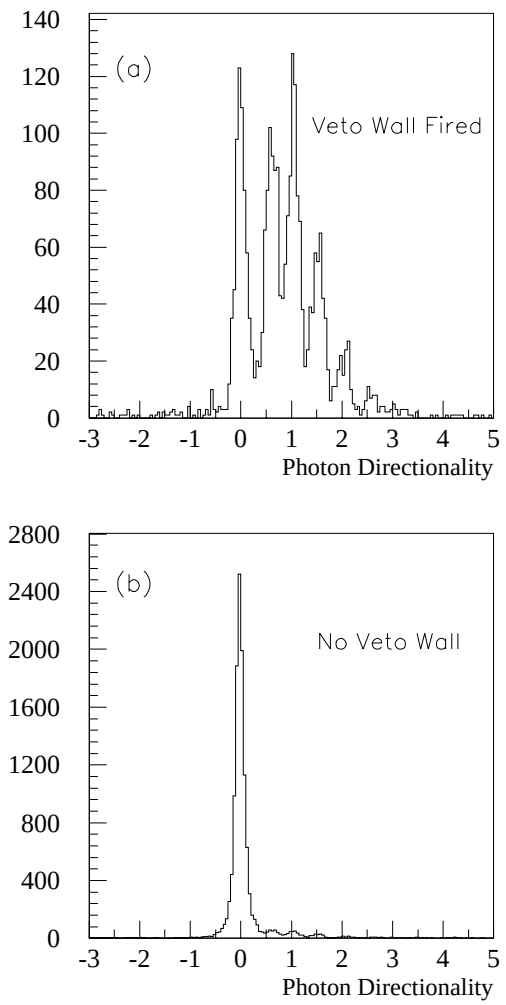

Figure 7.1 Directionality of the highest energy photon from two photon pairs with $p_T > 5.5$ GeV/c in the π^0 mass region when (a) the veto wall fired (off-line) (b) there was no veto wall signal in the triggering octant. The peak at 0 corresponds to photons from the target direction. Positive directionality is indicative of muons.

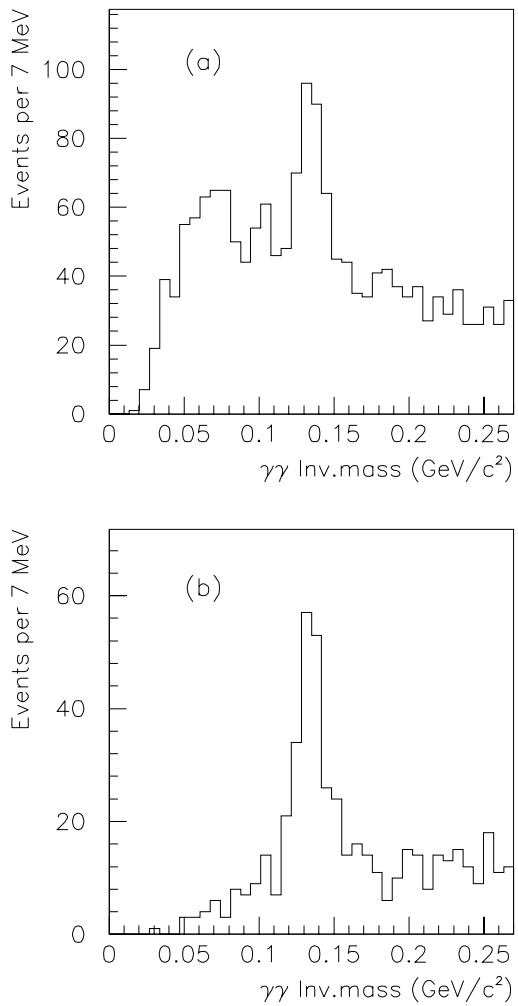

Figure 7.2 The effect of muon cuts on the two photon mass spectrum in the π^0 region when $\pi^0\gamma$ p_T ranges from 7 to 8 GeV/c, in the events preselected for omega analysis. The absolute value of π^0 and γ energy asymmetry is less than 0.6 and all other reconstruction cuts are implemented.

7.2 Vertex Cut

The z-position of the reconstructed vertices for high p_T events with 3 or more photons in the triggering octant is presented in Figure 7.3. The elements of the target, as well as the apparatus surrounding the target, are clearly visible, with few events reconstructed in between (some of which occur in the target holder). Scatterplots of the transverse location of vertices in the target region spanning the Be and Cu target locations are presented in Figure 7.4. The square on the plots is an outline of the approximate location of the beam hodoscope that defined beam for the experiment. The physical locations of the Be and Cu targets are marked with the circle (Be) and the truncated circle (Cu). The plot shows that the incident beam and hence the vertices reconstructed, are well centered on the beam hodoscope, but not on the target pieces. To minimize normalization complications, a target transverse fiducial cut was established. Only events with vertices within the areas on x-y plane common to both targets and the hodoscope are retained. The correction for this cut was determined from the ratio of the vertices reconstructed within the fiducial target region in the 2 upstream SSD planes over all vertices in these planes in the area shadowed by the hodoscope. The correction was determined to be 34% with an uncertainty of 2% .

7.3 Trigger Probabilities

7.3.1 Trigger Turn On Curves

The Single Local High (SLH) trigger was designed to select events containing a localized deposition of high transverse momentum in the LAC detector. The trigger unit used as an input the time-integrated energies from 16 consecutive r-channels of the LAC (the details of the trigger formation are reviewed in the RABBIT P_T System section in chapter 3 and illustrated in Figure 3.6). The radial

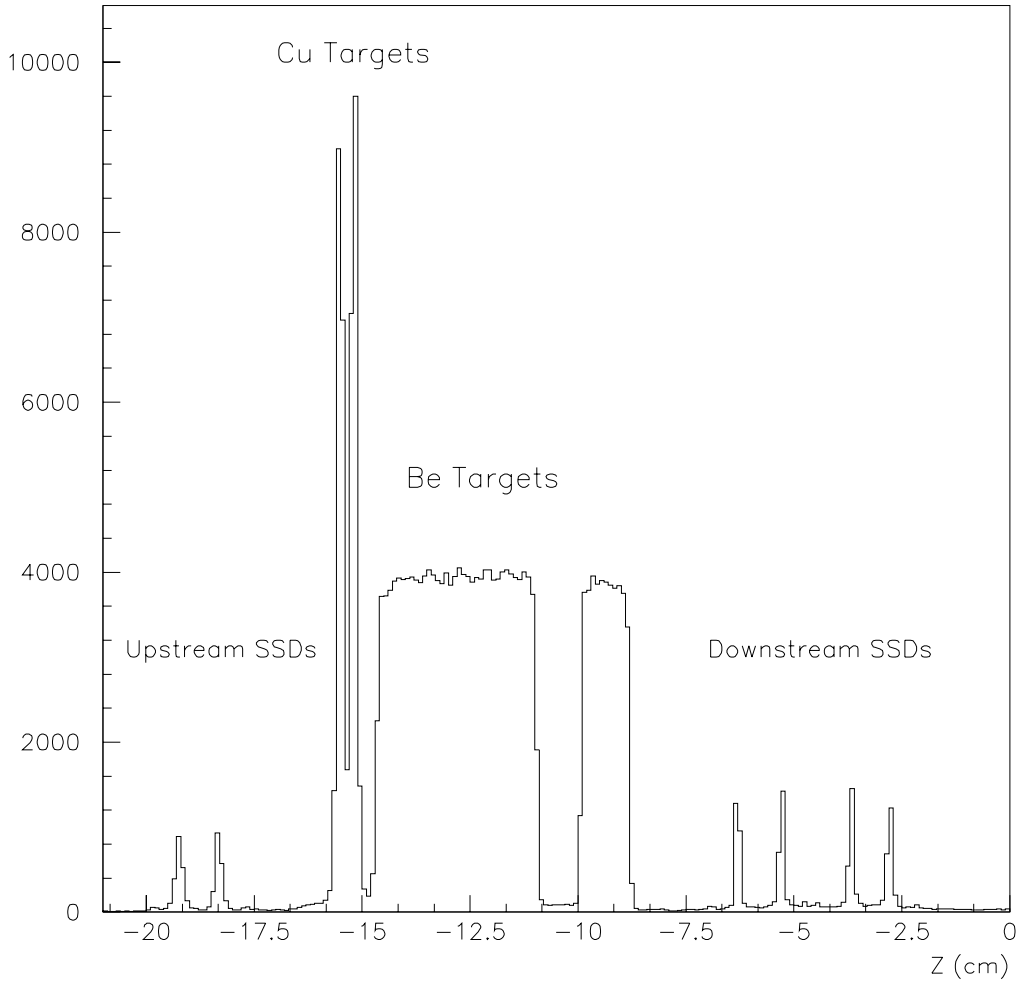

Figure 7.3 Vertex distribution for the events pre-selected for ω analysis.

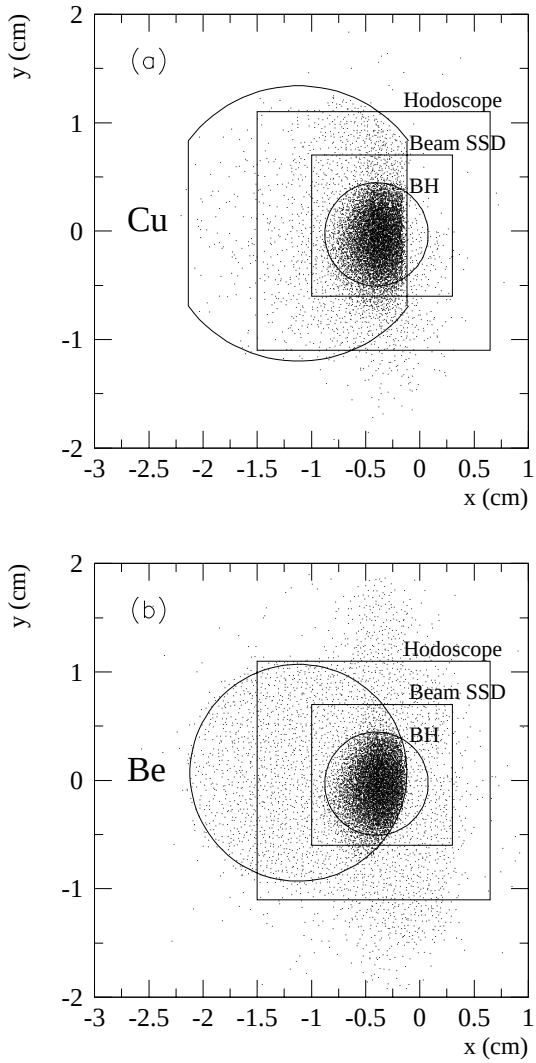

Figure 7.4 X-Y position of the reconstructed vertices in Cu (a) and Be (b). The transverse size and location of assorted relevant items are shown.

span covered by each local trigger unit was about 8 cm. The events selected by the trigger and recorded were analyzed off-line to study the response of each of the trigger units to the energy deposited in the LAC. The transverse energy in an octant opposite to a trigger octant was examined and the status of the corresponding trigger units (stored with each event) was checked. The details of the method used for determining the turn-on probabilities can be found in [57]. A few examples of these curves, for a typical octant, are shown in Figure 7.5. The distributions represent the probability that the trigger will fire versus the trigger p_T for 4 selected trigger units, from the inner and the outer regions of the LAC. The trigger turn-on curves were measured separately for the data in each of the trigger sets, as listed in Table 5.1. The trigger p_T, that is the p_T used by the trigger unit, corresponded only approximately to the reconstructed π^0 or γ p_T due to the time-dependent change of the energy response of the detector.

Based on the trigger turn-on curves for a group of 16 strips in an octant and the energy deposited in that group in a given event, the triggering probability P_i for that group was obtained. The probability that the energy deposition in an octant fired a SLH trigger was formed as a linear superposition of probabilities P_i of each of the 31 trigger units in that octant:

$$P_{octant} = 1 - [\prod_{i=1}^{31}(1 - P_i)]$$

For the LGH trigger P_{octant} was calculated directly from the LGH trigger turn-on curves. The sums-of-8 values summed over the entire octant (with the exception of the few outermost groups which were not included in the global trigger formation) were used as the relevant p_T variable. P_{octant} for LGH trigger was then combined with the probability to fire a SLL trigger in that octant. The inverse of P_{octant}, combined with the probability to satisfy the pretrigger requirements,

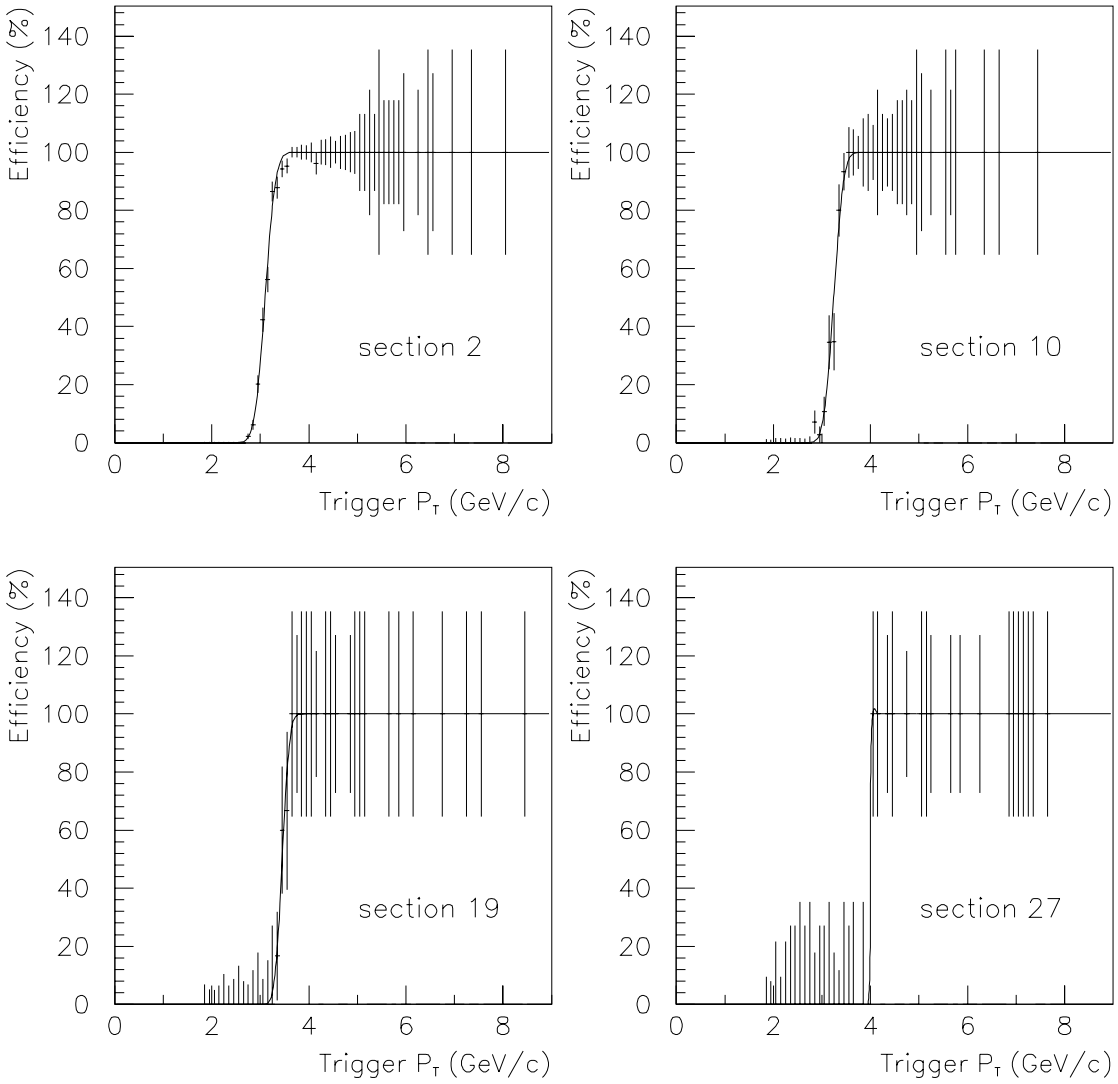

Figure 7.5 Turn-on curves for Single Local High trigger for four different regions of a typical octant as a function of trigger p_T.

was used as a trigger weight applied to the data. This correction was not allowed to exceed a value of 10, that is, all events with triggering probability less than 10% were excluded from this analysis while the remaining events were weighted. The motivation for the cut-off value stemmed from the fact that a statistically insignificant sample of events with $P_{octant} < 0.1$ might have had a large impact on the measurement due to their very large weights. Also, the uncertainty in the turn-on determination increases as the probabilities become small and hence establishing a cut-off value protected us against the region of poorly determined trigger probabilities. In principle, it would be preferable to use only events for which the trigger is 80-100% efficient and rely on lower threshold triggers to cover the lower p_T ranges, as it is done in e.g., the π^0 analysis. But in the case of the ω measurement the luminosity associated with the low p_T prescaled triggers was insufficient to reliably observe the ω.

The Local Global High (LGH) trigger requirements could be satisfied if the transverse momentum in any of the local discriminators in an octant exceeded the Single Local Low (SLL) threshold (compare Table 3.1) and the summed p_T in that octant exceeded the LGH threshold. As was discussed in the RABBIT PT System section in chapter 3, the summing of the p_T reported in each local trigger unit occurred after the suppression of positive image charge signals. However, the voltage level selected for this suppression also caused a suppression of a portion of the negative-going trigger signal in each local unit. Therefore this suppression introduced a bias against events in which a small p_T was widespread over octant[55]. Nevertheless, the LGH trigger did provide a larger pool of omega meson events than the SLH trigger since it had a lower local threshold requirement. The total number of unweighted ωs reconstructed in the p_T range from n 3.5 to 8 GeV/c in the events selected via the LGH trigger is 4130±620 whereas the corresponding number is about 2370±350 for events that satisfied the SLH trigger.

7.3.2 Rapidity Holes

Rapidity holes are defined as regions in rapidity for a specified p_T range where the trigger corrections are found to be less reliable than in the other sections of the detector. One can observe rapidity holes by plotting the π^0 rapidity in slices of transverse momentum (e.g. $4.0 < p_T < 4.5$) for each octant and each trigger set (group of runs of constant trigger characteristics) separately. These distributions are already corrected for triggering probability, up to the maximum allowed weight of 10. Any large differences between the 8 octant distributions may be viewed as indications that trigger corrections were inadequate in a given domain. Figure 7.6 shows the π^0 rapidity distributions for trigger set 3 (see Table 5.1). The average rapidity distribution from all octants is overlaid on top of each of the octant distribution (the average was taken after the exclusion of problematic regions in the octants). We notice that in several regions in rapidity trigger corrections do not correct up to the level observed in other octants (e.g., regions of octants 3, 4 and 7). In some regions of other octants the correction appears to be too large (as in the backward rapidity section of octant 6). We will therefore exclude those regions from the measurement.

The rapidity holes arise from several sources. Some trigger units had higher threshold then others and accepted significantly fewer events in a given p_T interval. The correction factor cut-off (of 10) that we applied would prevent us from fully accounting for this kind of losses in these plots. Some trigger units could have been improperly calibrated and been assigned an unnecessarily large correction factor due to mismeasured trigger gain factors, causing a visible distortion of the rapidity distribution compared to other octants. The majority of the rapidity holes disappear at p_T values higher than the 4.0 to 4.5 GeV/c range presented in Figure 7.6. However, if we want to use trigger corrections close to the region

of trigger turn-ons, (e.g., near 4.0 GeV/c), we can only use them in the regions in which the corrections are adequate. To avoid rapidity holes, we test each π^0 and γ and reject combinations when either the π^0 or the γ fall into a region of rapidity for a given p_T, where the trigger correction is unreliable. Each surviving combination is tested whether it could have passed the rapidity hole cut in the remaining 7 octants. The rapidity hole correction is a scale factor (1, $\frac{8}{7}$,$\frac{8}{6}$, etc.) that depends upon the number of octants in which the tested combination would have fallen into regions used in the cross section measurement.

Unfortunately the events selected via LGH triggers exhibit quite a few areas where the trigger corrections are unreliable, especially in the p_T range below 4.5 GeV/c. The $\pi^0\gamma$ events are severely cut by the rapidity hole cut (approximately 50% of events are eliminated). Because of the large loss of ω events the impact was evaluated based upon the cross section result, that is, the cross section was measured before and after the rapidity hole removal/correction. This comparison is presented in a later chapter.

7.4 Conversion Correction

Photons created as a result of interactions (either direct photons or photons from the decay of a resonance) had to traverse material before reaching LAC. Due to interactions in matter, some of the photons converted to e^+e^- pairs. When the conversion occurred in the area before the analysis magnet, the photon could not be reconstructed as one shower at the LAC due to the splitting effect of magnetic field on the e^+e^- pair. If the photon was converted to an e^+e^- pair behind the magnet, the electrons were not split but still left tracks in the PWC section of the tracking system. The charged track cut, defined in section 5.1, would remove these showers from the photon sample. In either case, the reconstruction of an ω particle

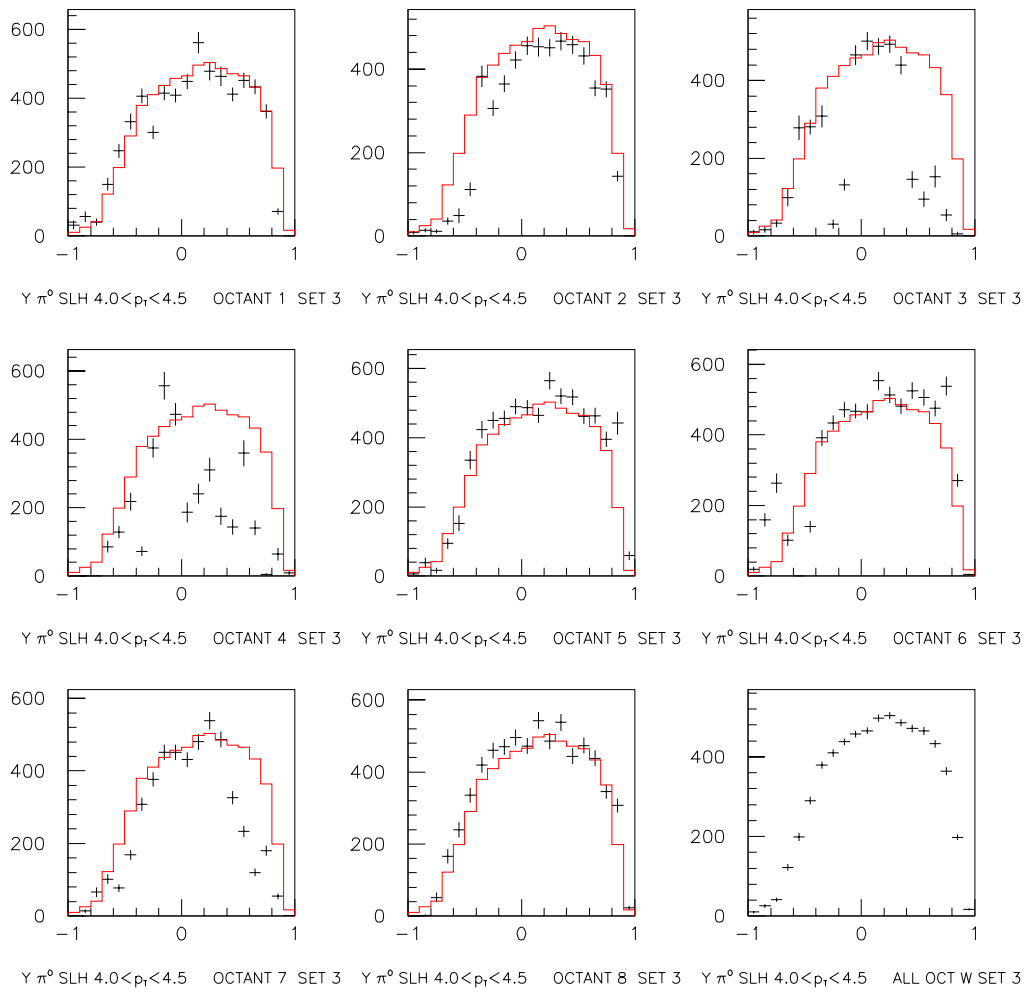

Figure 7.6 Rapidity distributions for π^0 of $4.0 < p_T < 4.5$ for each of the octants of the detector (points). Data belong to trigger set 3 and were selected by the SLH trigger. Overlaid is the average of the octants rapidity distribution for this set, taken after the problematic regions have been removed.

whose photon (or photons) converted to an e^+e^- pair would not be possible. The conversion correction accounts for omegas lost due to these conversions.

The conversion probability was calculated individually for each photon using the so called material lists, where all the material found in the path of photons was included and the probabilities of conversion during passage through a unit length of each material was stored. Careful attention was given to properly represent the details of the locations and sizes of all materials in the material lists, since the conversion probability strongly depended on the amount and type of material found in the path of each photon. Using Monte Carlo information, we could count the converted photons directly or determine a fraction of photons that converted to e^+e^- pairs through the conversion probability calculation. These two numbers agreed very well, which verified the validity of the conversion correction and the MC material representations. The loss of ω particles due to the conversion of any of its photons to e^+e^- pairs was relatively high at about 23% for ωs originating in Be, and 41% for Cu.

7.5 Reconstruction of the Omega Signal

In this section we discuss the measurement of the corrected number of high p_T neutrally decaying omegas produced in $\pi^- + Be \rightarrow \omega + X$ interactions during 1990 run of this experiment. The rapidity range of this measurement spans from -0.5 to 0.75 in the center of mass of the collisions. First a summary of the selection criteria and of the reconstruction procedure is presented. This is followed by the discussion of the event weighting and a review of the corrections applied to the data. Next the background fitting procedure is illustrated in some detail and the resulting numbers of omega events in various p_T intervals are given.

7.5.1 Summary of the Reconstruction Procedure

Below we summarize the selection criteria that were established as a result of event reconstruction and the search for the omega particle.

- vertex for the event passed target fiducial cuts
- events survived muon cuts: veto wall, directionality cut for the highest p_T photon, and balanced p_T cut
- events were selected via SLH or LGH triggers
- triggering probability for the relevant octant was greater than 0.1
- photons considered for $\pi^0\gamma$ combinations passed the photon selection criteria: LAC fiducial volume cut, E_{front}/E_{total} cut, and charged track cut
- all 3 photons of $\pi^0\gamma$ combinations were selected from the same octant
- π^0 energy asymmetry was less than 0.75
- $\pi^0\gamma$ transverse momentum was greater than 3.5 GeV/c
- center of mass rapidity of $\pi^0\gamma$ ranged from -0.5 to 0.75
- $\pi^0\gamma$ combinations were rejected if a π^0 or a γ fell into a rapidity hole region
- $cos\theta^\star$ for the $\pi^0\gamma$ system was between -0.6 and 0.6

7.5.2 Summary of the Event Weighting

To reconstruct the number of omega events produced in the recorded $\pi^- Be$ interactions, events were weighted by corrections that accounted for the cuts and losses (e.g., due to low triggering probabilities) that the sample of high p_T omegas suffered during the data-taking and event analysis phases. After the corrections were applied, we calculated the numbers of omega events ($\omega \rightarrow \pi^0\gamma$) produced

in these interactions. The corrections included event-dependent corrections (measured on the sample of events passing the selection criteria):

- trigger weight
- rapidity hole correction
- conversion correction

as well as event-independent (even though p_T dependent) weights :

- geometrical acceptance
- reconstruction efficiency (includes corrections for $E_{front}/E_{total} < 0.2$, charged track cut, $A_{\pi^0} < 0.75$, $|cos\theta^\star| < 0.6$, and triggering probability cut of 0.1)
- veto wall cut correction
- directionality cut correction
- balance pt cut correction
- vertex reconstruction efficiency correction
- $\pi^0 \to \gamma\gamma$ branching ratio correction

Symbolically we represent the corrected number of ωs ($\omega \to \pi^0\gamma$) observed in $\triangle Y \triangle p_T$ interval as $N^{corr}(p_T)$. The $N^{corr}(p_T)$ is obtained as a sum of event weights W_i over all detected N_{det} omega particles.

$$N^{corr} = \sum_{k=1}^{N_{det}} W_i$$

where W_i stands for the product of event-dependent and event-independent corrections listed above. N_{det}, the number of detected omegas, was derived through the fitting procedure.

7.5.3 Fitting Procedure

The signal and the background region of the weighted $\pi^0_{sbs}\gamma$ invariant mass histograms were fit simultaneously. The functions used in the fits were a third order polynomial (P3) combined with a Gaussian. The Gaussian parameters were allowed to vary from 0.766 to 0.798 GeV/c^2 for the mean value and from 0.28 to 0.42 GeV/c^2 for the width of the Gaussian. The fitting range was taken as the largest range over which a polynomial (P3) could fit the background well – e.g., from 0.35 to 1.4 GeV/c^2. In a series of additional fits, the fitting range was reduced or varied and the sensitivity of the answer to the selection of the fitting range was tested. Three different mass ranges were selected for the fits. (The range was selected differently between the different p_T intervals due to the variation in the shape of the background with p_T.) A change to the mass bin size could result in either a stronger or a weaker appearance of the signal due to shifting of the histogram content between the bins. Therefore a parallel set of 3 fits was performed on histograms with mass bin sizes decreased by 20%. Both sets of results were considered equally valid and were averaged to minimize the effect of such statistical fluctuations.

Table 7.1 presents the numbers of weighted $\pi^0\gamma$ combinations counted in the omega mass range above the estimated background, in the events selected by the SLH trigger. Events were weighted by the corrections described in the preceding section. The five columns labeled Fit 1 through Fit 5 correspond to the results of 5 different fits to the background and signal region. The best 5 fits out of 6 (3 fit ranges times 2 sets of mass bins) contribute to Table 7.1.

As can be seen from Table 7.1 the corrected numbers of reconstructed ωs differ substantially between the results of Fit 1 through Fit 5. It is however very difficult to claim that any of the particular fits represents the background shape

P_T **Interval (GeV/c)**	**Fit 1**	**Fit 2**	**Fit 3**	**Fit 4**	**Fit 5**	**Average**
3.5-4.0	121146	127465	112272	122868	106111	118000± 37000± 12000
4.0-4.33	75600	89810	75621	84610	84700	82000± 16500± 6300
4.33-4.67	33922	35834	40007	36931	39633	37300± 7000± 2600
4.67-5.0	17472	13720	16157	14594	17201	15800± 3700± 1600
5.0-5.5	7849	8034	8168	8129	7530	8000± 1500± 260
5.5-6.0	2670	2736	2850	3046	2745	2800± 760± 200
6.0-6.5	1894	1762	1897	1814	1842	1850± 400± 110
6.5-7.0	485	542	541	523	520	520± 230± 60
7.0-8.0	139	127	120	61	104	110± 100± 30

Table 7.1 Corrected number of ωs reconstructed in p_T bins (SLH trigger).

better than the remaining fits. All of the fits were examined as far as the value of fit χ^2 and general plausibility of the background representation, and no fits that were considered inadequate were included in Table 7.1. Figure 7.7 illustrates the variation in the functional forms for the background and signal region obtained for several fitting ranges, for the p_T bin of 4.0-4.33 GeV/c. Figure 7.8 shows the signal and different fit results for the p_T bin of 5.5-6.0 GeV/c.

The average value of fit results was taken as the best representation of the number of reconstructed omegas and is presented in the last column in Table 7.1. The first row of the uncertainties quoted with the average are statistical errors based on the total number of entries in unweighted, unsubtracted $\pi^0\gamma$ mass histograms in the ω mass range combined with the statistical uncertainty due to the π^0 sideband subtraction. The second row of the errors listed above gives the variation in the results due to the uncertainty in the background determination, in the form of the RMS of the distribution of 5 fit results.

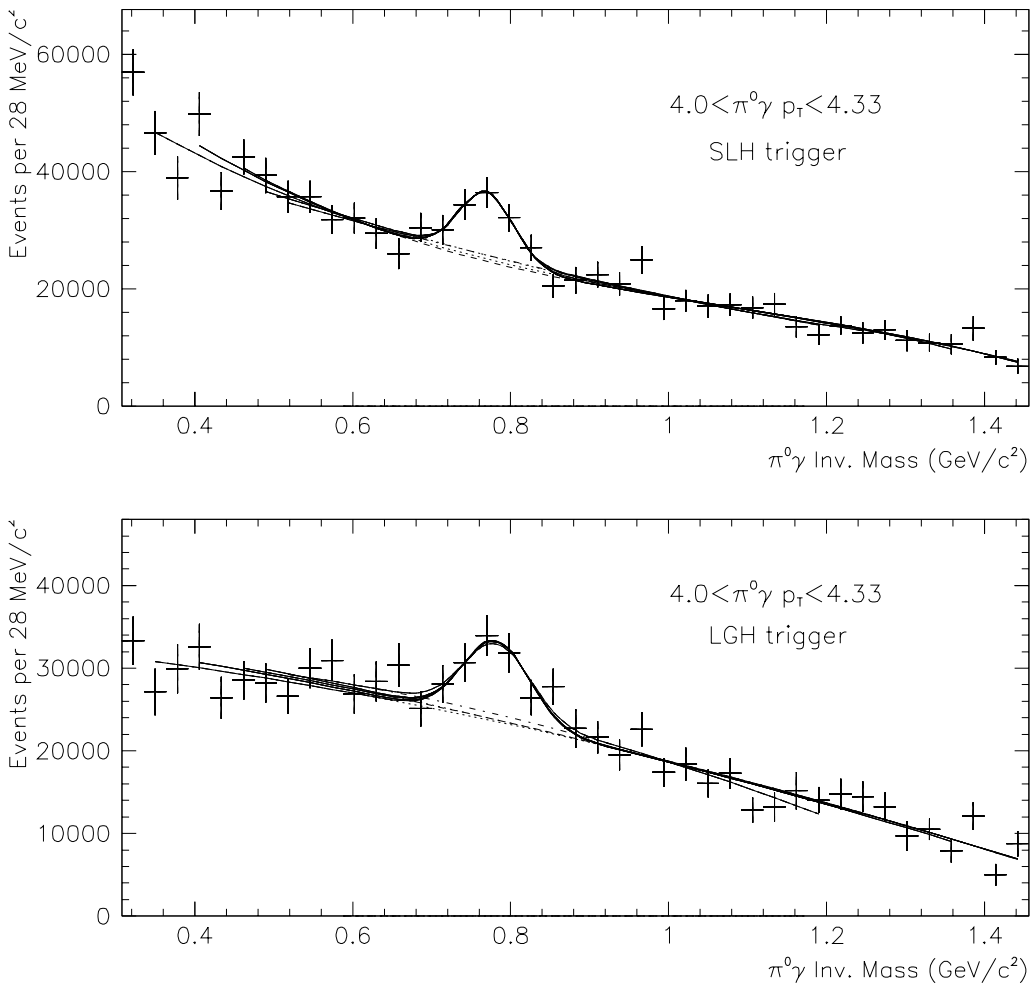

Figure 7.7 Weighted $\pi^0\gamma$ mass plot and fits to the background and signal region in the vicinity of omega mass range. Third order polynomial combined with the Gaussian shape was used over a varied fit range. $\pi^0\gamma$ combinations are from the p_T range of 4.0 to 4.33 GeV/c, selected by the SLH (top plot) or LGH (bottom plot) trigger.

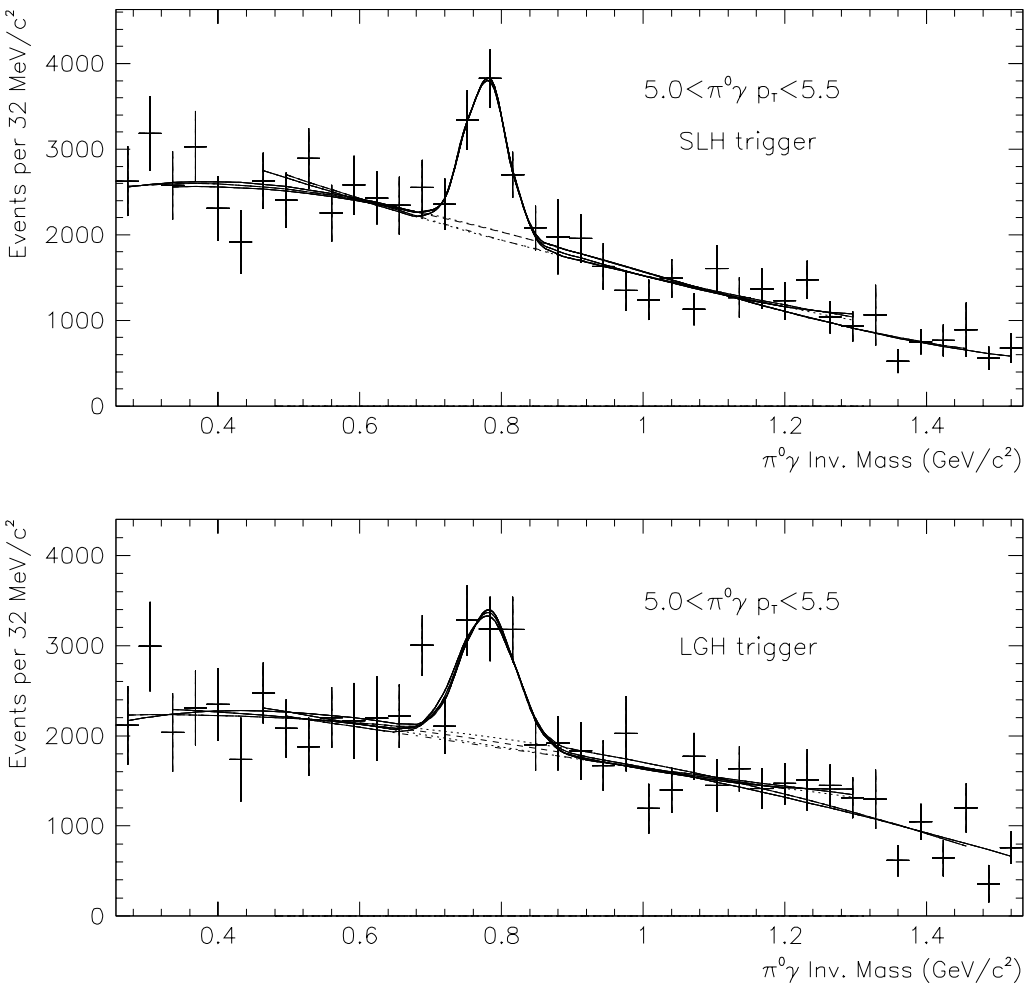

Figure 7.8 Weighted $\pi^0\gamma$ mass plot and fits to the background and signal region in the vicinity of omega mass range. Third order polynomial combined with the Gaussian shape was used over a varied fit range. $\pi^0\gamma$ combinations are from the p_T range of 5.5 to 6.0 GeV/c, selected via SLH (top plot) or LGH (bottom plot) trigger.

The use of fits with completely unbound parameters was also tested. In general the fit results fell within the range of values as given in Table 7.1. In a few instances, the estimated uncertainty in the background determination was increased to account for a larger spread of the results than that suggested by the bounded fits.

Table 7.2 presents the numbers of omegas observed in the data in unweighted events. These numbers were derived from the $\pi^0_{sbs}\gamma$ invariant mass histograms in $\triangle p_T$ bins by the fitting procedure. No event weights were applied to these combinations. However, all of the selection criteria and reconstruction cuts were implemented.

P_T **Interval**	**Fit 1**	**Fit 2**	**Fit 3**	**Fit 4**	**Fit 5**	**Average**
3.5-4.0	615	483	515	500	526	530 ± 150 ± 70
4.0-4.33	280	284	372	302	301	310 ± 100 ± 50
4.33-4.67	413	398	305	336	358	360 ± 80 ± 50
4.67-5.0	207	194	206	209	221	210 ± 60 ± 15
5.0-5.5	242	256	260	341	316	280 ± 50 ± 50
5.5-6.0	77	78	114	76	69	80 ± 30 ± 20
6.0-6.5	80	69	66	88	89	80 ± 20 ± 10
6.5-7.0	23	31	19	22	25	24 ± 12 ± 6
7.0-8.0	11	14	12	11.2	13	12 ± 9 ± 1

Table 7.2 Number of unweighted ω events in p_T bins (SLH trigger).

P_T **Interval**	**Fit 1**	**Fit 2**	**Fit 3**	**Fit 4**	**Fit 5**	**Average**
3.5-4.0	202274	178919	185868	170825	184472	185000± 35600± 15000
4.0-4.33	87913	86116	77330	81063	83106	83000± 14600± 4800
4.33-4.67	47275	45737	49646	45148	47270	47000± 6600± 1700
4.67-5.0	17270	15647	14980	17987	16471	16500± 3300± 1400
5.0-5.5	8490	9054	7785	7795	7073	8000± 1600± 750
5.5-6.0	2522	2878	2525	3268	2798	2800± 850± 350
6.0-6.5	1434	1385	1710	1608	1576	1550± 490± 150
6.5-7.0	343	356	464	388	390	390± 250± 70
7.0-8.0	240	236	240	301	254	250± 110± 30

Table 7.3 Corrected number of ωs reconstructed in p_T bins (LGH trigger).

P_T **Interval**	**Fit 1**	**Fit 2**	**Fit 3**	**Fit 4**	**Fit 5**	**Average**
3.5-4.0	754	583	599	580	600	620 ± 160 ± 90
4.0-4.33	650	631	606	616	543	610 ± 110 ± 50
4.33-4.67	579	639	541	589	572	580 ± 80 ± 50
4.67-5.0	241	246	318	324	319	290 ± 60 ± 40
5.0-5.5	195	211	175	258	234	220 ± 50 ± 40
5.5-6.0	36	52	67	49	45	50 ± 30 ± 20
6.0-6.5	50	50	64	58	58	60 ± 20 ± 10
6.5-7.0	11	15	10	11	19	15 ± 10 ± 5
7.0-8.0	19	19	19	18	18	19 ± 8 ± 1

Table 7.4 Number of unweighted ω events in p_T bins (LGH trigger).

The remaining two tables in this section present the reconstructed omega signal in events selected by the LGH trigger; Tables 7.3 and 7.4 parallel the Tables 7.1 and 7.2 for SLH triggers.

The data in Tables 7.1 and 7.3 are plotted in Figures 7.9 and 7.10. In each p_T interval all 5 different fit results are plotted. The uncertainty in the background determination that we can visualize from these plots does contribute to a systematic error in the omega meson production measurement.

7.5.4 Presentation of the Omega Signal

The omega signal reconstructed in the $\pi^0\gamma$ decay mode, in the p_T intervals selected for the measurement, is presented in Figures 7.11 to 7.19 for the SLH trigger and in Figures 7.20 to 7.28 for the LGH trigger. The top section of each plot shows the fitted signal and background region of π^0 sideband subtracted ($\pi^0_{sbs}\gamma$) distribution, where the events underwent the reconstruction procedure summarized in section 7.5.1 and were weighted by the set of corrections mentioned in section 7.5.2. The background to the omega signal is reduced compared to the unsubtracted $\pi^0\gamma$ distribution due to the process of the sideband subtraction. However, the error bars represented in the plots account for the true statistical uncertainty related to the content of unsubtracted $\pi^0\gamma$ as well as $\pi^0_{sb}\gamma$ histograms. The bottom part of each plot was obtained by subtraction of the fitted polynomial shaped background from the $\pi^0_{sbs}\gamma$ distribution. Fit ranges and fitted functions presented in Figures 7.11 to 7.19 correspond to the Fit 1 selection described in the previous section.

7.6 Other Corrections to the Cross Section

The beam absorption correction accounted for the interaction of beam particles as they traversed the target. The count of the total number of beam particles incident on the target and the live triggerable beam N_{LTB} calculation were discussed in section 3.3.1 of the Data Acquisition and Trigger Systems chapter. In the count of N_{LTB} we needed to correct for beam particles that

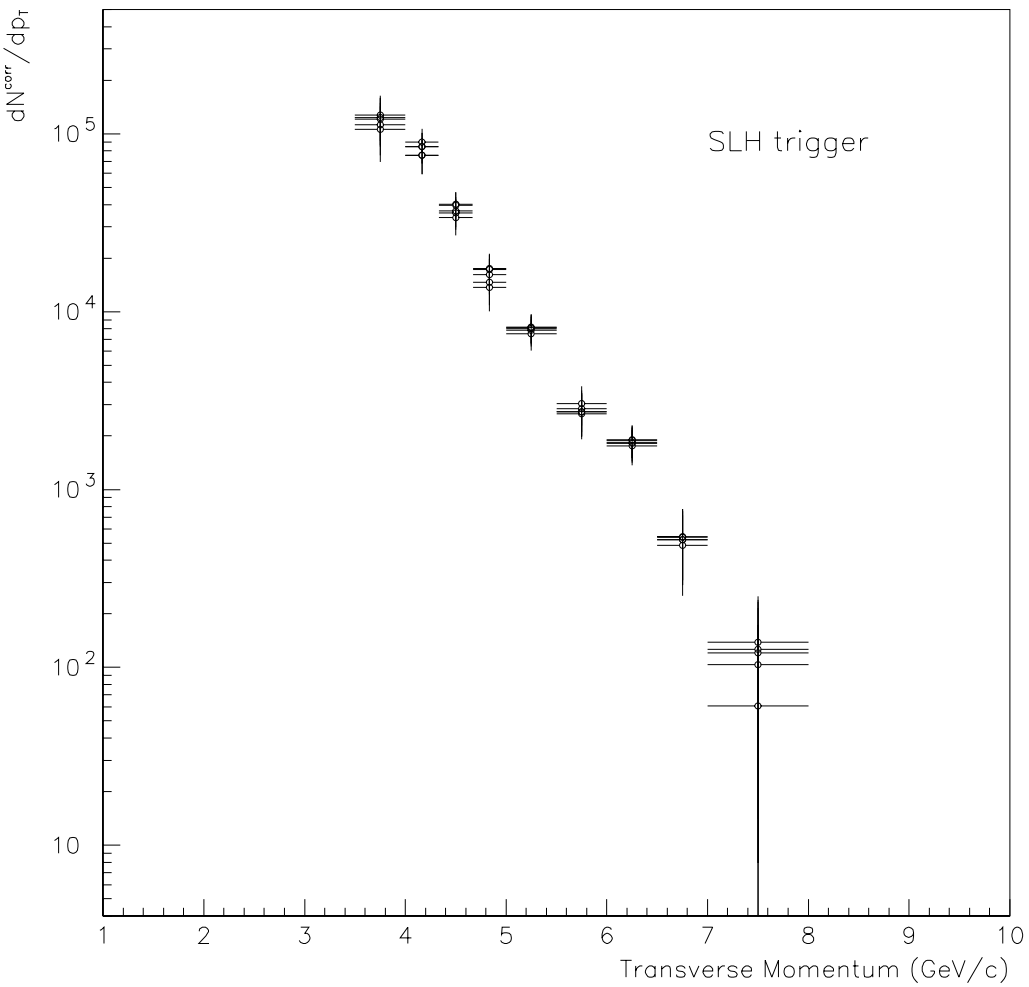

Figure 7.9 Corrected number of high p_T omegas ($\omega \rightarrow \pi^0\gamma$) reconstructed in $\triangle Y \triangle p_T$ intervals. Five different fit results, from Table 7.1 are plotted in each p_T bin. Error bars represent statistical errors.

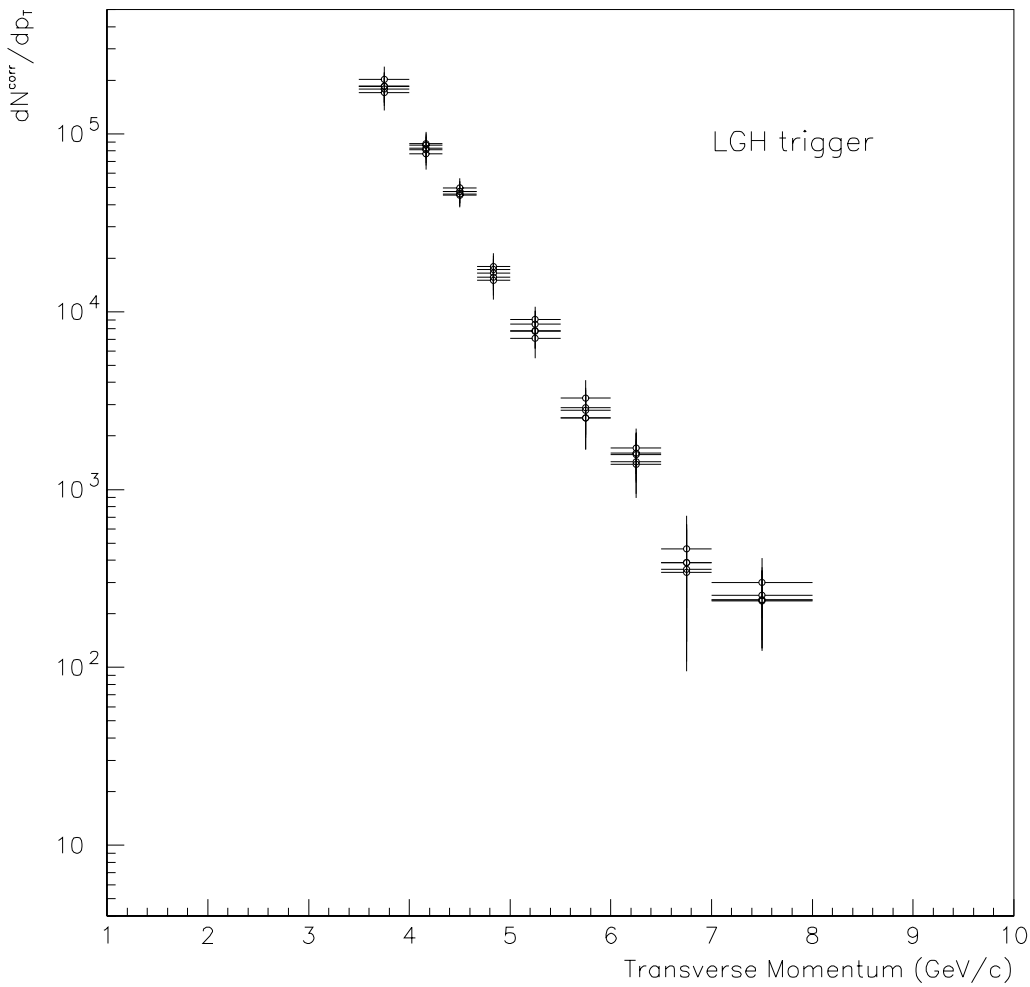

Figure 7.10 Corrected number of high p_T omegas ($\omega \rightarrow \pi^0\gamma$) reconstructed in $\triangle Y \triangle p_T$ intervals in events selected via LGH triggers. Five different fit results, from Table 7.3 are plotted in each p_T bin. Error bars represent statistical errors.

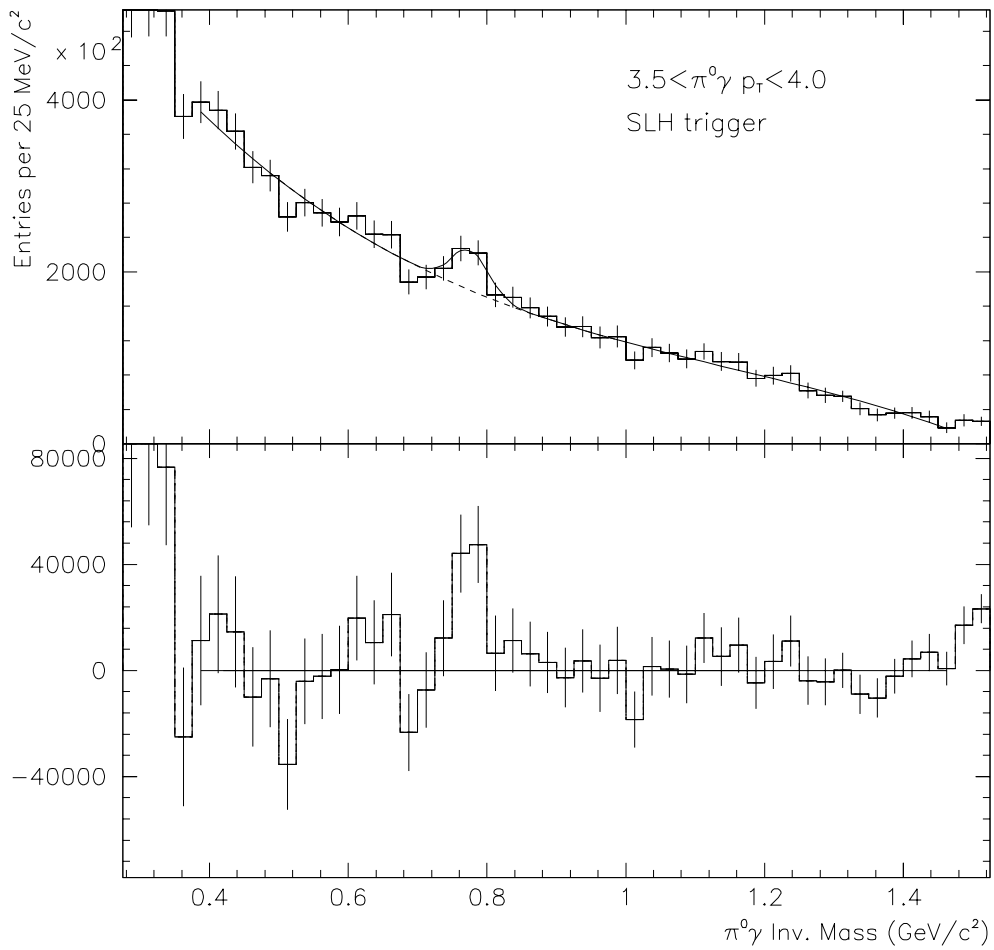

Figure 7.11 Top: π^0 sideband subtracted weighted $\pi^0\gamma$ distribution reconstructed in E706 data. p_T of $\pi^0\gamma$ ranges from 3.5 to 4.0 GeV/c, rapidity is from -0.5 to 0.75. Third order polynomial (P3) and a Gaussian shape are fitted to the data. Bottom: Same signal after the background P3 function is subtracted.

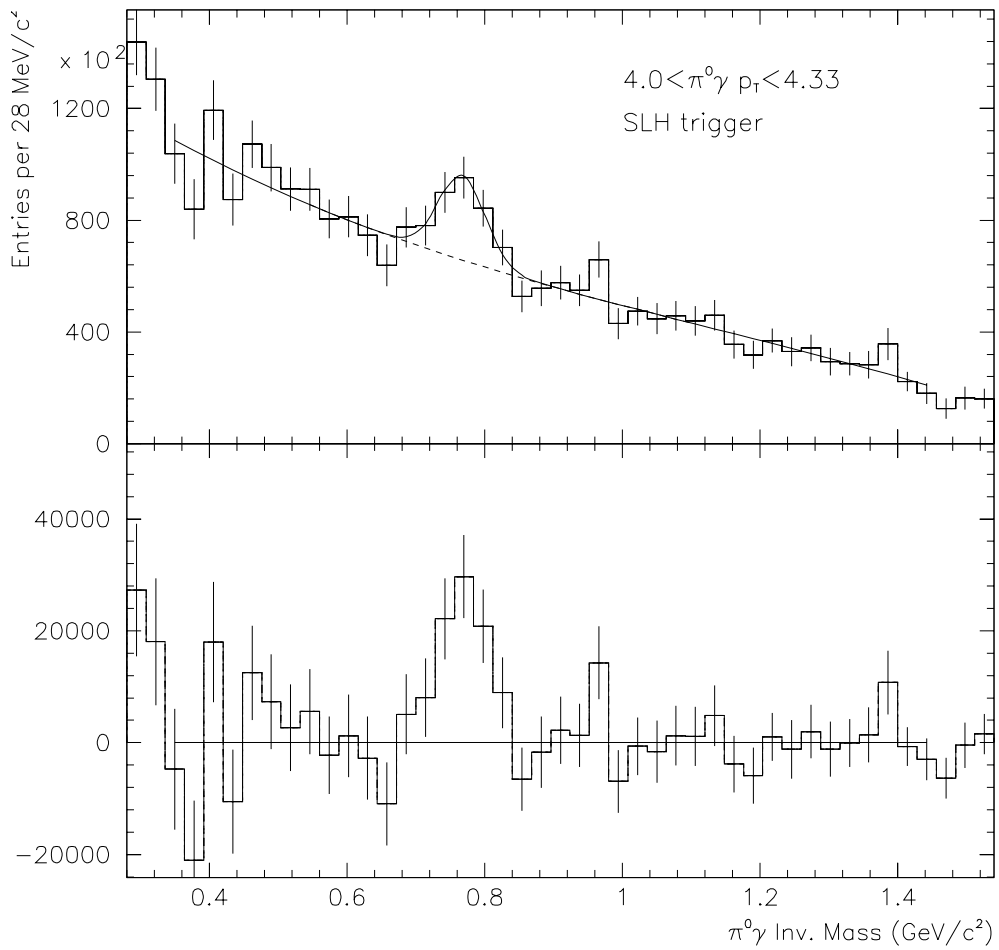

Figure 7.12 Top: π^0 sideband subtracted weighted $\pi^0\gamma$ distribution reconstructed in E706 data. p_T of $\pi^0\gamma$ ranges from 4.0 to 4.33 GeV/c, rapidity is from -0.5 to 0.75. Third order polynomial (P3) and a Gaussian shape are fitted to the data. Bottom: Same signal after the background P3 function is subtracted.

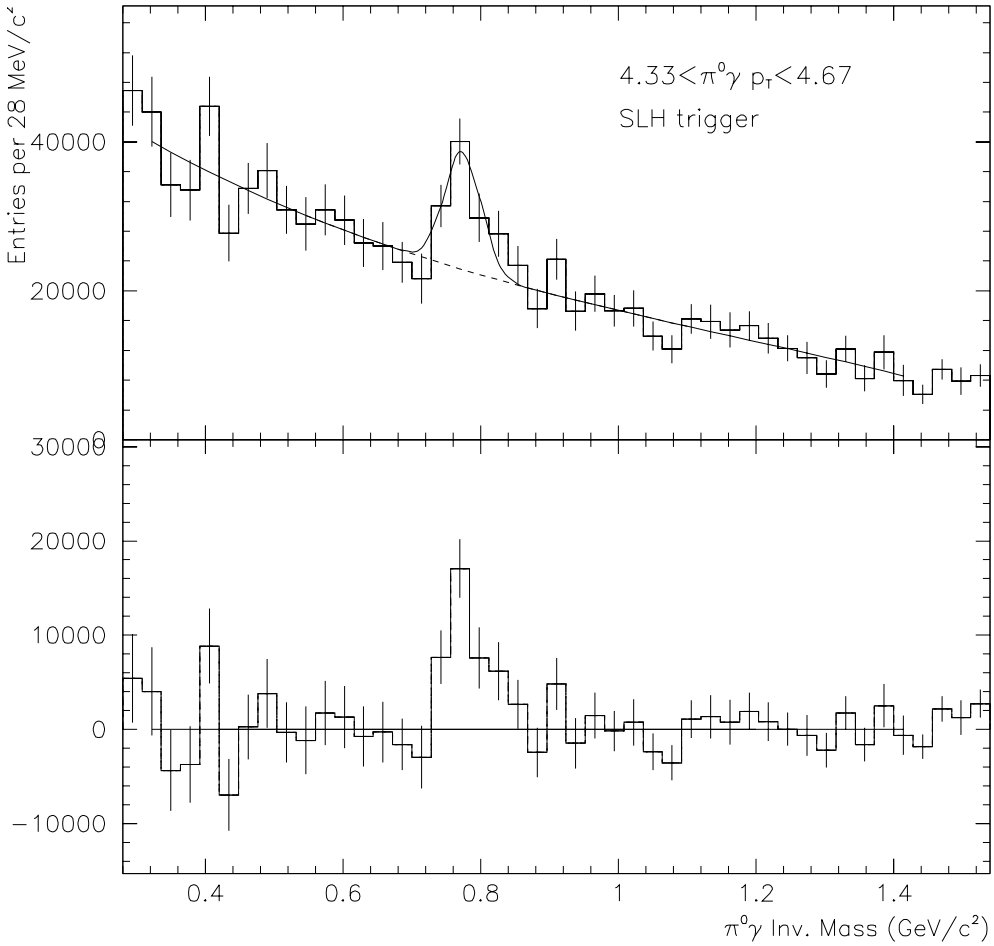

Figure 7.13 Top: π^0 sideband subtracted weighted $\pi^0\gamma$ distribution reconstructed in E706 data. p_T of $\pi^0\gamma$ ranges from 4.33 to 4.67 GeV/c, rapidity is from -0.5 to 0.75. Third order polynomial (P3) and a Gaussian shape are fitted to the data. Bottom: Same signal after the background P3 function is subtracted.

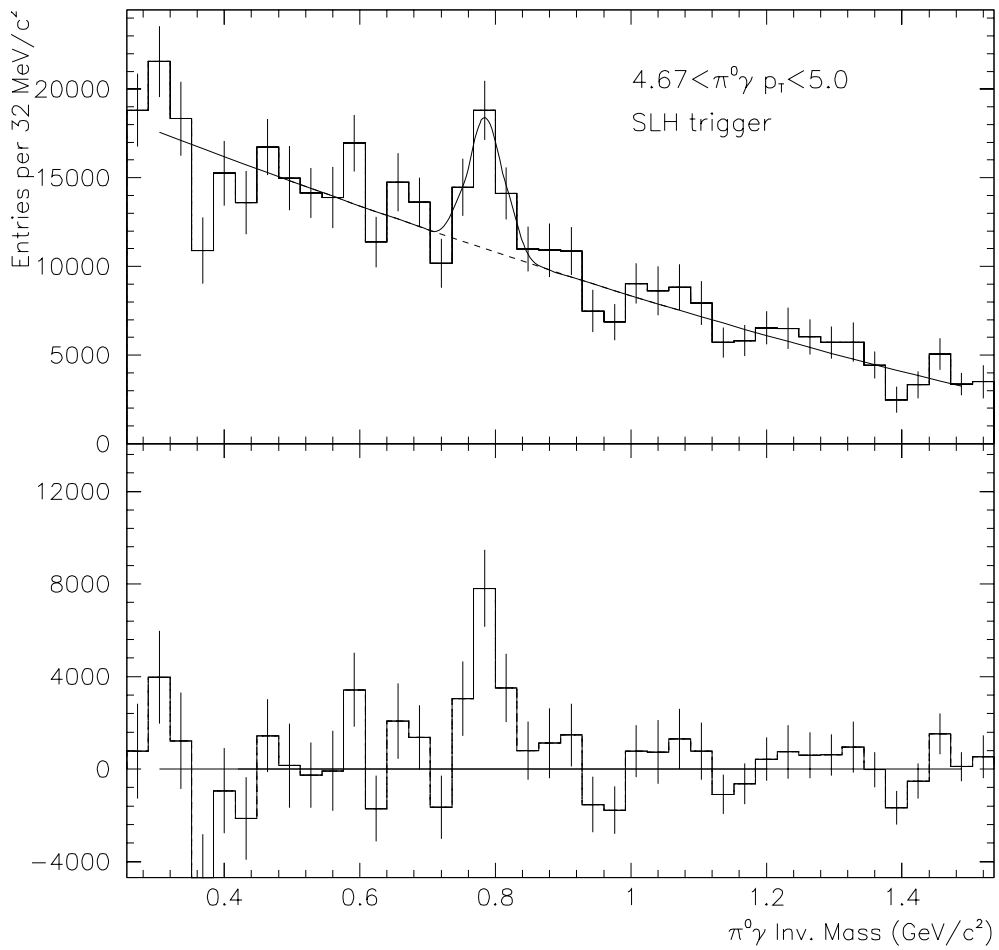

Figure 7.14 Top: π^0 sideband subtracted weighted $\pi^0\gamma$ distribution reconstructed in E706 data. p_T of $\pi^0\gamma$ ranges from 4.67 to 5.0 GeV/c, rapidity is from -0.5 to 0.75. Third order polynomial (P3) and a Gaussian shape are fitted to the data. Bottom: Same signal after the background P3 function is subtracted.

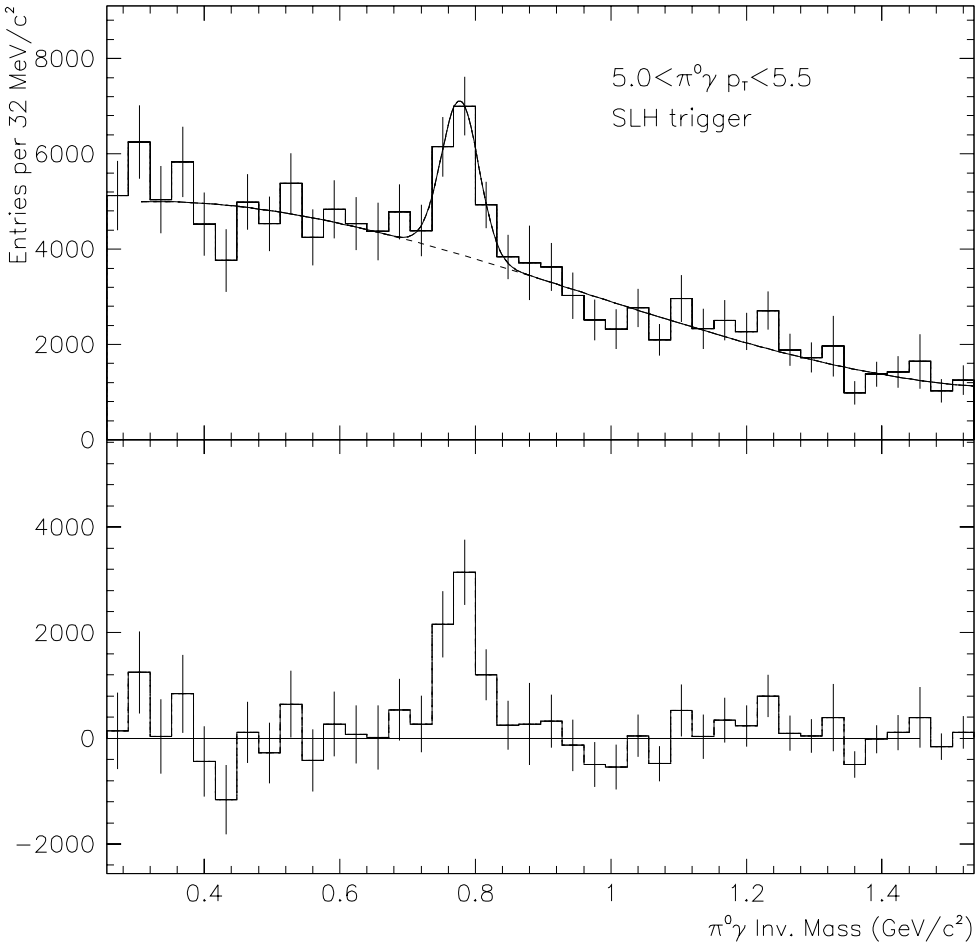

Figure 7.15 Top: π^0 sideband subtracted weighted $\pi^0\gamma$ distribution reconstructed in E706 data. p_T of $\pi^0\gamma$ ranges from 5.0 to 5.5 GeV/c, rapidity is from -0.5 to 0.75. Third order polynomial (P3) and a Gaussian shape are fitted to the data. Bottom: Same signal after the background P3 function is subtracted.

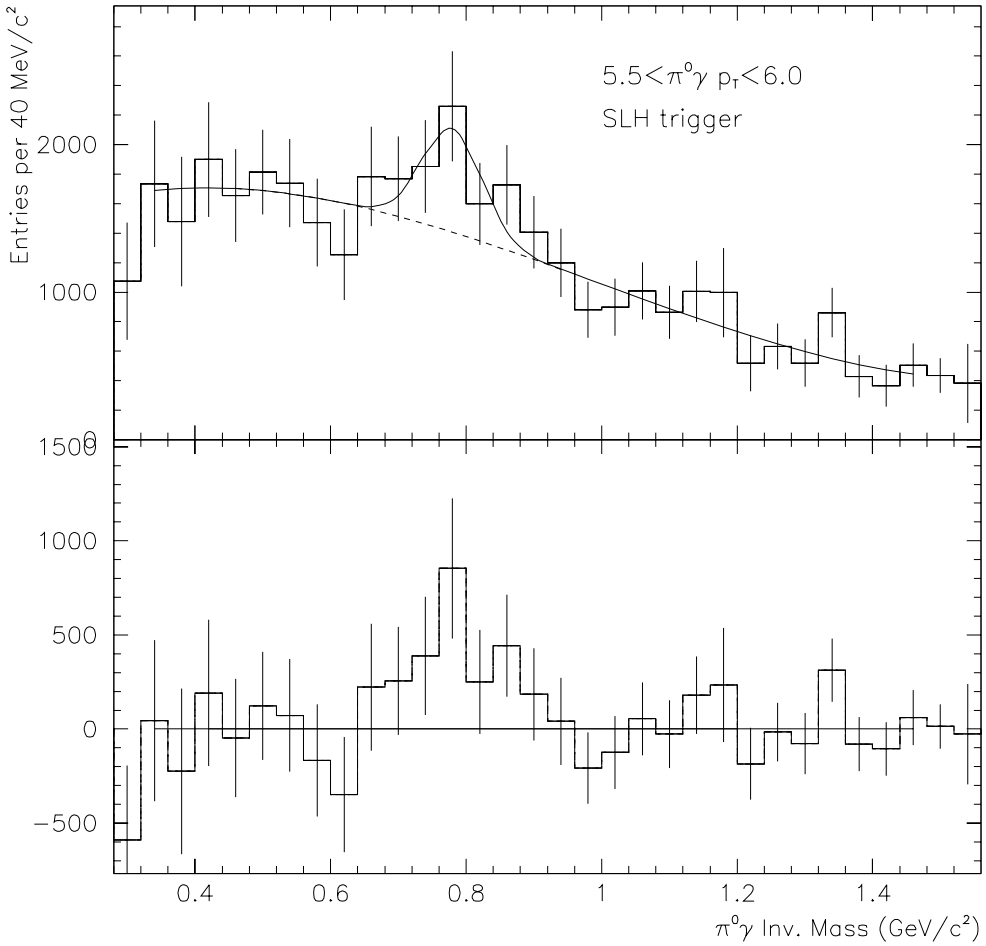

Figure 7.16 Top: π^0 sideband subtracted weighted $\pi^0\gamma$ distribution reconstructed in E706 data. p_T of $\pi^0\gamma$ ranges from 5.5 to 6.0 GeV/c, rapidity is from -0.5 to 0.75. Third order polynomial (P3) and a Gaussian shape are fitted to the data. Bottom: Same signal after the background P3 function is subtracted.

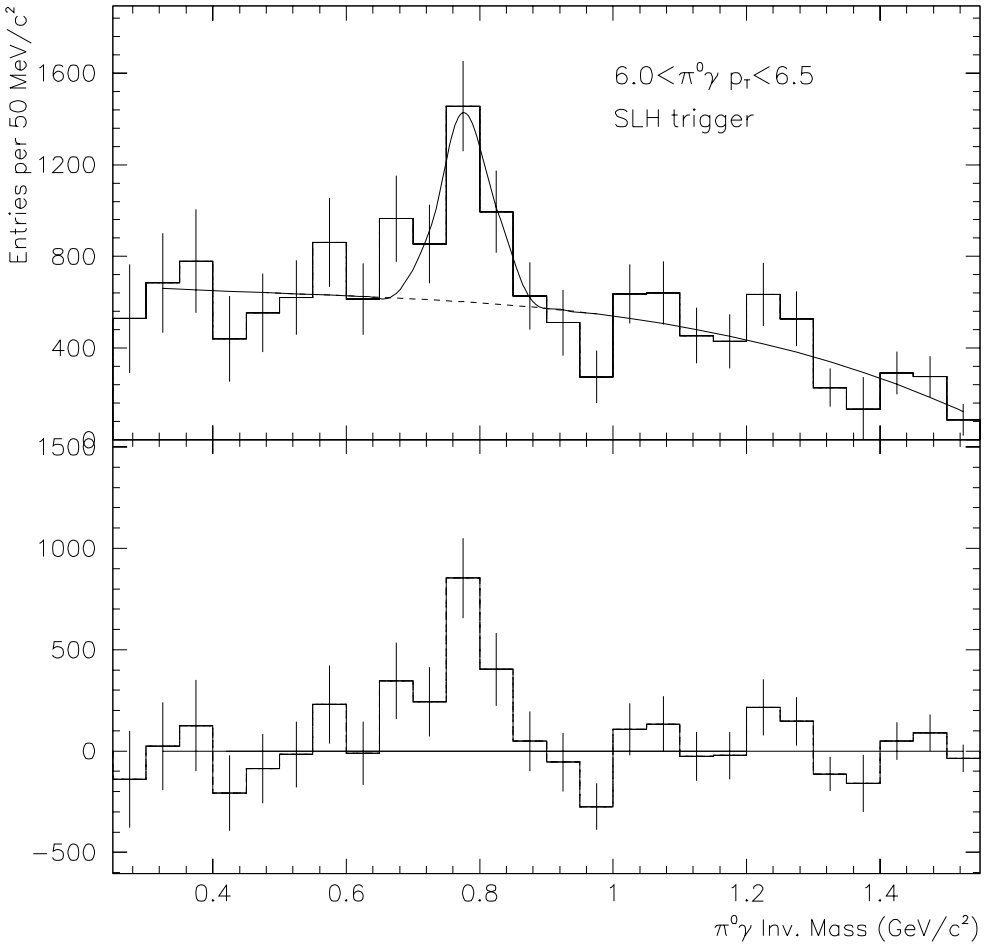

Figure 7.17 Top: π^0 sideband subtracted weighted $\pi^0\gamma$ distribution reconstructed in E706 data. p_T of $\pi^0\gamma$ ranges from 6.0 to 6.5 GeV/c, rapidity is from -0.5 to 0.75. Third order polynomial (P3) and a Gaussian shape are fitted to the data. Bottom: Same signal after the background P3 function is subtracted.

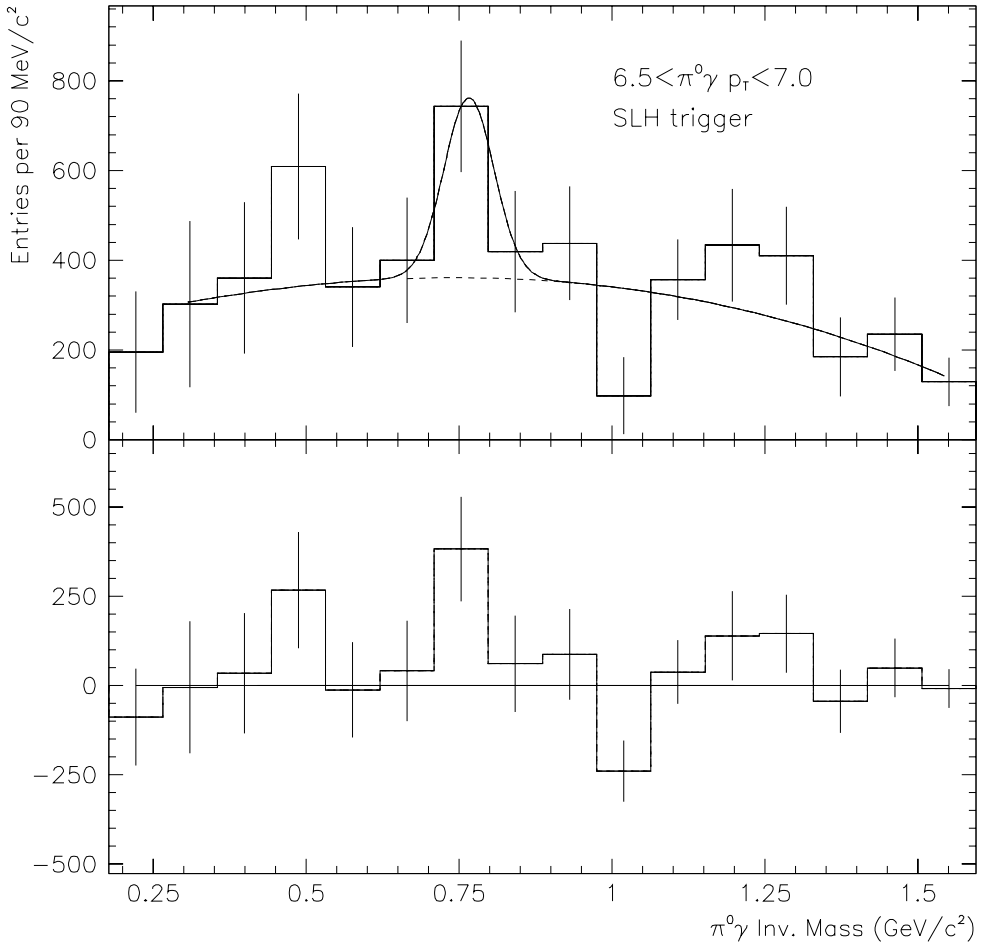

Figure 7.18 Top: π^0 sideband subtracted weighted $\pi^0\gamma$ distribution reconstructed in E706 data. p_T of $\pi^0\gamma$ ranges from 6.5 to 7.0 GeV/c, rapidity is from -0.5 to 0.75. Third order polynomial (P3) and a Gaussian shape are fitted to the data. Bottom: Same signal after the background P3 function is subtracted.

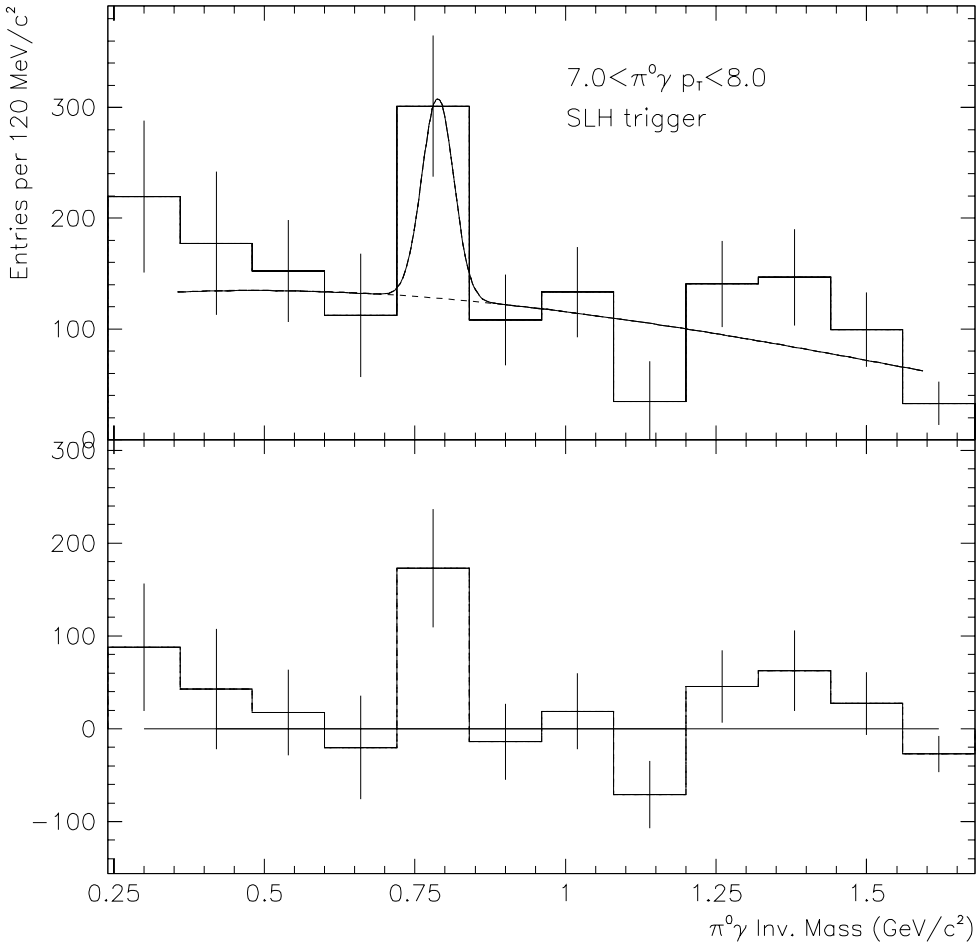

Figure 7.19 Top: π^0 sideband subtracted weighted $\pi^0\gamma$ distribution reconstructed in E706 data. p_T of $\pi^0\gamma$ ranges from 7.0 to 8.0 GeV/c, rapidity is from -0.5 to 0.75. Third order polynomial (P3) and a Gaussian shape are fitted to the data. Bottom: Same signal after the background P3 function is subtracted.

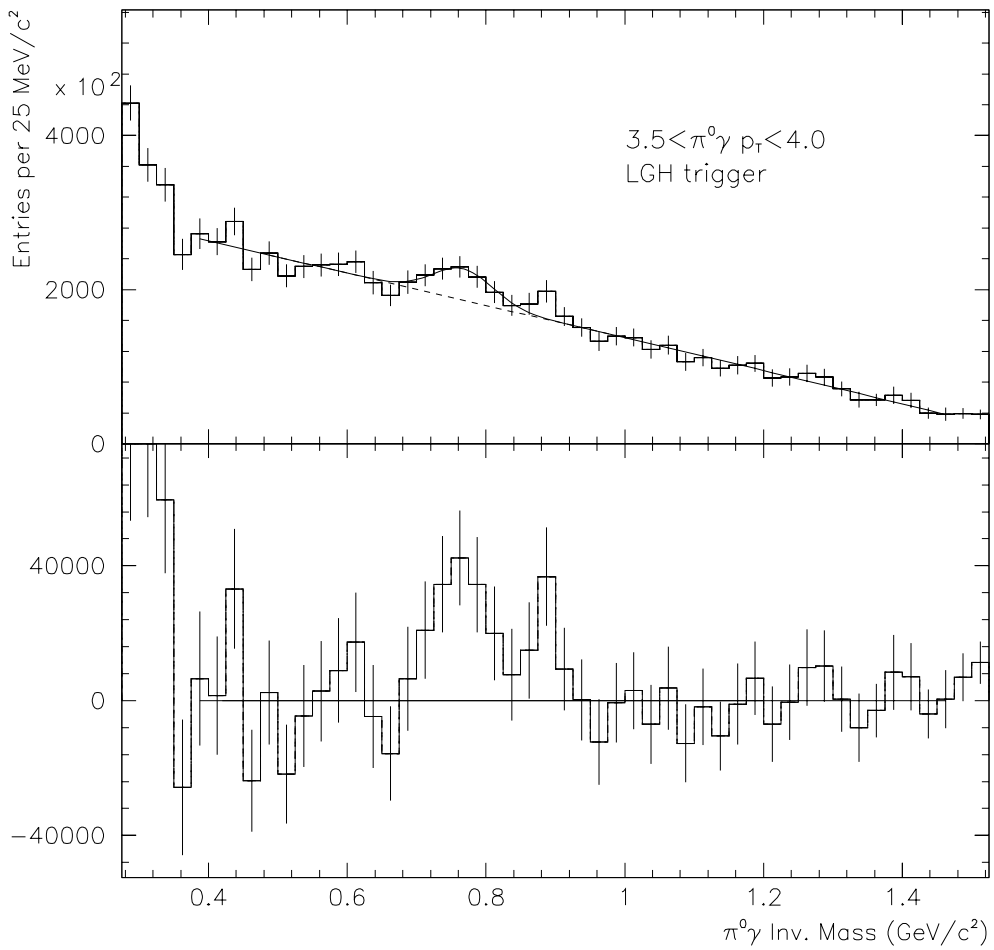

Figure 7.20 Top: π^0 sideband subtracted weighted $\pi^0\gamma$ distribution reconstructed in E706 data. p_T of $\pi^0\gamma$ ranges from 3.5 to 4.0 GeV/c, rapidity is from -0.5 to 0.75. Third order polynomial (P3) and a Gaussian shape are fitted to the data. Bottom: Same signal after the background P3 function is subtracted.

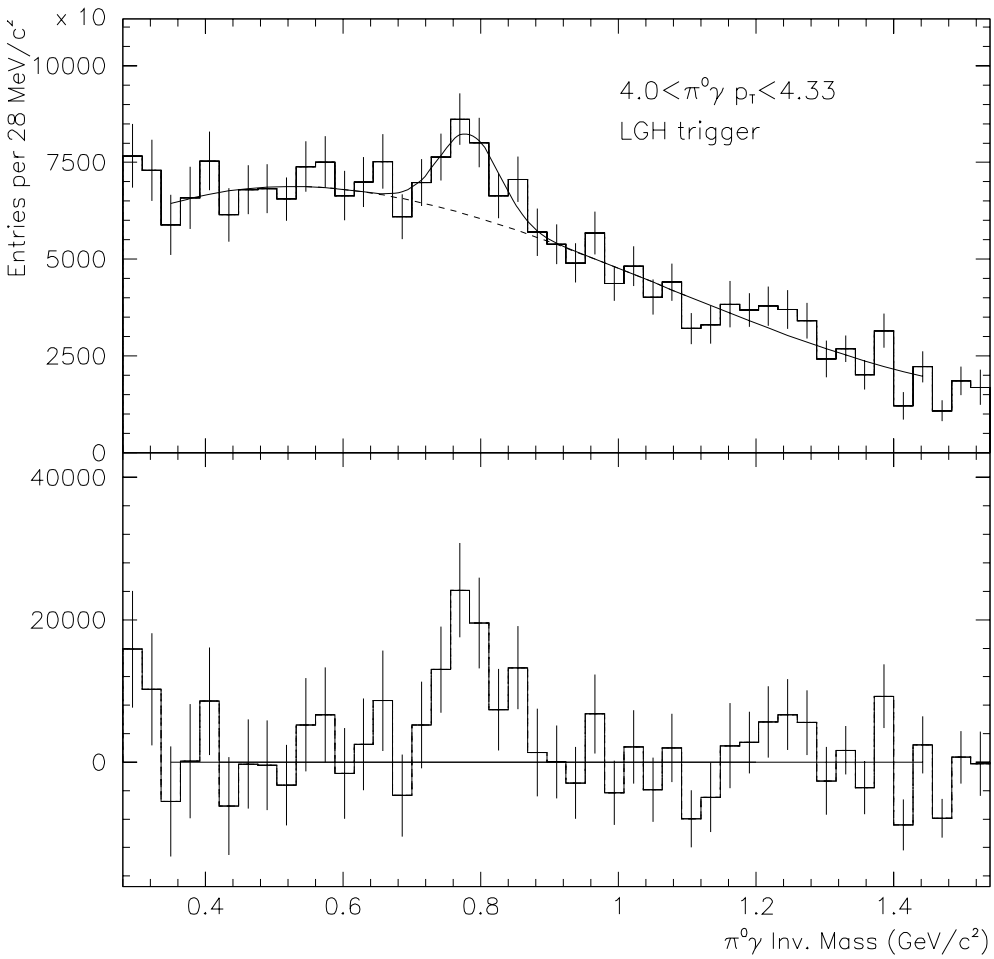

Figure 7.21 Top: π^0 sideband subtracted weighted $\pi^0\gamma$ distribution reconstructed in E706 data. p_T of $\pi^0\gamma$ ranges from 4.0 to 4.33 GeV/c, rapidity is from -0.5 to 0.75. Third order polynomial (P3) and a Gaussian shape are fitted to the data. Bottom: Same signal after the background P3 function is subtracted.

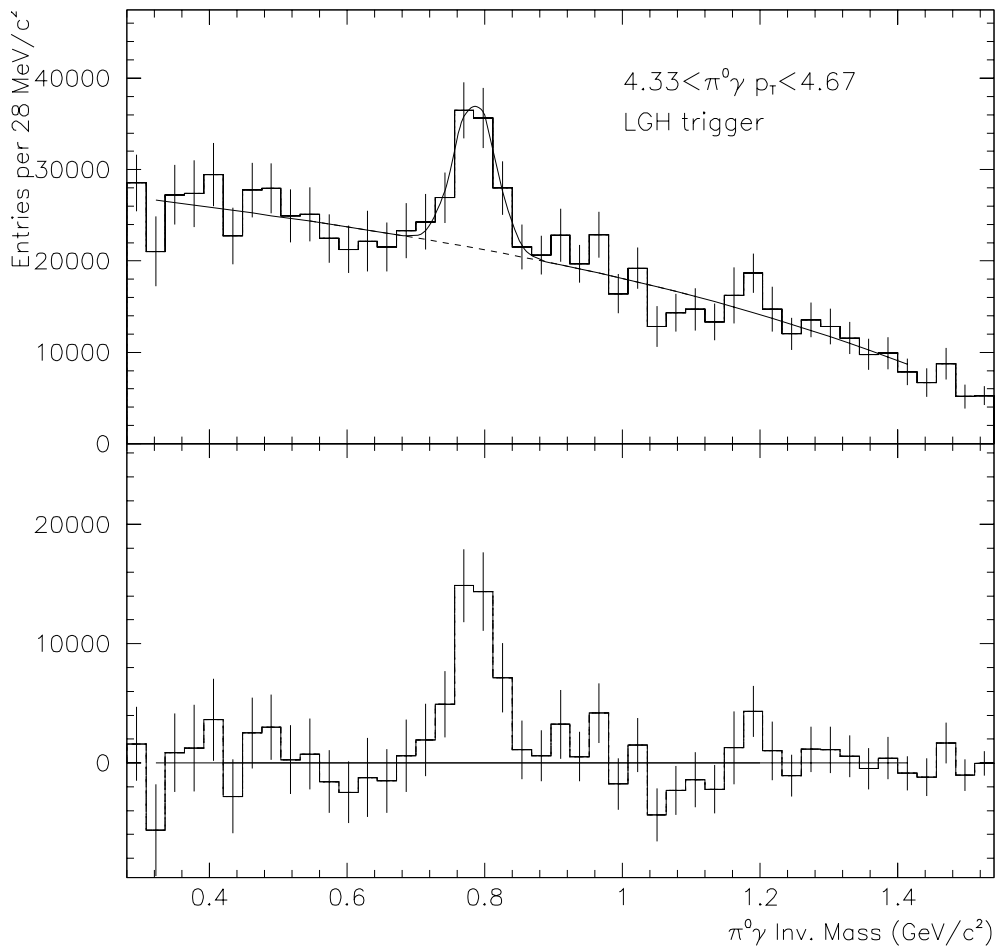

Figure 7.22 Top: π^0 sideband subtracted weighted $\pi^0\gamma$ distribution reconstructed in E706 data. p_T of $\pi^0\gamma$ ranges from 4.33 to 4.67 GeV/c, rapidity is from -0.5 to 0.75. Third order polynomial (P3) and a Gaussian shape are fitted to the data. Bottom: Same signal after the background P3 function is subtracted.

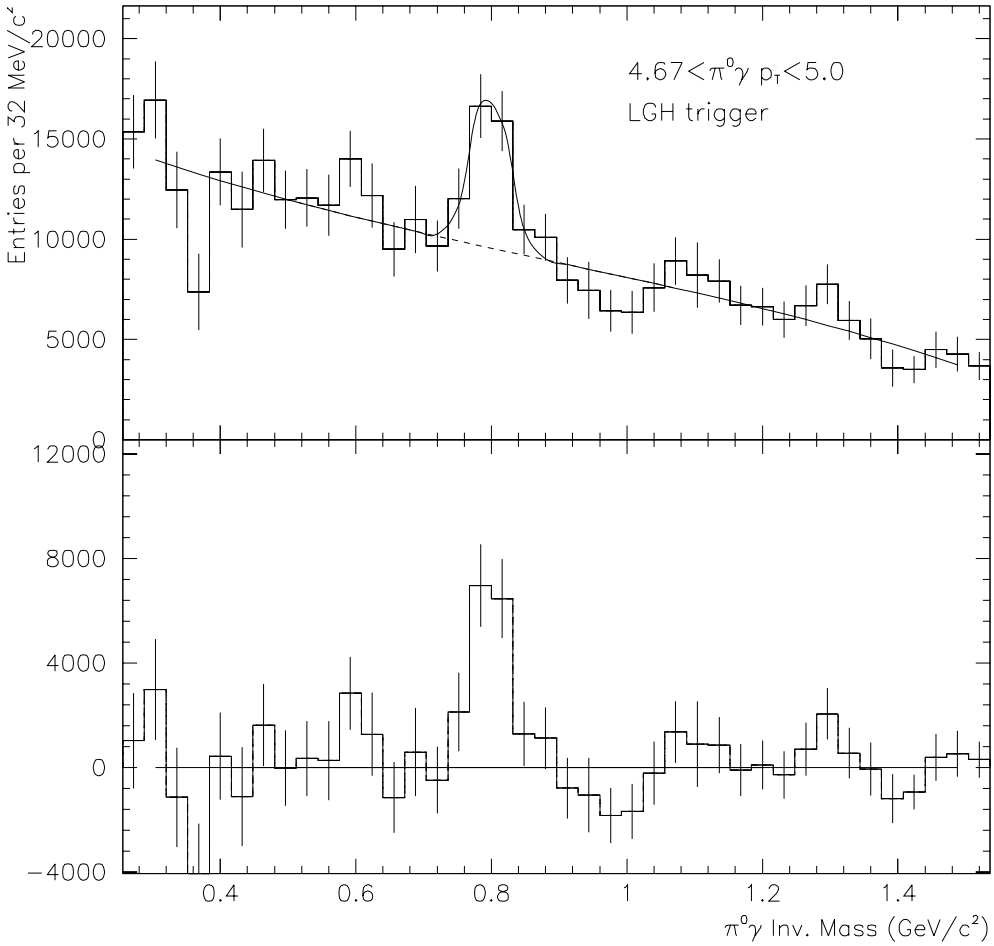

Figure 7.23 Top: π^0 sideband subtracted weighted $\pi^0\gamma$ distribution reconstructed in E706 data. p_T of $\pi^0\gamma$ ranges from 4.67 to 5.0 GeV/c, rapidity is from -0.5 to 0.75. Third order polynomial (P3) and a Gaussian shape are fitted to the data. Bottom: Same signal after the background P3 function is subtracted.

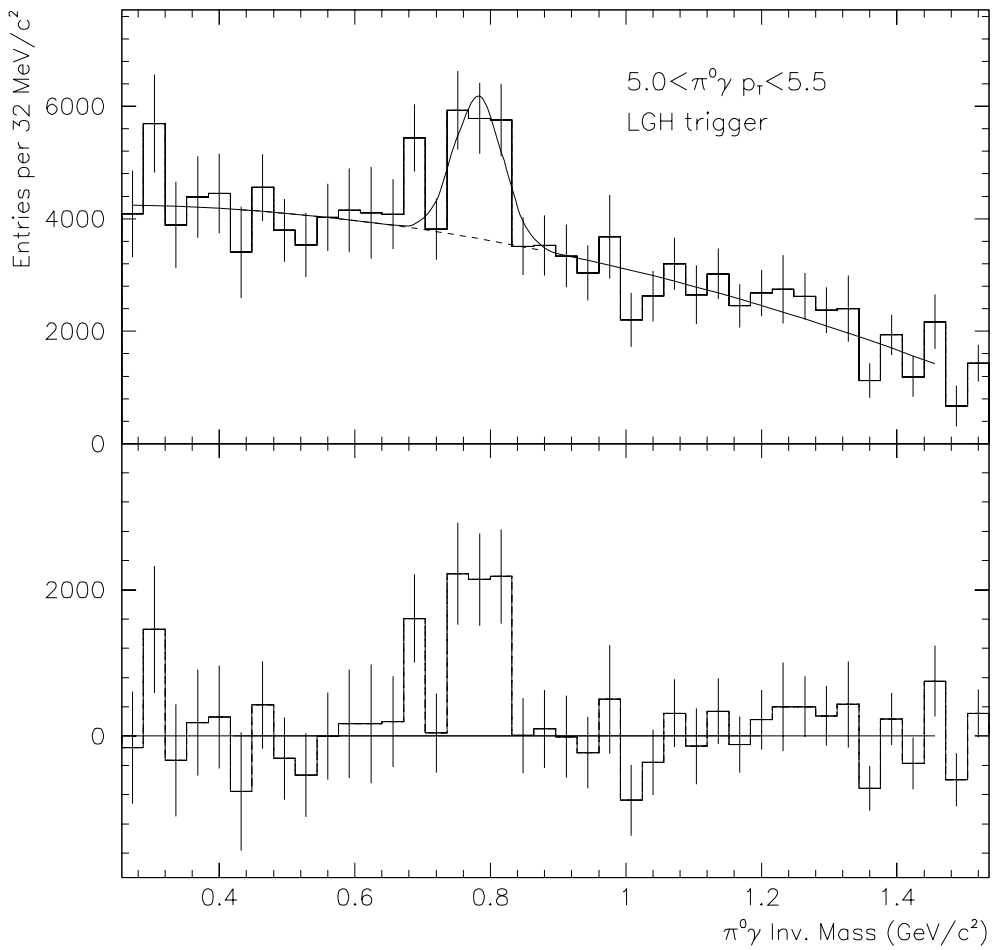

Figure 7.24 Top: π^0 sideband subtracted weighted $\pi^0\gamma$ distribution reconstructed in E706 data. p_T of $\pi^0\gamma$ ranges from 5.0 to 5.5 GeV/c, rapidity is from -0.5 to 0.75. Third order polynomial (P3) and a Gaussian shape are fitted to the data. Bottom: Same signal after the background P3 function is subtracted.

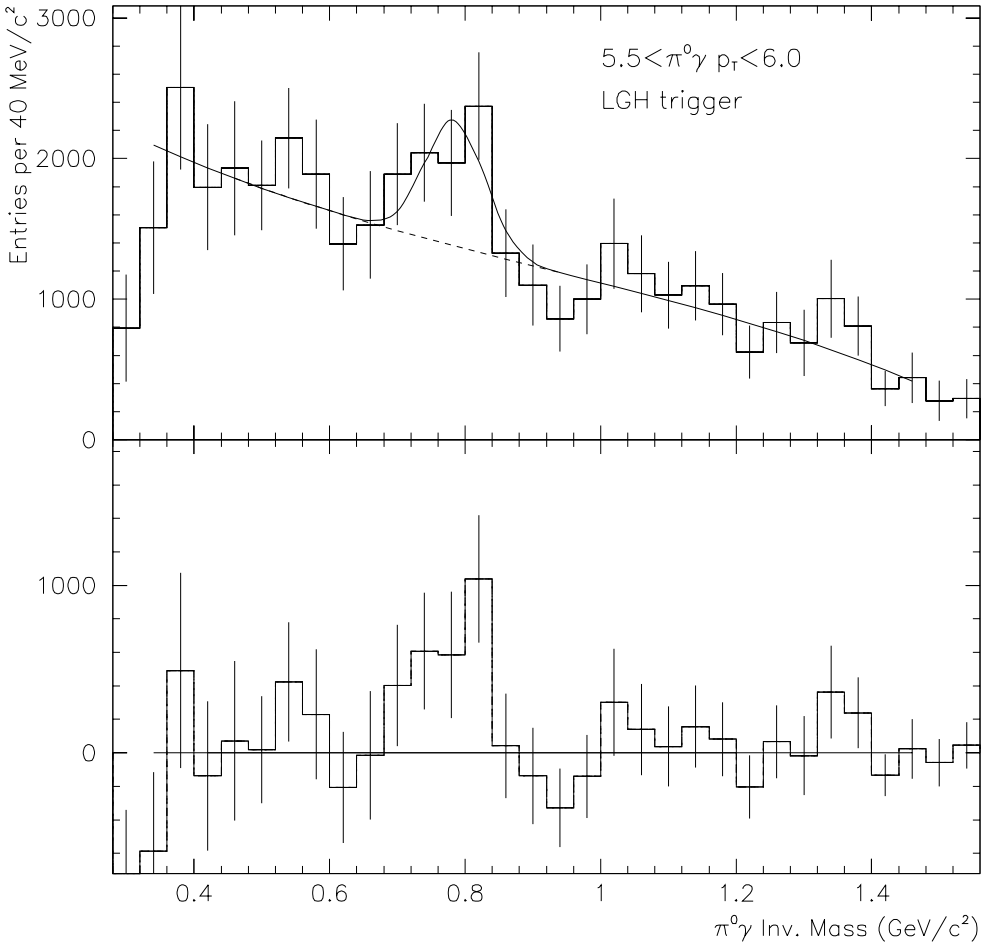

Figure 7.25 Top: π^0 sideband subtracted weighted $\pi^0\gamma$ distribution reconstructed in E706 data. p_T of $\pi^0\gamma$ ranges from 5.5 to 6.0 GeV/c, rapidity is from -0.5 to 0.75. Third order polynomial (P3) and a Gaussian shape are fitted to the data. Bottom: Same signal after the background P3 function is subtracted.

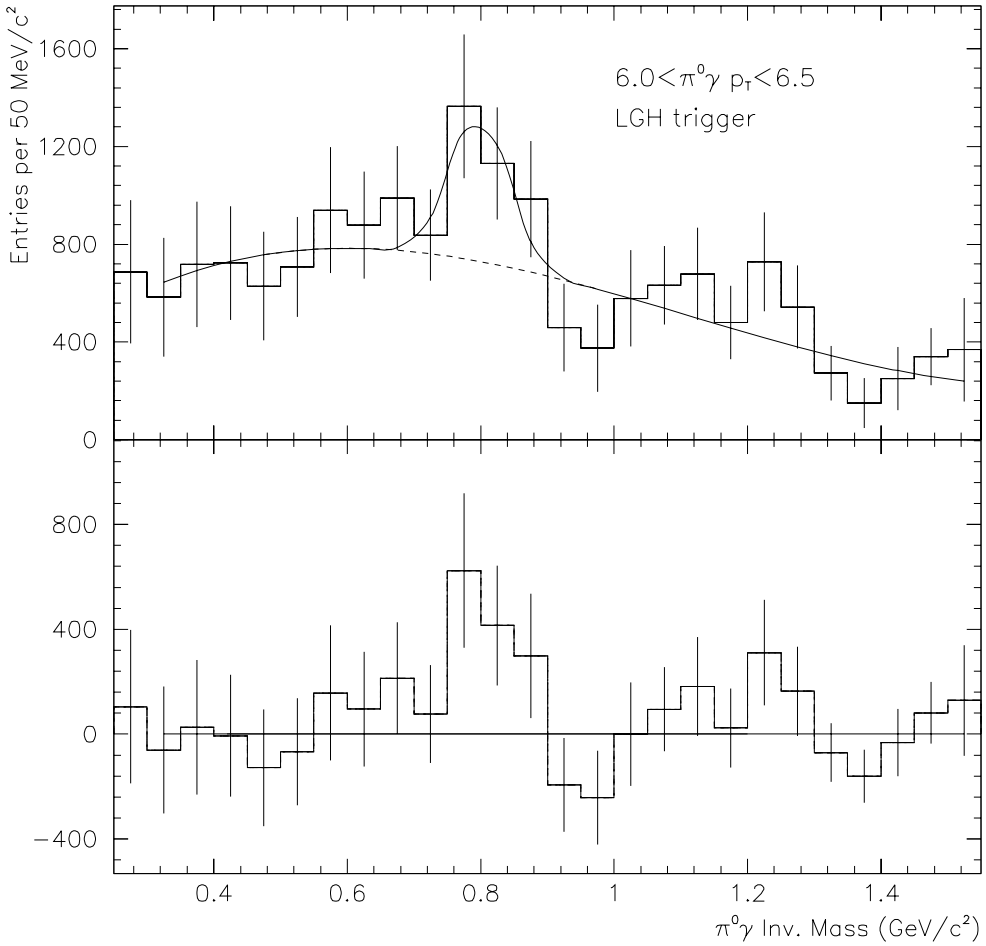

Figure 7.26 Top: π^0 sideband subtracted weighted $\pi^0\gamma$ distribution reconstructed in E706 data. p_T of $\pi^0\gamma$ ranges from 6.0 to 6.5 GeV/c, rapidity is from -0.5 to 0.75. Third order polynomial (P3) and a Gaussian shape are fitted to the data. Bottom: Same signal after the background P3 function is subtracted.

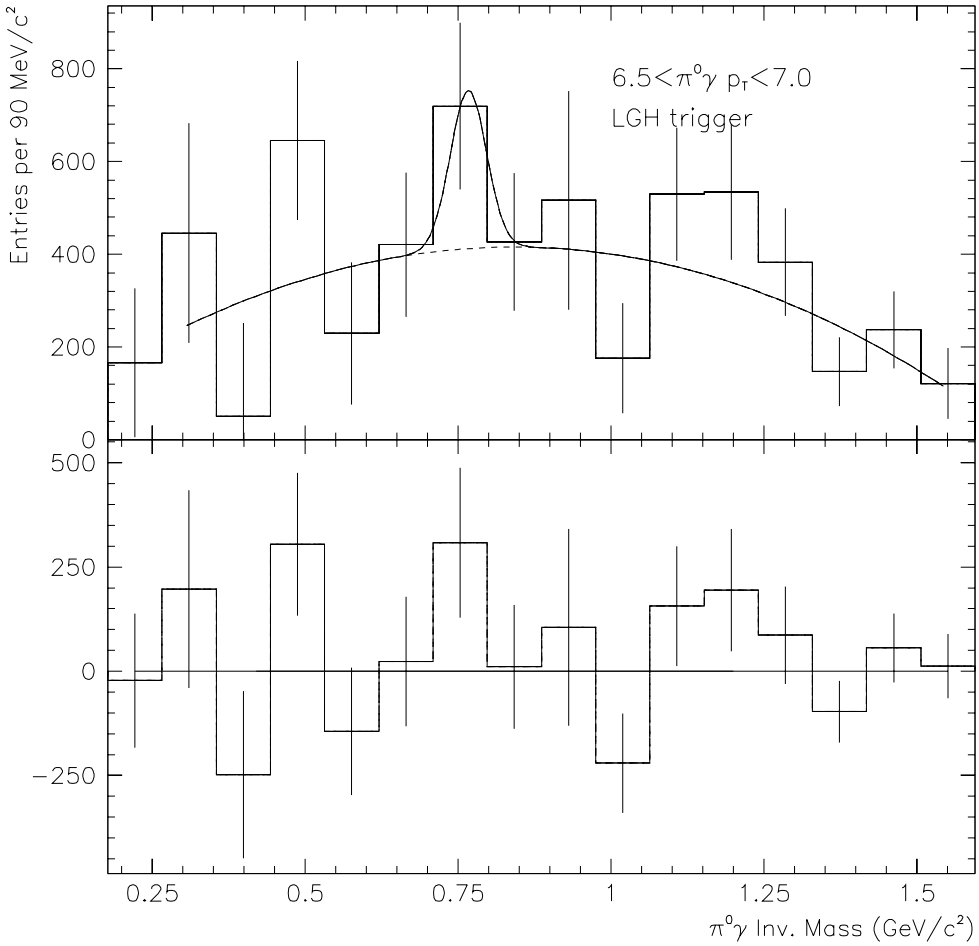

Figure 7.27 Top: π^0 sideband subtracted weighted $\pi^0\gamma$ distribution reconstructed in E706 data. p_T of $\pi^0\gamma$ ranges from 6.5 to 7.0 GeV/c, rapidity is from -0.5 to 0.75. Third order polynomial (P3) and a Gaussian shape are fitted to the data. Bottom: Same signal after the background P3 function is subtracted.

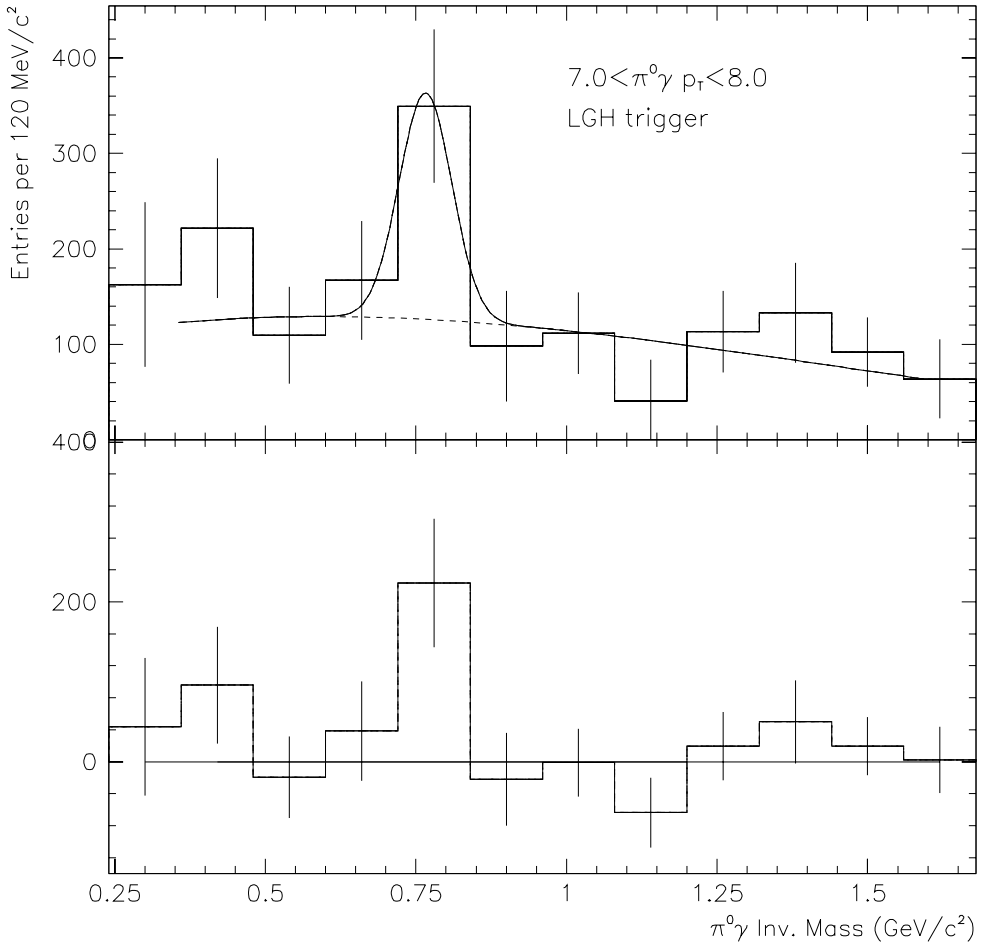

Figure 7.28 Top: π^0 sideband subtracted weighted $\pi^0\gamma$ distribution reconstructed in E706 data. p_T of $\pi^0\gamma$ ranges from 7.0 to 8.0 GeV/c, rapidity is from -0.5 to 0.75. Third order polynomial (P3) and a Gaussian shape are fitted to the data. Bottom: Same signal after the background P3 function is subtracted.

were absorbed in the material between the hodoscope and the interaction point in the target. That correction, calculated on an event by event basis, averaged at about 5.4% for Be and 0.7% for Cu target.

The loss of events due to a failure to reconstruct the vertex was estimated to be very small (0.4%)[59]. Equally small was the correction for the contamination of π^- beam with muon particles (which were not likely to cause an interaction in the target).

7.7 Invariant Cross Section Definition

The invariant cross section per nucleon for inclusive omega meson production can be expressed as follows:

$$E\,\frac{d^3\sigma}{dp^3} = \frac{1}{2\pi p_T \triangle p_T \triangle Y} \times \frac{N_{xs}^{corr}(p_T)}{N_{LTB} \times \rho L N_A}$$

where the $2\pi p_T \triangle p_T \triangle Y$ term constitutes the phase space factor after integration over the azimuthal angle, the N_{LTB} is the live triggerable beam count, defined in chapter 3 and $\rho L N_A$ represent the target nucleon count per unit area , with ρ representing the target density, L - the target length, and N_A is Avogadro number. Finally the $N_{xs}^{corr}(p_T)$ is the corrected number of observed ωs in the $\triangle p_T$ and $\triangle Y$ interval. The $N_{xs}^{corr}(p_T)$ differs from $N^{corr}(p_T)$ defined in section 7.5.2 in that a few more corrections, relevant for the cross section measurement, were implemented in the event weighting:

- branching ratio correction for $\omega \to \pi^0\gamma$
- beam absorption correction
- beam contamination correction
- target transverse fiducial volume correction

Mean values of the weights applied to the data to obtain $N_{xs}^{corr}(p_T)$ are given in Table 7.5. The averaged values of several items listed in Table 7.5 are presented only for general illustrative purposes, because the corrections vary strongly with p_T. In such cases the average was taken from the data with $\pi^0\gamma$ $p_T > 4.0$ GeV/c.

Correction Type (W_i)	**Averaged Correction**
Trigger Correction (strongly varying with p_T)	1.3(SLH) 1.4(LGH)
Rapidity Hole Cut (strongly varying with p_T)	1.43(SLH) 2.12(LGH)
Photon Conversions	1.302(Be) 1.687(Cu)
Reconstruction Efficiency and Geometrical Correction (strongly varying with p_T)	9.9(SLH) 10.2(LGH)
Veto Wall Cut	1.05
Directionality Cut	1.021
Balanced p_T Cut	1.053
Vertex Reconstruction	1.004
Branching Ratio $\omega \to \pi^0\gamma$	11.7647
Branching Ratio $\pi^0 \to \gamma\gamma$	1.012
Beam Absorption	1.054(Be) 1.007(Cu)
Beam Contamination	1.005
Target Transverse Fiducial Region	1.35

Table 7.5 Summary of corrections and multiplicative factors applied to data.

Chapter 8 Results

8.1 The ω Differential Cross Section Versus p_T

The ω meson cross section for the reaction $\pi^- + Be \rightarrow \omega + X$ was calculated as a function of ω transverse momentum and integrated over the center of mass rapidity range from -0.5 to 0.75. Figure 8.1 displays the cross section per nucleon in 9 p_T bins from 3.5 to 8 GeV/c. Table 8.1 contains the corresponding values of the cross section. The two uncertainties quoted with each cross section value represent the statistical uncertainty stemming from the total number of events in the ω mass region (1st value) and the uncertainty related to the background shape determination (2nd value). Both statistical and systematic effects are included in the latter quantity which contributes only a relatively small increase in the error bars plotted in Figure 8.1.

P_T **Interval** (GeV/c)	$\pi^- + Be \rightarrow \omega + X$ (pb/(GeV/c)^2)
3.5-4.0	12500 ± 2400 ± 1070
4.0-4.33	5100 ± 950 ± 400
4.33-4.67	2370 ± 380 ± 150
4.67-5.0	840 ± 180 ± 70
5.0-5.5	380 ± 75 ± 15
5.5-6.0	120 ± 35 ± 13
6.0-6.5	68 ± 18 ± 5
6.5-7.0	19 ± 10 ± 3
7.0-8.0	6 ± 4 ± 1

Table 8.1 The ω invariant cross section per nucleon on a Be target.

The cross section as a function of transverse momentum was fitted with the phenomenological formula[67]:

$$E\,\frac{d^3\sigma}{dp^3} = \frac{C(1-x_T)^m}{p_T^n}$$

where $x_T = 2p_T/\sqrt{s}$, $\sqrt{s}$ is the center of mass energy, and C is a constant. As can be seen from Figure 8.1, the data are described very well by this functional form. The values for the exponents m and n were found to be 4.5 ± 0.9 and 8.7 ± 0.2, respectively.

This cross section result is an average of two differential cross section measurements. One was conducted using events that satisfied the SLH trigger and the other was performed using the sample of events selected by the LGH trigger. The p_T dependence of the cross section measured in these two data sets is compared in Figure 8.2. The corresponding cross section values are listed in Tables 8.2 and 8.3. Further comparison of these two measurements is available in Figures 8.3 and 8.4, where each of the differential cross sections is compared with the generated omega meson spectrum obtained from the HERWIG Monte Carlo. The high p_T spectrum of omegas produced in π^- proton collisions using the Monte Carlo program was fitted with the above phenomenological formula, and the resulting fit compared to the measured cross section. The Monte Carlo prediction was scaled to match the data at the $4.0 < p_T < 4.33$ GeV/c interval. The measured p_T dependence of the cross section agrees very well with the Monte Carlo prediction.

The two data samples selected by the different triggers (SLH, LGH) are not statistically independent, since they share a substantial number of events (with an increasing overlap as p_T increases). However, these two sets are not the same either, which can be seen by comparing the numbers of unweighted,

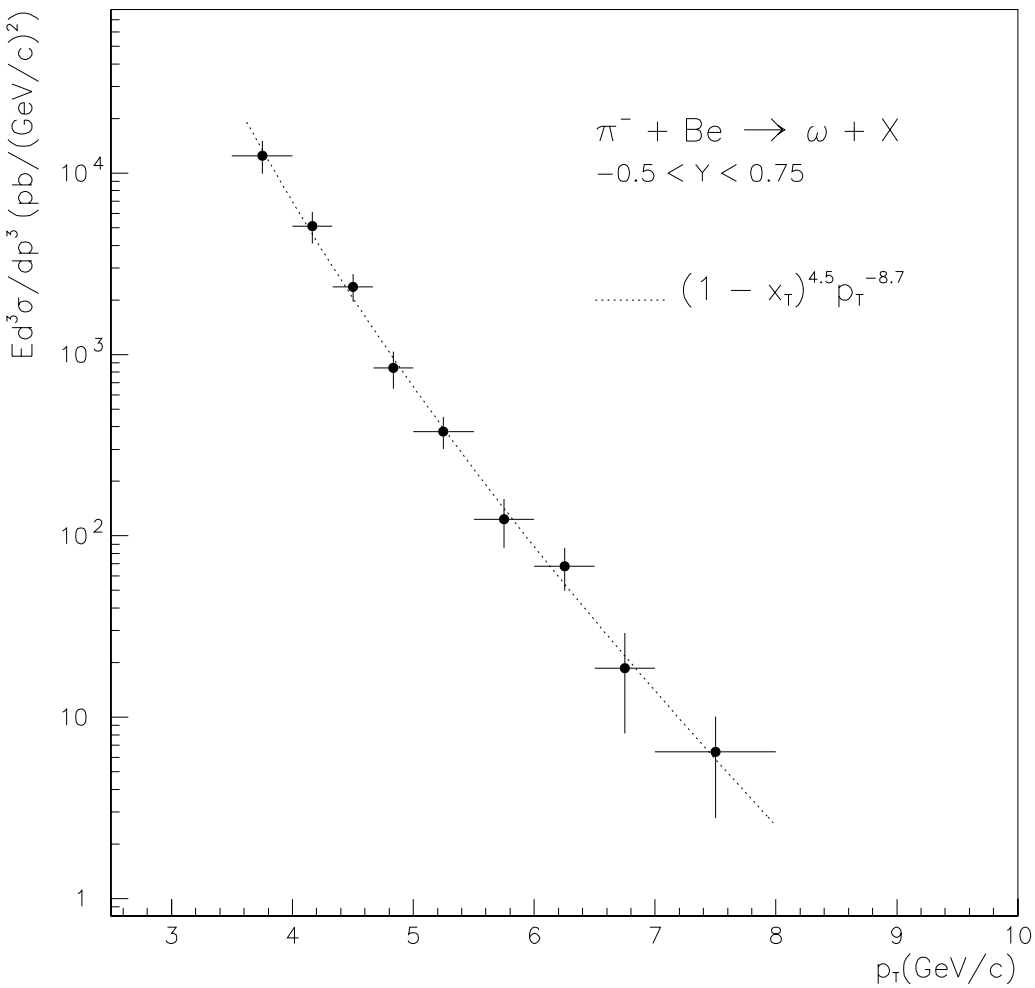

Figure 8.1 The p_T dependence of the ω invariant production cross section per nucleon on a Be target. The error bars correspond to the statistical uncertainty and the uncertainty related to the signal extraction, combined in quadrature. The dotted line is a fit to the data using the phenomenological formula given in the text.

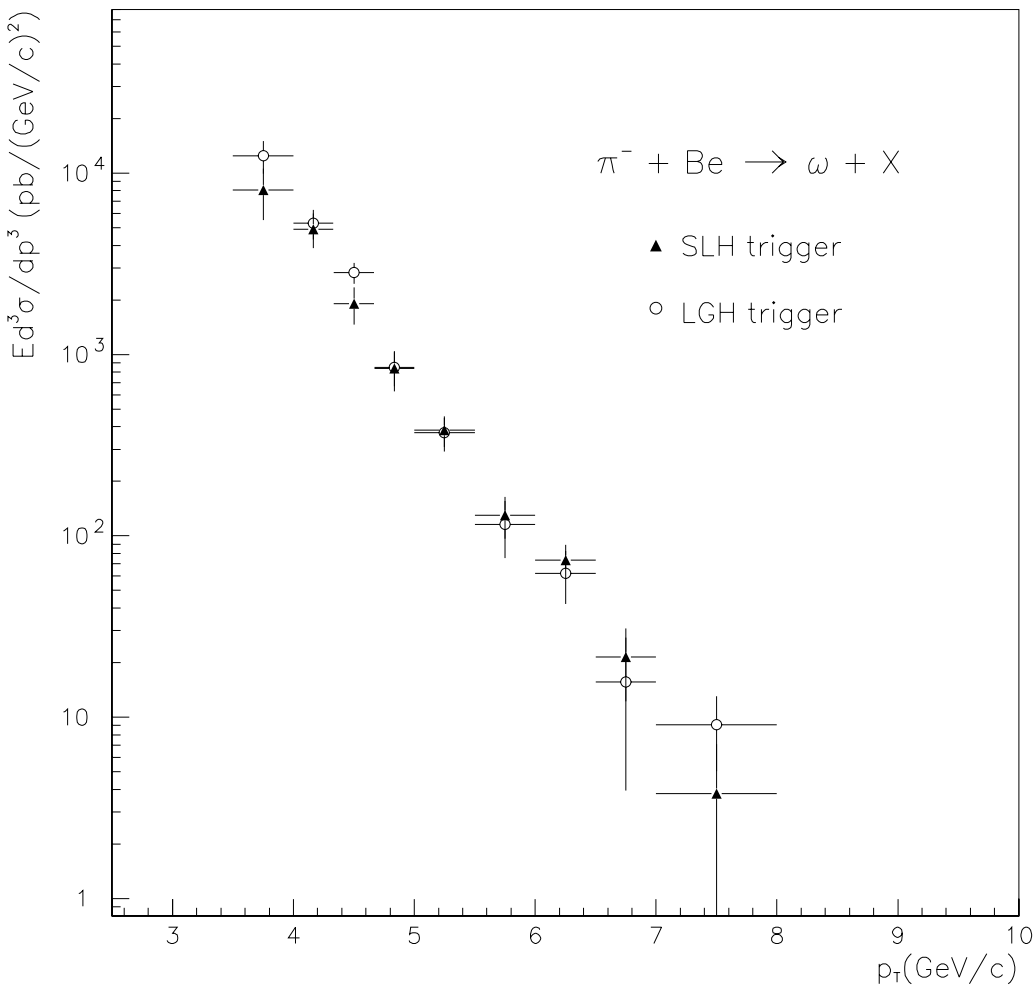

Figure 8.2 The p_T dependence of the ω invariant cross section measured in events selected via SLH trigger (triangles) and LGH trigger (open circles). The error bars correspond to the statistical uncertainty and the uncertainty related to the signal extraction, combined in quadrature.

P_T **Interval** (GeV/c)	$\pi^- + Be \rightarrow \omega + X$ (pb/(GeV/c)^2)
3.5-4.0	8060 ± 2500 ± 790
4.0-4.33	4900 ± 1000 ± 360
4.33-4.67	1910 ± 390 ± 200
4.67-5.0	840 ± 190 ± 90
5.0-5.5	380 ± 70 ± 12
5.5-6.0	130 ± 30 ± 11
6.0-6.5	75 ± 16 ± 5
6.5-7.0	22 ± 9 ± 4
7.0-8.0	4 ± 3 ± 1

Table 8.2 The ω invariant cross section measured using SLH triggered events.

P_T **Interval** (GeV/c)	$\pi^- + Be \rightarrow \omega + X$ (pb/(GeV/c)^2)
3.5-4.0	12500 ± 2400 ± 1070
4.0-4.33	5300 ± 880 ± 430
4.33-4.67	2830 ± 360 ± 90
4.67-5.0	850 ± 170 ± 60
5.0-5.5	370 ± 80 ± 18
5.5-6.0	116 ± 38 ± 15
6.0-6.5	62 ± 20 ± 5
6.5-7.0	16 ± 12 ± 2
7.0-8.0	9 ± 4 ± 1

Table 8.3 The ω invariant cross section measured using LGH triggered events.

uncorrected events selected by each trigger, presented in Tables 7.2 and 7.4 in the previous chapter. These two data sets differ in systematic effects related to the trigger corrections, and they also exhibit different background behavior (compare Figures 7.11 through 7.19 with Figures 7.20 through 7.28). The two measurements were combined in order to take advantage of the somewhat different statistical content of each data set and to minimize the systematic uncertainty related to the event selection (trigger) and due to the omega signal extraction. An average of the two cross section values was taken in each p_T interval [1]. The corresponding uncertainties were also averaged. However, the first point of the cross section ($3.5 < p_T < 4.0$ GeV/c) was treated differently. The SLH trigger acceptance for omega events in that p_T range is small, and substantially lower than the acceptance of the LGH trigger. The uncertainty in determining the Monte Carlo correction for events lost in the SLH trigger is the largest for this low p_T bin. A study of systematic effects (discussed in the next chapter) indicate an additional substantial uncertainty in the p_T range from 3.5 to 4.0 GeV/c for SLH trigger. It is believed therefore that events selected via the LGH trigger offer a better chance of correctly measuring the cross section in this p_T range, and the LGH answer is used as the measured value of the cross section for the p_T interval from 3.5 to 4.0 GeV/c.

[1] The two results can not be treated as independent measurements of the cross section due to the fact that many events are shared between the two samples.

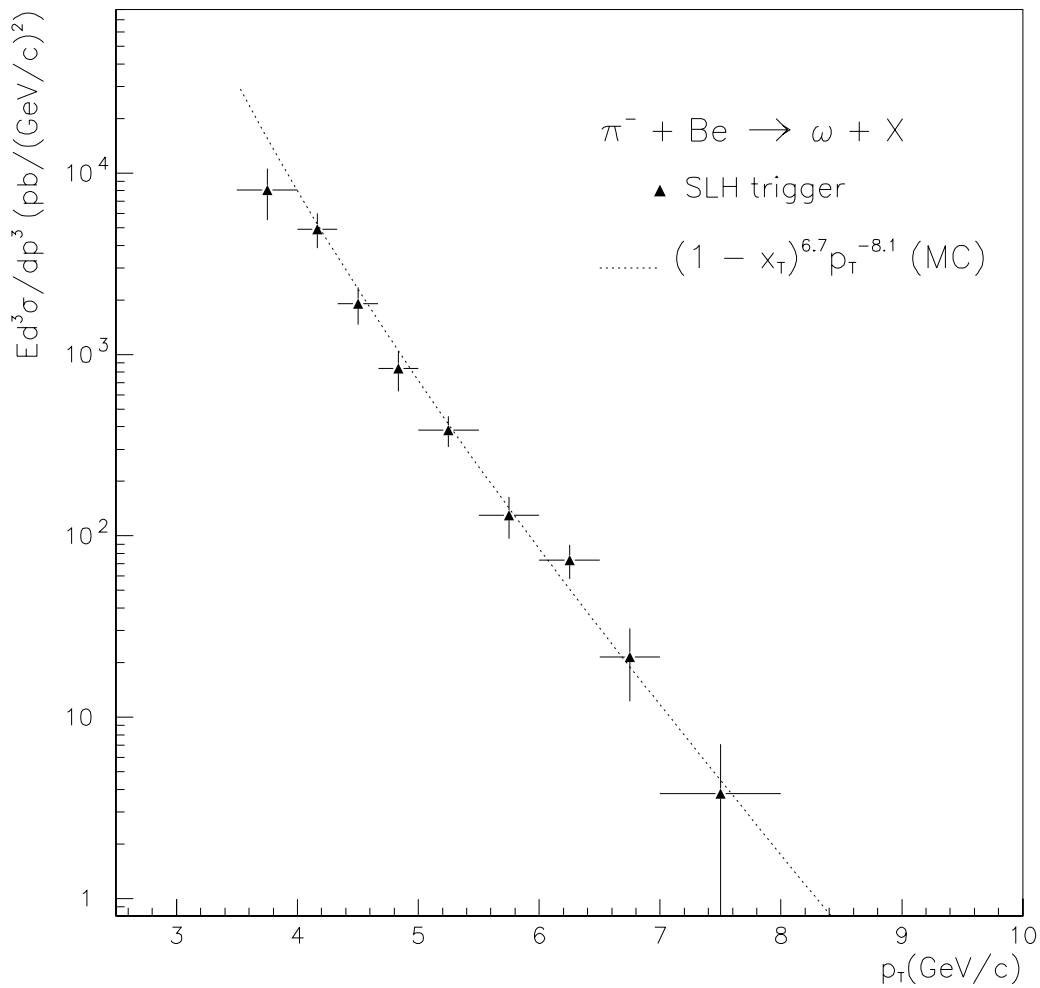

Figure 8.3 The p_T dependence of the ω cross section measured in events selected via SLH trigger (triangles) compared to the Monte Carlo prediction of this dependence (dotted line). The MC curve was scaled to match the value of the averaged SLH and LGH cross sections measured in the $4.0 < p_T < 4.33$ bin.

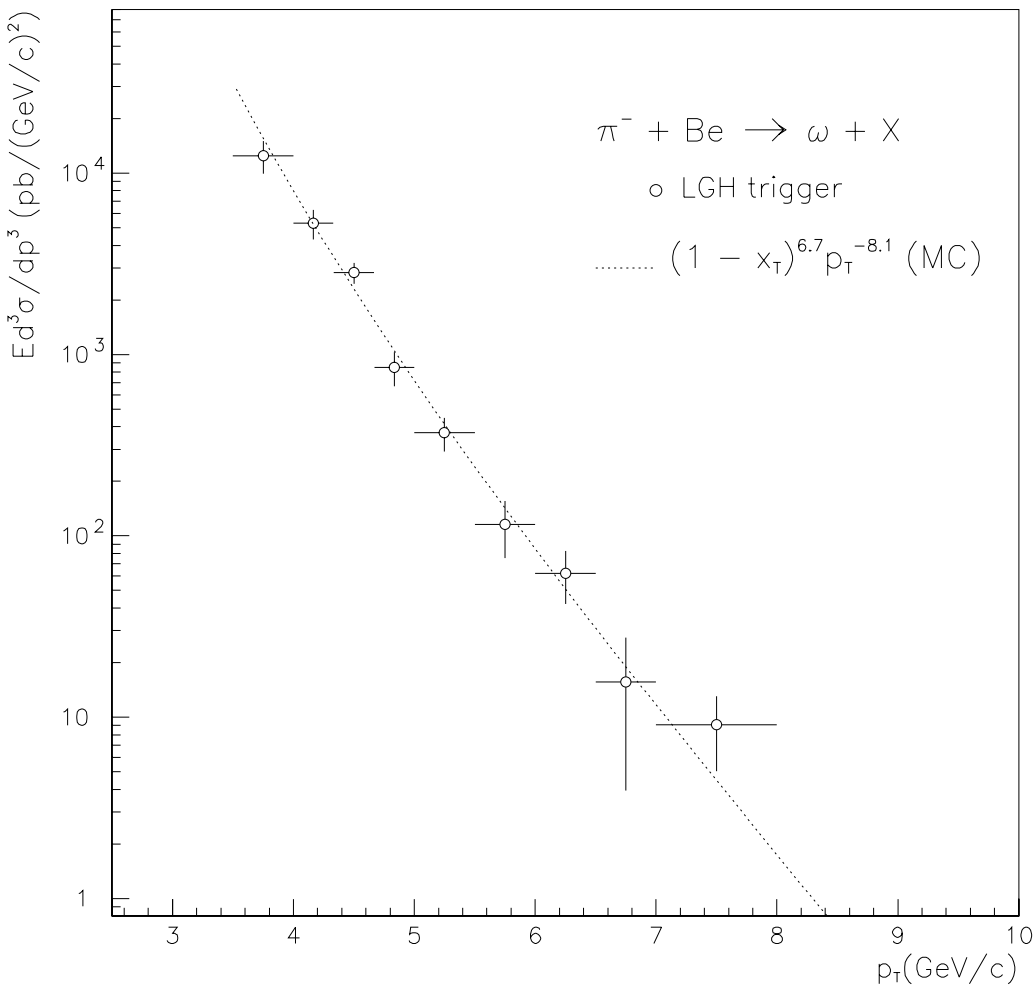

Figure 8.4 The p_T dependence of the ω cross section measured in events selected via LGH trigger (open circles) compared to the Monte Carlo prediction of this dependence (dotted line). The MC curve was scaled to match the value of the averaged SLH and LGH cross sections measured in the $4.0 < p_T < 4.33$ bin.

8.2 Integrated Omega Signal

The integrated invariant cross section for the production of omega mesons in 515 GeV/c π^- interactions on Be was measured over the span of our data. The data extend over the center of mass rapidity range from -0.5 to 0.75, with a transverse momentum coverage from 3.5 to 8.0 GeV/c.

The signal extraction was performed on the integrated histograms in a manner similar to that previously described in detail for the differential distributions. A third order polynomial and a Gaussian shape were fitted to the fully weighted $\pi^0\gamma$ mass spectrum. Some part of the background, estimated from the sidebands to the π^0 distribution, was subtracted from the $\pi^0\gamma$ mass spectrum prior to the fitting. Fit parameters were allowed to vary freely. The range of the fit was varied. Results of acceptable fits, including those performed on a set of histograms with mass bins 20% smaller than original histograms, were averaged. The signal was counted as a total number of weighted entries in the omega mass range after the background subtraction. The background was described by the third order polynomial resulting from the fit. The variation between the results of different fits (the RMS of the distribution) was taken as a measure of the uncertainty related to the background shape determination.

Figure 8.5 presents the $\omega \rightarrow \pi^0\gamma$ (weighted) signal from events selected via the SLH trigger, in the range $p_T > 4.0$ GeV/c. The width of the reconstructed omega signal is found to be 34 ± 5 MeV/c^2, and the mean mass is 776 ± 5 MeV/c^2. Similarly, Figure 8.6 illustrates the signal in the events selected via the LGH trigger. The mean mass is measured to be 787 ± 5 MeV/c^2, and the width of this signal is 40 ± 6 MeV/c^2. Both values for the mean mass are about one standard deviation from the PDG value of 782 MeV/c^2, and the widths of the signal are within the range expected based upon the detector resolution.

Table 8.4 lists the results of the measurement of the integrated cross section using events selected by the two different triggers, as well as the averaged result. The starting point of the integration over p_T was varied as indicated in the table. By the same argument as used in the first section of this chapter, the measurement of the cross section in the p_T range above 3.5 GeV/c using SLH trigger was excluded while taking the average. The errors quoted represent the statistical uncertainty related to the total number of events in the signal region (in the unsubtracted histogram as well as in π^0 sideband histogram, combined in quadrature). The second number gives the uncertainty related to the background shape determination.

Trigger Type	P_T **Interval** (GeV/c)	$\pi^- + Be \rightarrow \omega + X$ (nb/(GeV/c)^2)
	3.5 - 8.0	7.0 ± 1.1 ± 1.2
SLH	4.0 - 8.0	3.55 ± 0.35 ± 0.27
	5.0 - 8.0	0.40 ± 0.05 ± 0.01
	6.0 - 8.0	0.065 ± 0.016 ± 0.003
	3.5 - 8.0	1.3 ± 1.0 ± 1.1
LGH	4.0 - 8.0	4.10 ± 0.33 ± 0.2
	5.0 - 8.0	0.42 ± 0.05 ± 0.02
	6.0 - 8.0	0.063 ± 0.015 ± 0.005
	3.5 - 8.0	1.3 ± 1.0 ± 1.1
AVER	4.0 - 8.0	3.8 ± 0.34 ± 0.24
	5.0 - 8.0	0.41 ± 0.05 ± 0.015
	6.0 - 8.0	0.064 ± 0.015 ± 0.005

Table 8.4 The ω integrated invariant cross section.

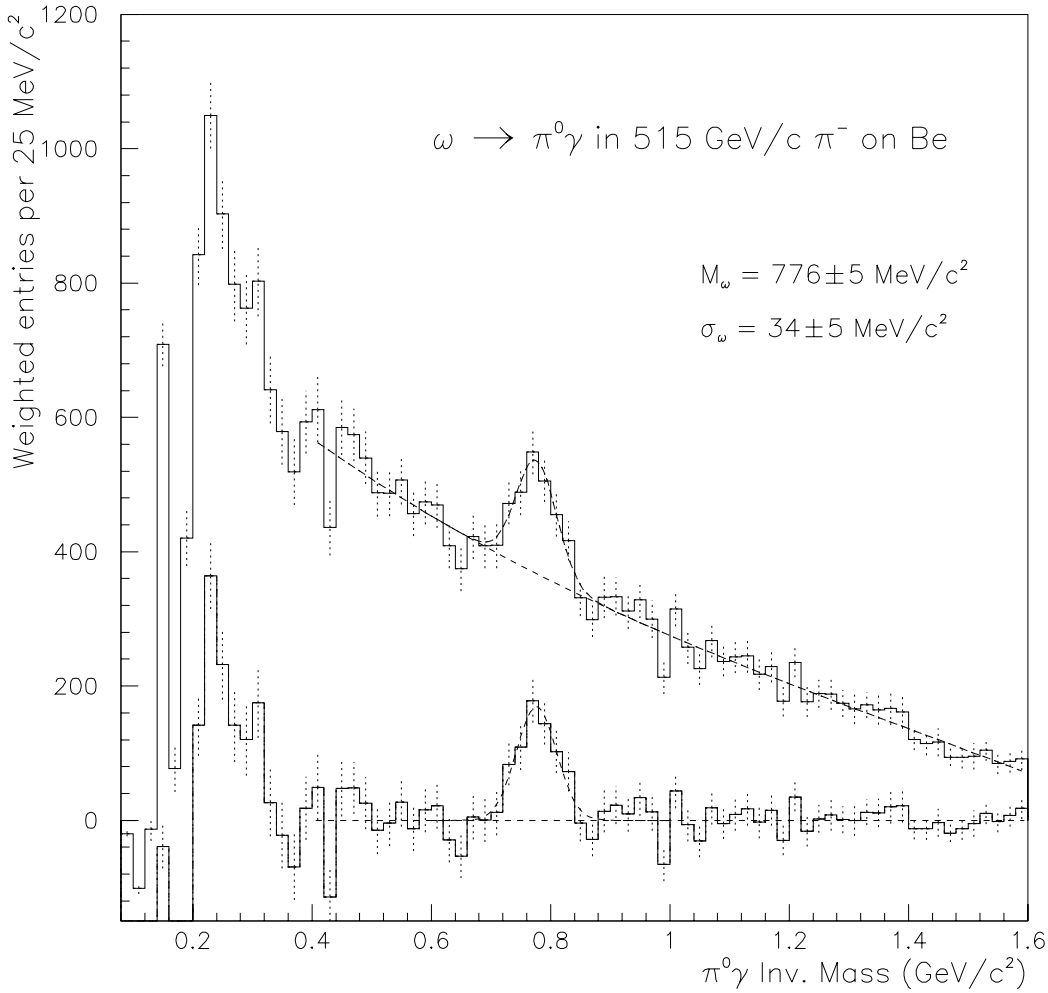

Figure 8.5 $\pi^0\gamma$ invariant mass distribution and the background subtracted signal. Entries to these histograms were fully weighted with all weights related to the cross section determination. $\pi^0\gamma$ $p_T > 4.0$ GeV/c. Events were selected via the SLH trigger.

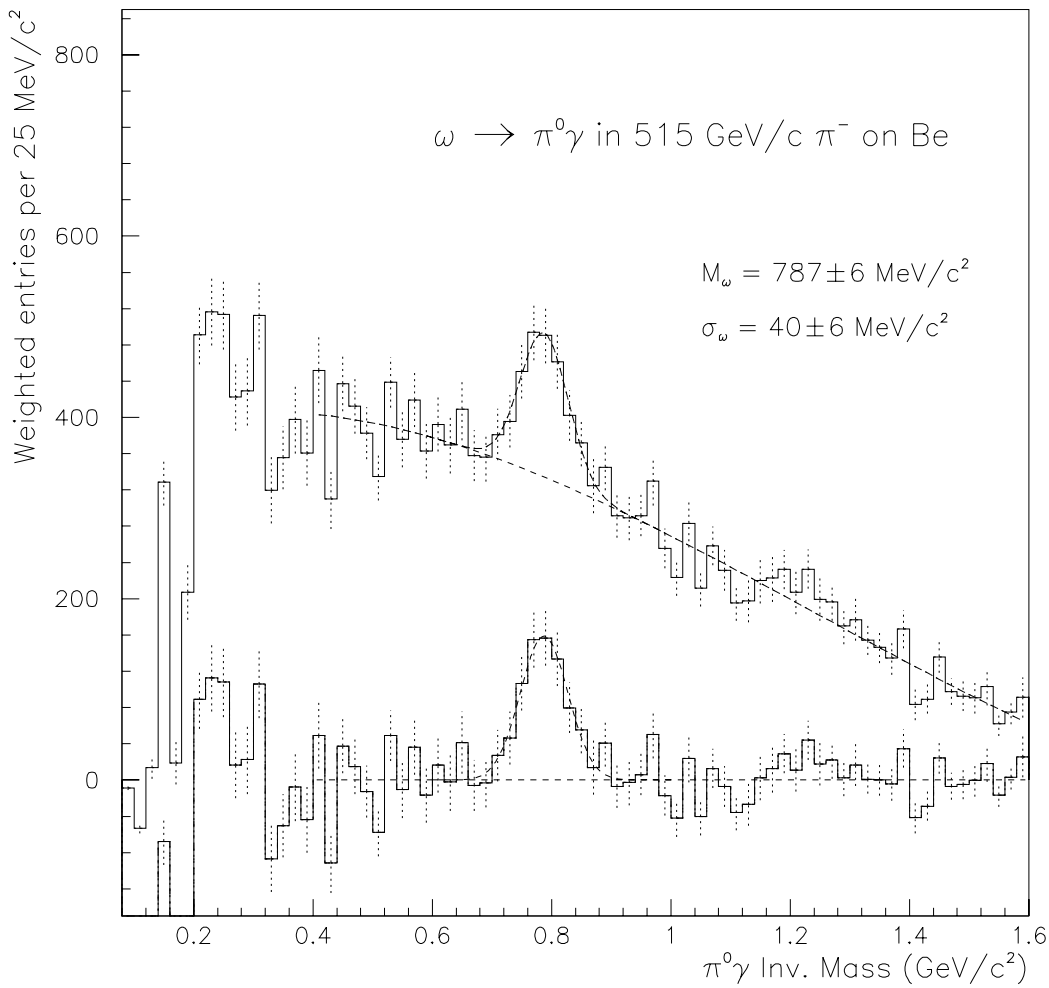

Figure 8.6 $\pi^0\gamma$ invariant mass distribution and the background subtracted signal. Entries to these histograms were fully weighted with all weights related to the cross section determination. $\pi^0\gamma$ $p_T > 4.0$ GeV/c. Events were selected via the LGH trigger.

8.3 ω/π^0 Ratio

The π^0 cross section used in calculating this ratio was determined from E706 data. The details of π^0 analysis can be found in [63][15]. Lower threshold triggers were used to determine the π^0 cross section in the p_T range up to about 4.5 GeV/c, which makes this determination less susceptible to uncertainty in the trigger corrections in comparison to ωs. The kinematic cuts on the π^0 rapidity and p_T were adjusted to those for the ω.

The ratio of ω to π^0 production for π^- beam on beryllium target is shown in Figure 8.7. Both SLH and LGH results were used for the ω. The average value of ω/π^0 was found using the results for the integrated cross section, as presented in Table 8.4, for the average of the SLH and LGH. The ω/π^0 ratio is $0.86 \pm 0.07 \pm 0.07$ for $p_T > 3.5$GeV/c, $1.0 \pm 0.09 \pm 0.06$ for $p_T > 4.0$ GeV/c and $1.24 \pm 0.14 \pm 0.04$ for $p_T > 5.0$ GeV/c.

Figure 8.8 presents a comparison of the ω/π^0 ratio in the data events and in the Monte Carlo. The HERWIG events were generated at a few values of the minimum outgoing parton p_T and the total number of both π^0s and ωs created in the fragmentation process was recorded versus p_T. The generated samples were combined using data at 0.5 GeV/c or more above the minimum parton p_T threshold to avoid any unphysical behavior that the presence of the threshold might introduce. The Monte Carlo ω/π^0 ratio was then fit with a simple function, as shown in Figure 8.8(a). This fitted result was then compared with the ω/π^0 ratio measured in the data (Figure 8.8(b)). An identical procedure was applied to compare the PYTHIA Monte Carlo with the data. This comparison is illustrated in Figure 8.9.

Sensitivity to the selection of a π^0 sideband range was investigated in a study of systematic uncertainties (see section 9.9). For a test, the ω/π^0

ratio was obtained using a new definition of π^0 sideband, as described in that section. Figure 8.10 presents this new result compared to HERWIG and PYTHIA predictions. Table 8.5 contains the measured values for ω/π^0 ratio using both π^0 sideband definitions.

In both cases the overall level of the ω/π^0 ratio in the data agrees with that in the Monte Carlo within the uncertainties of the measurement. The agreement with HERWIG is particularly good in the p_T range below 6 GeV/c, whereas in the case of PYTHIA all 6 data points fall slightly below the Monte Carlo prediction.

P_T **Interval** (GeV/c)	ω/π^0 **ratio** stand. π^0 sb.	ω/π^0 **ratio** new π^0 sb.
3.5-4.0	0.69 ± 0.13 ± 0.06	0.77 ± 0.15 ± 0.07
4.0-4.33	0.97 ± 0.18 ± 0.08	0.84 ± 0.18 ± 0.09
4.33-4.67	1.08 ± 0.17 ± 0.07	1.17 ± 0.17 ± 0.13
4.67-5.0	0.91 ± 0.19 ± 0.08	0.91 ± 0.19 ± 0.06
5.0-5.5	1.05 ± 0.21 ± 0.04	1.08 ± 0.20 ± 0.09
5.5-6.0	1.10 ± 0.3 ± 0.12	1.04 ± 0.3 ± 0.1
6.0-6.5	1.8 ± 0.5 ± 0.13	1.3 ± 0.5 ± 0.2
6.5-7.0	1.4 ± 0.7 ± 0.2	1.1 ± 0.7 ± 0.2
7.0-8.0	1.9 ± 1.3 ± 0.3	2.1 ± 1.3 ± 0.3

Table 8.5 ω/π^0 ratio versus p_T.

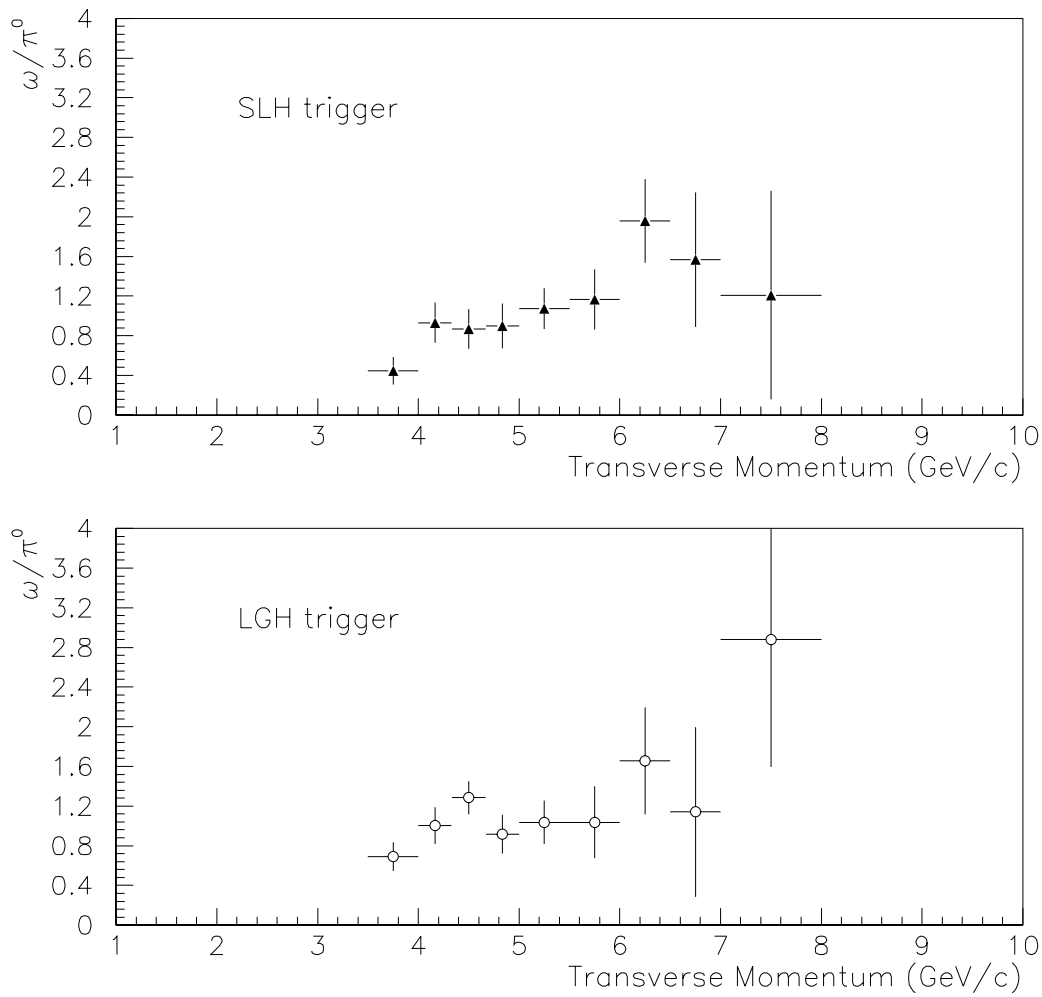

Figure 8.7 The ω/π^0 ratio versus p_T calculated from ω cross sections measured in events selected by SLH or LGH triggers.

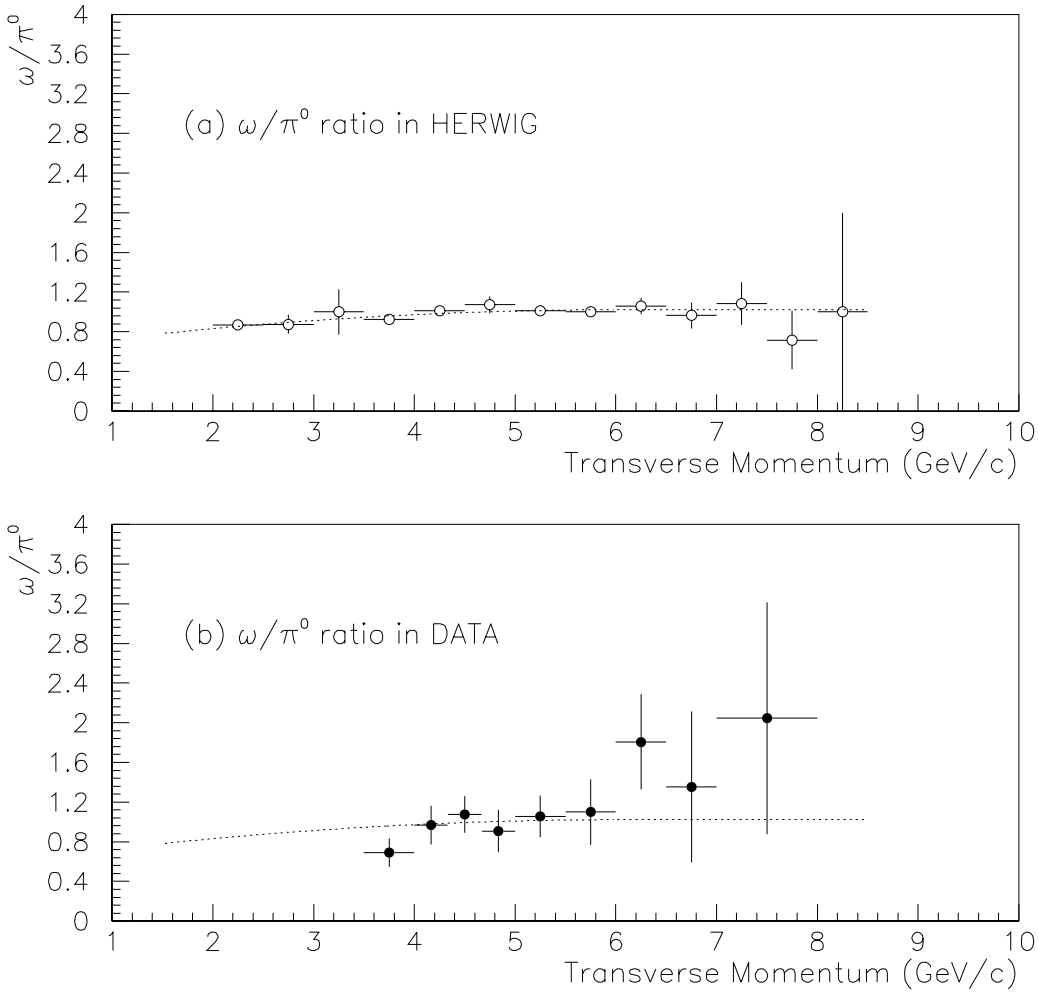

Figure 8.8 (a) The ω/π^0 ratio in HERWIG MC and the fit through the points. (b) The DATA result overlaid with the MC fit.

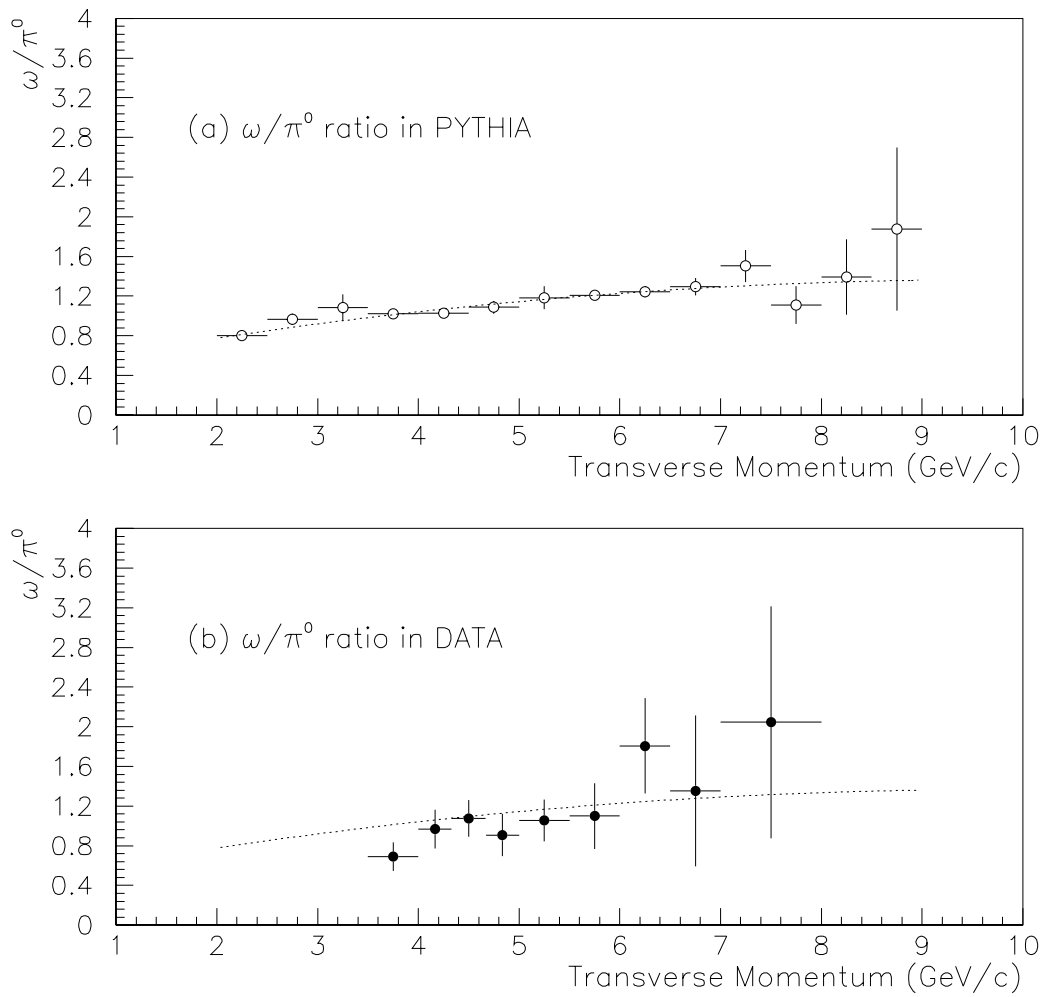

Figure 8.9 (a) The ω/π^0 ratio in the PYTHIA MC and the fit through the points. (b) The DATA result overlaid with the MC fit.

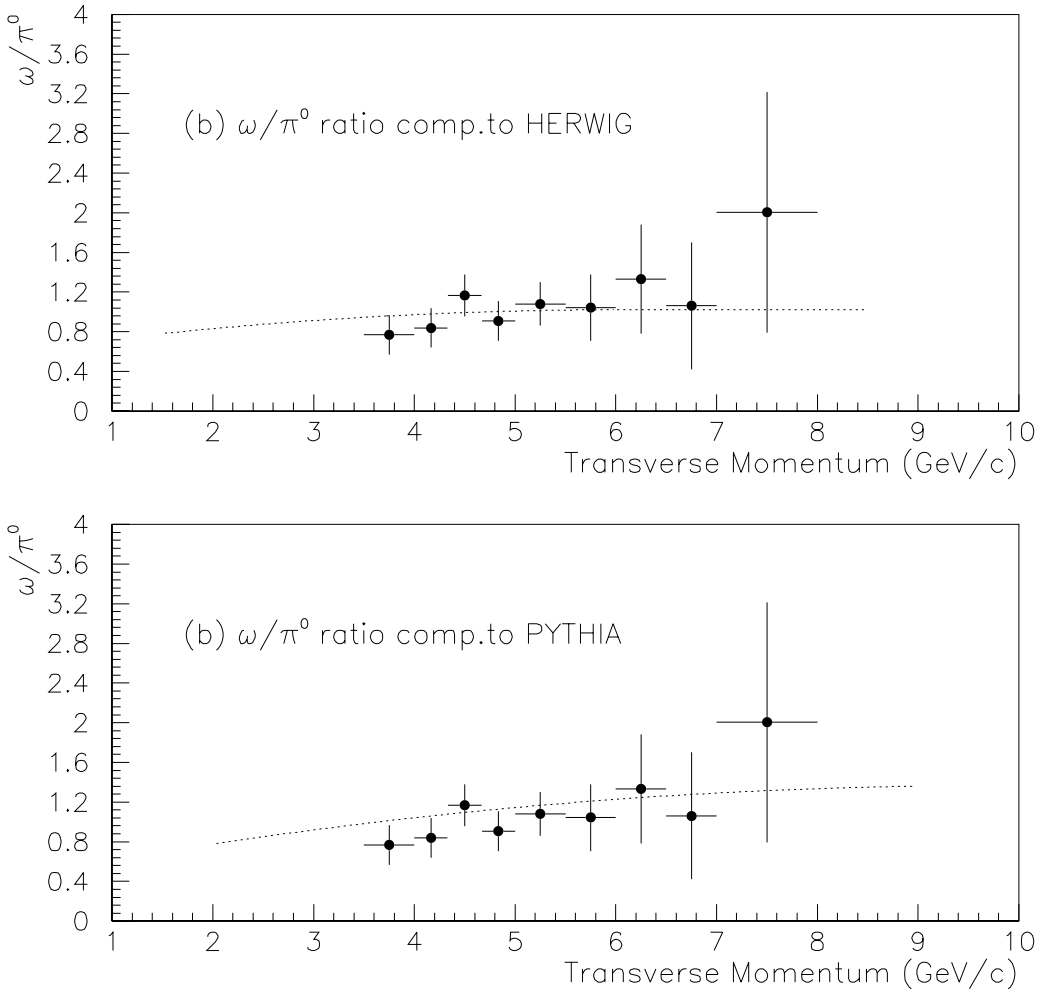

Figure 8.10 The ω/π^0 ratio versus p_T calculated with a different selection for π^0 sideband region (see section 9.9). (a) The DATA result compared to HERWIG MC prediction (curve). (b) The DATA result compared to PYTHIA MC prediction (curve).

8.4 Nuclear Dependence

The nuclear dependence of omega production was also measured. The dependence of the measured cross section (σ) on the type of target material was parametrized as $\sigma = \sigma_0 A^{\alpha_\omega}$, where A is the atomic mass of the target, and σ_0 and α_ω are free parameters. Two different target materials were used to extract the nuclear dependence. The ω signal was reconstructed, and the cross section measured, in events originating in Cu and in Be using the reconstruction procedures described in earlier chapters. The separation of vertices between Cu and Be was very good, as can be seen in Figure 7.3. The α_ω parameter was calculated according to

$$\alpha_\omega = 1 + \frac{ln(\sigma_{Cu}/\sigma_{Be})}{ln(A_{Cu}/A_{Be})}$$

where subscripts indicate that the measured cross section per nucleon (σ), or atomic mass (A), correspond to either Cu or Be.

The transverse momentum intervals selected for the measurement of α_ω were chosen to be relatively large, due to the statistical limitation of the sample of ω events reconstructed in Cu (the ratio of Cu events to Be events is about 10%). The measurement was also conducted using intervals integrated over the p_T range of interest – e.g., between 3.5 to 8.0 GeV/c, 4.0 to 8.0 GeV/c, etc. The resulting values for α_ω were found to fluctuate between 1.0 and 1.4 in a manner that did not show any consistency between the results of the two different triggers or the results from consecutive integrated p_T intervals. The presence of possibly large trigger weights applied to the statistically limited sample of events originating in Cu prevented a reliable extraction of the alpha exponent by this method.

Hence, a different approach was chosen for the extraction of α_ω. Assuming that the trigger corrections for ω events generated in Be are the same as for

the events generated in Cu, those corrections are expected to cancel in the ratio σ_{Cu}/σ_{Be}. The validity of this assumption was verified through a Monte Carlo study. It was already shown earlier that the geometrical acceptance correction did not depend on the z-location of the vertex of the event (see Figure 6.8). The p_T spectrum of the $\pi^0\gamma$ events originating in Cu and Be were also found to be consistent, and thus would result in the same reconstruction efficiency corrections for Cu and Be events. The only two corrections to the cross section that were found to be different between ω events from interactions in Cu and Be were the conversion correction and the beam absorption correction. These two corrections were applied to the two event samples, on event by event basis, while the other corrections were omitted since they should cancel in the ratio. Figure 8.11(a) presents the result of the measurement of the nuclear dependence for ω production by 515 GeV/c π^- beam. The error bars on the plot correspond to the statistical uncertainty and systematic uncertainty related to the background shape determination, combined in quadrature. Figure 8.11(b) illustrates α_ω extracted from the Be/Cu $\pi^0\gamma$ mass histograms integrated over four different p_T ranges. The points in the plot correspond to the measured mean p_T in each interval, while the span of the horizontal bar indicates the range of the p_T integration. The corresponding data are presented in Table 8.6. These data were obtained by taking an average of the α_ω exponents measured in events satisfying SLH and LGH triggers. To summarize, the nuclear dependence of the omega production can be characterized by $\alpha_\omega = 1.12 \pm 0.07 \pm 0.07$ over the transverse momentum range from 3.5 to 8.0 GeV/c.

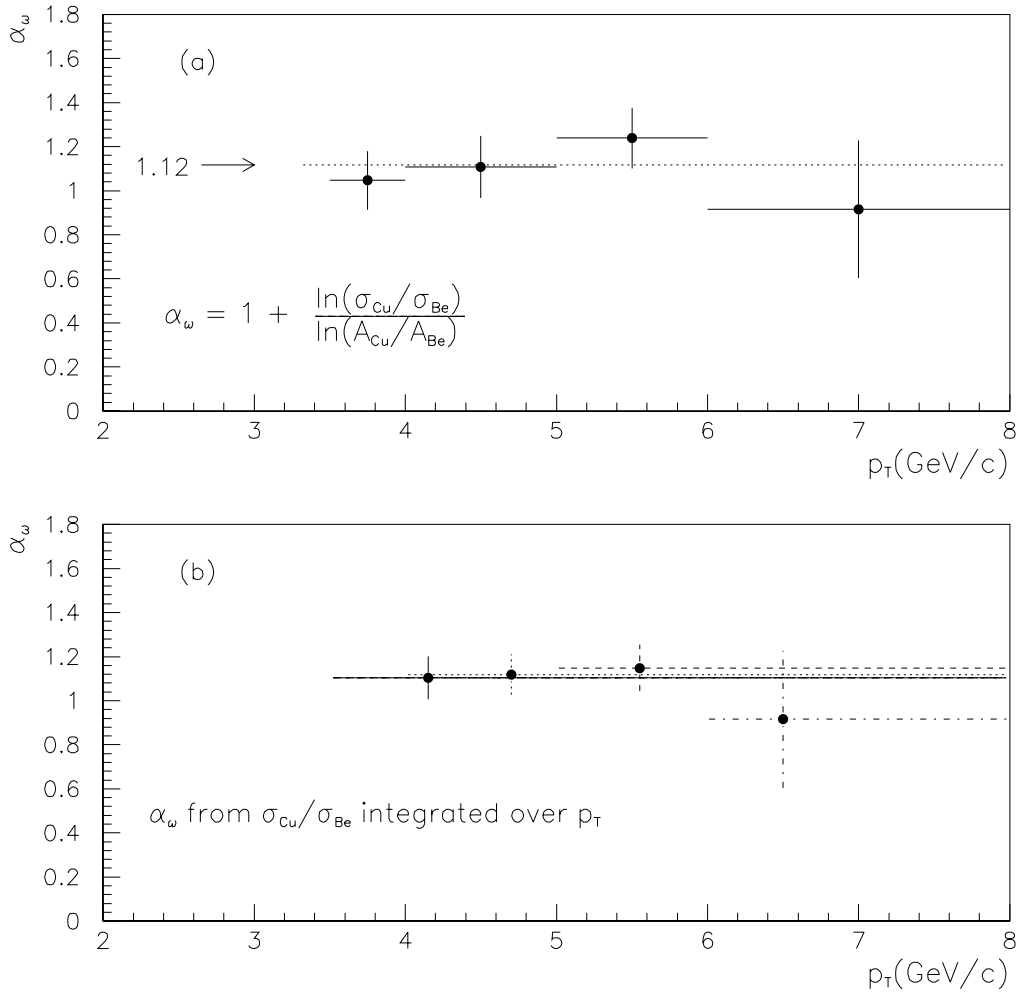

Figure 8.11 (a) The p_T dependence of α_ω. (b) The α_ω measured over integrated p_T ranges, as indicated by the span of the horizontal bar at each point. Errors are both statistical and systematic, related to the fit of the background shape, combined in quadrature.

The comparison of the values for α_ω obtained in data samples selected by either SLH or LGH trigger is presented in Figure 8.12. The dotted lines in the plots come from linear fits to the points. Finally, the nuclear dependence for ω production is compared to that for π^0 production measured in E706 in Figure 8.13. The π^0 and η mesons produced at high p_T show enhancement of the cross section with increasing atomic mass A ($\alpha_{\pi^0} = 1.110 \pm 0.003 \pm 0.019$ for π^0 production in the p_T range from 4.0 to 8.5 GeV/c, and $\alpha_\eta = 1.14 \pm 0.02 \pm 0.02$ for production in the p_T range from 3.5 to 7.0 GeV/c[55]). The dependence of ω meson production on nuclear matter is consistent with that for π^0s and ηs. The nuclear dependence of neutral meson production agrees with the previous measurements made for high p_T charged particle production[68]. The enhancement ($\alpha > 1.0$) may be interpreted as evidence of rescattering of the outgoing partons (which fragment into π^0, η or ω mesons) in nuclear matter. This conclusion can be reached in the light of the measurement of the nuclear dependence for the direct photon production at large p_T. That $\alpha_\gamma = 1.02 \pm 0.02 \pm 0.03$ suggests that the rescattering of the incident partons in the high p_T collisions is not very important[2].

8.5 Contribution of ω Decays to $\gamma\gamma$ Mass Spectrum

The measured yield of omega mesons decaying to $\omega \rightarrow \pi^0\gamma$ was used in assessing the potential contribution of ω particles to the high p_T $\gamma\gamma$ mass spectrum. While studying high p_T η production[16], a small enhancement of $\gamma\gamma$ combinations with invariant masses below 0.8 GeV/c^2 was observed in the data in the vicinity of the η mass (0.547 GeV/c^2), as illustrated in Figure 8.14. A background subtracted $\gamma\gamma$ distribution which highlights this feature is shown in Figure 8.14(b). The background was defined via a linear fit excluding the mass region from 0.45 to 0.8 GeV/c^2.

[2] A similar result, regarding the incident parton rescattering, comes also from measurements of nuclear dependence in Drell-Yan processes.

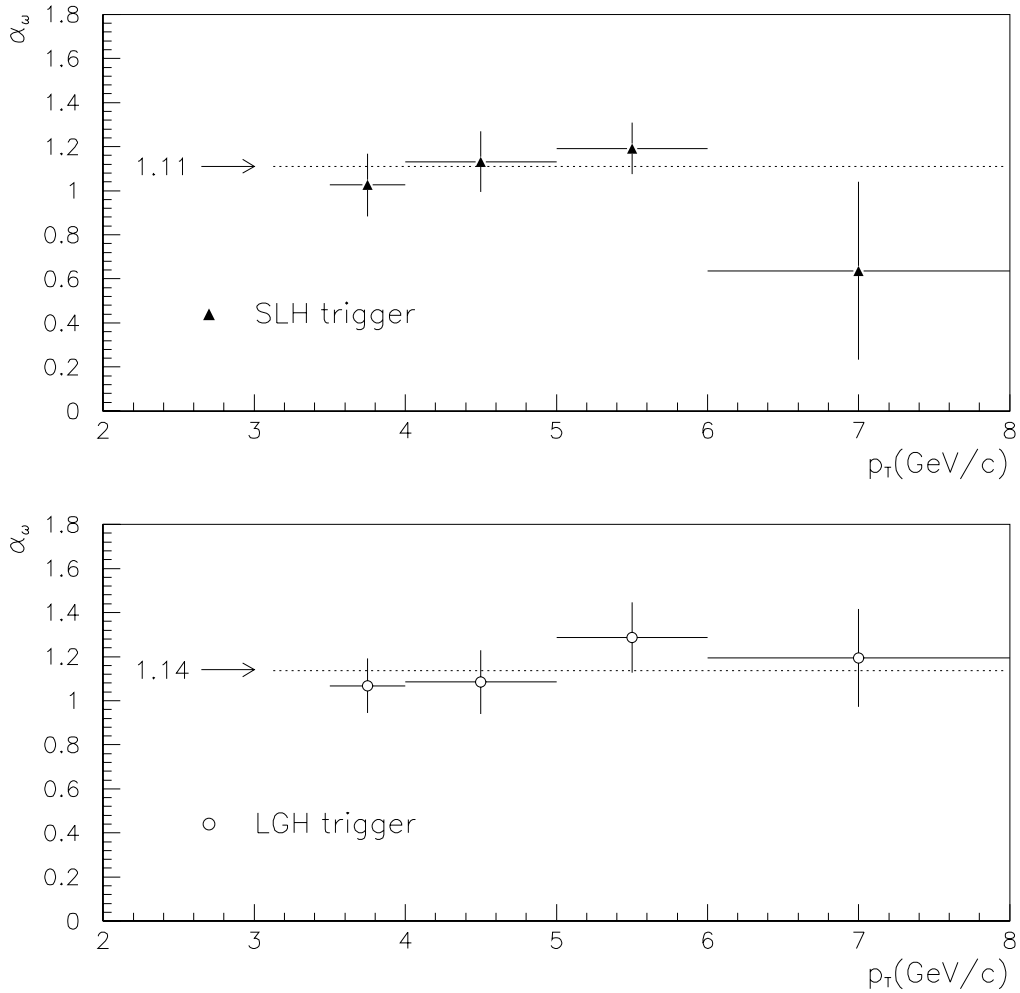

Figure 8.12 Comparison of α_ω measured in events satisfying SLH and LGH triggers. Linear fits to the data points are also shown.

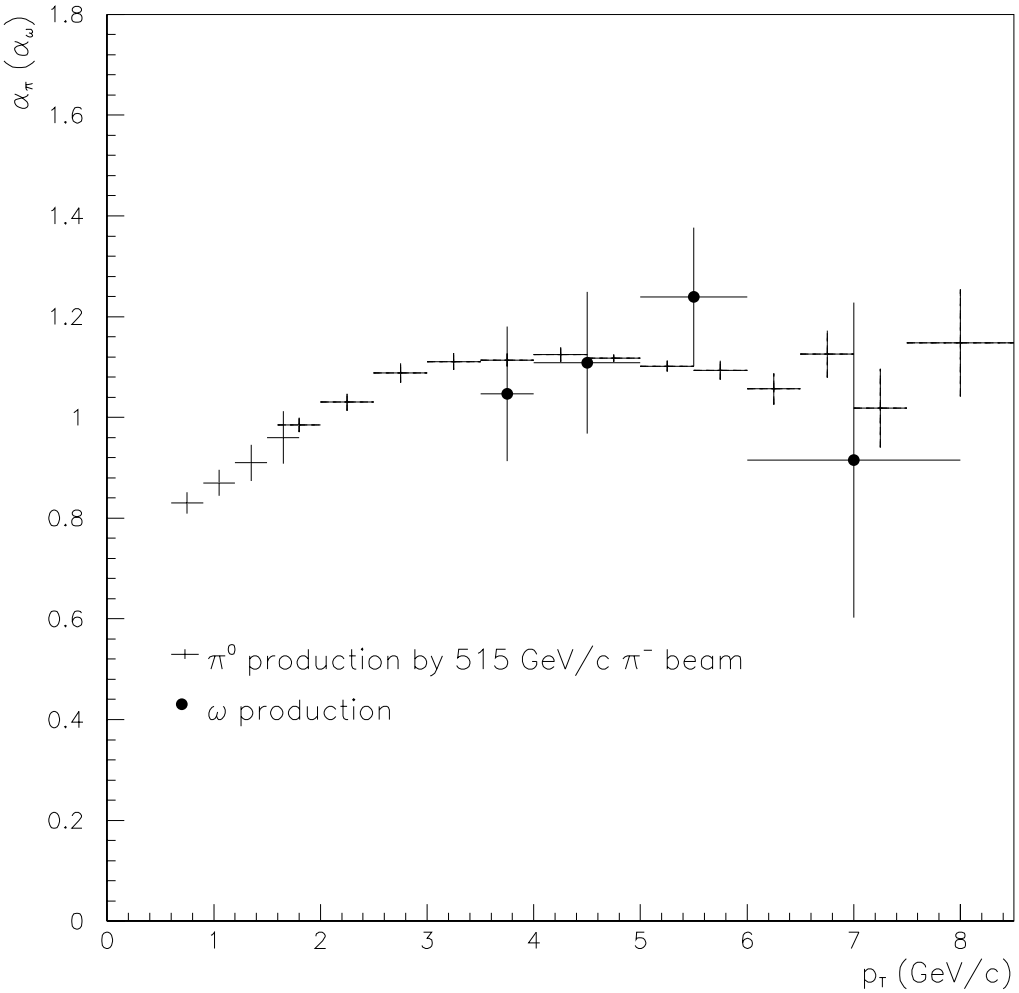

Figure 8.13 Nuclear dependence of π^0 and ω production by 515 GeV/c beam.

P_T **(GeV/c)**	α_ω
3.5 - 4.0	1.30 ± 0.14 ± 0.15
4.0 - 5.0	1.11 ± 0.09 ± 0.07
5.0 - 6.0	1.24 ± 0.11 ± 0.08
6.0 - 8.0	0.92 ± 0.27 ± 0.14
3.5 - 8.0	1.10 ± 0.07 ± 0.07
4.0 - 8.0	1.12 ± 0.07 ± 0.06
5.0 - 8.0	1.15 ± 0.09 ± 0.05
6.0 - 8.0	0.92 ± 0.27 ± 0.14

Table 8.6 The α_ω exponent of the nuclear dependence for the ω production.

We used the dedicated omega Monte Carlo events to study the distribution of $\gamma\gamma$ pairs in the events with high p_T omegas. This study employed the same selection criteria used in the η analysis resulting in the mass plots shown in Figure 8.14. In particular, the $\gamma\gamma$ pairs were restricted to the rapidity interval -0.75 to 0.75, had $p_T > 4.0$ GeV/c, and had energy asymmetry less than 0.75. At the same time, we kept track of the number of generated ωs in the rapidity interval -0.5 to 0.75 and with $p_T > 4.0$ GeV/c among these events. This allowed us to normalize the Monte Carlo prediction to the measured ω yield in the data. The resulting contribution to the two photon invariant mass distribution from photon combinations associated with $\omega \rightarrow \pi^0\gamma$ decays is presented in Figure 8.15. We compare this scaled Monte Carlo prediction with the data from Figure 8.14(b). The agreement between the size of enhancement observed in the data and our scaled Monte Carlo prediction is remarkable and remains very good for $\gamma\gamma$ pairs in other high p_T intervals as well, within the statistical and systematic uncertainty associated with this prediction. This uncertainty was estimated to be 20%, based on the relevant systematic uncertainties in the measurement of the ω spectrum

and on the statistical uncertainty in the ω signal. This study indicates that the excess $\gamma\gamma$ combinations in the vicinity of the η mass can be attributed to ω meson production thus reducing our uncertainly in the background determination for the η meson measurement.

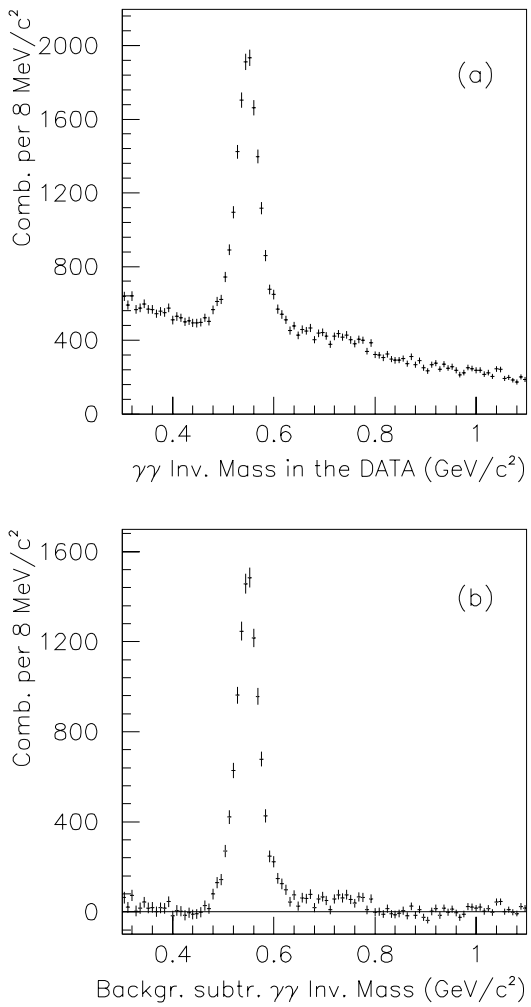

Figure 8.14 (a) Two photon invariant mass reconstructed in the data using η analysis cuts in the events selected via SLH trigger. The p_T interval for $\gamma\gamma$ pairs is 4.0 to 4.5 GeV/c. (b) A background subtracted $\gamma\gamma$ mass distribution. The background was fit with the straight line outside of the region from 0.45 to 0.8 GeV/c^2 in mass.

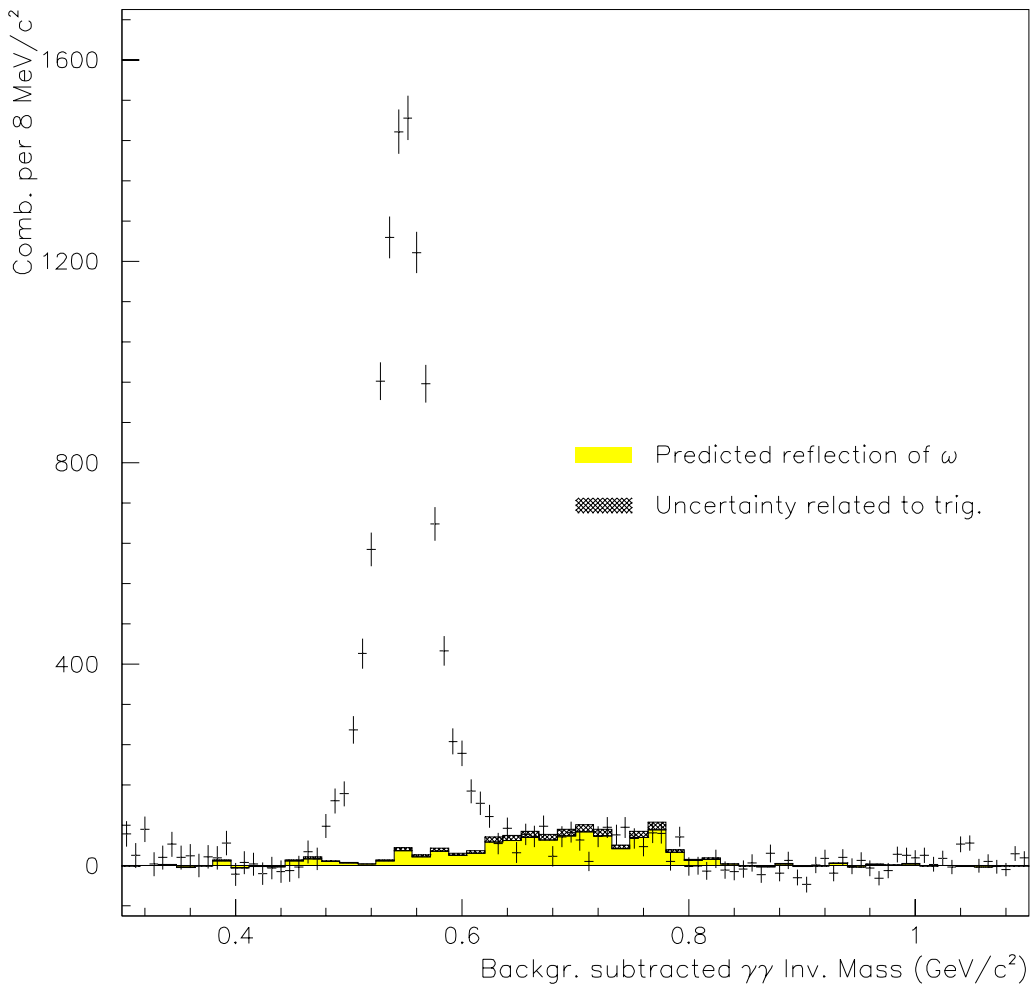

Figure 8.15 The background subtracted $\gamma\gamma$ distribution from Figure 8.14(b) (points) overlaid with the expected $\gamma\gamma$ contribution from $\omega \to \pi^0\gamma$ (solid histogram). Number of MC ωs that contributed to this reflection was normalized to the measured spectrum for the ω meson, $\omega \to \pi^0\gamma$, in the data. The $\gamma\gamma$ pairs from MC and from the data have p_T from 4.0 to 4.5 GeV/c. The uncertainty in the prediction related to trigger effects was 10% compared to the total uncertainty of 20%.

Chapter 9 Study of Systematic Uncertainties

A study of the systematic uncertainties in the measurement of omega production is summarized in this chapter. The study covers several issues specific to the ω analysis presented in this thesis – e.g., the assumption about the linearity of the background under the π^0 peak which was used in the π^0 sideband subtraction, or the assumption about a lack of polarization in the ω sample. Other, more general, contributions to the systematic uncertainty of the measurement are also discussed.

9.1 Trigger Uncertainty

The two trigger types studied in this analysis have different characteristics. The SLH trigger was sensitive to a local deposition of transverse energy, while the LGH trigger responded to the transverse energy deposited and summed over the whole octant. A comparison of the results obtained using samples of data selected by each trigger gives a valuable measure of the possible systematic uncertainty remaining in the data, even after the corrections for trigger effects were applied.

One of the large corrections related to the trigger were the rapidity hole cut and correction. The necessity for the cuts was illustrated in Figure 7.6 in the Analysis chapter. In this section, Figure 9.1 compares the cross section obtained in the samples of SLH and LGH triggered events, where no rapidity hole cuts or corrections were implemented. The reconstruction efficiencies applied to data in this study were also measured without the rapidity hole rejection. Clearly, the results based on the two triggers differ substantially, and we would need to assign a large systematic error to the measurement of the cross section to account for the observed difference. The rejection of "suspect" regions in rapidity and p_T was based on a comparison of π^0 rapidity distributions between all octants of

the LAC, as discussed in section 7.3.2. The decisions to retain or reject a given region were made completely independently for each trigger, and were aimed at achieving an internal consistency between the results from different octants. The resulting cross sections, that is the cross sections with the rapidity hole corrections, were presented in Figure 8.2 and Tables 8.2 and 8.3. The measurements from different trigger samples agree quite well after the cuts, which indicates that the problematic regions in rapidity and p_T were removed successfully.

Based on the corrected numbers, we can estimate the remaining uncertainty related to the trigger effects that are not common between the SLH and LGH. For $p_T > 4.0$ GeV/c, Table 8.4 indicates that there is a difference of 0.55 nb/(GeV/c)^2 (on a cross section of 3.83 nb/(GeV/c)^2) between the integrated cross section measured in the sample of events selected by SLH trigger and that selected by LGH trigger. From that we can conclude that the observed difference amounts to a 7% systematic uncertainty in the measurement. The data from Table 8.4 shows that some difference between the results from these two triggers persists in the higher p_T range. However, that difference falls within an uncertainty related to the signal extraction quoted with each measurement. The statistical contents differ between the two samples of events by at least 40% at lower p_Ts and by at least 26% at high p_T. The resulting background shapes between the two samples of events are not the same (compare, for example, Figures 7.17 and 7.26); hence we may expect that the errors quoted in Table 8.4 are at least partially uncorrelated between the two samples. From that, the uncertainty steming from trigger effects at high p_T is estimated to be 2%.

A similar study has been conducted using cross section results obtained with a different π^0 sideband definition (described in section 9.4). From that study, we estimated the systematic error needed to accommodate the observed difference

between two trigger types to be 17% for the 3.5 to 4.0 GeV/c bin, 10% for the 4 to 5 GeV/c bin and zero at higher p_Ts. The higher of the two estimates at a given p_T (each determined with a different π^0 sideband) was taken as a measure of the systematic uncertainty. That choice allows us to account for trigger effects as well as for some of the uncertainty due to the π^0 sideband subtraction.

Another test performed on the data, in an attempt to uncover any systematic effects related to the trigger, was a test with a different cutoff for the trigger weights. In this analysis the trigger weights were allowed to be as high as 10 while the remaining tail of the distribution of weights was cut out. Monte Carlo simulation was used to account for omega events with triggering probability of less than 0.1. In the test, the cutoff for the trigger weights was changed to 5.0 and new Monte Carlo reconstruction efficiencies were calculated to account for the remaining events. Figure 9.2 compares the cross section results obtained with these two cutoffs. There is a very little difference between the two methods, except in the first p_T bin for the SLH selected events. The ratio of the cross sections is 1.25 in that bin. The result from this bin using the SLH trigger was excluded from the original cross section measurement (see section 8.1). This study confirms that the result from the first p_T bin in SLH selected events carries a much larger systematic error than the other points.

9.2 Rapidity Dependence of the Reconstruction Efficiency

The data sample studied in this analysis was integrated over the range of center of mass rapidity from -0.5 to 0.75. The detector coverage was larger and extended from about -0.9 to 0.9 in that variable. To avoid regions of rapidly changing acceptance and poor reconstruction efficiency, the rapidity range of the inclusive π^0 measurement was restricted to -0.75 to 0.75. The backward rapidity region -0.75 to -0.5 was found to exhibit a trigger inefficiency for π^0s with p_T

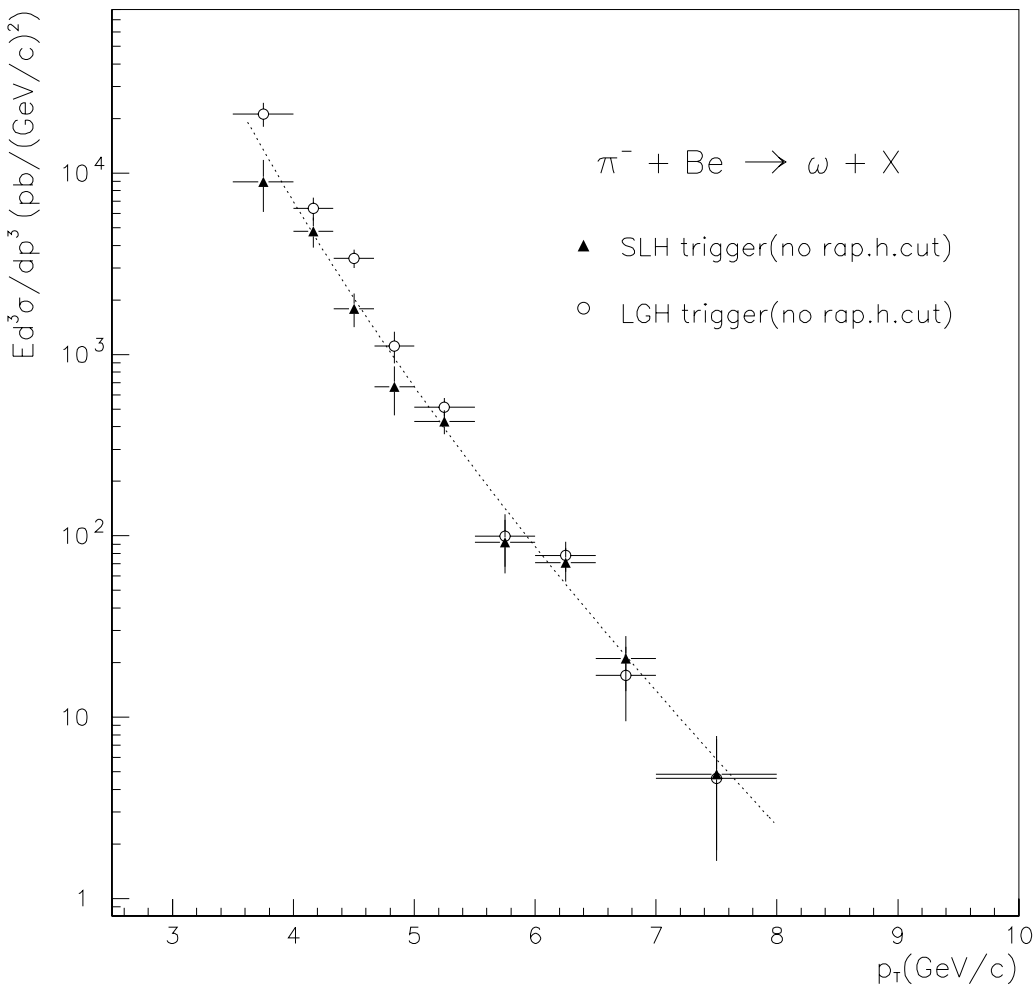

Figure 9.1 Differential cross section per nucleon for the omega production by 515 GeV/c pions on Be target, measured in events selected via SLH trigger (triangles) and LGH trigger (open circles). No rapidity hole rejection was applied.

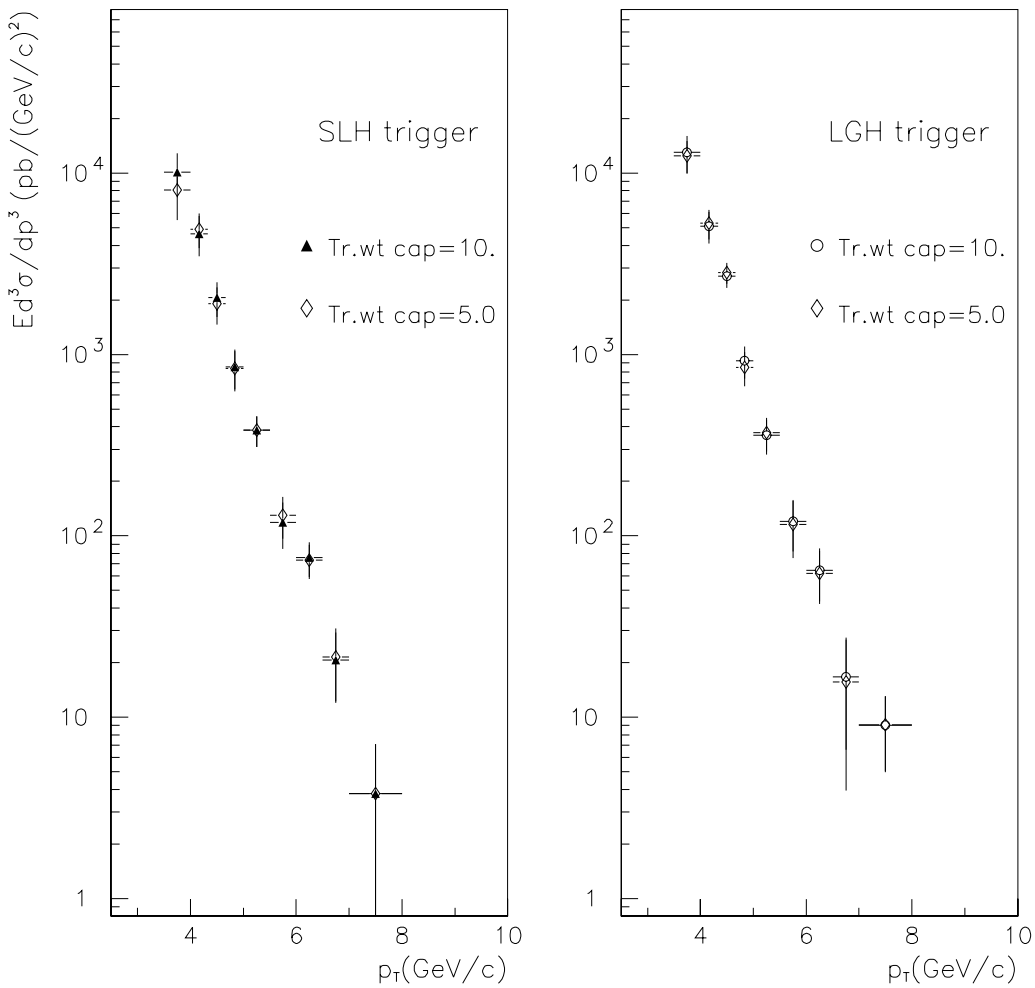

Figure 9.2 Comparison of the cross sections obtained with the trigger weight cutoff at 10 and 5, for events selected with SLH and LGH triggers.

below 4.2 GeV/c in the high threshold triggers and was therefore excluded from the ω analysis.

Figure 9.3 illustrates the rapidity dependence of three correction functions measured for the omega events. The geometrical acceptance for the ωs, the reconstruction efficiency, and the two functions combined are represented. The Monte Carlo ω events with p_T from 4 to 5 GeV/c and from 6 to 8 GeV/c were used to produce these sets of plots. We can observe that both the geometrical acceptance and the reconstruction efficiency for the omega depend quite strongly on rapidity. However, the dependence is diminished for the combined function. Based on the last column of plots in Figure 9.3, we can estimate a possible systematic uncertainty introduced to the measurement due to averaging of reconstruction efficiency and of geometrical acceptance over rapidity. A systematic offset could have been introduced due to the fact that our data and the Monte Carlo sample do not have exactly the same rapidity distribution (compare Figure 6.5). Based on Figure 6.5, we estimated a mean discrepancy between MC and data of 17% at p_T from 4 to 5 GeV/c (about 8% of the total number of events events exhibit a 100% discrepancy at the backward rapidities, about 18% of events are in the region where the discrepancy is 30%, etc.). The rapidity distributions are in a much better agreement between MC and data at high p_Ts. The variation in the combined reconstruction efficiency and geometrical acceptance function is about 20%, as visible in Figure 9.3(c). From that we calculated a systematic uncertainty from the inaccuracy of the Monte Carlo simulation of the data to be 3.5% at 4 GeV/c, diminishing to an insignificant number at the high p_T end of the spectrum. A similar result was arrived at for LGH triggered events.

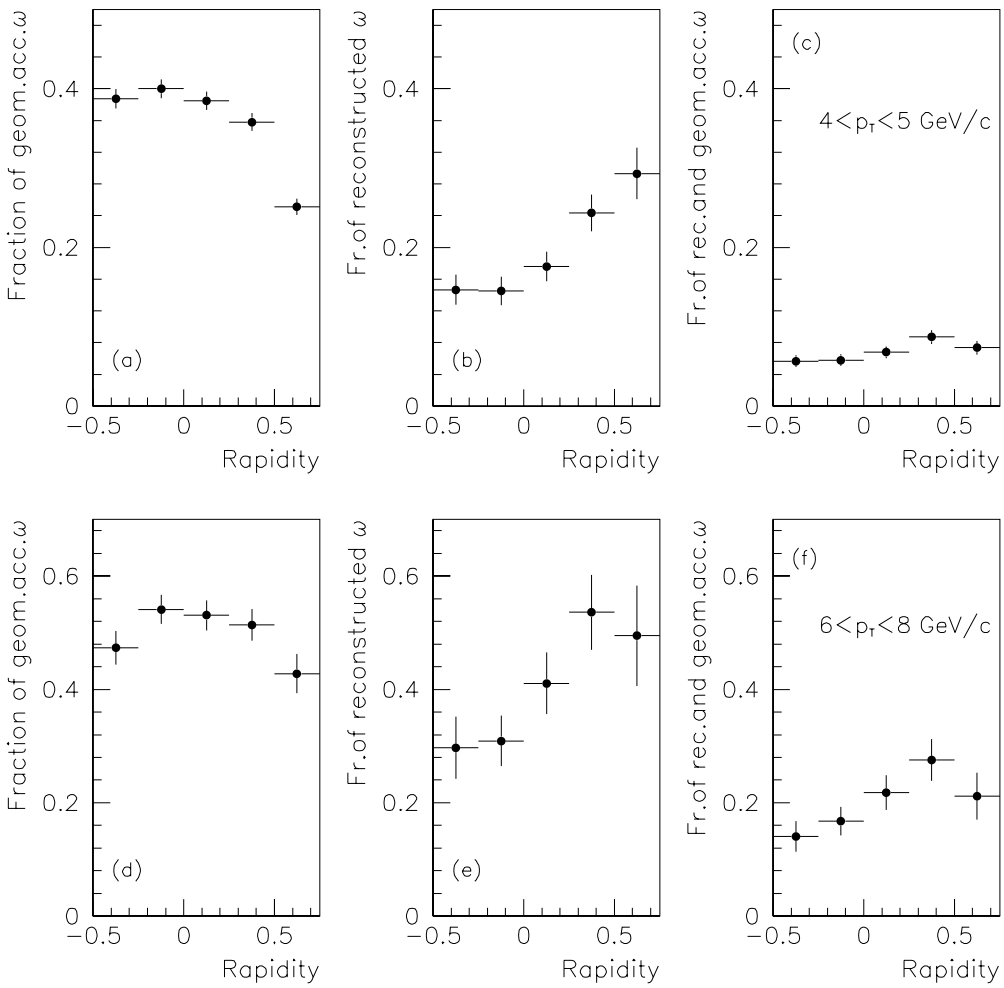

Figure 9.3 Rapidity dependence of the geometrical acceptance (a),(d), reconstruction efficiency (b),(e), and combined geometrical acceptance and reconstruction efficiency function for the ω. The probability to satisfy a SLH trigger was required to be greater than 0.1 in the measurement of reconstruction efficiency. Events from p_T range 4 to 5 GeV/c (a),(b),(c) and from 6 to 8 GeV/c (d),(e),(f) were used.

9.3 $cos\theta^\star$ Uncertainty

One of the main assumptions in this analysis was that the omegas were produced unpolarized, and therefore the spectrum of radiated photons γ (in $\omega \rightarrow \pi^0\gamma$), which carried away the spin of the ω, was uniform. A polarization in the ω sample – e.g., along the z axis – would manifest itself as a $1 + cos^2\theta^\star$ dependence of the spectrum on azimuthal and polar angles in the center of mass of the decaying particle. This type of dependence could very closely resemble the behavior of the background (compare Figure 5.4), and also the effect of the trigger selection mechanism on the omega sample. It is therefore difficult to rule out the polarization in a simple fashion.

To address the question of possible polarization, the following comparison was made: Two samples of ω events, one reconstructed within an interval $|cos\theta^\star| < 0.3$ and the other in the interval $0.3 < |cos\theta^\star| < 0.6$, were compared. All corrections, including the reconstruction efficiency correction calculated from Monte Carlo for each $|cos\theta^\star|$ interval separately, were applied to the data. The two cross section results obtained agreed within statistical uncertainties. This indicates that there was no significant enhancement of the signal towards larger $cos\theta^\star$ values. Hence we concluded that no polarization was observed in the ω sample, and that our assumption about the lack thereof was justified.[1]

The correction for omegas outside of $|cos\theta^\star| < 0.6$ does not carry a systematic error associated with that cut (unpolarized ωs have a flat $cos\theta^\star$ distribution).

[1] A similar assumption was used by other groups – e.g., in the analysis of ρ^0 meson production in e^+e^- annihilation at $\sqrt{s}$=29 GeV[21].

9.4 Background Subtraction

The method of the background subtraction was extensively discussed in earlier sections, mainly in 7.5.3. The uncertainties and systematic errors that arise in fitting the mass distributions were studied by choosing different mass ranges for the fit, varying the binning of the mass distribution, and selecting different fit methods (bound and unbound fit parameters). The resulting fit results were averaged to minimize the overall uncertainty. The RMS value of the distributions of the various fit results was in each case assigned as the uncertainty in the background shape determination.

Among other fitting procedures that were also tried was a method of "zeroing" the signal region and fitting the background alone, in the area outside of the "zeroed" mass range. Another method investigated was the use of different functional forms for the background representation like exponential functions and polynomials of order different than 3. These were found not to contribute additional information compared to the method selected originally.

Some part of the background was subtracted from the $\pi^0\gamma$ mass distribution through the π^0 sideband subtraction. The subtraction was studied to verify that the result did not depend strongly on the selection of the sideband region or on the determination of scale factors $N_{\pi^0 mr}/N_{\pi^0 sb}$ (see section 5.5). Figure 9.4 illustrates the difference in the cross section for SLH and LGH selected events when a new π^0 mass range as well as different π^0 sideband were defined in the analysis. The new π^0 region was 10 MeV/c^2 smaller than the original, and the sidebands were moved closer to the peak region by 10 MeV/c^2 each. The ratios of the original and the new cross section results were fit with a straight line. We observed that the new cross section was 4% systematically lower than the original cross section for SLH selected events (only the points with $p_T > 4$ GeV/c were used in the fit). The same

fit showed a 2% shift in the opposite direction for events selected via LGH trigger. The ratio for the averaged cross section, fitted with the straight line, did not show a significant offset. However, two points in 6 to 7 GeV/c p_T bin were shifted by 30%. From that we concluded that the selection of a π^0 sideband may introduce some systematic error in the measurement in some of the p_T bins. Statistical content between the original and the new π^0 sideband mass histograms was very similar, hence a fluctuation on the order of the size of statistical uncertainty (26% and 50% respectively) was not expected. A systematic uncertainty of 10% was assigned to the measurement of the cross sections at the $p_T > 6$ GeV/c as a result of these findings.

9.5 Other Systematic Uncertainties

The additional main systematic uncertainties in the cross section measurement arise from the following sources:

- Energy Scale Determination

The energy scale for the liquid argon calorimeter was set using the samples of ηs and moderate p_T π^0s, which were corrected for the dependence of the reconstructed mean mass versus time, detector radius, particle energy as well as the detector octant, as described in section 4.2.4. It was determined that the resulting energy scale had an uncertainty of 0.5%[15]. That contributes to a 5% systematic uncertainty in the cross section at p_T of 4 GeV/c and 6% at 7 GeV/c. The Monte Carlo energy scale was set using a similar procedure. The associated errors were determined to be of the same size (0.5%[69]).

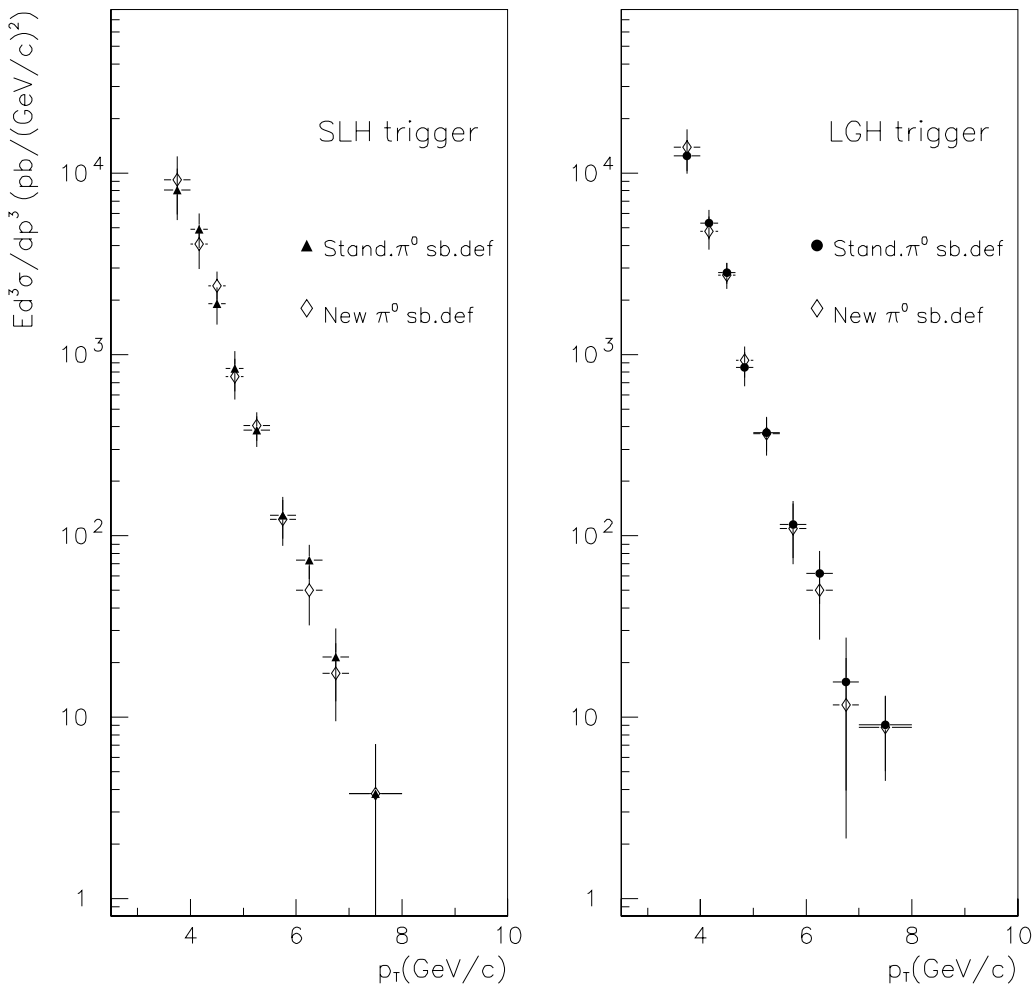

Figure 9.4 Comparison of the cross sections per nucleon obtained with the original and a new π^0 sideband definition, for events selected with SLH and LGH triggers.

- Reconstruction Efficiency

It was determined that possible statistical fluctuations in the Monte Carlo sample contribute a 7% uncertainty to the resulting reconstruction efficiency weights (see section 6.5). The exception was in a first p_T bin, 3.5 to 4 GeV/c p_T, where a very limited acceptance for the SLH triggered events rendered it more sensitive to fluctuations – up to 15%.

The background under the omega was very different in the Monte Carlo sample employed to determine the reconstruction efficiency than in the data. A test was performed where the background (and signal) from the data was added to the Monte Carlo sample to simulate the background more realistically. That allowed us to use exactly the same techniques of ω signal extraction in MC as in the real data. The resulting signals were then corrected for the presence of ωs from the data and the reconstruction efficiency re-measured. The result agreed with the original measurement within a few percent. The MC reconstruction efficiency was also tested for stability in relation to several parameters – e.g., sensitivity to a cutoff value in p_T away from the generation threshold for a given sample, the method of combining of the reconstruction efficiency results from different samples, the selection of the binning for the mass histograms, variation in the fits to the π^0 signal used for the π^0 sideband subtraction, etc. A somewhat larger width for the omega meson in the Monte Carlo was observed as compared to the data, which had implications for the signal region definition and for accounting for non-Gaussian tails of the mass distribution. These various effects were found to contribute a combined additional uncertainty of 10% to the reconstruction efficiency measurement.

• Beam Normalization

The measurement of Live Triggerable Beam (LTB) used in the cross section had an uncertainty of 10%. The uncertainty was due to problems in or limitations of the electronic units, losses during the data acquisition and processing stages, systematic effects such as vetoing of backscattered events, upstream interactions, intricacies of the clean interaction requirements, etc.[70]

• Photon Conversion Correction

This correction was estimated to be uncertain up to 10% of its value[70] due to various approximations related to the amount and position of the material on the photon's path. It could therefore contribute a 1.7% uncertainty to the ω cross section measurement.

• Target Fiducial Region

The uncertainty associated with the measurement of the fraction of beam particles falling into the target fiducial region, as defined in section 7.2, was estimated to be 2%. This estimate was obtained by comparing the fraction of particles falling within the fiducial cut in the SSD planes upstream of the target and downstream of the target, and extrapolating to estimate the variations over the length of the target region.

Adding in quadrature all uncertainties discussed in this chapter (except for the uncertainties related to the background shape determination, which are listed separately in the cross section tables and were included in the plots), resulted in an overall uncertainty of 20% in the ω cross section at 4 GeV/c and 21% at 7 GeV/c p_T. All of the uncertainties estimated above are collected in Table 9.1. For comparison, the estimated statistical uncertainties for the three p_T intervals shown in Table 9.1 are 19%, 17% and 50% while the uncertainties related to the ω signal extraction are 9%, 7% and 16%.

	3.5-4. GeV/c	4.-5. GeV/c	7.-8. GeV/c
energy scale	5%	5%	6%
MC energy scale	5%	5%	6%
reconstruction eff. (stat)	15%	7%	7%
reconstruction eff. (syst)	10%		
trigger effects	17%	10%	2%
π^0 sideband subtr.	-	-	10%
rapidity dep.of rec.eff.	4.0%	3.5%	-
target fiducial cut	2%		
photon conv. corr.	1.7%		
normalization	10%		
TOTAL	28%	20%	21%

Table 9.1 Estimation of systematic uncertainties in the differential cross section measurement.

9.6 Systematic Uncertainty in the Measurement of α

For the nuclear dependence measurements, the systematic uncertainties came primarily from the following sources:

• Trigger or reconstruction efficiency effects that did not cancel completely between Be and Cu. This was estimated to contribute an uncertainty of 2% to the α_ω measurement.

• Offset of the targets relative to the beam defining elements. We implemented the target fiducial cut, but there remained a possibility that the fraction of the beam passing through the Cu target was somewhat different than that for Be. This was estimated to contribute a 1% uncertainty to the α_ω.

• Photon conversion correction, which was the largest correction that differed between the two targets. Some of the materials in the path of photons that were known to have contributed large uncertainties to this correction were the same for photons originating in Cu and Be, and hence a large fraction of the uncertainty canceled out. In the worst case scenario, with the remaining uncertainty fully correlated between the three photons of the omega, the correction was estimated to contribute an error of about 1% to the measurement of a nuclear dependence.

• Target definitions, which arise when vertices in Cu are separated from those in Be. The tails of the distribution of vertices lead to an estimation of an uncertainty of 0.5% from that source[70].

• Target specifications, which are known with a 0.7% uncertainty with respect to the dimensions of the targets and 0.3% uncertainty for the density of the targets[70]. That contributes uncertainties of half of that size to the value of alpha.

The overall systematic uncertainty attributed to the measurement of the nuclear dependence parameter α_ω is obtained by adding the above numbers in quadrature and is 2.5%.

The contribution to the uncertainty from the determination of the background shape and of the signal extraction was presented in section 8.5. These uncertainties are not completely uncorrelated between Cu and Be. They arise in part from the statistical fluctuations in the background, which clearly are independent. However, the systematic contribution to these uncertainties is related to the presence of "structures" in the background that exist as reflections of various resonances in the reconstructed mass distribution. Another source of a correlated systematic error could be due to π^0 sideband subtraction. Since some of the

assumptions about the shape of the background affect both targets in the same way, the uncertainty associated with them should partially cancel out. That would suggest that the uncertainty in the ratio σ_{Cu}/σ_{Be} resulting from the fitting is somewhat smaller than what was estimated in section 8.5.

9.7 Systematic Uncertainty in the Measurement of ω/π^0 Ratio

Trigger uncertainties are not expected to cancel out for this measurement, since the π^0s and ωs were affected differently by the trigger selection and because lower threshold triggers were additionally utilized in the π^0 cross section measurement. Reconstruction efficiency also contributes an error for each of the particles separately. For the π^0 it was estimated to be 5% at 4 GeV/c and 8% at $p_T > 6$ GeV/c[63]. The effects related to the uncertainty in the energy scale determination, beam normalization, etc., are expected to largely cancel out. The overall systematic uncertainty in the measurement of the ω/π^0 ratio was calculated to be 17% at p_T of 4 GeV/c and 18% at 7 GeV/c.

Chapter 10 Conclusions

This thesis reports on the production of ω mesons by 515 GeV π^- beam incident on Be and Cu targets. The data were collected using the E706 spectrometer, which consisted of a finely segmented lead liquid argon calorimeter and a high precision charged particle tracking system. The experiment triggered on events containing high p_T electromagnetic showers detected in the calorimeter. The ω meson was observed in E706 in the decay modes $\omega \rightarrow \pi^+\pi^-\pi^0$ and $\omega \rightarrow \pi^0\gamma$, but only the latter mode was used in the measurements reported in this thesis. The measurements were conducted at $\sqrt{s} = 31$ GeV.

10.1 Cross Sections and A-dependence Measurements

The p_T dependence of the inclusive ω cross section was studied in the central rapidity range and for transverse momentum of the ω extending from 3.5 to 8 GeV/c. The cross section was found to fall as p_T^{-n} with n = 8.7 $\pm$ 0.2. At this time, there is no other experimental data on ω production in this kinematic range available for comparison [1]. The slope of the measured cross section shows very good agreement with the prediction from the HERWIG Monte Carlo program.

The total inclusive cross section for ω production in the rapidity range from -0.5 to 0.75, and for ω p_T above 3.5 GeV/c, in 515 GeV/c π^- - nucleon interactions was measured to be 13.0 $\pm$ 1.0 $\pm$ 3.6 nb/(GeV/c)^2, and for p_T above 4.0 GeV/c,

[1] Several high energy experiments ($\sqrt{s}$ > 20 GeV) report on inclusive ω production by protons, π^-, or kaon beams, but the results are limited to below 2 GeV/c in transverse momentum [27][26][28][29]. A measurement of ω inclusive cross section in deep inelastic μ - p interactions at 280 GeV/c[71], and the production of ω mesons in $\bar{\nu}$- and ν- neon charged current interactions[72] in a similar kinematic range have also been reported.

to be $3.8 \pm 0.3 \pm 0.85$ nb/(GeV/c)^2, where the first of the errors quoted is statistical and the second the systematic uncertainty.

The nuclear dependence of ω production was found to be consistent with that measured in E706 for other neutral mesons; all measured mesons exhibit a small anomalous nuclear enhancement in the production cross section off various nuclei. The exponent α in the parametrization of the cross section as $\sigma = \sigma_0 A^\alpha$ was determined to be $1.12 \pm 0.07 \pm 0.07$ (statistical and systematic uncertainties, respectively). The measured value of α did not show any significant p_T dependence in the range under study.

10.2 The ω/π^0 Ratio

As noted in the Introduction chapter, the naive expectation for the ratio of directly produced vector to pseudoscalar mesons is 3/1 and is in disagreement with experimental results. The ω/π^0 ratio is well suited to the study of this apparent suppression of vector mesons (V) relative to pseudoscalar meson production (P). Firstly, both π^0s and ωs have the same valence quark content and hence any effects of valence quark recombination should be minimized. Sensitivity to the beam and target quark composition should also be minimal in this comparison. The ω and π^0 differ in isospin. However, experimental data on relative production rates of isovectors compared to isoscalars indicate that, for a given composition of valence quarks, the isospin states 0 and 1 are equally copiously produced[27][71]. In order to measure the V/P ratio using ωs and π^0s from our experiment, we need to subtract the indirect contribution to π^0 production stemming from the decay of other particles to π^0s. In contrast to several other experiments which measure V/P, the E706 data require a relatively small correction for indirect contributions because production of high mass states that could decay to a high p_T π^0 is kinematically greatly reduced in the high p_T range of our measurements.

Before correcting the ω/π^0 ratio for indirect contributions, we can compare the E706 measurement with the results from other experiments. Figure 10.1 presents available data on the ω/π^0 ratio in the center of mass energy range comparable to that of E706. The data are from a proton - proton ISR experiment[35] at $\sqrt{s}$ of 62 GeV, and from FNAL experiments[33][34] with proton beams on Be and C targets. In E706 we have determined that the effect of nuclear matter on high p_T π^0 and ω production is similar, hence a direct comparison of ω/π^0 ratio in proton - proton and proton - Be interactions is reasonable. Also, a Monte Carlo study suggests that this ratio may not be affected by the differences in $\sqrt{s}$, within the scope of the energy ranges considered. Similarly, it was verified that the ω/π^0 or V/P ratios were not sensitive to changes of beam and target particles. As can be seen from Figure 10.1, the ISR measurements at p_T of 3.5 to 7 GeV/c agree with the E706 results, and with the HERWIG MC prediction, within errors. The two ω/π^0 results at much lower p_T are not consistent with the MC prediction in that p_T region.

Figure 10.2 presents the ω/π^0 ratio obtained for ω and π^0 mesons produced directly in the fragmentation chain compared to the ratio of all ωs and π^0s observed in the "final state" (that is reconstructed from their respective decays). The HERWIG MC was used in this study. Figure 10.2(b), obtained from the ratio of two histograms in (a), gives an estimator for a correction for the indirect contribution to ω/π^0. Using this correction, we measure the direct ω/π^0 ratio as $1.21 \pm 0.1 \pm 0.2$. The systematic error reflects the uncertainty in the ω/π^0 ratio. No additional error was assigned as due to uncertainty from the MC prediction of direct versus indirect production rates. As illustrated in Figure 10.2(a), HERWIG indicates that the direct ω/π^0 ratio is independent of p_T within the range studied in E706, whereas the total ω/π^0 ratio exhibits a slow rise with p_T due to decreasing contributions from higher mass resonance decays.

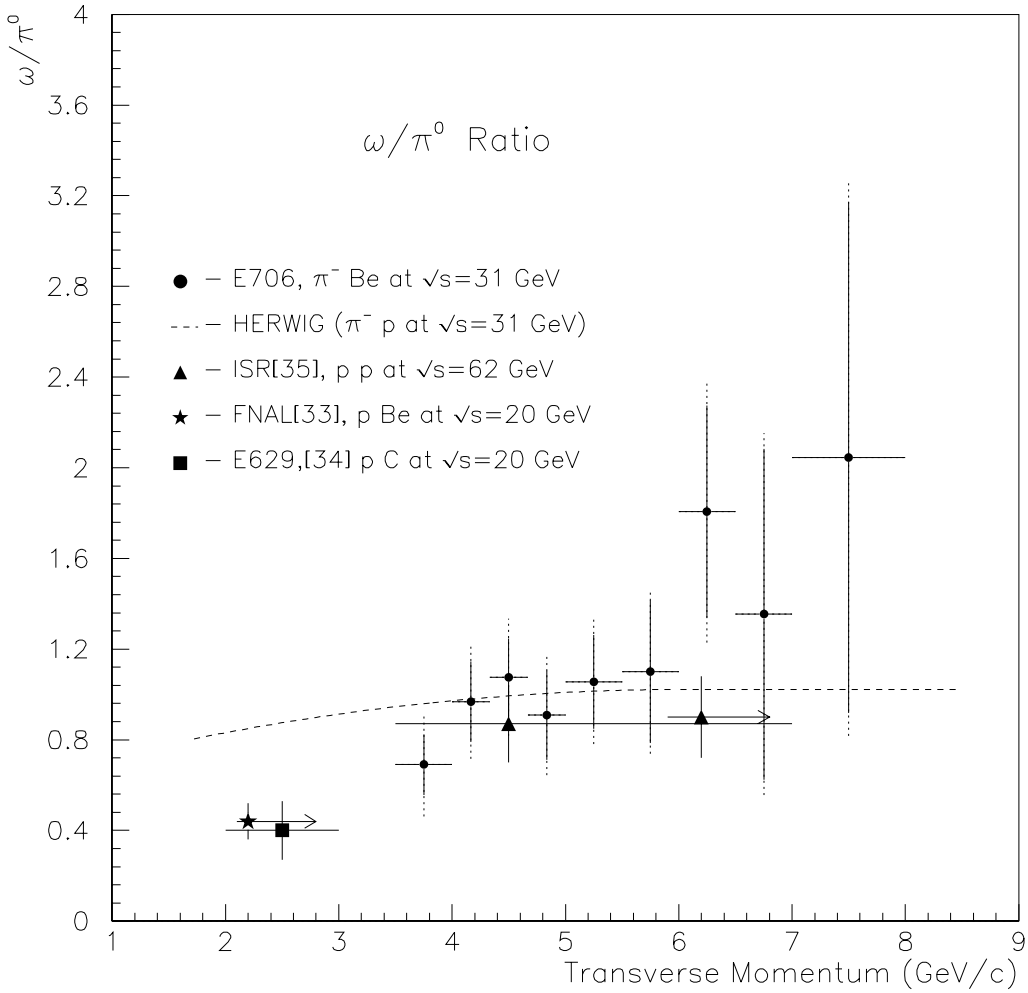

Figure 10.1 ω/π^0 ratio measured in E706 compared with other available ω/π^0 measurements. The solid error bars on E706 data indicate the statistical uncertainty. The extended error bars (dotted lines) give the combined statistical and systematic error. The Monte Carlo prediction from HERWIG is also shown.

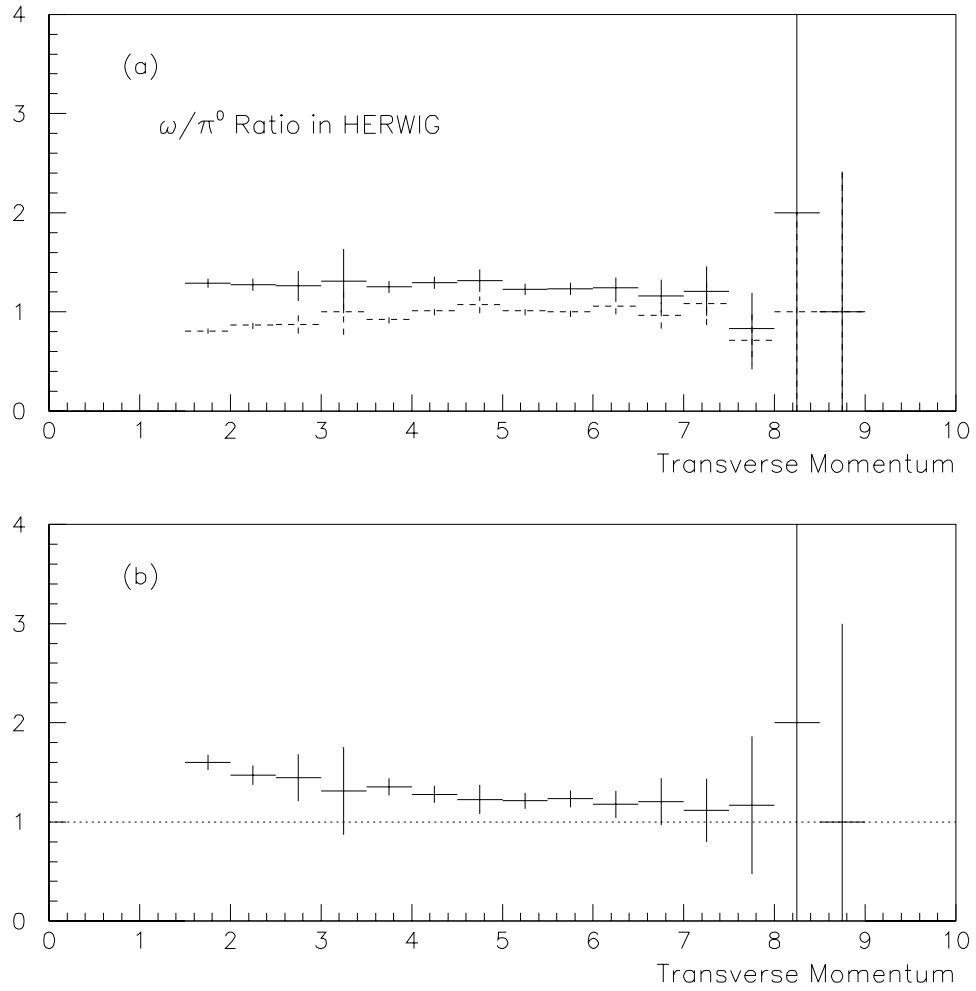

Figure 10.2 (a) The ω/π^0 ratio in HERWIG, for mesons produced directly in the fragmentation process (solid line), and for total meson production (dashed line); (b) Ratio of direct ω/π^0 to total ω/π^0 versus p_T.

The corrected, direct ω/π^0 ratio can be compared with a multitude of measurements of V/P. Figure 10.3 presents some of the available data on this ratio (converted to a more frequently reported form V/(V+P)). Vector and pseudoscalar mesons of different flavors are compared separately. The results from TASSO[19], JADE[20], HRS[21], TPC[73], NA27[27] and the ISR SFM experiment[74] are plotted versus the mass ratio of the corresponding mesons. Two more recent results, from OPAL[75] and DELPHI[23] collaborations, are also included in the plot. Also overlaid on the plot is the prediction based on a semi-classical tunneling model fit to the data, which gives (V/P = $3(M_P/M_V)^{0.5\pm0.1}$)[30][20]. The error bars represent both the statistical and systematic uncertainties quoted with the measurements. The E706 ω/π^0 ratio agrees very well with all other measurements of V/(V+P) for the u,d flavored mesons.

Since our measured ω/π^0 ratio is consistent with expectations based upon the HERWIG Monte Carlo, it supports the conclusion that the apparent V/P suppression for mesons in the u,d sector may be explained by a relative suppression of the available phase-space due to the mass difference between the heavier vector mesons and lighter pseudoscalars.

Lastly, we compare the ω/π^0 ratio with the $\rho^0/$"π^0", measured in an ISR SFM experiment[74] in proton - proton collisions at $\sqrt{s}$ of 62 GeV. In this experiment only charged particles were reconstructed, and therefore the flavor symmetric "π^0" production was obtained as an average from π^+ and π^- data. Figure 10.4 illustrates their result, measured in two different detector configurations, labeled A and B. Figure 10.4(b) shows that the E706 result for ω/π^0 is completely consistent with these data. This agreement is expected in the light of the arguments given in this chapter (ρ^0 and ω differ only by isospin). The V/(V+P) measurement from $\rho^0/$"π^0" data, reported by SFM experiment[74], is also included in Figure 10.3.

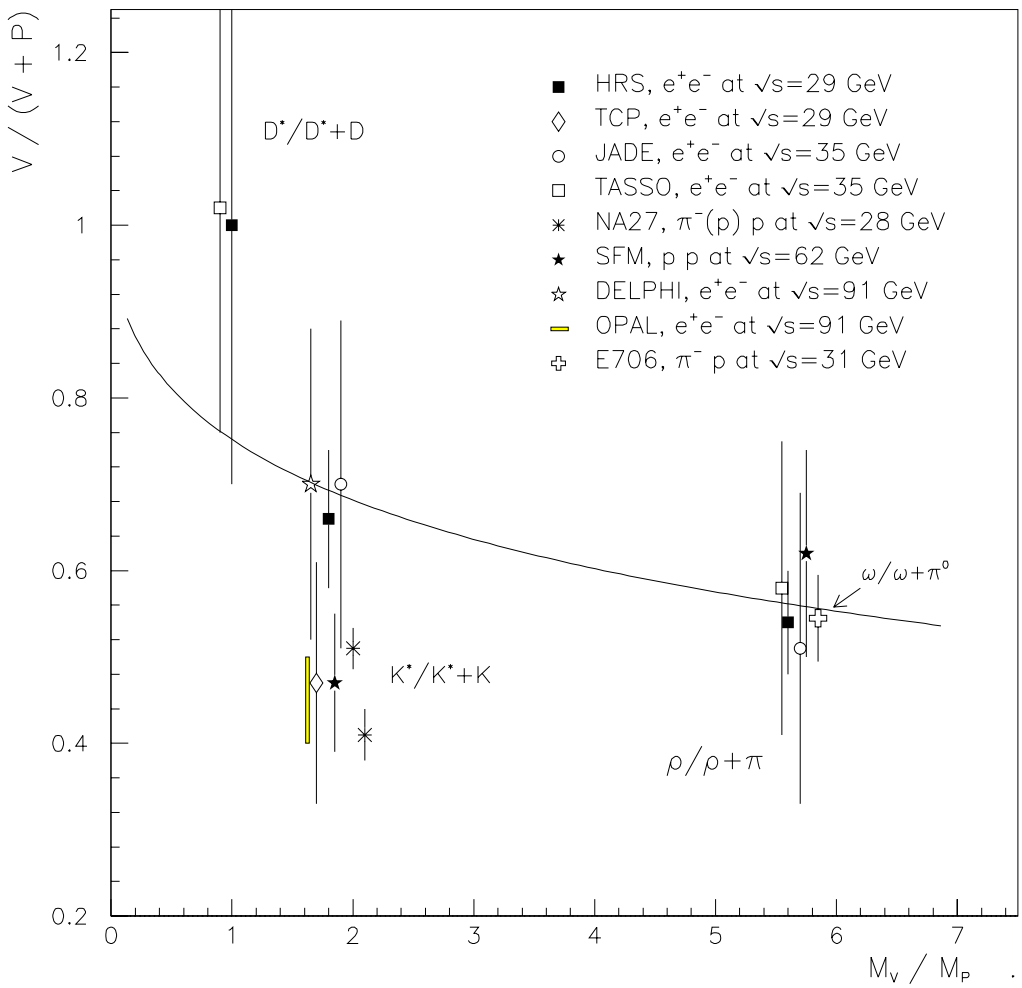

Figure 10.3 V/(V+P) ratio versus M_V/M_P, the ratio of vector to pseudoscalar meson masses, obtained for charm, strange, and u,d mesons in various experiments. Statistical and systematic errors are combined in quadrature. The curve represents the tunneling model prediction (fitted to match the data[20]) for this ratio.

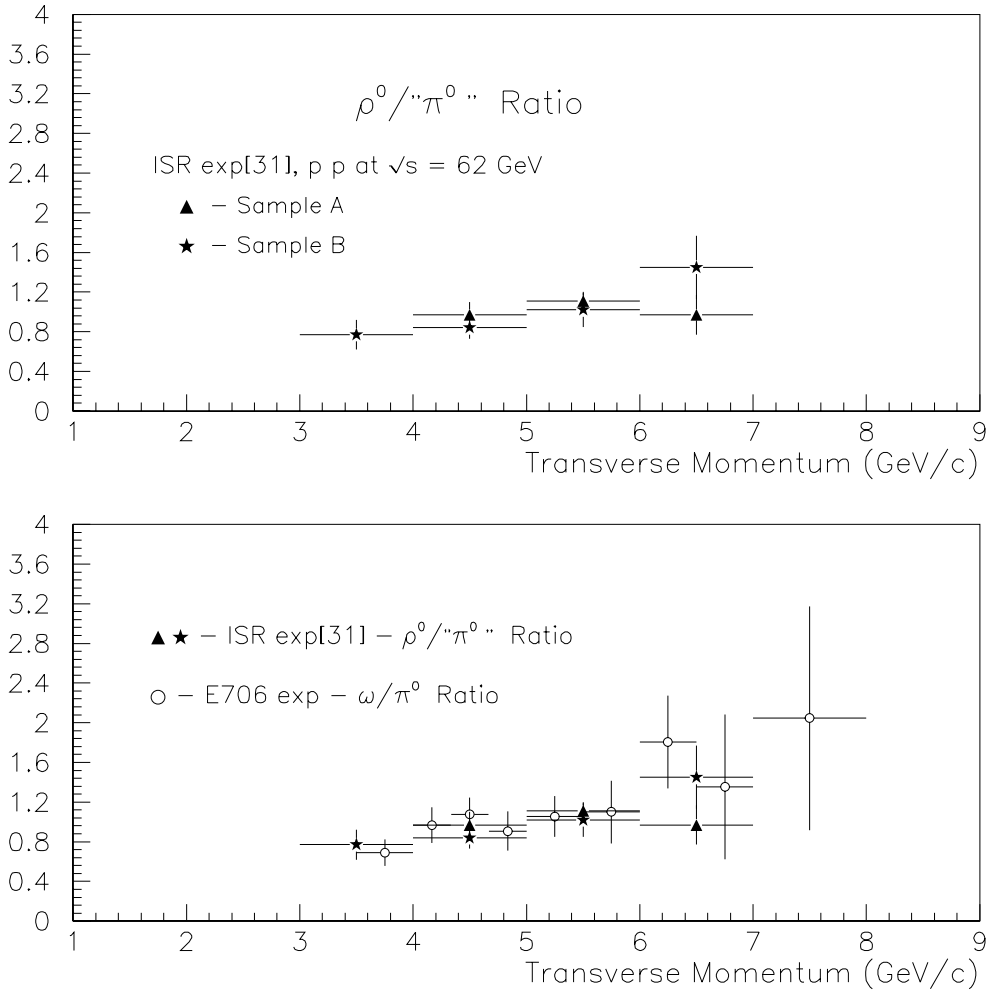

Figure 10.4 $2\rho^0/(\pi^+ + \pi^-)$ ratio obtained in ISR SFM experiment compared with the E706 measurement of ω/π^0. Only statistical errors are shown for both experiments.

References

[1] Proceedings of the Seventh Annual Rochester Conference, 1957.

[2] J. Sakurai, Ann. Phys. **11**, 1 (1960).

[3] B. Maglic *et al.*, Phys. Rev. Lett. **7**, 178 (1961).

[4] M. Gell-Mann, Phys. Lett. **8**, 214 (1964).

[5] G. Zweig, CERN report 8182/Th 401, 1964.

[6] M. Breidenbach *et al.*, Phys. Rev. Lett. **23**, 16 (1969).

[7] D. Perkins, *Introduction to High Energy Physics* (Addison-Wesley, New York, 1987), pp. 262–313.

[8] I. Aitchison and A. Hey, *Gauge Theories in Particle Physics* (IOP Publishing Ltd, New York, 1989), pp. 422–468.

[9] J. Owens, Rev. Mod. Phys. **59**, 465 (1987).

[10] T. Ferbel and W. Molzen, Rev. Mod. Phys. **56**, 181 (1984).

[11] S. Aid *et al.*, DESY 95-081, 1995.

[12] G. Alverson *et al.*, Production of Direct Photons and Neutral Mesons at Large Transverse Momenta from π^- and p Beams at 500 GeV/c, Phys. Rev. D **45**, 3899 (1992).

[13] G. Alverson *et al.*, Phys. Rev. D **48**, 5 (1993).

[14] G. Alverson *et al.*, Phys. Rev. D **49**, 3106 (1993).

[15] N. Varelas, π^0 Production at High Transverse Momenta from π^- Collisions at 520 GeV/c on Be and Cu Targets, Ph.D. thesis, University of Rochester, 1994.

[16] R. Roser, Eta Production at High Transverse Momentum by Negative 520 GeV/c Pions Incident on Beryllium and Copper Targets, Ph.D. thesis, University of Rochester, 1994.

[17] J. Cronin *et al.*, Phys. Rev. D **11**, 3105 (1975).

[18] D. Antreasyan *et al.*, Phys. Rev. Lett. **38**, 112 (1977).

[19] M. Althoff *et al.*, Phys. Lett. **126B**, 493 (1983).

[20] W. Bartel *et al.*, Phys. Lett. **145B**, 441 (1985).

[21] M. Derrick *et al.*, Neutral $K^*(890)$ and ρ^0 meson production in e^+e^- annihilation at $\sqrt(s) = 29$ GeV, Phys. Lett. **158B**, 519 (1985).

[22] P. Acton *et al.*, Phys. Lett. B **305**, 407 (1993).

[23] P. Abreu *et al.*, Phys. Lett. B **275**, 231 (1992).

[24] D. Buskulic *et al.*, CERN PPE/92-74, 1992.

[25] B. Adeva *et al.*, Phys. Lett. B **259**, 199 (1991).

[26] M. Aguilar-Benitez *et al.*, Vector meson production in π^-p interactions at 360 GeV/c, Z. Phys. C **44**, 531 (1989).

[27] M. Aguilar-Benitez *et al.*, Inclusive particle production in 400 GeV/c pp-interactions, Z. Phys. C **50**, 405 (1990).

[28] N. Agababyan *et al.*, Inclusive production of vector mesons in π^+p interactions at 250 GeV/c, Z. Phys. C **46**, 387 (1989).

[29] N. Agababyan *et al.*, Inclusive meson resonance production in K^+p interactions at 250 GeV/c, Z. Phys. C **41**, 539 (1988).

[30] B. Andersson *et al.*, Phys. Rep. **97**, 31 (1983).

[31] G. Marchesini, I.G. Knowles, M.H. Seymour, and B.R. Webber, *HERWIG Reference Manual*, v5.7 ed.

[32] T. Sjostrand, *Pythia 5.7 and Jetset 7.4 Physics Manual*, 1993.

[33] G. Donaldson *et al.*, Observation of inclusive ω production at large transverse momentum, Phys. Rev. D **21**, 828 (1980).

[34] J. Povlis *et al.*, Phys. Rev. Lett. **51**, 967 (1983).

[35] M. Diakonou *et al.*, Inclusive high-p_T ω and η prime production at the ISR, Phys. Lett. **89B**, 432 (1979).

[36] G. Ballocchi, A Measurement of π^0 Production at Low Transverse Momentum, Ph.D. thesis, University of Rochester, 1989.

[37] R. Benson, Characteristics of Forward Energy Production in Proton-Nucleus and Pion-Nucleus Collisions at 530 GeV/c, Ph.D. thesis, University of Minnesota, 1989.

[38] D. Brown, A Comparison of High Transverse Momentum Direct Photon and Neutral Pion Events in Negative Pion and Proton-Nucleus Collisions at 31.5 GeV Center of Mass Energy, Ph.D. thesis, Michigan State University, 1992.

[39] W. DeSoi, Construction and Performance of a Liquid Argon Calorimeter for Use in E-706 at the Fermi National Accelerator Laboratory, Ph.D. thesis, University of Rochester, 1990.

[40] S. Easo, Structure of Events Containing Direct Photon and Neutral Pion in Hadronic Interactions, Ph.D. thesis, Pennsylvania State University, 1989.

[41] K. Hartman, Hadronic Production of π^0 Pairs and Associated Event Structure at 530 GeV, Ph.D. thesis, Pennsylvania State University, 1990.

[42] V. Kapoor, Fragmentation Properties of Strange Particles Produced in High Transverse Momentum Hadronic Interactions, Ph.D. thesis, University of Delhi, 1990.

[43] I. Kourbanis, The A-dependence of Leading Particle Production by 800 GeV Protons, Ph.D. thesis, Northeastern University, 1989.

[44] A. Lanaro, π^0 Production with K^- and π^+ Beams at 530 GeV/c, Ph.D. thesis, University of Rochester, 1989.

[45] C. Lirakis, A Study of High Transverse Momentum η Production in 530 GeV/c Hadronic Interactions, Ph.D. thesis, Northeastern University, 1990.

[46] S. Mani, A Silicon Microvertex Detector for Studying QCD Jets Associated with Direct Photons, Ph.D. thesis, University of Pittsburgh, 1986.

[47] J. Mansour, High Transverse Momentum π^0 Production from π^- and p Beams at 530 GeV/c on Be and Cu, Ph.D. thesis, University of Rochester, 1989.

[48] E. Prebys, A Study of High Transverse Momentum Direct Photon Production from Beryllium and Copper Targets with 530 GeV/c Incident π^- and Proton Beams, Ph.D. thesis, University of Rochester, 1990.

[49] A. Sinanidis, Particles Produced in Association with High Transverse Momentum Single Photons and $\pi^0 s$ in Hadronic Collisions, Ph.D. thesis, Northeastern University, 1989.

[50] D. Skow, A Study of High Momentum Eta Meson Production, Ph.D. thesis, University of Rochester, 1990.

[51] P. Weerasundara, A Study of Large Transverse Momentum Direct Photon plus Away-Side Jet Production using 500 GeV/c proton and π^- Beams Incident on a Beryllium Target, Ph.D. thesis, University of Pittsburgh, 1993.

[52] C. Yosef, Production of High Transverse Momentum π^0 Mesons in Interactions of 530 GeV/c proton and π^- Beams on Beryllium and Copper Targets, Ph.D. thesis, Northeastern University, 1990.

[53] D. Striley, private communication.

[54] *VAXONLINE Users Guide*, FNAL Computer Department, Fermilab, Batavia, Ill., pN-252.

[55] L. Sorrell, The E706 Trigger System, Sept. 21, 1994, E706 Note 201.

[56] A. Maul, private communication.

[57] P. Chang, Massive $\pi^0\pi^0$,$\pi^0\pi^-$ and $\pi^0\pi^+$ Production from 515 GeV/c π^- Collisions with Beryllium and Copper Targets, Ph.D. thesis, Northeastern University, 1994.

[58] W. Chung, A Study of the Event Structure in High P_t Direct Photon and π^0 Production by 515 GeV/c π^- and 800 GeV/c Proton Beams Incident on Nuclear Targets, Ph.D. thesis, University of Pittsburgh, 1995.

[59] S. Blusk, Measurement of the Charm Cross Section in High p_T Collisions of 515 GeV/c π^- Beams Incident on a Beryllium and Copper Targets, Ph.D. thesis, University of Pittsburgh, 1995.

[60] L. de Barbaro and F. Lobkowicz, E706 Internal Note 167, 1988.

[61] J. Bacigalupi, Ph.D. thesis, University of California at Davis, 1995.

[62] G. Osborne, private communication.

[63] W. Dlugosz, The Production of High p_T π^0 Mesons in 515 GeV/c π^- - Nucleus Collisions, Ph.D. thesis, Northeastern University, 1994.

[64] M. Begel, private communication.

[65] H. Albrecht *et al.*, Inclusive Production of K*(892),ρ^0(770), and ω(783) Mesons in the Υ Energy Region, 1993, DESY 93-084.

[66] F. Carminati, *GEANT, Detector Description and Simulation Tool*, 1993.

[67] M. W. P. Aurenche, RAL-89-106 preprint, 1989.

[68] H. Frisch *et al.*, Phys. Rev. D **27**, 1001 (1983).

[69] M. Begel, private communication.

[70] G. Ginther, private communication.

[71] M. Arneodo *et al.*, ρ^0 and ω production in Deep Inelastic $\mu - p$ interactions at 280 GeV/c, Z. Phys. C **33**, 167 (1986).

[72] W. Wittek *et al.*, Production of $\rho(770)$, $\eta(550)$, $\omega(783)$ and f_2 (1270) mesons in $\bar{\nu}$ neon and ν neon charged current interactions, Z. Phys. C **44**, 175 (1989).

[73] H. Aihara *et al.*, Phys. Lett. **53**, 2378 (1984).

[74] A. Breakstone *et al.*, Production of meson resonances as leading particles in jets in proton-proton collisions at $\sqrt(s) = 62$ GeV at the CERN ISR, Z. Phys. **43**, 185 (1989).

[75] P. Acton *et al.*, Inclusive Neutral Vector Meson Production in Hadronic Z^0 Decays, 1992, CERN PPE/92-116.

Table of Contents

Curriculum Vitae — **iii**

Acknowledgments — **v**

Abstract — **vii**

Chapter 1 Introduction — **1**

1.1 Historic Overview . . . 1

1.2 Physics Goals of E706 . . . 7

1.2.1 Direct Photon and Neutral Meson Production . . . 7

1.2.2 Nuclear Dependence . . . 11

1.3 Measurement of Omega Meson Production . . . 12

Chapter 2 The Experimental Apparatus — **15**

2.1 Beam Line and the Target Region . . . 15

2.2 The Tracking System . . . 17

2.3 Liquid Argon Calorimeter . . . 19

2.3.1 EMLAC . . . 19

2.3.2 The Gantry and Cryogenic Support System . . . 21

2.3.3 HALAC . . . 23

2.4 Forward Calorimeter . . . 23

Chapter 3 Data Acquisition and Trigger Systems — **25**

3.1 Overview of the Data Acquisition System . . . 25

3.2 LAC DA System . . . 25

3.2.1 RABBIT System . . . 25

3.2.2 Fastbus System . . . 29

3.2.3 Amplifier Gain Measurement . . . 32

3.3 E706 Trigger 36

3.3.1 Beam and Interaction Definition 36

3.3.2 RABBIT PT System 38

3.3.3 Pretrigger Formation 38

3.3.4 Trigger Level 40

Chapter 4 Event Reconstruction **43**

4.1 Charged Particle Reconstruction 43

4.1.1 Momentum Scale 46

4.2 Electromagnetic Shower Reconstruction 47

4.2.1 Raw Data Preparation 47

4.2.2 Shower Finding Algorithm 49

4.2.3 View Photon Correlations 50

4.2.4 Energy Scale 51

Chapter 5 Search for the Omega Meson **59**

5.1 Data Selection 59

5.2 Definition of the π^0 Signal 62

5.3 Cos$\theta^\star$ Cut 63

5.3.1 Motivation 63

5.4 Structure in the Background 66

5.5 π^0 Sideband Subtraction 70

5.6 Definition of the ω Signal 74

Chapter 6 Monte Carlo **77**

6.1 Comparison of Data with Monte Carlo 78

6.2 Geometrical Acceptance 88

6.3 Trigger Acceptance for ω 89

6.4 Trigger Probability and the Cos$\theta^\star$ Cut. 93

6.5 Reconstruction Efficiency 95

Chapter 7 Analysis **105**

7.1 Muon Rejection 105

7.2 Vertex Cut 110

7.3 Trigger Probabilities 110

7.3.1 Trigger Turn On Curves 110

7.3.2 Rapidity Holes 116

7.4 Conversion Correction 117

7.5 Reconstruction of the Omega Signal 119

7.5.1 Summary of the Reconstruction Procedure 120

7.5.2 Summary of the Event Weighting 120

7.5.3 Fitting Procedure 122

7.5.4 Presentation of the Omega Signal 128

7.6 Other Corrections to the Cross Section 128

7.7 Invariant Cross Section Definition 149

Chapter 8 Results **151**

8.1 The ω Differential Cross Section Versus p_T 151

8.2 Integrated Omega Signal 159

8.3 ω/π^0 Ratio 163

8.4 Nuclear Dependence 169

8.5 Contribution of ω Decays to $\gamma\gamma$ Mass Spectrum 172

Chapter 9 Study of Systematic Uncertainties **179**

9.1 Trigger Uncertainty 179

9.2 Rapidity Dependence of the Reconstruction Efficiency 181

9.3 $cos\theta^\star$ Uncertainty 186

9.4 Background Subtraction 187

9.5 Other Systematic Uncertainties 188

9.6 Systematic Uncertainty in the Measurement of α 192

9.7 Systematic Uncertainty in the Measurement of ω/π^0 Ratio 194

Chapter 10 Conclusions **195**

10.1 Cross Sections and A-dependence Measurements 195

10.2 The ω/π^0 Ratio 196

References **203**

List of Tables

1.1 Summary of E706 data sets. 10
3.1 E706 trigger characteristics 41
5.1 1990 Data Subdivided into Trigger Sets 59
6.1 Number of MC ω events generated in various p_T bins. 86
7.1 Corrected number of ωs reconstructed in p_T bins (SLH trigger). 123
7.2 Number of unweighted ω events in p_T bins (SLH trigger). 126
7.3 Corrected number of ωs reconstructed in p_T bins (LGH trigger). 127
7.4 Number of unweighted ω events in p_T bins (LGH trigger). 127
7.5 Summary of corrections and multiplicative factors applied to data. 150
8.1 The ω invariant cross section per nucleon on a Be target. 151
8.2 The ω invariant cross section measured using SLH triggered events. 155
8.3 The ω invariant cross section measured using LGH triggered events. 155
8.4 The ω integrated invariant cross section. 160
8.5 ω/π^0 ratio versus p_T. 164
8.6 The α_ω exponent of the nuclear dependence for the ω production. 175
9.1 Estimation of systematic uncertainties in the differential cross section measurement. 192

List of Figures

1.1 Pictorial representation of a high p_T hadronic interaction. 5

2.1 Schematic layout of MWEST detectors. 16

2.2 Detailed view of the electromagnetic calorimeter. 20

2.3 The gantry and cryostat of the LAC. 22

3.1 Schematic diagram of the E706 DA system. 26

3.2 Modules of the RABBIT crate. 28

3.3 Partial schematic of LACAMP board. The electronic elements presented here were reproduced either 16 times (LACAMP channel) or 4 times (TVC system) on the LACAMP board. 30

3.4 Amplifier gains distribution for a typical cold start, divided into left R, right R, inner Φ, outer Φ groups for the Front Section of the LAC. 34

3.5 Amplifier gains distribution divided into left R, right R, inner Φ, outer Φ groups for Back Section of the LAC. 35

3.6 Trigger signal formation in the RABBIT PT system 39

4.1 K_S^0 and J/ψ signals used in the tracking system momentum calibration, after the momentum scale adjustment. 48

4.2 Time dependence of the reconstructed π^0 mass normalized to the Particle Data Group value. 52

4.3 Radial dependence of the reconstructed π^0 (solid points) and η (open points) masses relative to the PDG values. 54

4.4 E/P ratio for $\gamma \to e^+e^-$ electrons as a function of electron energy for data (black points) and Monte Carlo (open cirles). 56

4.5 The π^0 (solid points) and η (open points) masses as a function of the octant number, p_T and radial position of the particle. Masses are normalized to the PDG values. 57

5.1 (a) Positions of photons at the front face of the LAC after the fiducial volume cut was implemented. (b) E_{front}/E_{total} ratio for reconstructed LAC showers. Photon candidates with E_{front}/E_{total} below 0.2 are rejected. 61

5.2 Two photon invariant mass distributions in the π^0 region for $\gamma\gamma$ pairs that could form an object of $p_T > 4.0$ GeV/c when combined with other photons in the event. The four plots correspond to four different π^0 photon energy asymmetry regions. The $cos\theta^\star$ cut on $\pi^0\gamma$ pairs was applied. 64

5.3 Illustration of the definition of $\theta^\star$. 65

5.4 The $cos\theta^\star$ distribution for the π^0 γ pairs from the triggering octant for the data events (histogram) and Monte Carlo (points). Events were selected via SLH trigger and the distribution is shown for $\pi^0\gamma$ combinations with invariant mass between 0.6 and 0.96 GeV/c^2. 67

5.5 The $\pi^0\gamma$ mass distribution for all combinations of photons found in the triggering octant for which $4.0 < p_T < 10$ GeV/c and for π^0 energy asymmetry $A_{\pi^0} < 0.75$. Events were selected by the SLH trigger. 68

5.6 The $\pi^0\gamma$ mass distribution for all combinations of photons found in the triggering octant with π^0 energy asymmetry $A_{\pi^0} < 0.75$ after the $|cos\theta^\star| < 0.6$ cut. The p_T of $\pi^0\gamma$ is in the range $4.0 < p_T < 10$ GeV/c and the events were selected by the SLH trigger. 69

5.7 The π^0 γ mass distribution for photons passing $|cos\theta^\star| < 0.6$ when π^0 energy asymmetry $A_{\pi^0} > 0.75$ and the p_T of the 3 photons is in the range 4.0 to 10 GeV/c. 71

5.8 The $\gamma\gamma$ mass distribution of the larger energy photon of the π^0 candidate and the third photon originally used to make $\pi^0\gamma$. The candidate π^0 energy asymmetry A_{π^0} was > 0.75. The π^0 and η peaks are clearly visible indicating that a substantial fraction of the high asymmetry candidate π^0s are accidental combinations of a photon from another source with a photon from a π^0 (or η). 72

5.9 Monte Carlo events with high p_T ηs reconstructed in the $\pi^0\gamma$ mode, for π^0 energy asymmetry $A_{\pi^0} < 0.75$ (dashed line) and $A_{\pi^0} > 0.75$ (solid line). Dotted line shows the mass spectrum after the π^0 sideband subtraction. P_T of the combinations ranged from 4 to 10 GeV/c. 75

6.1 (a) Multiplicity of photons in events with reconstructed π^0s of $p_T > 3.5$ GeV/c for SLH triggers in data (histogram) and for MC events (open circles). (b) Number of photons in the triggering octant of these events. MC distributions were scaled to match the data histograms near the maximum of the distributions. 79

6.2 Energy distribution for photons with $0.11 < m_{\gamma\gamma} < 0.165$ GeV/c^2 (a) and their energy asymmetry A_{π^0} (b), for data (histogram) and Monte Carlo (open circles) events. Data events were selected via the SLH triggers, and MC events were weighted with SLH trigger probability. The MC distributions were scaled to the data. 80

6.3 Comparison of invariant mass distributions for $\gamma\gamma$ pairs between the data(histogram) and E706 Monte Carlo (open points). Events were preselected for omega analysis. The p_T of $\pi^0\gamma$ combinations was from 3.5 to 5 GeV/c (a) or from 5 to 10 GeV/c (b). The distributions were normalized at their peaks. 82

6.4 The mean π^0 mass versus π^0 p_T in the data (square) and the Monte Carlo (open circle) for π^0s with asymmetry $A_{\pi^0} < 0.75$; (b) is the comparison of the widths of the π^0 peak versus the p_T of the π^0. 83

6.5 Comparison of $\pi^0\gamma$ rapidity distribution between data (histogram) and E706 Monte Carlo (open circles), for $\pi^0\gamma$ combinations from the omega mass range. Dotted histograms were obtained with the dedicated omega Monte Carlo. The MC distributions are scaled to the data in an arbitrary manner. 84

6.6 Comparison of $\pi^0\gamma$ invariant mass distributions between data (histogram) and E706 Monte Carlo (open circles). Monte Carlo points were scaled to match the data histogram in the high mass region; $A_{\pi^0} < 0.75$ 87

6.7 (a) Effect of the fiducial region requirement on the 3 photons of the $\omega \to \pi^0\gamma$ versus ω p_T. (b) All 3 photons of the ω are required to fall into the fiducial region of the same octant. Only particles passing $|cos\theta^\star| < 0.6$ and $-0.75 < Y < 0.75$ cut are considered. 90

6.8 (a) Geometrical acceptance for $\omega \to \pi^0\gamma$ plotted as a function of rapidity Y; $|cos\theta^\star| < 0.6$ is required. Transverse momentum is between 4 and 5 GeV/c. (b) Percentage of ωs accepted within fiducial region of one octant versus the z-position of the event vertex. The points with large error bars correspond to the edges of the target where only a few events are reconstructed. 91

6.9 Simulation of the trigger acceptance for $\omega \to \pi^0\gamma$ events versus p_T. Even at 6 to 7 GeV/c p_T, well above the SLH trigger turn-on for a single local group, the acceptance is not 100 % due to the spread of ω's energy over several triggering units. 92

6.10 Probability to fire the SLH trigger for $\pi^0\gamma$ combinations from the ω mass region, with $p_T > 3.5$ GeV/c, for both data (histogram) and MC (points). The squares are for all reconstructed MC $\pi^0\gamma$s, the open circles are the same MC events weighted with the simulated SLH trigger. 94

6.11 (a),(c),(e) Trigger acceptance for $\omega \to \pi^0\gamma$ plotted as a function of ω's energy asymmetry, for 3 different ranges of p_T, relative to all geometrically accepted ω particles in this decay mode. (b),(d),(f) Trigger acceptance now calculated relative to all generated ωs, in the same p_T ranges. The fall-off of the geometrical acceptance towards -1 and 1 in the ω asymmetry evens out the overall (trigger and geometrical) acceptance. 96

6.12 $\pi^0\gamma$ invariant mass reconstructed in ω MC (solid points) compared to the true ω mass spectrum (one entry per one generated omega) as determined from the generated information (histogram); P_T of ω is from 3.5 to 6.0 GeV/c. Fig.(b) shows the difference between the two spectra. 100

6.13 Reconstruction efficiency, as defined in the text, combined with geometrical acceptance for the $\omega \to \pi^0\gamma$ versus ω's p_T for SLH (a) and LGH (b) triggers. 102

6.14 Reconstruction efficiency combined with geometrical acceptance for the $\omega \rightarrow \pi^0\gamma$ versus ω's p_T for SLH (a) and LGH (b) triggers. Only the Monte Carlo ωs which decay to photons not falling into any of rapidity holes were used in this measurement. 103

7.1 Directionality of the highest energy photon from two photon pairs with $p_T >$ 5.5 GeV/c in the π^0 mass region when (a) the veto wall fired (off-line) (b) there was no veto wall signal in the triggering octant. The peak at 0 corresponds to photons from the target direction. Positive directionality is indicative of muons. 108

7.2 The effect of muon cuts on the two photon mass spectrum in the π^0 region when $\pi^0\gamma$ p_T ranges from 7 to 8 GeV/c, in the events preselected for omega analysis. The absolute value of π^0 and γ energy asymmetry is less than 0.6 and all other reconstruction cuts are implemented. 109

7.3 Vertex distribution for the events pre-selected for ω analysis. 111

7.4 X-Y position of the reconstructed vertices in Cu (a) and Be (b). The transverse size and location of assorted relevant items are shown. 112

7.5 Turn-on curves for Single Local High trigger for four different regions of a typical octant as a function of trigger p_T. 114

7.6 Rapidity distributions for π^0 of $4.0 < p_T < 4.5$ for each of the octants of the detector (points). Data belong to trigger set 3 and were selected by the SLH trigger. Overlaid is the average of the octants rapidity distribution for this set, taken after the problematic regions have been removed. 118

7.7 Weighted $\pi^0\gamma$ mass plot and fits to the background and signal region in the vicinity of omega mass range. Third order polynomial combined with the Gaussian shape was used over a varied fit range. $\pi^0\gamma$ combinations are from the p_T range of 4.0 to 4.33 GeV/c, selected by the SLH (top plot) or LGH (bottom plot) trigger. 124

7.8 Weighted $\pi^0\gamma$ mass plot and fits to the background and signal region in the vicinity of omega mass range. Third order polynomial combined with the Gaussian shape was used over a varied fit range. $\pi^0\gamma$ combinations are from the p_T range of 5.5 to 6.0 GeV/c, selected via SLH (top plot) or LGH (bottom plot) trigger. 125

7.9 Corrected number of high p_T omegas ($\omega \rightarrow \pi^0\gamma$) reconstructed in $\triangle Y \triangle p_T$ intervals. Five different fit results, from Table 7.1 are plotted in each p_T bin. Error bars represent statistical errors. 129

7.10 Corrected number of high p_T omegas ($\omega \rightarrow \pi^0\gamma$) reconstructed in $\triangle Y \triangle p_T$ intervals in events selected via LGH triggers. Five different fit results, from Table 7.3 are plotted in each p_T bin. Error bars represent statistical errors. 130

7.11 Top: π^0 sideband subtracted weighted $\pi^0\gamma$ distribution reconstructed in E706 data. p_T of $\pi^0\gamma$ ranges from 3.5 to 4.0 GeV/c, rapidity is from -0.5 to 0.75. Third order polynomial (P3) and a Gaussian shape are fitted to the data. Bottom: Same signal after the background P3 function is subtracted. 131

7.12 Top: π^0 sideband subtracted weighted $\pi^0\gamma$ distribution reconstructed in E706 data. p_T of $\pi^0\gamma$ ranges from 4.0 to 4.33 GeV/c, rapidity is from -0.5 to 0.75. Third order polynomial (P3) and a Gaussian shape are fitted to the data. Bottom: Same signal after the background P3 function is subtracted. 132

7.13 Top: π^0 sideband subtracted weighted $\pi^0\gamma$ distribution reconstructed in E706 data. p_T of $\pi^0\gamma$ ranges from 4.33 to 4.67 GeV/c, rapidity is from -0.5 to 0.75. Third order polynomial (P3) and a Gaussian shape are fitted to the data. Bottom: Same signal after the background P3 function is subtracted. 133

7.14 Top: π^0 sideband subtracted weighted $\pi^0\gamma$ distribution reconstructed in E706 data. p_T of $\pi^0\gamma$ ranges from 4.67 to 5.0 GeV/c, rapidity is from -0.5 to 0.75. Third order polynomial (P3) and a Gaussian shape are fitted to the data. Bottom: Same signal after the background P3 function is subtracted. 134

7.15 Top: π^0 sideband subtracted weighted $\pi^0\gamma$ distribution reconstructed in E706 data. p_T of $\pi^0\gamma$ ranges from 5.0 to 5.5 GeV/c, rapidity is from -0.5 to 0.75. Third order polynomial (P3) and a Gaussian shape are fitted to the data. Bottom: Same signal after the background P3 function is subtracted. 135

7.16 Top: π^0 sideband subtracted weighted $\pi^0\gamma$ distribution reconstructed in E706 data. p_T of $\pi^0\gamma$ ranges from 5.5 to 6.0 GeV/c, rapidity is from -0.5 to 0.75. Third order polynomial (P3) and a Gaussian shape are fitted to the data. Bottom: Same signal after the background P3 function is subtracted. 136

7.17 Top: π^0 sideband subtracted weighted $\pi^0\gamma$ distribution reconstructed in E706 data. p_T of $\pi^0\gamma$ ranges from 6.0 to 6.5 GeV/c, rapidity is from -0.5 to 0.75. Third order polynomial (P3) and a Gaussian shape are fitted to the data. Bottom: Same signal after the background P3 function is subtracted. 137

7.18 Top: π^0 sideband subtracted weighted $\pi^0\gamma$ distribution reconstructed in E706 data. p_T of $\pi^0\gamma$ ranges from 6.5 to 7.0 GeV/c, rapidity is from -0.5 to 0.75. Third order polynomial (P3) and a Gaussian shape are fitted to the data. Bottom: Same signal after the background P3 function is subtracted. 138

7.19 Top: π^0 sideband subtracted weighted $\pi^0\gamma$ distribution reconstructed in E706 data. p_T of $\pi^0\gamma$ ranges from 7.0 to 8.0 GeV/c, rapidity is from -0.5 to 0.75. Third order polynomial (P3) and a Gaussian shape are fitted to the data. Bottom: Same signal after the background P3 function is subtracted. 139

7.20 Top: π^0 sideband subtracted weighted $\pi^0\gamma$ distribution reconstructed in E706 data. p_T of $\pi^0\gamma$ ranges from 3.5 to 4.0 GeV/c, rapidity is from -0.5 to 0.75. Third order polynomial (P3) and a Gaussian shape are fitted to the data. Bottom: Same signal after the background P3 function is subtracted. 140

7.21 Top: π^0 sideband subtracted weighted $\pi^0\gamma$ distribution reconstructed in E706 data. p_T of $\pi^0\gamma$ ranges from 4.0 to 4.33 GeV/c, rapidity is from -0.5 to 0.75. Third order polynomial (P3) and a Gaussian shape are fitted to the data. Bottom: Same signal after the background P3 function is subtracted. 141

7.22 Top: π^0 sideband subtracted weighted $\pi^0\gamma$ distribution reconstructed in E706 data. p_T of $\pi^0\gamma$ ranges from 4.33 to 4.67 GeV/c, rapidity is from -0.5 to 0.75. Third order polynomial (P3) and a Gaussian shape are fitted to the data. Bottom: Same signal after the background P3 function is subtracted. 142

7.23 Top: π^0 sideband subtracted weighted $\pi^0\gamma$ distribution reconstructed in E706 data. p_T of $\pi^0\gamma$ ranges from 4.67 to 5.0 GeV/c, rapidity is from -0.5 to 0.75. Third order polynomial (P3) and a Gaussian shape are fitted to the data. Bottom: Same signal after the background P3 function is subtracted. 143

7.24 Top: π^0 sideband subtracted weighted $\pi^0\gamma$ distribution reconstructed in E706 data. p_T of $\pi^0\gamma$ ranges from 5.0 to 5.5 GeV/c, rapidity is from -0.5 to 0.75. Third order polynomial (P3) and a Gaussian shape are fitted to the data. Bottom: Same signal after the background P3 function is subtracted. 144

7.25 Top: π^0 sideband subtracted weighted $\pi^0\gamma$ distribution reconstructed in E706 data. p_T of $\pi^0\gamma$ ranges from 5.5 to 6.0 GeV/c, rapidity is from -0.5 to 0.75. Third order polynomial (P3) and a Gaussian shape are fitted to the data. Bottom: Same signal after the background P3 function is subtracted. 145

7.26 Top: π^0 sideband subtracted weighted $\pi^0\gamma$ distribution reconstructed in E706 data. p_T of $\pi^0\gamma$ ranges from 6.0 to 6.5 GeV/c, rapidity is from -0.5 to 0.75. Third order polynomial (P3) and a Gaussian shape are fitted to the data. Bottom: Same signal after the background P3 function is subtracted. 146

7.27 Top: π^0 sideband subtracted weighted $\pi^0\gamma$ distribution reconstructed in E706 data. p_T of $\pi^0\gamma$ ranges from 6.5 to 7.0 GeV/c, rapidity is from -0.5 to 0.75. Third order polynomial (P3) and a Gaussian shape are fitted to the data. Bottom: Same signal after the background P3 function is subtracted. 147

7.28 Top: π^0 sideband subtracted weighted $\pi^0\gamma$ distribution reconstructed in E706 data. p_T of $\pi^0\gamma$ ranges from 7.0 to 8.0 GeV/c, rapidity is from -0.5 to 0.75. Third order polynomial (P3) and a Gaussian shape are fitted to the data. Bottom: Same signal after the background P3 function is subtracted. 148

8.1 The p_T dependence of the ω invariant production cross section per nucleon on a Be target. The error bars correspond to the statistical uncertainty and the uncertainty related to the signal extraction, combined in quadrature. The dotted line is a fit to the data using the phenomenological formula given in the text. 153

8.2 The p_T dependence of the ω invariant cross section measured in events selected via SLH trigger (triangles) and LGH trigger (open circles). The error bars correspond to the statistical uncertainty and the uncertainty related to the signal extraction, combined in quadrature. 154

8.3 The p_T dependence of the ω cross section measured in events selected via SLH trigger (triangles) compared to the Monte Carlo prediction of this dependence (dotted line). The MC curve was scaled to match the value of the averaged SLH and LGH cross sections measured in the $4.0 < p_T < 4.33$ bin. 157

8.4 The p_T dependence of the ω cross section measured in events selected via LGH trigger (open circles) compared to the Monte Carlo prediction of this dependence (dotted line). The MC curve was scaled to match the value of the averaged SLH and LGH cross sections measured in the $4.0 < p_T < 4.33$ bin. 158

8.5 $\pi^0\gamma$ invariant mass distribution and the background subtracted signal. Entries to these histograms were fully weighted with all weights related to the cross section determination. $\pi^0\gamma$ $p_T > 4.0$ GeV/c. Events were selected via the SLH trigger. 161

8.6 $\pi^0\gamma$ invariant mass distribution and the background subtracted signal. Entries to these histograms were fully weighted with all weights related to the cross section determination. $\pi^0\gamma$ $p_T > 4.0$ GeV/c. Events were selected via the LGH trigger. 162

8.7 The ω/π^0 ratio versus p_T calculated from ω cross sections measured in events selected by SLH or LGH triggers. 165

8.8 (a) The ω/π^0 ratio in HERWIG MC and the fit through the points. (b) The DATA result overlaid with the MC fit. 166

8.9 (a) The ω/π^0 ratio in the PYTHIA MC and the fit through the points. (b) The DATA result overlaid with the MC fit. 167

8.10 The ω/π^0 ratio versus p_T calculated with a different selection for π^0 sideband region (see section 9.9). (a) The DATA result compared to HERWIG MC prediction (curve). (b) The DATA result compared to PYTHIA MC prediction (curve). 168

8.11 (a) The p_T dependence of α_ω. (b) The α_ω measured over integrated p_T ranges, as indicated by the span of the horizontal bar at each point. Errors are both statistical and systematic, related to the fit of the background shape, combined in quadrature. 171

8.12 Comparison of α_ω measured in events satisfying SLH and LGH triggers. Linear fits to the data points are also shown. 173

8.13 Nuclear dependence of π^0 and ω production by 515 GeV/c beam. 174

8.14 (a) Two photon invariant mass reconstructed in the data using η analysis cuts in the events selected via SLH trigger. The p_T interval for $\gamma\gamma$ pairs is 4.0 to 4.5 GeV/c. (b) A background subtracted $\gamma\gamma$ mass distribution. The background was fit with the straight line outside of the region from 0.45 to 0.8 GeV/c^2 in mass. 177

8.15 The background subtracted $\gamma\gamma$ distribution from Figure 8.14(b) (points) overlaid with the expected $\gamma\gamma$ contribution from $\omega \to \pi^0\gamma$ (solid histogram). Number of MC ωs that contributed to this reflection was normalized to the measured spectrum for the ω meson, $\omega \to \pi^0\gamma$, in the data. The $\gamma\gamma$ pairs from MC and from the data have p_T from 4.0 to 4.5 GeV/c. The uncertainty in the prediction related to trigger effects was 10% compared to the total uncertainty of 20%. 178

9.1 Differential cross section per nucleon for the omega production by 515 GeV/c pions on Be target, measured in events selected via SLH trigger (triangles) and LGH trigger (open circles). No rapidity hole rejection was applied. ... 182

9.2 Comparison of the cross sections obtained with the trigger weight cutoff at 10 and 5, for events selected with SLH and LGH triggers. 183

9.3 Rapidity dependence of the geometrical acceptance (a),(d), reconstruction efficiency (b),(e), and combined geometrical acceptance and reconstruction efficiency function for the ω. The probability to satisfy a SLH trigger was required to be greater than 0.1 in the measurement of reconstruction efficiency. Events from p_T range 4 to 5 GeV/c (a),(b),(c) and from 6 to 8 GeV/c (d),(e),(f) were used. 185

9.4 Comparison of the cross sections per nucleon obtained with the original and a new π^0 sideband definition, for events selected with SLH and LGH triggers. 189

10.1 ω/π^0 ratio measured in E706 compared with other available ω/π^0 measurements. The solid error bars on E706 data indicate the statistical uncertainty. The extended error bars (dotted lines) give the combined statistical and systematic error. The Monte Carlo prediction from HERWIG is also shown. . 198

10.2 (a) The ω/π^0 ratio in HERWIG, for mesons produced directly in the fragmentation process (solid line), and for total meson production (dashed line); (b) Ratio of direct ω/π^0 to total ω/π^0 versus p_T. 199

10.3 V/(V+P) ratio versus M_V/M_P, the ratio of vector to pseudoscalar meson masses, obtained for charm, strange, and u,d mesons in various experiments. Statistical and systematic errors are combined in quadrature. The curve represents the tunneling model prediction (fitted to match the data[20]) for this ratio. 201

10.4 $2\rho^0/(\pi^+ + \pi^-)$ ratio obtained in ISR SFM experiment compared with the E706 measurement of ω/π^0. Only statistical errors are shown for both experiments. 202